# Ultra-fast, antenna-coupled mid-infrared quantum-well photodetectors

Quyang Lin

## ▶ To cite this version:

Quyang Lin. Ultra-fast, antenna-coupled mid-infrared quantum-well photodetectors. Micro and nanotechnologies/Microelectronics. Université de Lille, 2021. English. NNT : 2021LILUN009 . tel-03539479

HAL Id: tel-03539479

https://theses.hal.science/tel-03539479v1

Submitted on 21 Jan 2022

École doctorale n° 632: ENGSYS Sciences de l'ingénierie et des systèmes

THÈSE

pour obtenir le grade de docteur délivré par

**l'université de Lille**

**Spécialité : Electronique, photonique**

*présentée et soutenue publiquement le 18 octobre 2021 par*

**Quyang LIN**

Institut d'Electronique de Microélectronique et de Nanotechnologie (IEMN)

# Ultra-fast, antenna-coupled mid-infrared quantum-well photodetectors

# Détecteurs moyen-infrarouge à multi-puits quantiques ultra-rapides, à base d'antennes patch

devant le jury composé de:

*Rapporteur:* Prof. Gottfried Strasser Dr. Roland Teissier

*Examinateur:* Prof. Delphine Morini Prof. Ludovic Desplanque

*Directeur de thèse:* Dr. Stefano Barbieri

*Co-directeur de thèse:* Dr. Emilien Peytavit

A mes parents

心中有万千悔不能言说。

我永远爱你们。

致谢徐玉味，林天富

# Abstract

This Thesis is devoted to the conception, fabrication and experimental characterization of semiconductor-based ultra-fast photodetectors operating in the mid-infrared range (~3-12µm). More specifically, the detectors that I have developed, generally known as multi-quantum-well infrared photodetectors (QWIPs), rely on intersubband (ISB) transitions in a GaAs-$Al_{0.2}Ga_{0.8}As$ heterostructure, where an electron occupying the ground state of a quantum-well is photoexcited into an upper state, lying next to the energy continuum above the AlGaAs barriers.

In my work I have exploited a specific device geometry that allows light-coupling at normal incidence, based on a two-dimensional array of electrically connected metallic patch-antennas. Each antenna is obtained by sandwiching the GaAs-AlGaAs multi-quantum-well heterostructure between a top contact metal layer and a bottom metallic ground plane, effectively forming a square metal-dielectric-metal microcavity, where the fundamental TM electromagnetic mode is resonant with the energy of the ISB transition. Finally, to allow for broadband microwave extraction, the antenna array is connected to a 50Ω, monolithically integrated coplanar waveguide.

In the first part of my work I have designed the antennas for optimum detection at 10µm wavelength. This was done by running a set of simulations using a commercial electromagnetic solver based on the finite-difference time-domain (FDTD) method. Based on the results of the simulations I have fabricated a set of preliminary structures, without coplanar waveguide, to characterize the optical properties of the antenna array through Fourier transform micro-reflectance measurements. These measurements have allowed me to select the optimum patch array dimensions, namely the lateral size of the square-patch and the array periodicity.

The second part of my work has been dedicated to the fabrication of the complete QWIP detector, including the monolithically integrated coplanar waveguide. In these detectors the size of the two-dimensional antenna array has been kept to a minimum, without compromising the radiation collection, in order to reduce as much as possible the device parasitic RC time constant and therefore maximize the detector speed. I have fabricated two generations of detectors relying on two slightly different active regions, respectively based on a bound-to-bound and a bound-to-continuum design. In the final part of my PhD I have also fabricated a third generation of devices, where the patch array, rather than to a coplanar waveguide, is connected to a spiral THz antenna. This device has not been characterized in this work and I present its relevance in the context of this Thesis in the perspectives.

The last part of the Thesis is dedicated to the electro-optical characterization of the fabricated detectors. First, I have measured the dark current, the polarization dependence, and the dc photo-response, that allowed me to determine the responsivity at 77K and 300K. Then I characterized the microwave frequency response of the detectors. To this end I have participated to the setup of an experimental apparatus based a high-speed (67GHz) cryogenic probe station. In this apparatus the beams of two quantum cascade lasers (QCLs) emitting at 10.3µm wavelength, are simultaneously focused on the QWIP detector to generate a heterodyne signal at their difference frequency. By temperature/current tuning the emission wavelength of one QCL the heterodyne frequency can be swept continuously, thus allowing the measurement of the detector frequency response with the help of a spectrum analyzer. At room temperature I obtain a flat frequency response up to 70GHz, solely limited by the bandwidth of the acquisition electronics. This is the broadest RF- bandwidth reported to date for a QWIP photodetector. To analyze the experimental data, I have modelled the electrical behavior of the QWIP using a small-signal equivalent circuit model. Using this model I have reproduced quantitatively the detector frequency response, and, thanks its very short RC-limited response time (~1ps), I was also able to extract the values of the carrier's recombination and transit times.

At the end of the Thesis I summarize and discuss the results obtained, give some guidelines for the optimization of future ultrafast QWIP detectors and, finally, present the future possible development of the work done in my Thesis. In particular I discuss the possibility to exploit the demonstrated devices as mid-infrared photo-mixers for the generation of sub-mm and THz radiation.

# Résumé

Cette Thèse est consacrée à la conception, la fabrication et la caractérisation expérimentale de photodétecteurs ultra-rapides à base de semi-conducteurs fonctionnant dans le moyen infrarouge (~3-12µm). Plus précisément, les détecteurs que j'ai développés, généralement appelés photodétecteurs infrarouges à multi-puits quantiques (QWIP), reposent sur des transitions inter-sous-bandes (ISB) dans une hétérostructure GaAs/$Al_{0.2}Ga_{0.8}$ As, où un électron occupant l'état fondamental d'un puits quantique est photoexcité dans un état supérieur, se trouvant à côté du continuum d'énergie au-dessus des barrières d'AlGaAs.

Dans mon travail, j'ai exploité une géométrie de dispositif spécifique qui permet le couplage de la lumière à incidence normale, basée sur un réseau bidimensionnel d'antennes patch métalliques connectées électriquement. Chaque antenne est obtenue en intercalant l'hétérostructure multipuits quantique GaAs-AlGaAs entre une couche métallique de contact supérieure et un plan de masse métallique inférieur, formant ainsi une microcavité carrée métal-diélectrique-métal, où le mode électromagnétique TM fondamental est en résonance avec le l'énergie de la transition ISB. Enfin, pour permettre l'extraction de micro-ondes sur une large bande, le réseau d'antennes est connecté à un guide d'onde coplanaire 50Ohm, intégré de façon monolithique.

Dans la première partie de mon travail, j'ai conçu les antennes pour une détection optimale à une longueur d'onde de 10 µm. Cela a été fait par le biais de simulations à l'aide d'un solveur électromagnétique commercial basé sur la méthode des éléments finis (FDTD). Sur la base des résultats des simulations, j'ai fabriqué un ensemble de structures préliminaires, sans guide d'onde coplanaire, afin caractériser les propriétés optiques du réseau d'antennes par des mesures de micro-réflectance par transformée de Fourier. Ces mesures m'ont permis de sélectionner les dimensions optimales du réseau de patchs, à savoir la taille latérale du patch carré et la périodicité du réseau.

La deuxième partie de mon travail a été consacrée à la fabrication du détecteur QWIP complet, y compris le guide d'onde coplanaire intégré. Dans ces détecteurs, la taille du réseau d'antennes bidimensionnelles a été réduite au minimum, sans pour autant compromettre la collection de la radiation incidente, afin de réduire autant que possible la constante de temps RC du dispositif et donc de maximiser la vitesse du détecteur. J'ai fabriqué deux générations de détecteurs reposant sur deux régions actives légèrement différentes, respectivement basées sur une transition ISB de type lié-lié et lié-continu. Dans la dernière partie de mon doctorat, j'ai également fabriqué une troisième génération de dispositifs, où le réseau de patchs, plutôt qu'à un guide d'onde coplanaire, est connecté à une antenne THz spirale. Ce dispositif n'a pas été caractérisé dans ce travail et je présente sa pertinence dans le cadre de cette Thèse dans les perspectives.

La dernière partie de la Thèse est consacrée à la caractérisation électro-optique des détecteurs fabriqués. Tout d'abord, j'ai mesuré le courant d'obscurité, la dépendance à la polarisation et la photoréponse continue, ce qui m'a permis de déterminer la responsivité à 77K et 300K. Ensuite, j'ai caractérisé la réponse en fréquence micro-onde des détecteurs. A cet effet, j'ai participé à la mise en place d'un banc expérimental basé sur une station sous pointes cryogénique large bande (67GHz). Dans ce banc, les faisceaux de deux lasers à cascade quantique (QCL) émettant à une longueur d'onde de 10.3 µm sont focalisés simultanément sur le détecteur QWIP pour générer un signal de battement hétérodyne à leur différence de fréquence. En changeant la température/courant d’un QCL, la fréquence de battement hétérodyne peut être balayée en continu, permettant ainsi la mesure de la réponse en fréquence du détecteur à l'aide d'un analyseur de spectre. A température ambiante j'obtiens une réponse en fréquence plate jusqu'à 70GHz, uniquement limitée par la bande passante de l'électronique d'acquisition. Il s'agit de la bande passante RF la plus large mesurée à ce jour pour un photodétecteur QWIP. Pour analyser les données expérimentales, j'ai modélisé le comportement électrique du QWIP à l'aide d'un modèle de circuit équivalent petit-signal. À l'aide de ce modèle, j'ai reproduit quantitativement la réponse en fréquence du détecteur et, grâce à sa constante de temps RC de très courte (~1ps), j'ai pu également extraire les valeurs des temps de recombinaison et de transit des porteurs.

À la fin de la Thèse, je résume et discute les résultats obtenus, donne quelques lignes directrices pour l'optimisation des futurs détecteurs QWIP ultrarapides et, enfin, présente le développement possible des travaux effectués dans ma Thèse. En particulier, je discute autours de la possibilité d'exploiter les dispositifs démontrés en tant que photo-mélangeurs moyen-infrarouges pour la génération de rayonnement sub-mm et THz.

# Résumé grand public

Cette Thèse est consacrée à la conception, la fabrication et la caractérisation expérimentale de photodétecteurs ultra-rapides à base de semi-conducteurs. Ces détecteurs fonctionnent dans la région du moyen-infrarouge, qui couvre grosso modo la gamme spectrale allant de 3µm a 12µm. L’objectif principal de mon travail a été celui de démontrer des détecteurs avec des temps de réponse allant au-delà de l’état de l’art. Pour ce faire j’ai utilisé une géométrie s’appuyant sur un réseau d’antennes métalliques. Cette architecture permet de fabriquer des détecteurs de taille inférieure à la longueur d’onde, sans pour autant compromettre la collection de la radiation incidente. Ceci permet de réduire de façon considérable la surface du détecteur par rapport à des architectures plus standard. Ainsi on atteint des capacités parasites extrêmement réduites, qui amènent à des temps de réponse de l’ordre de la ps ( $10^{-12}$ s). Grace à cette propriété j’ai pu démontrer des bandes passantes (limitées par la vitesse de l’électronique d’acquisition) qui vont au-delà de 70GHz à température ambiante.

# Preface

Through the maturation of III-V semiconductor technology, research on intersubband (ISB) optoelectronic devices has developed rapidly during the last three decades due to their potential as efficient photon sources and detectors in the mid-infrared (MIR). Mainstream interband MIR semiconductor photodetectors, like HgCdTe (MCT) detectors, despite their high-responsivity and low-noise are intrinsically slow owing to their long carrier life time, on the ns timescale. Instead, MIR photodetectors based on ISB transitions in III-V heterostructures, also called quantum-well infrared photodetectors (QWIPs), are very well adapted for ultra-high-speed operation up to several hundreds of GHz thanks to the intrinsically short carrier life time. To date, ultrafast QWIPs, with bandwidths of a few tens of GHz, have relied on a conventional "mesa" geometry, where the active semiconductor structure sits on top of a semi-insulating substrate. In order to cope with ISB transition selection rules this geometry requires illumination from the substrate at 45deg incidence, which is unpractical for applications

In this context, the main motivation of this work is to demonstrate an optimized QWIP detector that allows at the same time illumination at normal incidence, and ultrafast operation beyond the current state of the art. To this end I have realized a detector based on a ~350nm-thick GaAs/$Al_{0.2}Ga_{0.8}As$ multi-quantum-well heterostructure, and consisting of a 50$\Omega$ coplanar waveguide, monolithically integrated with a 2D-array of sub-wavelength patch antennas, electrically interconnected by suspended bridges. With this device architecture, we have obtained responsivities of 0.15A/W and 1.5A/W respectively at 300K and 77K, together with a flat frequency response up to 70GHz at room temperature, solely limited by the bandwidth of the detection electronics. This represents the broadest RF-bandwidth reported to date for a quantum-well mid-infrared photodetector (QWIP). Thanks to a small-signal equivalent circuit model we extract a parasitic capacitance of ~30fF, corresponding to the static capacitance of the antennas, yielding a RC-limited 3dB cutoff frequency >150GHz at 300K. Using this model, we have reproduced quantitively the detector frequency response and found an intrinsic roll-off time constant as low as 1ps at room temperature.

## Structure of the thesis

**Chapter 1** presents a general introduction on the infrared spectral range, and black body radiation. I also present a brief history of IR detectors, and their main applications.

**Chapter 2** describes the physics of semiconductor photodetectors, and introduces the main physical parameters used to quantify their performance, e.g. photocurrent, responsivity, noise, noise equivalent power (NEP), detectivity, and response time. In the second part I present a comparison between the main interband and intersubband MIR semiconductor detectors and materials, encompassing their technology, cost and performance in terms of detectivity, operating temperature, speed etc. By illustrating their advantages and drawbacks I justify the reasons why we choose the GaAs/AlGaAs semiconductor materials system to realize ultra-fast MIR QWIP detectors.

**Chapter 3** begins by presenting the basic concept and operation of QWIP detectors, together with the related technology and applications. I then introduce the physics of ISB transitions in semiconductor multi-quantum-well heterostructures: starting from the envelope function Hamiltonian, I derive the electronic states wavefunctions, the oscillator strength and absorption coefficient. Since the operation of photoconductive QWIPs is similar to that of extrinsic semiconductor detectors, starting from the conventional theory of photoconductivity, I revisit the figures of merit for QWIPs: photocurrent, responsivity, dark current, detector noise, NEP, and detectivity. In this chapter, I also introduce QWIPs based on patch antenna resonators (PARs), the structure of choice for this Thesis. After describing the electromagnetic properties of PARs, I derive the figures of merit of PAR QWIPs and compare them to QWIPs based on conventional mesas. In the last part of the Chapter I present ultra-fast QWIPs, from their intrinsic response time, to the use of heterodyne detection to determine their frequency response, and, finally, the derivation of a small-signal electrical circuit model.

**Chapter 4** begins by describing the two active region designs used for the growth of the QWIP heterostructures. The first of these structures has been processed in a standard mesa geometry in order to experimentally verify the position of the ISB transition energy through dc photocurrent measurements. Based on this data I then present the results of the simulations based on a commercial FDTD solver with the objective of defining the optimum QWIP PAR array geometry, in order to achieve the highest possible radiation absorption. The parameters optimized through the simulations are (i) the patch size, (ii) the array periodicity, and (iii) the width of the metallic suspended bridges connecting the patches together. I then conclude this part by describing the design of the integrated 50Ω coplanar waveguide (CPW). In the second part of the Chapter I describe in detail the fabrication process and technology used to realize this PARs QWIP.

**Chapter 5** describes the electro-optical characterization of the ultrafast QWIP, including the optical and electrical *dc* characterization and the frequency response. I begin by presenting the PAR array reflectivity spectra measured through FTIR microscopy, as a function of the period of the array to show the achievement of the critical coupling condition. I then present the dc photocurrent spectra, followed by the full dc electrical characterization of the optimized QWIP PAR array integrated with the 50Ω CPW. From these measurements I derive the polarization dependence, photocurrent, dark current, and responsivity. Then I introduce the heterodyne experimental setup used to characterize the detector's frequency response at different temperatures and applied biases, and present the results of the measurements. In the last part of the Chapter I describe the analysis of the QWIP frequency response obtained using the small-signal electrical circuit model presented in Chapter 3: by relying on the measurements of the QIWP impedance, this model allows me to take into account the effect of the QWIP Schottky contacts and to derive the carrier’s capture and transit times. I conclude the Chapter by briefly discussing the results.

**Chapter 6** summarizes the main results of this Thesis and presents the possible future development of my work.

# Contents

# 1. General introduction

## 1.1 The mid-infrared spectral range

From higher to lower frequencies, the electromagnetic spectrum can be separated into the following regions: Gamma-ray, X-ray, Ultraviolet, Visible, Infrared, Microwave, and Radio frequency (Fig. 1.1). Infrared radiation was discovered in 1800 by Sir William Herschel [1], and broadly covers the wavelength range from about 800 nm (frequency 430 THz) up to 1 mm (300 GHz), lying between the Visible, and Microwave range.

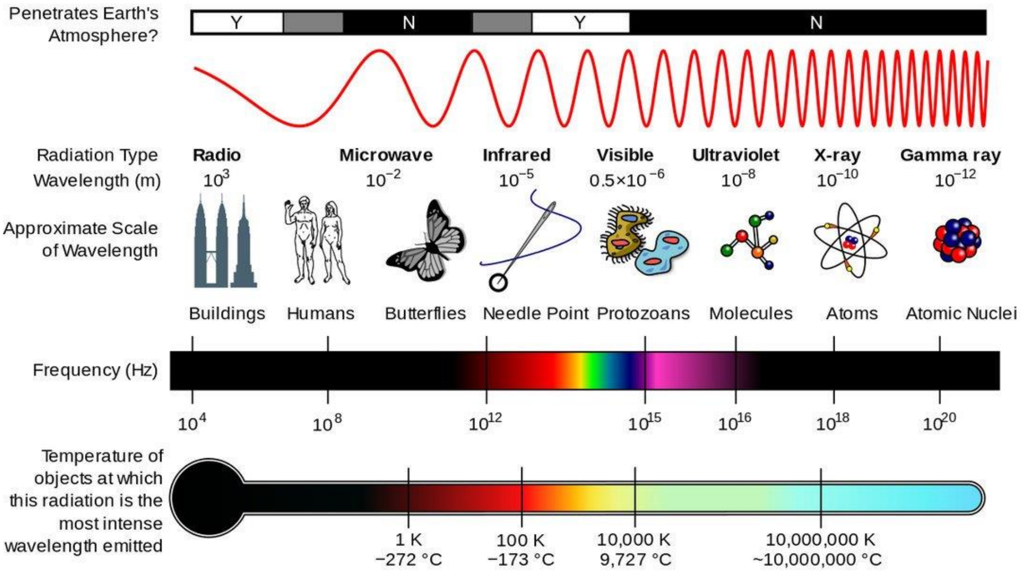

Figure 1.1. Frequency bands of the electromagnetic spectrum [2].

Any object above absolute zero emits electromagnetic radiation. According to Planck's law (which will be explained in detail in Section 1.2), the intensity and peak wavelength of the emitted radiation is related to the object's thermodynamic temperature. As a result, objects in nature emit typically in the infrared range. This property allows the observation of these objects by infrared thermal imaging without the help of an outside light source. Instead, in the visible range most objects are secondary sources, i.e. we see them because they reflect or diffuse the light generated by the sun or other primary sources. Thanks to its properties, infrared (IR) radiation covers a wide range of applications in disparate fields, such as medicine, astronomy, agriculture, communications, etc. In the context of communications, compared to the visible, IR radiation has a better penetration in fog and haze. This is the reason why it has been explored for Free Space Optical Communications for both civil and military applications [3]. In addition, compared to microwave and radio-frequency waves the advantage of IR free space optical links is three-fold: (i) orders of magnitude broader bandwidth; (ii) no licensing concerns since the IR spectrum is unlicensed; (iii) higher directionality, thus providing a higher degree of security from interception by a third party.

The IR range is divided in the following spectral regions: (i) the far-IR (FIR, 25-1000µm), (ii) the mid-IR (MIR, 2.5-25µm), and (iii) the near-IR (NIR, 0.7-2.5µm). In this thesis, we are interested in the MIR. This region is further divided into the following ranges: (i) Mid-Wavelength Infrared (MWIR), from 3 to 8 µm and (ii) Long-Wavelength Infrared (LWIR), from 8 to 15 µm

## 1.2 Blackbody radiation

In this Section, we present the blackbody thermal radiation which constitutes the standard calibration source for photoconductive devices the MIR [4].

Objects are made of continuously vibrating atoms and molecules. At higher temperatures atoms vibrate faster, which generates photons of higher energy. As a result, any object kept at a temperature above absolute zero will emit electromagnetic radiation. The spectrum of the emitted radiation will depend on the temperature of the object and on its composition. An ideal object at a given temperature T, that absorbs all radiation incident on it at all wavelengths, i.e. without any reflection and transmission, is called *blackbody*. The emission spectrum of a blackbody, which, by Kirkoff principle, is identical to its absorption spectrum, has a characteristic, continuous frequency distribution that depends only on its temperature. The spectral irradiance of a blackbody is described by Planck's law [5]. It is the power emitted per unit area and wavelength:

$$M(\boldsymbol{\lambda}, \boldsymbol{T}) = \frac{\boldsymbol{2\pi h c^2}}{\boldsymbol{\lambda^5}\left(\boldsymbol{exp}\left\{\frac{\boldsymbol{hc}}{\boldsymbol{\lambda k_B T}}\right\}\boldsymbol{-1}\right)} \quad [\mathrm{W\mu m^{-1}cm^{-2}}] \quad (1.1),$$

where $h$ is the Planck constant, $\lambda$ is the wavelength, $c$ is the speed of light, $k_\mathrm{B}$ is the Boltzmann constant, and $T$ is the temperature of the blackbody. The spectral irradiance for different blackbody temperatures is shown in Fig.1.2.

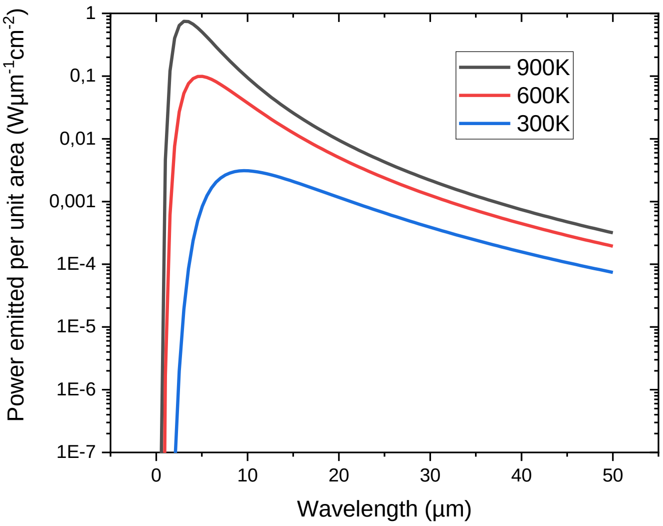

Fig. 1.2 Blackbody spectral irradiance with different temperatures vs. wavelength.

At a given temperature, the total emitted power per unit surface is obtained by integrating Eq.(1.1) over **λ**, yielding the well-known Stephan-Boltzmann equation:

$$M(T) = \int_0^{\infty} M(\lambda, T) d\lambda = \sigma T^4 \quad [\mathrm{W/m^2}] \quad (1.2),$$

where $\sigma = 2\pi^5 k_B / 15c^2h^3 = 5.67\times10^{-8}$ W/m$^2$K$^4$.

By definition, a blackbody presents the highest possible irradiance, which means that the irradiance of a real object is always lower. Therefore, to characterize the power emitted by a real object it useful to define the *emissivity*, as the ratio between the object's spectral irradiance and that of a blackbody at the same temperature:

$$\varepsilon(\lambda, T) = \frac{M(\lambda,T)_{object}}{M(\lambda,T)_{blackbody}} \quad (1.3),$$

$\varepsilon(\boldsymbol{\lambda},\mathrm{T}) \leqslant 1$. For real bodies, the emissivity depends on wavelength. In practice for many materials used in engineering, assuming a constant emissivity is a good approximation: a body with constant emissivity is called a *greybody*. For a greybody the total emitted power per unit surface is then:

$$M^{gb}(T) = \varepsilon\sigma T^4 \quad [\mathrm{W/m^2}] \quad (1.4).$$

As shown in Fig. 1.2, as temperature increases, the peak position of the blackbody spectral irradiance is shifted toward higher energy (shorter wavelength). For a blackbody with a temperature close to 300K, the wavelength corresponding to the maximum spectral irradiance is around 10μm, which is the reason why thermal imaging generally exploits radiation in the MIR. As a result, for imaging applications, it is important to evaluate atmospheric transmission in this frequency range. In Fig. 1.3 we report the MIR transmission spectrum of the atmosphere, together with the molecules with the strongest absorption lines. Two main transmission windows can be identified: between 3 and 5µm (so-called Mid-Wavelength Infrared - MWIR), and between 8 and 13µm (so-called Long-Wavelength Infrared - LWIR).

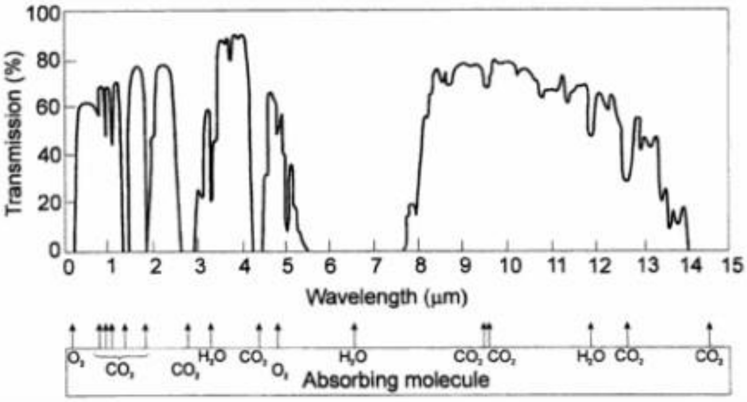

Fig. 1.3 Transmission of atmosphere from 0-15µm for different gas compositions [6].

## 1.3 MIR detectors: a brief historical overview

Infrared detectors are classified into thermal and quantum detectors. Thermal detectors use infrared energy as heat and their photosensitivity is independent of wavelength, and do not require cooling, however they typically have a slow response time and relatively low sensitivity. In contrast, quantum detectors offer a higher sensitivity and a higher speed. However, in general, quantum detectors must be cooled for optimum performance [7].

IR radiation was unknown until 200 years ago when Herschel's experiment with a thermometer and a prism was firstly reported. This work can also be considered as the first reported infrared detector [1]. In 1880, the first bolometer was invented by Langley [8]. The study of thermal detectors is mainstream at that moment. Thermal detectors can be divided into (i) bolometers, (ii) thermocouples, and (iii) pyroelectric detectors. Bolometers respond to infrared radiation by changing the electrical conductivity of semiconductors when the detection element absorbs the incident energy, which causes a temperature increase [9]. Thermocouples operate based on the thermoelectric effect. Pyroelectric detectors were based on the variation of temporary voltage in a pyroelectric crystal [10].

In the means while, In the late 19th century the discovery by Hertz of the photoelectric effect, followed, in 1905, by its interpretation by Einstein in terms of light-quanta [11], laid the foundation for the future development of photodetectors. In 1933, Edgar W. Kutzscher at the University of Berlin, discovered that lead sulfide (PbS) was photoconductive and had a response around 3 µm wavelength [12]. PdS photoconductors were brought to the manufacturing stage of development in Germany in the early 40s. After World War II other semiconductors of the lead salt family was found (lead selenide PbSe and Lead telluride PbTe) which could be used for infrared detection [13] [14]. In the late 1950s, Indium antimonide (InSb) detectors were developed. The operating frequency band of these intrinsic semiconductor photodetectors is around 1-5 µm. To expand this range many kinds of extrinsic semiconductors were developed, such as Ge:Au, Ge:Hg [15] [16]. In the late 1960s, the technology of HgCdTe (MCT) detectors was mature, with operation in the 8-14µm range at liquid nitrogen temperatures [17]. At present MCT is the most widely used material for IR photo-detectors. In the 1980s, the discovery of broken−gap type−II InAs/GaSb superlattices was reported by G.A. SAI−HALASZ, R. TSU, and L. ESAKI [18] [19]. Quantum well infrared photodetectors (QWIPs) were also demonstrated at the end of the 1980s [20], based on molecular beam epitaxy (MBE) or metalorganic chemical vapor deposition (MOCVD) grown III–V semiconductors (e.g GaAs/GaAlAs) and covering the MWIR and LWIR spectral ranges. The chronology of the development of infrared detectors and systems is presented in Fig. 1.4. A detailed description of the operation and performance of the main MIR semiconductor photodetectors will be given in the Section 2.2.

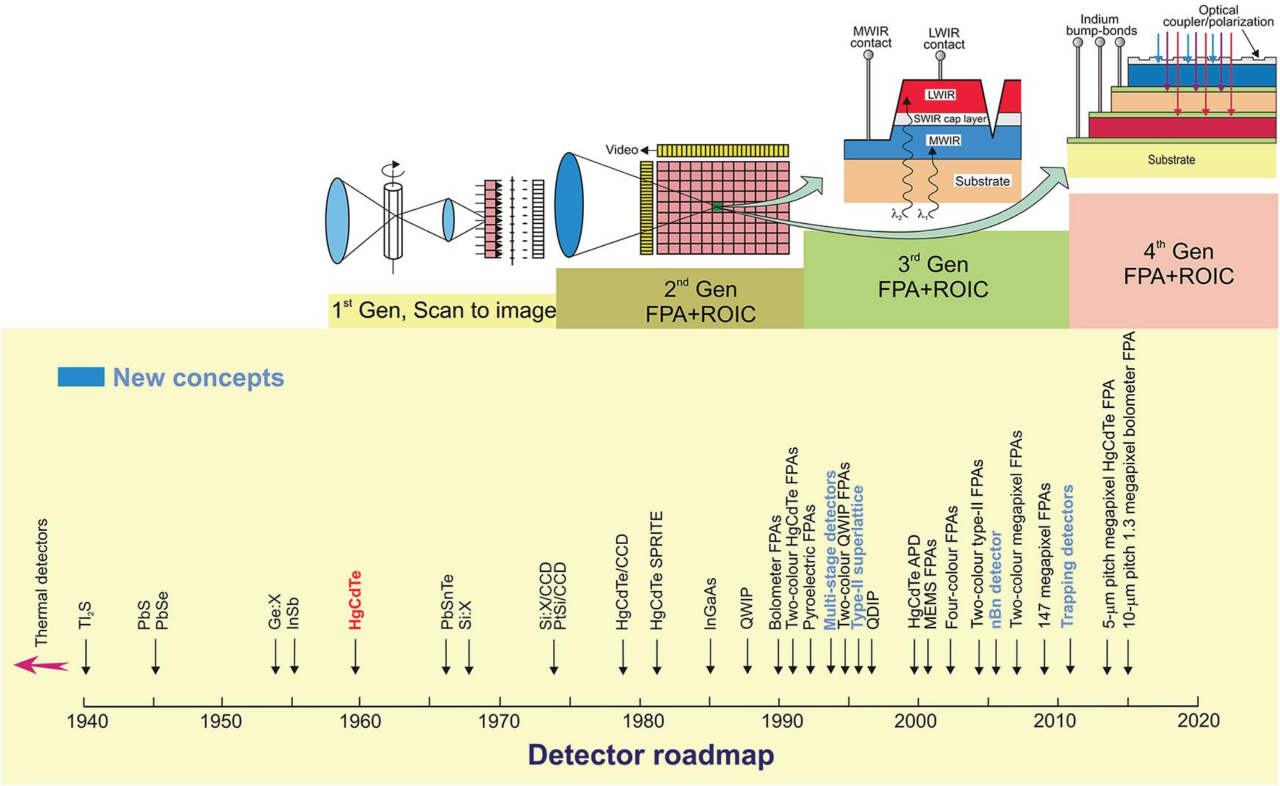

Fig. 1.4 History of the development of infrared detectors and systems (FPA: the focal plane array) [21].

## 1.4 Main applications

IR technology has progressed thanks to the development of high−performance infrared detectors over the last six decades. While the main interest has focused on the two atmospheric windows shown in Fig. 1.3, in recent years, stimulated by space applications, there has been an increasing interest towards longer wavelengths. The demand for IR technology is quickly growing due to its effectiveness in several applications, e.g., in global monitoring of environmental pollution and climate change, long time prognoses of agriculture crop yield, chemical process monitoring, Fourier transform IR spectroscopy, IR astronomy, car driving, IR imaging in medical diagnostics, and others. The rapid deployment of civilian IR technology is mainly connected to the development of uncooled IR cameras. Currently, uncooled microbolometric cameras are produced in larger volumes than all other IR array technologies together, and it is predicted that this tendency will further increase in the future [22].

Among the most common applications of IR detectors is thermal imaging. IR thermal imaging is used to observe objects without the need for an external light source. Thermal imaging is widely applied in medical treatment, product monitoring, etc. Thermal cameras based on QWIP focal plane arrays (FPAs) are already used as part of the enhanced vision system for military, aerospace, and space applications [23]. Many molecules have distinct spectral features in the IR which can be revealed by the means of spectroscopy. IR spectroscopy, an analytical technique that takes advantage of the vibrational transitions of a molecule, has been of great significance to scientific researchers in many fields such as protein characterization, nanoscale semiconductor analysis and space exploration, for many applications such as environmental monitoring, pollution control, industrial process monitoring, non-invasive disease diagnosis, and leak detection [24]. In a different direction, high frequency and high-speed detectors may create new applications, for example, in environmental remote sensing of molecules and $CO_2$ laser-based (or other long wavelength laser-based) communications, as well as for laboratory use [25] [26]. The main application areas of infrared detectors are shown in Fig. 1.5. In this thesis, ultra-fast QWIPs in the MIR have been investigated. The state of the art of MIR detectors is fully discussed in Section 2.2.

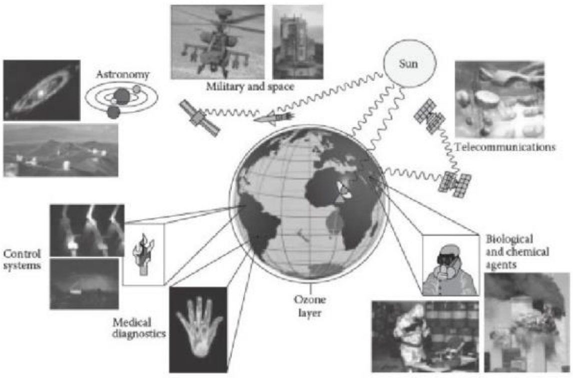

Fig. 1.5 Application areas of Infrared detectors [27].

# Bibliography

[1] W. Herschel, "Experiments on the refrangibility of the invisible rays of the Sun", *Phil. Trans. Roy. Soc. London,* vol. 90, pp. 284-292, 1800.

[2] C. L. Andrews, "Optics of the electromagnetic sepctrum", Englewood Cliffs: Prentice-Hall, 1960.

[3] R. Martini et E. Whittaker, "Quantum cascade laser-based free space optical communications", *Journal of Optical and Fiber Communications Reports,* vol. 2, no. 4, pp. 279-292.

[4] Vyacheslav, B. Podobedov, George et P. Eppeldauer, "Calibration of spectral responsivity of IR detectors in the range from 0.6 µm to 24 µm", *Proc. of SPIE, Infrared Technology and Applications XLII,* vol 9819, May 2016.

[5] M. Planck, "Ueber das Gesetz der Energieverteilung im Normalspectrum", Annalen der Physik, 1900, p. 553–563.

[6] R. D. Hudson, Infared System Engineering, New Yok, 1963.

[7] HAMAMATSU Photonics, "characterisics and use of infrared detectors", Solid State Division, 2004. [En ligne]. Available: http://www.hamamatsu.com.

[8] E. Barr, "The Infrared Pioneers— III. Samuel Pierpont Langley", *Infrared Physics,* no. 3, pp. 195-206, 1963.

[9] P. L. Richards, "Bolometers for infrared and millimeter waves", *Journal of Applied Physics,* vol. 76, no. 1, 1994.

[10] C. Kittel, Introduction to Solid State Physics, 8th Edition, 2016.

[11] K. Wiederkehr , "Photoeffects, Einstein's light quanta and the history of their acceptance", *Sudhoffs Arch,* vol. 90, no. 2, pp. 132-142, 2006.

[12] E. W. Kutzscher, "Review on detectors of infrared radiation", *Electro−Opt. Syst. Design,* vol. 5, no. 30, 1973.

[13] J. Barrett, *SPIE,* vol. 409, no. 76, 1983.

[14] T. Johnson, *SPIE,* vol. 443, no. 60, 1983.

[15] E. H. Puttley, "Semiconductors and Semimetals", New York: Academic Press, 1970.

[16] N. Sclar, *IR physics,* vol. 435, no. 16, 1976.

[17] M. B. Reine, «SPIE,» vol. 443, no. 2, 1983.

[18] G. A. Sai-Halasz, R. Tsu et . L. Esaki, "A new semiconductor superlattice", *Applied Physics Letters,* vol. 30, no. 12, p. 651–653, 1977.

[19] L. Esaki, "InAs-GaSb superlattices-synthesized semiconductors and semimetals", *Journal of Crystal Growth,* vol. 52, no. 1, p. 227–240, 1981.

[20] B. F. Levine, K. K. Choi, C. G. Bethea, J. Walker et R. J. Malik, “New 10 micron infrared detector using intersubband absorption in resonant tunneling {GaAlAs} superlattices"*, Appl. Phys. Lett.* vol. 50, no. 16, 1987, p. 1092–1094.

[21] A. Rogalski, "Infrared Detectors", Florida: CRC Press, 2010.

[22] A. ROGALSKI, "History of infrared detectors", *Opto−Electron. Review,* vol. 20, no. 3, pp. 279-308, 2012.

[23] S. D. Gunapala, S. V. Bandara, . J. K. Liu, J. M. Mumolo, . S. Rafol, D. Z. Ting, A. Soibel et C. Hill, "Quantum well infrared photodetector technology and applications", *Selected Topics in Quantum Electronics, IEEE Journal,* vol. 20, no. 6, 2014.

[24] C. L. Putzig, M. A. Leugers, M. L. McKelvy, G. E. Mitchell, R. A. Nyquist, R. R. Papenfuss, and L. Yurga , "Infrared Spectroscopy ", *Anal. Chem,* vol. 66, no. 12, pp. 26-66, 1994.

[25] R. Paiella, F. Capasso, C. Gmachl, D. L. Sivco, J. N. Baillargeon, A. L. Hutchinson, A. Y. Cho and H. C. Liu, *Science,* vol. 290, no. 1739, 2000.

[26] R. Paiella, . F. Capasso, C. Gmachl, H. Y. Hwang, D. L. Sivco, A. L. Hutchinson, A. Y. Cho et H. C. Liu, *Appl. Phys. Lett,* vol. 77, no. 169, 2000.

[27] A. Rogalski, "Infrared detectors", CRC Press, 2010.

# 2. Semiconductor infrared photodetectors

## 2.1 Semiconductor photodetectors

### 2.1.1 Photocurrent and responsivity

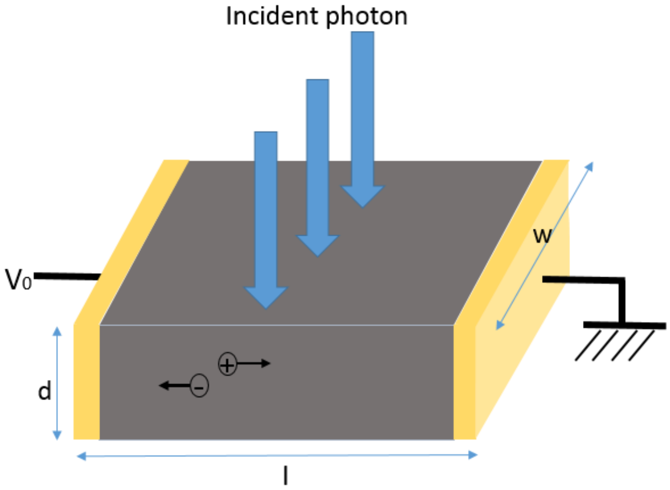

Figure 2.1. Geometry of a photoconductive detector.

In Fig 2.1, we present the behavior of an ideal photoconductor, made of a homogeneous semiconductor material of thickness d, width w and length l. A flux of photons is incident on the semiconductor surface, and the photons energy, $h\nu$, is larger than the semiconductor bandgap $E_p$. We suppose that the intensity of the light impinging on the semiconductor is $S_0$. The light flux in the semiconductor decays exponentially as:

$$\Phi(z) = (1-R)\xi_0 e^{-\alpha z} \quad \text{[number of photons/s m}^2\text{]} \quad (2.1),$$

where $\xi_0 = \frac{S_0}{h\nu}$ is the incident photon flux, α is the absorption coefficient and R is the reflectivity.

The density of electron-hole pairs created is given by:

$$g(z,t) = -\frac{\partial \Phi}{\partial z} = \alpha(1-R)\xi_0 e^{-\alpha z} \quad \text{[number of photons/s m}^3\text{]} \quad (2.2).$$

Assuming that a bias V is applied in the direction perpendicular to the incident photon flux (see Fig. 2.1), and neglecting the holes contribution, the carrier density of electrons in the semiconductor $n(\vec{r},t)$ is given by the continuity equation:

$$\frac{\partial n(\vec{r},t)}{\partial t} = g(\vec{r},t) - \frac{n}{\tau} + \frac{1}{e}\nabla\vec{J}(\vec{r},t) \quad (2.3),$$

where n/τ corresponds to the recombination/trapping rate of the free carriers, with τ the carriers lifetime, and $\vec{J}(\vec{r},t)$ is the current density, including the diffusion and drift components: $\vec{J}_{diff} = -eD\,\vec{\nabla}n$ and $\vec{J}_{drift} = ne\mu\vec{E}$.

The current density is expressed as:

$$\vec{J}(\vec{r},t) = \vec{J}_{diff} + \vec{J}_{drift} = -eD\,\vec{\nabla}n + ne\mu\vec{E} \quad [\mathrm{A/m^2}] \quad (2.4),$$

where $\vec{E}$ is the electric field.

Here we assume that the charge neutrality is maintained in the material. Due to the short carriers recombination/trapping life-time (in the order of ps for QWIP detectors), the diffusion current can be neglected. This is the case also for the drift current component, for sufficiently small electric fields. With these approximations, the continuity equation of $n(\vec{r},t)$ is given by:

$$\frac{\partial n(\vec{r},t)}{\partial t} = g(\vec{r},t) - \frac{n(\vec{r},t)}{\tau} \quad (2.5).$$

From Eq. (2.5), the steady-state electron concentration can be then written as:

$$n(z,t) = \tau\alpha(1-R)\xi_0 e^{-\alpha z} \quad (2.6).$$

The number of generated carriers per unit surface is then given by integrating Eq. (2.6):

$$\Delta n_{tot} = \int_0^d n(z,t)\,dz = \tau(1-R)\xi_0(1-e^{-\alpha d}) = \tau\eta\xi_0 \quad (2.7),$$

where $\eta = (1-R)(1-e^{-\alpha d})$ is the so-called *optical quantum efficiency*.

The applied bias produces a transverse electric field E ($E = \frac{V}{l}$) under which a photocurrent begins to circulate within the structure. The current density is $j_{ph} = ne\mu_n E$, with $e$ and $\mu_n$ respectively the electron's charge and the mobility. The photocurrent is then given by (see Fig. 2.1):

$$I_{ph} = \eta e\mu_n\tau\frac{w}{l}\xi_0 V \quad [\mathrm{A}] \quad (2.8).$$

By dividing Eq. (2.8) by the total incident power $P_{inc} = h\nu\xi_0 wl$, we obtain the *detector responsivity* $\mathcal{R}$:

$$\mathcal{R} = \frac{I_{ph}}{P_{inc}} = \eta\frac{\mu_n\tau}{l^2}\frac{V}{h\nu/e} \quad [\mathrm{A/W}] \quad (2.9).$$

The responsivity quantifies the ability to generate a current for a given incident power. It can also be written as:

$$\mathcal{R} = \eta g \frac{1}{h\nu/e} \quad (2.10),$$

where $g$ is defined as *photoconductive gain* given by:

$$g = \frac{\tau}{\tau_{tr}}; \; \tau_{tr} = \frac{l}{\mu_n E} = \frac{l^2}{\mu_n V} \quad (2.11).$$

Here, $\tau_{tr}$ , also called *transit* time, is the time taken by electrons to travel between the two contacts. As an example, in Fig.2.2 we show the spectral shape of the responsivity of a Silicon photodetector as a function of wavelength. We note that the latter follows approximately the linear dependence $\mathcal{R} = \eta g \frac{\lambda(\mu m)}{1.24}$, derived from Eq. (2.10), until the photon energy gets close to the semiconductor bandgap, producing a rather sharp cutoff.

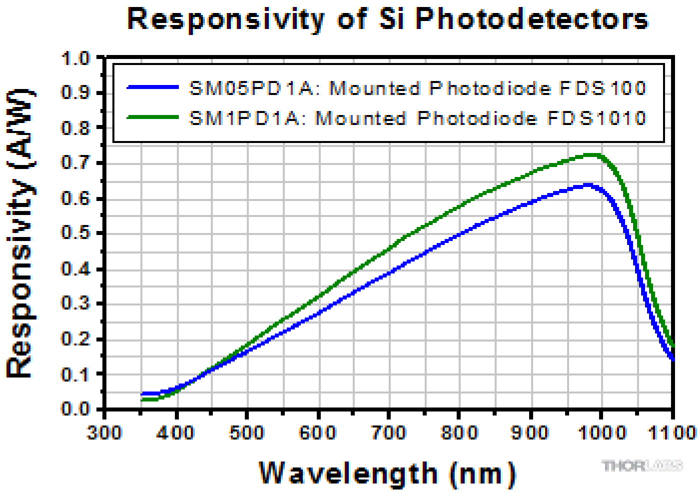

Figure 2.2. Responsivity spectrum of two commercial Si photodetectors [1].

### 2.1.2 Generation-recombination noise and thermal noise

In photoconductors, there are two main noise mechanisms:

- **Generation-recombination noise** caused by the statistical fluctuation of the number of carriers (generation and recombination) in a photoconductor following a Poisson distribution [2]. The generation-recombination noise current is expressed as:

$$i_{GR} = \sqrt{4egI_0 \Delta f} \quad [\mathrm{A}] \quad (2.12),$$

where $I_0$ is the average current flowing across the photodetector, and $\Delta f$ is the frequency integration bandwidth ($\Delta f = \frac{1}{2t_{int}}$ with $t_{int}$ the integration time).

- **Thermal noise or Johnson-Nyquist noise** [3] [4]. It is an electrical noise present in all resistive devices caused by the thermal fluctuations of the velocity of charge carriers. The thermal noise current is given by:

$$i_R = \sqrt{{}^{4k_BT\Delta f}/_{R}} \quad [\mathrm{A}] \quad (2.13),$$

where R is photoconductor resistance.

For a detector under illumination, the total noise is then given by:

$$i_N = \sqrt{i_{GR}^2 + i_R^2} = \sqrt{({}^{4k_BT}/_{R} + 4eg(I_{dark} + I_s)) * \Delta f} \quad [\mathrm{A}] \quad (2.14),$$

where we have made a distinction between the dark current $I_{dark}$ and the photogenerated current $I_s = \mathcal{R} \times P_{inc}$.

### 2.1.3 Noise equivalent power, Detectivity, and BLIP regime

We define the signal-to-noise ratio as:

$$^{S}/_{N} = {}^{i_s}/_{i_N} \quad (2.15).$$

The *noise equivalent power* (NEP) is defined as the incident power yielding a signal-to-noise ratio equal to 1 for a frequency integration bandwidth, i.e. it represents the minimum detectable power:

$$NEP = \frac{i_N}{\mathcal{R}\sqrt{\Delta f}} \quad [\mathrm{W/Hz^{1/2}}] \quad (2.16).$$

Since $i_N = j_N \times A_{det}$, where $A_{det} = w \times l$ is the detector surface and $j_N$ the noise current density, is clear, from Eq. (2.14) and Eq. (2.16), that the NEP is proportional to $\sqrt{A_{det}}$. To eliminate the dependence from these parameters, and allow to classify detector materials according to a more objective figure of merit, we introduce the *detectivity D**, defined as:

$$D^* = \frac{\sqrt{A_{det}}}{NEP} \quad [\mathrm{cm\ Hz^{1/2}\ W^{-1}\ or\ Jones}] \quad (2.17).$$

So, for instance, the detectivity of a photoconductor dominated by dark current noise is given by:

$$D^* = \frac{\mathcal{R}\sqrt{A_{det}}}{\sqrt{4egI_{dark}}} = \frac{\mathcal{R}}{\sqrt{4egJ_{dark}}} \quad (2.18),$$

where $J_{dark}$ is the dark current density.

In the presence of background radiation, considering the environment as a blackbody at a temperature $T_B$, the generated current density is given by:

$$J_B = eg \int_{\lambda_1}^{\lambda_2} \eta(\lambda) \frac{d\Phi_B(\lambda)}{d\lambda} d\lambda \ \ [\mathrm{A/m^2}] \quad (2.19),$$

where $\eta(\lambda)$ is the optical quantum efficiency for photons of wavelength λ; the spectral detection range is given by $\lambda_1$ and $\lambda_2$; $\frac{d\Phi_B(\lambda)}{d\lambda}$ $\Delta\lambda$ presents the photon flux over the wavelength range $\Delta\lambda$ per unit surface. This latter quantity can be expressed in the terms of the blackbody spectral irradiance (see Eq. (1.1)): $\frac{d\Phi_B(\lambda)}{d\lambda} = M(\lambda)\frac{\lambda}{hc}$.

The dark current in the absence of light sources is generated thermally in the active region of the detector increasing exponentially with its temperature. It can be put into the form [2]:

$$I_{dark} = A_{det} J_0 \exp(-h\nu/k_B T_{det}) \quad (2.20),$$

where $J_0$ is a constant depending on the detector active region. The photoconductors detectivity at a given wavelength $\lambda_0$ and a background temperature $T_B$ is then the given by:

$$\begin{aligned} D^*(\lambda_0, T_B) &= \frac{\mathcal{R}}{\sqrt{4egJ_0 \exp\left(-h\nu/_{k_B T_{det}}\right) + 4egJ_B}} \\ &= \eta(\lambda_0) g \frac{1}{h\nu/e} \frac{1}{\sqrt{4egJ_0 \exp\left(-h\nu/_{k_B T_{det}}\right) + 4g^2e^2 \int_{\lambda_1}^{\lambda_2} \eta(\lambda) \frac{d\Phi_B(\lambda)}{d\lambda} d\lambda}} \quad (2.21). \end{aligned}$$

From Eq. (2.21) it is possible to define a temperature below which the detectivity is dominated by background noise, i.e. it is useless to cool the detector further to improve the detectivity. In this case, the detector is said to operate in *background limited infrared performance* regime (BLIP regime). The BLIP temperature is defined as the temperature for which the background noise equals the dark current noise, and is given by:

$$T_{BLIP} = \frac{h\nu}{k_B \ln\left(\frac{J_0}{eg \int_{\lambda_1}^{\lambda_2} \eta(\lambda) \frac{d\Phi_B(\lambda)}{d\lambda} d\lambda}\right)} \quad (2.22).$$

The detectivity in the BLIP regime is given by:

$$D^*_{BLIP}(\lambda_0, T_B) = \frac{\eta(\lambda_0)}{h\nu} \frac{1}{\sqrt{4 \int_{\lambda_1}^{\lambda_2} \eta(\lambda) \frac{d\Phi_B(\lambda)}{d\lambda} d\lambda}} \quad (2.23).$$

The detector is typically mounted inside a cryostat. The photocurrent is measured by opening a window on the cryo-shield, such that the incident radiation from the background is collected only under an angle $2\alpha$. We define a field of view (FOV) to the external radiation as we shown in Fig 2.3.

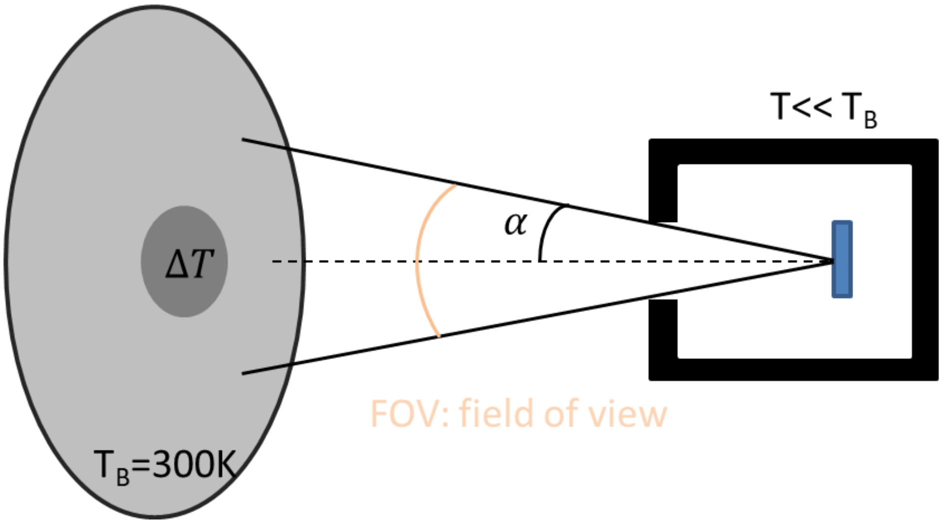

Figure 2.3. The background flux is screened by the detector enclosure with an acceptance angle α.

The noise due to the background blackbody flux $\Phi_B$ therefore diminishes according to $sin^2\alpha$ [5]. From the Eq. (2.23), we know the detectivity is inversely proportional to the square root of the background black body flux $\Phi_B$. The detectivity in the BLIP regime now is given by:

$$D^*_{BLIP}(\lambda_0, T_B, \alpha) = \frac{\eta(\lambda_0)}{h\nu}\frac{1}{\sqrt{4\int_{\lambda_1}^{\lambda_2}\eta(\lambda)\frac{d\Phi_B(\lambda)}{d\lambda}sin^2\alpha d\lambda}} = \frac{D^*_{BLIP}(\lambda_0,T_B)}{sin\alpha} \quad (2.24).$$

Infrared photodetectors are widely used for thermal imaging. In this context, a useful parameter is the so-called *noise equivalent temperature difference* (NETD) which quantifies the change in temperature leading to a signal-to-noise ratio of 1 assuming a integration frequency bandwidth $\Delta f = 1\ Hz$.

A change of blackbody temperature $\Delta T$ leads to a variation in the blackbody emitted power over the spectral range $\Delta\lambda$. The NETD can then be written as [2]:

$$NEP = NETD\ A_{det}\frac{d}{dT}\int_0^{\Delta\lambda} M(\lambda, 300K)d\lambda = A_{det}C_d(\Delta\lambda)NETD \quad (2.25),$$

where $C_d(\Delta\lambda) = \frac{d}{dT}\int_0^{\Delta\lambda} M(\lambda)d\lambda$ is the emitted power per unit surface, per degree K in a $\Delta\lambda$ band (in W cm$^{-2}$ K$^{-1}$).

### 2.1.4 Time response of photoconductor

Integrating Eq. (2.5) over the thickness of the material (from 0 to d), we can get the dynamic equation of the number of generated carriers per unit area ($\Delta n_{tot}$), expressed as:

$$\frac{\partial \int_0^d n(z,t)dz}{\partial t} = \int_0^d g(z,t)dz - \frac{\int_0^d n(z,t)dz}{\tau}$$
$$\rightarrow \frac{d\Delta n_{tot}}{dt} = (1-R)(1-e^{-\alpha d})\xi_0(t) - \frac{\Delta n_{tot}}{\tau}$$
$$\rightarrow \frac{d\Delta n_{tot}}{dt} + \frac{\Delta n_{tot}}{\tau} = \eta\xi_0(t) \quad (2.26),$$

where $\eta$ is the quantum efficiency, $\tau$ is the carrier lifetime, $\xi_0(t)$ is the incident photon flux. Let's assume a photon flux with an intensity varying sinusoidally, hence $\xi_0(t) = \xi_0 sin\omega t$. By integrating Eq. (2.26) we obtain: $\Delta n_{tot}(t) = \Delta n_{tot}(\omega)\sin(\omega t+\phi)$ with $\Delta n_{tot}(\omega) = \frac{\xi_0\tau\eta}{\sqrt{1+\omega^2\tau^2}}$ (2.27). The photodetector behaves therefore as a low-pass filter with a cut-off frequency $^1/_{2\pi\tau}$.

## 2.2 Interband and intersubband MIR photodetectors

Semiconductor photodetectors involve two kinds of transitions: interband transitions and intersubband (ISB) transitions. Interband transitions take place between the valence band and the conduction band, therefore the transition energy has a minimum cut-off limited by the bandgap. In ISB transitions the optical excitation takes place between quantized energy levels within the conduction or valence band of a semiconductor heterostructure. As a result, the excitation energy is not limited by the bandgap but rather by the band offset between the different semiconductor materials of which the heterostructure is made.

The Quantum Well Infrared Photodetector (QWIP) is a semiconductor device based on ISB transitions. Another type of MIR detector relying ISB transitions is the so-called photovoltaic quantum cascade detector (QCD), which, thanks to a built-in field produced by a ladder of subbands, does not require an external bias [6]. Besides QWIPs, there are several other types of MIR semiconductor photodetectors, such as InSb, PbSe, and HgCdTe (MCT) detectors. These detectors have their own strengths and weaknesses, and their target absorption wavelengths are different too. Fig. 2.4 shows a general comparison of the detectivity of various infrared detector technologies in the range of 1-40 µm. The dashed line corresponds to the maximum achievable detectivity for an ideal photodetector (photovoltaic, photoconductor, thermal detector). A photovoltaic detector consists of a junction between two opposite-polarity semiconductors (a p-n junction). Photons absorbed at or near the junction cause the emission of charge carriers. These are separated by the built-in electric field producing a photo-voltage. The magnitude of the voltage is proportional to the number of incident photons.

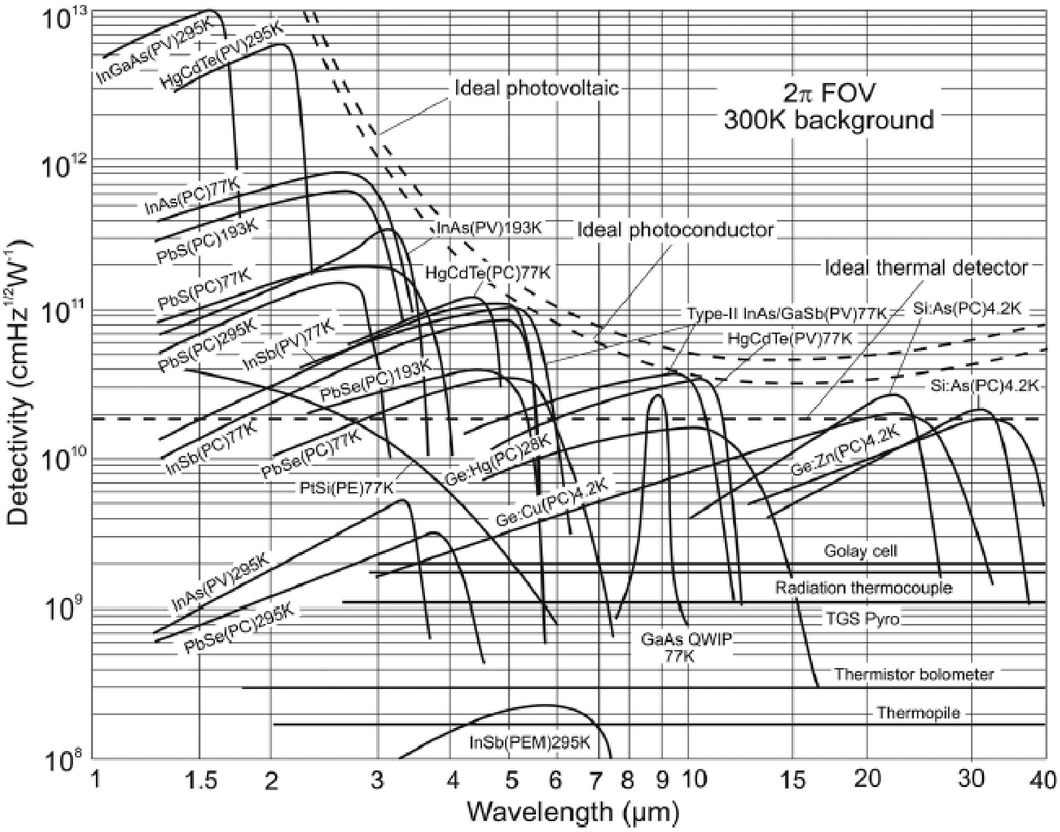

Figure 2.4. Comparison of the D* of various commercially available infrared detectors when operated at the indicated temperature. The chopping frequency is 1000 Hz for all detectors except the thermopile (10 Hz), thermocouple (10 Hz), thermistor bolometer (10 Hz), Golay cell (10 Hz), and pyroelectric detector (10 Hz). Each detector is assumed to view a hemispherical surround at a temperature of 300 K. Theoretical curves for the background limited D* for ideal photovoltaic and photoconductive detectors and thermal detectors are also shown (adapted from [7]). PC indices photoconductive detectors; PV is photovoltaic detectors; PEM means photo electromagnetic detectors.

Below, we give a brief survey of the main semiconductor photodetectors, namely Lead Salt (PbSe and PbS), InSb and MCT detectors.

### 2.2.1 Lead salt detectors

Lead salts such as PbS and PbSe were the first compound semiconductors used to fabricate MIR photodetectors since the 1940s [8]. As shown in Fig. 2.4, at room temperature the wavelength operating ranges are ~1-3µm for PbS, and ~1-5µm for PbSe. Unlike most semiconductors, the bandgaps of PbS and PbSe decrease with decreasing temperature, producing a red shift of the spectral response. As shown in Fig. 2.4, at 77K this results into extended operating ranges up to ~4 µm and ~6 µm respectively for PbS and PbSe.

Unlike most other semiconductor IR detectors, lead salt photoconductive materials are used in the form of polycrytalline films approximately 1 µm thick and with individual crystallites ranging in size from approximately 0.1–1.0 µm [7]. They are usually prepared by chemical deposition [9, 10, 11, 12, 13, 14], which generally yields better uniformity of response and more stable results than the evaporative methods [15, 16, 17, 18, 19, 20].

Lead salt detectors offer the highest detectivities at room temperature with typical values of ~$10^{11}$ cmHz$^{1/2}$/W (PbS) and ~$10^{9}$ cmHz$^{1/2}$/W (PbSe). Together with their low cost, this makes of PbSe and PbS polycrystalline thin films the materials of choice for uncooled infrared detector systems in the 1-3 µm and 1-5 µm spectral ranges [20]. Their response speed is limited by Auger recombination, with typical lifetimes in the µs range (PbS~20 µs, PdSe~2 µs [21] [22]), making them unsuitable for high-speed operations.

### 2.2.2 InSb detectors

Indium antimonide (InSb) is a semiconductor material from the III-V group, discovered in the 1950s. At the time it presented the smallest known semiconductor energy gap, therefore its application to MWIR detection became obvious. Moreover, InSb offers good fabrication and material quality (high uniformity over large areas, high yield, controllability of dopants…).

The main operating range is ~1-5 µm, which corresponds to that of PbS and PbSe detectors. While lead salts materials are only used as photoconductors, InSb is used to realise both photoconductive and photovoltaic detectors. The smaller energy gap of InSb brings a higher thermal noise at high temperature. As a result, unlike lead salt detectors which can reach high detectivities at room temperature, typical operating temperatures of InSb are ~200K and ~77K when operated respectively as photoconductor (D*~$10^{9}$ cmHz$^{1/2}$/W) , or photovoltaic detector (D*~ $10^{10} \div 10^{11}$ cmHz$^{1/2}$/W) [23].

The interest for InSb as a material for IR detector stems not only from its small energy gap, but also from the fact that it can be prepared in single crystal form by conventional growth techniques. As a result the design of InSb detectors can be inferred directly from its bulk properties [24]. On the contrary, the fabrication of lead salts thin films (see the previous Section) through either vacuum evaporation or chemical deposition is much less obvious and reproducible, hence their performance cannot be predicted from a study of their bulk crystal properties. Thanks to the high-quality growth and uniformity, InSb-based FPAs with large number of pixels are easy to realize [25, 26, 27, 28, 29, 30].

InSb detectors are commonly exploited in thermal imaging systems, infrared homing missile guidance systems, astronomy, and astrophysics. For applications in astrophysics, these devices are very often operated at 4-7 K with a resistive or capacitive transimpedance amplifier to achieve the lowest noise performance.

As for lead salts, the response speed of InSb is also limited by Auger recombination, with carrier lifetimes in the ~ns range (~µs for lead salts), thus preventing ultrafast operation.

### 2.2.3 MCT detectors

In 1959, the first HgCdTe alloy was obtained by the group of Lawson [31]. Mercury-Cadmium-Telluride (MCT) presents a widely tunable bandgap from 1µm to 30µm, obtained by controlling the proportion of Cd/Hg in the alloy. For this reason, combined with its excellent detection performance, MCT is the most favorable material for IR detection.

From the late 1950s to the early 1970s, the main growth method was bulk crystal growth. Then, with the surge of epitaxial growth, HgCdTe was fabricated by epitaxy on either CdTe or CdZnTe substrates. MCT is a compound of CdTe and HgTe, where CdTe is a semiconductor and HgTe is a semimetal. At room temperature, CdTe has a bandgap of approximately 1.5 eV, while the bandgap of HgTe is 0 eV. As a result, by controlling the proportion of Cd/Hg in the alloy, one can obtain any bandgap from 0 to 1.5 eV. As shown in Fig. 2.5, in the 3-7µm range the absorption coefficient of MCT is comparable to that of PbS/PbSe/InSb. At the same time, MCT detectors respond over a broader range of wavelengths, up to ~12.5 µm, offering high sensitivities together with multicolor capabilities.

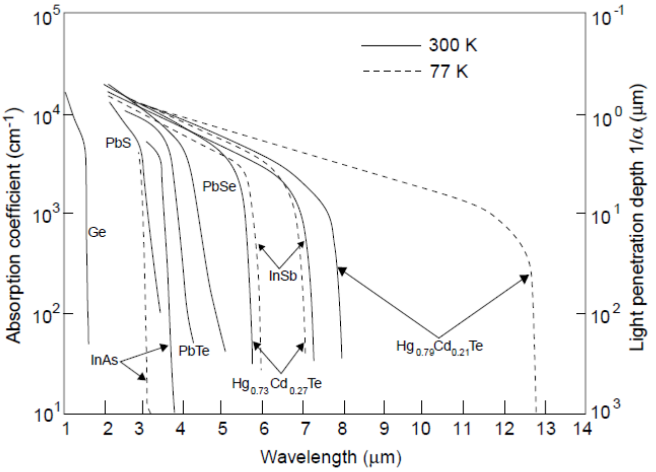

Figure 2.5. Absorption coefficient *vs* wavelength for various photodetector materials at 77K and 300K [32].

In the SWIR, the BLIP temperature of MCT detectors is around 200K, with detectivities up to $10^{13}$ cmHz$^{1/2}$/W at ~2$\mu$m and 300K (see Fig. 2.4). In the MWIR, the BLIP temperature is around 150K, with detectivities in the range $10^{11}$ - $10^{12}$ cmHz$^{1/2}$/W below 150K, while at 300K the detectivity is still close to $10^{10}$ cmHz$^{1/2}$/W [33, 34]. In the LWIR, the BLIP temperature is up to liquid nitrogen temperature. Below 77K, the detectivity is around $10^{11}$ cmHz$^{1/2}$/W, while at room temperature it is in the range of $10^8$ to $10^9$ cmHz$^{1/2}$/W.

Thanks to its excellent performance and its extremely wide wavelength range, at present MCT is the most widely used material for IR photodetectors. MCT technology development has been primarily aimed at military applications, remote sensing and infrared astronomy. To this end, MCT FPAs have been developed, presently offering a vast catalogue of commercially available sizes at different wavelengths (see table 1).

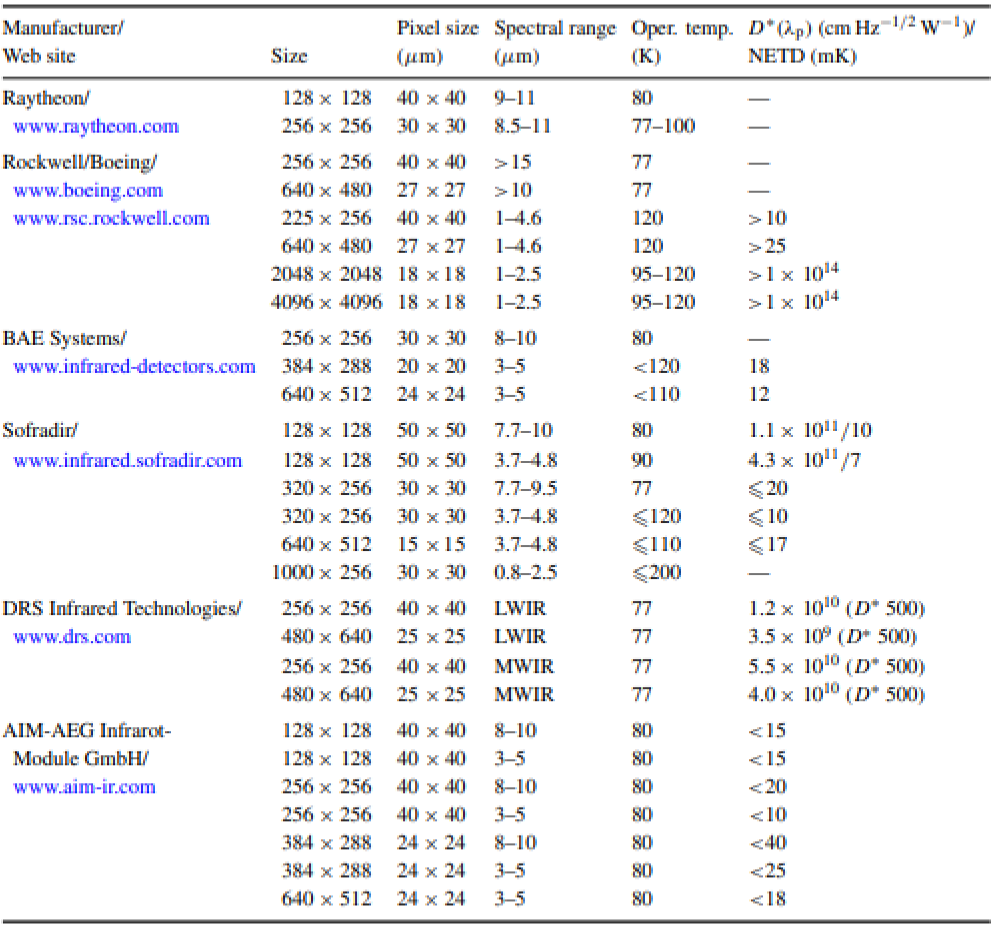

| Manufacturer/ Web site | Size | Pixel size ($\mu$m) | Spectral range ($\mu$m) | Oper. temp. (K) | $D^*(\lambda_p)$ (cm Hz$^{-1/2}$ W$^{-1}$)/ NETD (mK) |
|---|---|---|---|---|---|
| Raytheon/ | 128 × 128 | 40 × 40 | 9–11 | 80 | — |
| www.raytheon.com | 256 × 256 | 30 × 30 | 8.5–11 | 77–100 | — |
| Rockwell/Boeing/ | 256 × 256 | 40 × 40 | > 15 | 77 | — |
| www.boeing.com | 640 × 480 | 27 × 27 | > 10 | 77 | — |
| www.rsc.rockwell.com | 225 × 256 | 40 × 40 | 1–4.6 | 120 | > 10 |
| | 640 × 480 | 27 × 27 | 1–4.6 | 120 | > 25 |
| | 2048 × 2048 | 18 × 18 | 1–2.5 | 95–120 | $> 1 \times 10^{14}$ |
| | 4096 × 4096 | 18 × 18 | 1–2.5 | 95–120 | $> 1 \times 10^{14}$ |
| BAE Systems/ | 256 × 256 | 30 × 30 | 8–10 | 80 | — |
| www.infrared-detectors.com | 384 × 288 | 20 × 20 | 3–5 | <120 | 18 |
| | 640 × 512 | 24 × 24 | 3–5 | <110 | 12 |
| Sofradir/ | 128 × 128 | 50 × 50 | 7.7–10 | 80 | $1.1 \times 10^{11}/10$ |
| www.infrared.sofradir.com | 128 × 128 | 50 × 50 | 3.7–4.8 | 90 | $4.3 \times 10^{11}/7$ |
| | 320 × 256 | 30 × 30 | 7.7–9.5 | 77 | ⩽20 |
| | 320 × 256 | 30 × 30 | 3.7–4.8 | ⩽120 | ⩽10 |
| | 640 × 512 | 15 × 15 | 3.7–4.8 | ⩽110 | ⩽17 |
| | 1000 × 256 | 30 × 30 | 0.8–2.5 | ⩽200 | — |
| DRS Infrared Technologies/ | 256 × 256 | 40 × 40 | LWIR | 77 | $1.2 \times 10^{10}$ ($D^*$ 500) |
| www.drs.com | 480 × 640 | 25 × 25 | LWIR | 77 | $3.5 \times 10^{9}$ ($D^*$ 500) |
| | 256 × 256 | 40 × 40 | MWIR | 77 | $5.5 \times 10^{10}$ ($D^*$ 500) |
| | 480 × 640 | 25 × 25 | MWIR | 77 | $4.0 \times 10^{10}$ ($D^*$ 500) |
| AIM-AEG Infrarot- | 128 × 128 | 40 × 40 | 8–10 | 80 | < 15 |
| Module GmbH/ | 128 × 128 | 40 × 40 | 3–5 | 80 | < 15 |
| www.aim-ir.com | 256 × 256 | 40 × 40 | 8–10 | 80 | < 20 |
| | 256 × 256 | 40 × 40 | 3–5 | 80 | < 10 |
| | 384 × 288 | 24 × 24 | 8–10 | 80 | <40 |
| | 384 × 288 | 24 × 24 | 3–5 | 80 | <25 |
| | 640 × 512 | 24 × 24 | 3–5 | 80 | < 18 |

Table1. Representative HgCdTe hybrid FPAs offered by some major manufacturers [33].

The Achille’s heel of MCT is the softness and weakness of this material, making device processing a challenging task. Large detector arrays place high demands on device uniformity, which can be challenging to meet due to the fragility of HgTe chemical bonds, resulting into bulk, surface and interface instabilities. Issues related to growth uniformity and yield significantly increase the cost of MCT FPAs manufacture. As far as these issues are concerned, compared to HgCdTe, InSb or GaAs/AlGaAs are definitely more mature materials. Despite these drawbacks, HgCdTe remains the most important material for IR detector applications. Actually, MCT detectors represent a standard: whatever new materials or device technologies show up, they are inevitably benchmarked against HgCdTe technology.

### 2.2.4 QCD detectors

QCD detectors, are photovoltaic detectors, exploiting ISB transitions in quantum wells embedded in an asymmetric, saw-tooth-like conduction band structure, which allows transport of the excited electrons in one direction only, without the application of external bias. As for QWIPs, the active region of QCDs is obtained by the periodic repetition of the same basic unit. An example of such a unit for a QCL operating at 4.3µm wavelength is shown in Fig. 2.6 [35].

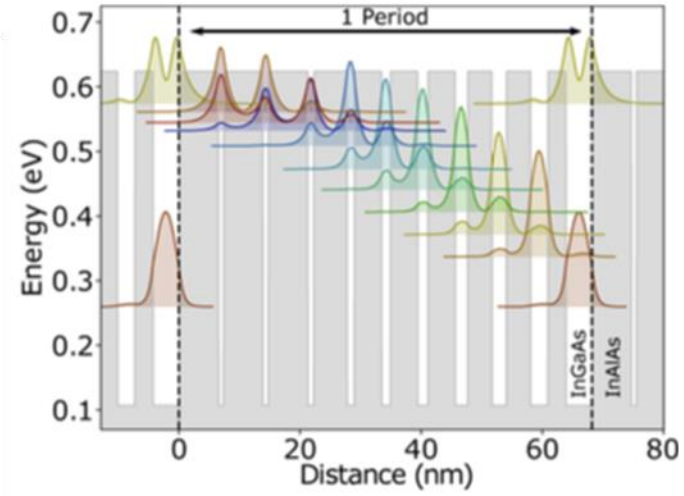

Figure 2.6. Simulated band diagram of one period of a QCD based on a InGaAs/InAlAs heterostructure, lattice-matched to InP, and operating at 4.3µm. Excited electrons are extracted from the active quantum well and injected into the next period via a LO phonon ladder [35].

Electrons are first photoexcited from the ground state to the upper state of the quantum well on the left. Next, they tunnel into the highest energy states of a ladder of subbands separated by approximately one optical phonon energy. Through this ladder, electrons are finally injected into the ground state of the well on the right. The same process is repeated at every period, generating a photovoltage across the device electrical contacts. The main advantage of QCDs compared to QWIPs (see next Section), is the absence of dark current. As a result, the dominating noise mechanism is Johnson noise, favoring operation at room temperature. For instance, specific detectivities of ~7 x $10^7$ cmHz$^{1/2}$/W at room temperature, have been reported at 4µm wavelength. As for QWIPs, QCDs are intrinsically fast devices since electron's relaxation is dominated by the emission of optical phonons, on the ps time scale. Recently, a technological effort has been devoted to the monolithic integration of coplanar-type access to QCDs processed in a mesa geometry, in order to optimize the extraction of RF signals. With these devices, 3dB cutoff frequencies of ~20GHz were demonstrated with facet-illuminated QCDs operating at 4.3 µm and 4.5 µm wavelength [35] [36].

### 2.2.5 QWIP detectors

QWIPs based on III–V materials and grown by MBE and MOCVD were demonstrated in the end of 1980s. The first QWIP was demonstrated by B. Levine in 1987 [37], and was based on the GaAs/GaAlAs III-V semiconductor materials system.

As already discussed at the beginning of this Section, QWIPs rely on intersubband transitions in semiconductor compounds, e.g., GaAs/GaAlAs or InGaAs/InAlAs, and cover the MWIR and LWIR spectral ranges. It is also possible to extend their operation to the VLWIR and the THz range by varying the thickness of the QWs or the material composition, such as, for instance, the portion of Al in a GaAs/AlGaAs multi-quantum well.

For QWIP detectors based on standard mesa geometry, the BLIP temperature is around 70K with typical values of detectivity in the range of $10^{10}$ -$10^{11}$ cmHz$^{1/2}$/W at ~8 µm (Fig. 2.4). The detectivity at room temperature is ~ $10^{6}$ cmHz$^{1/2}$/W [38]. For QWIPs based on PAR structures, the BLIP temperature can be raised up to 83K with detectivities at room temperature of $10^{7}$ -$10^{8}$ cmHz$^{1/2}$/W [38].

III-V QWIP technology is clearly more mature and reliable compared to HgCdTe technology, yielding high uniformity over large areas, high yield, and controllability of key parameters (such as the concentration of Al, QW and barrier thickness etc). As a result, QWIPs can be easily designed to have the response wavelength targeting a particular infrared band or multiple bands. In addition, the intrinsic materials lifetimes are in the ps range, which makes ultra-fast (> 100GHz) QWIP photodetectors achievable. In 2005, an ultra-fast GaAs/AlGaAs QWIP based on a standard mesa geometry was demonstrated at 10µm, showing heterodyne detection up to 110 GHz [39] [40].

QWIP technology is confronted with some disadvantages. Only the radiation polarized perpendicularly to the growth direction can excite the electrons, thus reducing the quantum efficiency. As a result, light coupling is typically obtained through diffraction gratings or other solutions, which increases manufacturing costs and decreases the yield. The other challenge is related to the high thermal dark current which brings in a relatively low operating temperature [41]. This is mainly the consequence of the ~ps timescale carriers lifetime in QWIP detectors, compared to ~ns for MCTs or InSb-based detectors. At 77K, QWIPs have a relatively high thermal generation rate compared to MCT [42]. Together with a lower absorption coefficient, this leads approximately to a $10^{5-6}$ reduction of the ratio between the absorption coefficient and the thermal generation compared to MCT (Fig. 2.7) [43] [44], and therefore much lower BLIP temperatures and detectivities. As an example, in Fig. 2.8, we report the theoretical detectivities of a QWIP and MCT detector operating a 14µm, showing BLIP temperatures of ~50K and ~80K respectively. QWIP's detectivity is competitive with MCTs at low temperature, but the degree of declining is larger as the temperature increases. Finally, it should be mentioned that the band edge discontinuity limits the maximum energy of the absorbed photons, hence QWIPs are rarely applied in the SWIR [45].

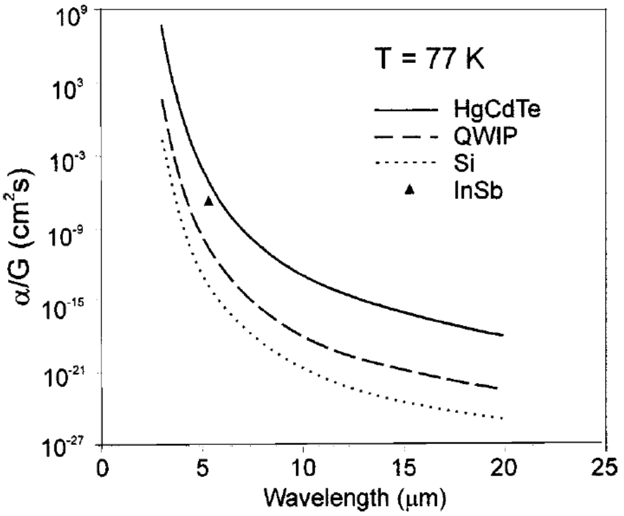

Figure 2.7. The ratio of the absorption coefficient to the thermal generation rate α/G versus cutoff wavelength for different types of photon detectors operated at 77K [44].

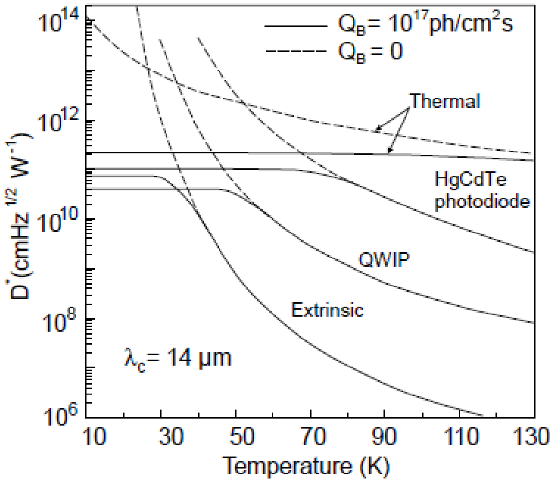

Figure 2.8. Theoretical detectivity vs temperature for LWIR photon and thermal detectors at 14 µm, for zero background and for a background of $10^{17}$ photons/cm$^2$s [46].

A final important feature of QWIP detectors stems from the fact that the electron transition occurs between two discrete energy levels, therefore the response is inherently narrowband (see Fig. 2.9).

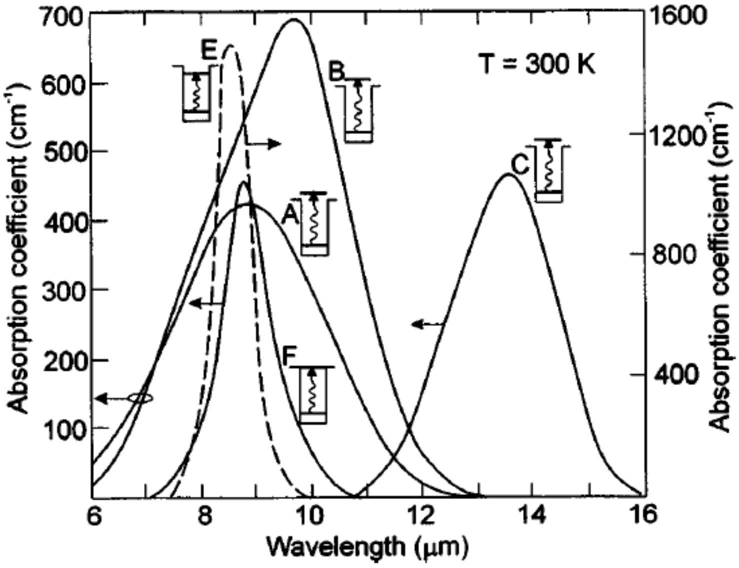

Figure 2.9. Absorption coefficient spectra measured at 300 K for different QWIP samples from [44].

### 2.2.6 Conclusion

From the brief comparison done above, it is clear that a single IR detector can’t provide simultaneously a high detectivity, a fast response speed and a high operating temperature.

In spite of their lower detectivity, which can be compensated by lowering the temperature, the advantages of QWIPs, namely their mature technology and intrinsic low carrier life time (to realize detectors with ultra-fast response speed beyond 100GHz), still makes them the most popular IR detectors after MCT detectors, especially in the MWIR and LWIR.

# Bibliography

[1] THORLABS, CALIBRATED PHOTODIODES, [En ligne]. Available: https://www.thorlabs.com/NewGroupPage9_PF.cfm?ObjectGroup_ID=2822.

[2] E. Rosencher et B. Vinter, *"Optoelectronics",* Cambridge University Press, 2002, pp. 486-488.

[3] J. B. Johnson, *“Thermal agitation of electricity in conductors”,* 1928, p. 97.

[4] H. Nyquist, *"Thermal agitation of electric charge in conductors",* Physical review, 1928, p. 110.

[5] R. C. Jones, "Proposal of the Detectivity for Detectors Limited by Radiation Noiset", *JOURNAL OF THE OPTICAL SOCIETY OF AMERICA,* vol. 50, no. 11, 1960.

[6] D. Hofstetter, M. Beck et . J. Faist, "Quantum-cascade-laser structures as photodetectors", *Appl. Phys. Lett,* vol. 81, nO. 15, pp. 2683-2685, 2002.

[7] A. Rogalski, *"Infrared detectors",* CRC Press, 2010.

[8] J. R. Barrett, *SPIE*, vol. 409, p. 76, 1983.

[9] I. Grozdanov, M. Najdoski et S. Dey, "A simple solution growth technique for PdSe thin films", *Materials Letters,* no. 38, pp. 28-32, 1999.

[10] w. Yu, J. Falkner et B. Shih, "Preparation and charaterization of monodisperse PdSe semiconductor nanocrystals in a noncoordinating solvent", *Journal of Materials Chemistry,* vol. 16, pp. 3318-3322, 2004.

[11] E. Salgado, M. Nair et P. Nair, "Chemically deposited thin films of PdSe as an absorber component in solar cell structures", *Thin Solid Films,* vol. 519, pp. 7432-7437, 2011.

[12] A. Molin et A. Dikusar, "Electrochemical deposition of PdSe thin films from aqueous solution", *Thin Solid Films ,* vol. 265, pp. 3-9, 1995.

[13] E. Strelstov, N. Osipovich et I. Ivashkevich, "Electrochemical deposition of PdSe films", *Electrochimical Acta,* vol. 43, pp. 869-873, 1998.

[14] D. Ivanou, E. Strelstov et A. Fedotov, "Electrochemical deposition of nanocrystalline PdSe layers onto p-Si(100) wafers", *Thin Solid Films,* vol. 487, pp. 49-53, 2005.

[15] H. Wu, X. Fang et R. Salas, "Molecular beam expitaxy growth of PdSe on the BF2-coated Si(111) and observation of the PdSe growth interface", *Journal of Vacuum Science and Technology B,* vol. 17, pp. 1263-1266, 1999.

[16] X. Wang, Y. Hou, Y. Chang et et al, "Growth of PdSe on ZnTe/GaAs(211)B by molecular beam epitaxy", *Journal of Crystal Growth,* vol. 312, pp. 910-913, 2010.

[17] R. Herrero, M. Supervielle et A. Ramirez, "VPD PdSe technology: the road towards the industrial maturity",*Proceedings of SPIE,* vol. 7660, 2010.

[18] K. Zhang, A. Pillai, K. Bollenbach et et al, "Atomic layer deposition of nanolaminate structures of alternating PdTe and PdSe thermoelectric films", *ECS Journal of Solid State Science and Technology ,* vol. 3, pp. 207-212, 2014.

[19] M. Khanlary et E. Salvati, "Optical properties and charaterization of prepared Sn-doped PdSe thin film", *Advances in Condensed Matter Physics ,* 2012.

[20] J. Vincent et J. Vampola, "Fundamentals of Infrared and Visible Detector Operation and Testing", New York: John Wiley and Sons.

[21] Y. Ravich, "Semiconducting Lead Chalcogenides", Leningrad: Springer, 1970.

[22] V. Tetyorkin, A. Yu, F. Sizov, A. Fedorenko et A. Fedorov, "(001)-oriented lead selenide films grown on silicon substrates", *Infrared physics and Technology,* vol. 37, pp. 379-384, April 1996.

[23] HAMAMATSU, "Characteristics and use of infrared detectors", *Technical information.*

[24] R. Willardson, "Semiconductors and semimetals", NewYork and London: Academic press, 1970.

[25] J. T. Wimmers et D. S. Smith, "Characteristics of InSb photovoltaic detectors at 77K and below", *Proceedings of SPIE,* vol. 364, p. 123–131, 1983.

[26] J. T. Wimmers, R. M. Davis, C. A. Niblack et D. S. Smith, "Indium antimonide detector technology at Cincinnati Electronics Corporation", *Proceedings of SPIE,* vol. 930, p. 125–138, 1998.

[27] A. Fowler, J. Heynssens, I. Gatley, F. Vrba, H. Ables, A. Hoffman et J. Woolaway, *Proceedings of SPIE ,* vol. 2475, pp. 27-33, 1995.

[28] A. M. Fowler, I. Gatley, P. McIntyre, F. J. Vrba et A. Hoffman, *Proceedings of SPIE,* vol. 2816, pp. 150-160, 1996.

[29] M. Beckett, "High resolution infrared imaging", Cambridge University, 1995.

[30] P. Love et et al, "Large-format infrared arrays for future space and ground-based astronomy applications", *Proc.SPIE,* vol. 4486, 2002.

[31] W. Lawson, S. Nielson, E. Putley et A. Young, "Preparetion and properties of HgTe and mixed crystals of HgTe-CdTe", *J Phys. Chem. Solids,* pp. 325-329, 1959.

[32] A. Rogalski, "Infrared detectors: status and trends", Warsaw, Institute of Applied Physics, Military University of Technology: Progress in Quantum Electronics, 2003, p. 59–210.

[33] A. Rogalski, "HgCdTe infrared detector material: history, status and outlook", *Rep. Prog. Phys. 68,* pp. 2267-2336, 2005.

[34] M. B. Reine, "Status Of HgCdTe Detector Technology", *SPIE,* vol. 0443, no. 2, 1983.

[35] J. Hillbrand, "High-speed quantum cascade detector characterized with a mid-infrared femtosecond oscillator", *Optics express,* vol. 29, no. 5774, 2021.

[36] T. Dougakiuchia, "Ultimate response time in mid-infrared high-speed low-noise quantum cascade detectors", *Applied Physics Letters,* vol. 118, no. 041101, 2021.

[37] B. F. Levine, K. K. Choi, C. G. Bethea, J. Walker et R. J. Malik, “New 10 micron infrared detector using intersubband absorption in resonant tunneling {GaAlAs} superlattices"*, Appl. Phys. Lett*. vol. 50, no. 16, 1987, p. 1092–1094.

[38] D. Palaferri et al, "Room-temperature nine-µm-wavelength photodetectors and GHz-frequency heterodyne receivers", *Nature,* 2018.

[39] P. Grant, R. Dudek, M. Buchanan, L. Wolfson et H. C. Liu, "An ultra fast quantum well infrared photodetector", *Infrared Physics & Technology,* pp. 144-152, 2005.

[40] P. D. Grant, R. Dudek, M. Buchanan et H. C. Liu , "Room-temperature heterodyne detection up to 110 GHz with a quantum-well infrared photodetector", *IEEE Photon. Technol. Lett.,* vol. 18, no. 2218, 2016.

[41] M. A. Kinch, "Fundamental Physics of Infrared Detector Materials", *Journal of ELECTRONIC MATERIALS,* vol. 29, no. 6, pp. 809-817, 2000.

[42] K. Choi, C. Lee, M. Tidrow, W. Chang et S. Gunapala, "Performance assessment of quantum well infrared photodetectors", *Applied physics letters,* vol. 65, no. 13, p. 1703–1705, 1994.

[43] M. A. Kinch et A. Yariv, "Performance limitations of GaAs / AlGaAs infrared superlattices", *Applied Physics Letters,* vol. 2093, no. 55, pp. 1-4, 1989.

[44] A. Rogalski, "Quantum well photoconductors in infrared detector technology", *Journal of Apllied Physics,* vol. 4355, no. 92, 2003.

[45] D. Hofstetter, S. Schaud, H. Wu, W. Schaff et L. Eastman, "GaN/AlN-based quantum well infrared photodetector for 1.55 um", *Appl. Phys. Lett,* vol. 83, pp. 572-574, 2003.

[46] R. Ciupa et A. Rogalski, "Performance limitations of photon and thermal infrared detectors", *Opto-Electronics Review,* vol. 5, p. 257–266, 1997.

# 3. Quantum well infrared photodetectors

## 3.1 Basic QWIP concept and operation

Since the advent of MBE (Molecular Beam Epitaxy) [1] and MOCVD (Metal Organic Chemical Vapor Deposition) [2] [3], the consequent evolution of semiconductor superlattices (SLs) and quantum well (QW) structures has boosted the development of devices based on intersubband (ISB) transitions.

Typically, a QW is obtained by sandwiching a thin layer of one type semiconductor material (well, e.g. GaAs) between two layers of another semiconductor having a larger bandgap (barrier, e.g. AlGaAs) [4]. As shown schematically in Fig.3.1, incident photons can for instance excite electrons from the ground subband to the first excited subband.

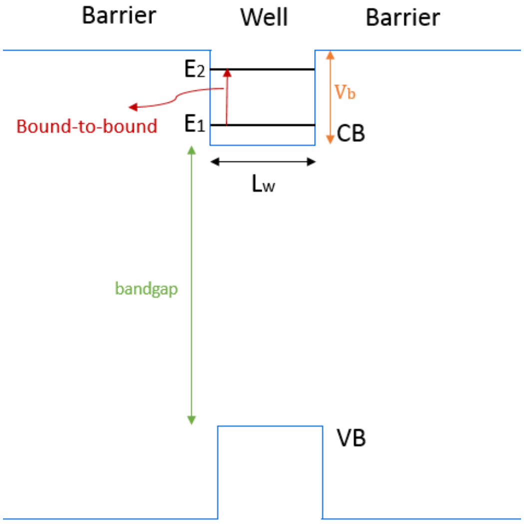

Figure. 3.1. Schematic illustration of a one-dimensional quantum well. Conduction band (CB) and valence band (VB); $V_b$ is the conduction band offset discontinuity; $L_w$ is the width of well.

In addition to GaAs/$Al_xGa_{1-x}As$, which is the most popular semiconductor compound for QWIPs, mid-infrared photodetectors can also be realized based on the following compounds: $In_xGa_{1-x}As/In_xAl_{1-x}As$ [5], $InAs/InAs_{1-x}Sb_x$ [6], $InAs/Ga_{1-x}In_xSb$ [7]. GaAs/AlGaAs and InGaAs/InAlAs QWIPs rely on ISB transition taking place in the conduction band, as described above. InAs/GaInSb and InAs/InAsSb MIR photodetectors are based on so-called *type-II transitions* in broken-gap QW systems: for InAs/GaInSb (InAsSb), the conduction band (CB) of InAs is below the valence band (VB) of GaInSb (InAsSb), and photons are absorbed between a hole and an electron miniband.

As shown in Fig.3.1, the resonant absorption wavelength of a QWIP is determined by the energy difference between the quantized states in the QWs. For a QW with infinitely high barriers, the energy of the quantized states inside the QW is given by:

$$E_n = \frac{\hbar^2 \pi^2 n^2}{2m^* L_w^2} \quad (3.1),$$

where $m^*$ is the effective mass, $\hbar$ is the reduced *Planck's constant* (1.04 x $10^{-34}$ J $s^{-1}$), $L_w$ is the width of the QW. From the electric dipole matrix element, optical transitions can take place only if the electric field vector of the incident light has a component parallel to the growth axis. Moreover, only states of opposite parity can be coupled, such as from state n to state (n+1) (see Section 3.3). From Eq (3.1), we see that, as long as the two states remain inside the QW, the energy difference $\Delta E_n$ (between state $E_n$ and $E_{n+1}$) equals $\frac{(2n+1)\hbar^2\pi^2}{2m^* L_w^2}$ , which can be changed by adjusting $L_w$.

In QWs, we distinguish 3 types of optical transitions:

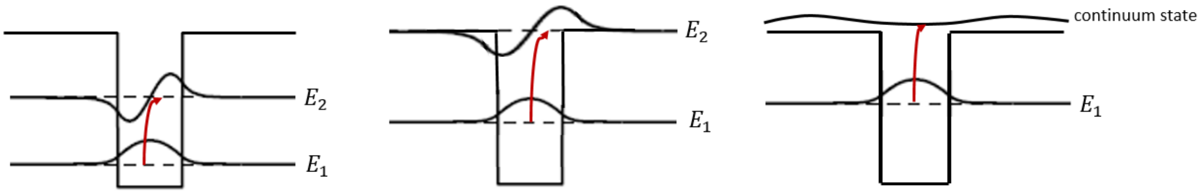

(a) bound-to-bound transition (b) bound-to-quasi bound transition (c) bound-to-continuum transition

Figure. 3.2. Illustration of different types of optical transitions in a QW: (a) bound-to-bound transition, (b) bound-to-quasi bound transition and (c) bound-to-continuum transition.

- Bound-to-bound transition. The transition takes place between two bound states. As shown in Fig. 3.2 (a), $E_1$ is the energy of the ground state, $E_2$ is the energy of the first excited state. The following condition must be satisfied: $E_{1,2} = E_1 – E_2 < V_b$, where $V_b$ is the conduction band offset. The resonant absorption wavelength is $\lambda = \frac{hc}{E_2 - E_1}$ .
- Bound-to-quasi bound transition. In this case the energy of the first excited state $E_2$ is just at the edge of the potential barrier (Fig. 3.2 (b)), i.e. $E_2 \sim V_b$.
- Bound-to-continuum transition. As shown schematically in Fig. 3.2 (c), the transition takes place between a bound state and the continuum of states above the barriers. When only one subband is present in the QW, the absorption peaks at E ~ $V_b$ - $E_1$, i.e. the resonant absorption wavelength is $\lambda = \frac{hc}{V_b - E_1}$ [9].

The bound-to-quasi bound transition allows to maximize the responsivity of a QWIP. Indeed the oscillator strength (see Section 3.3) is close to that of a bound-to-bound transition (as shown in Fig.3.2(b) the wavefunction is more delocalized compared to a bound-to-bound transition, leading to a smaller oscillator strength), with, however, a better extraction of the electrons, resulting into a higher photocurrent, for a given applied bias [4]. With respect to a bound-to-continuum QWIP, a bound-to-bound QWIP presents typically a higher oscillator strength and a reduced dark current [8].

Fig. 3.3 shows the ISB transition energy $E_2$-$E_1$ in a GaAs/$Al_xGa_{1-x}As$ QW as a function of well thickness and Al fraction [9].

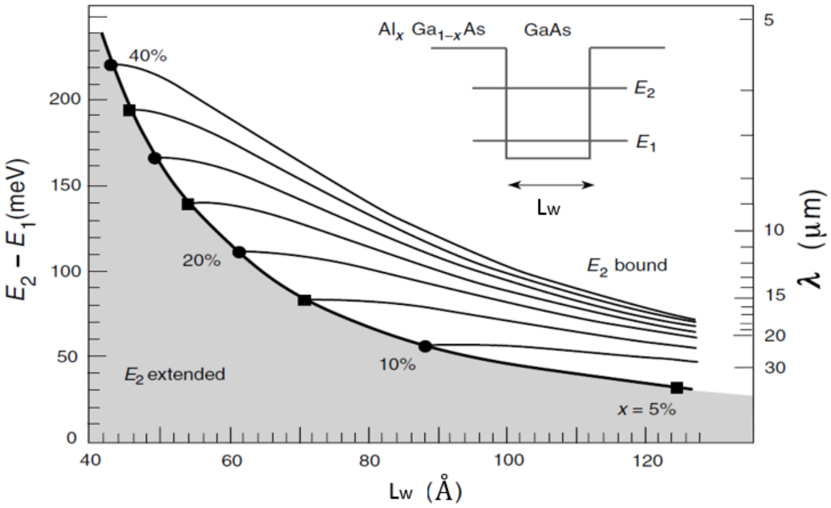

Figure. 3.3. Transition energy or resonant absorption wavelength for bound-to-bound (thin solid lines), bound-to-quasi-bound (thick solid line), and bound-to-continuum (shaded region) transitions in a GaAs/$Al_xGa_{1-x}As$ QW as a function of the Al fraction and QW thickness [9].

From Fig. 3.3, we note that, by adjusting the width of well and/or the fraction of Al, the resonant absorption wavelength can be changed, independently from the bandgap energy. For a given absorption wavelength, the quantum efficiency depends on the transition oscillator strength [4] [9]. This specific point will be addressed later on.

The operation of QWIPs is based on the photoemission of electrons from the QWs, as shown schematically in Fig. 3.4 for a n-type GaAs/AlGaAs QWIP. Photons of energy $h\nu$ excite electrons from the QWs, generating a photocurrent under an applied bias.

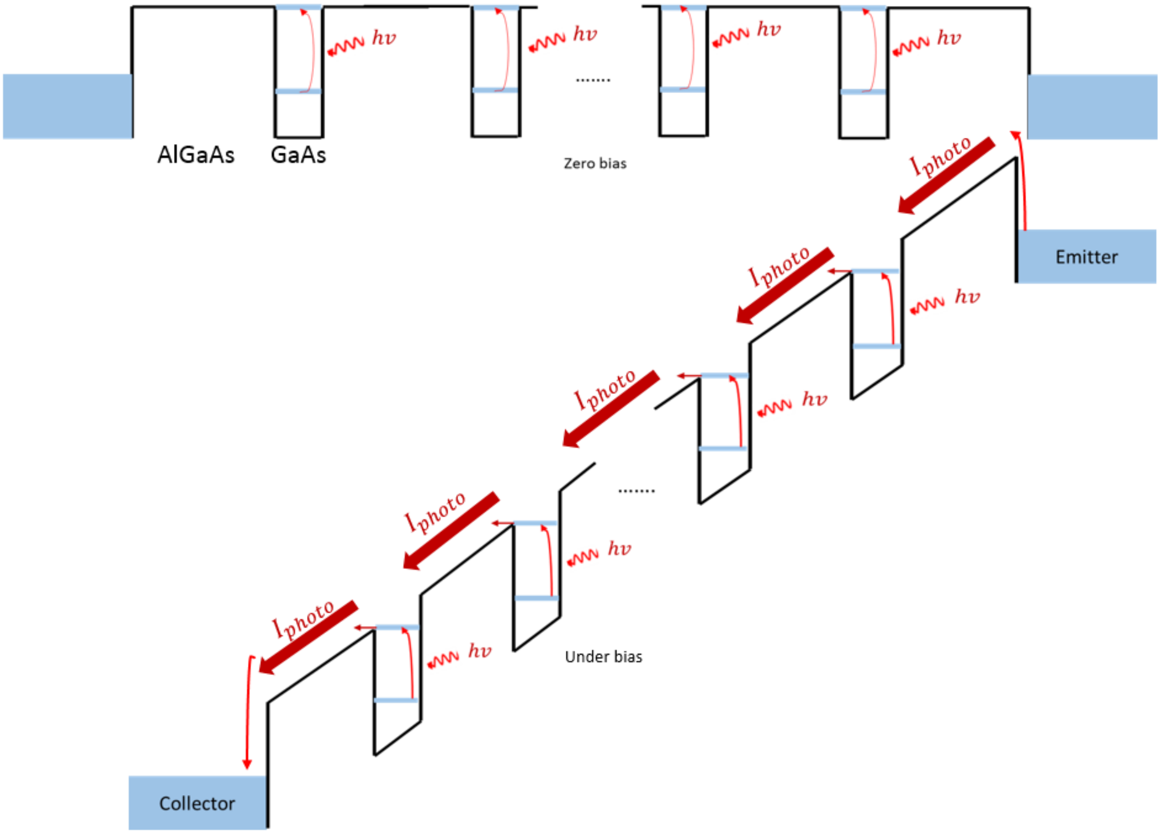

Figure. 3.4. Schematic conduction band profile of a GaAs/AlGaAs QWIP at zero bias (top) and under an applied bias (bottom).

## 3.2 Technology and main applications

Since their first demonstration in 1987 [10] QWIPs have been widely investigated for MIR detection, generally for operation in the atmospheric spectral windows (MWIR and LWIR), and mainly realized using the GaAs/AlGaAs semiconductor materials system (see Section 2.2).

QWIP detectors offer many advantages, such as high responsivity, wavelength tunability and ultra-fast response speed. One major drawback is the fact that the incident radiation must be polarized perpendicularly to the growth axis. To solve this issue, different solutions have been proposed and implemented, relying on back-substrate coupling using different mechanisms, such as linear or two-dimensional gratings; grating with optical cavity; random scatter reflectors; corrugated quantum wells or angle-polished facets (see Fig. 3.5 [11]). Another important drawback of QWIPs is the high dark-current noise, which limits their operating temperature. As a result, current applications based on QWIPs often require operation at cryogenic temperatures (typically close to liquid nitrogen temperature or lower) to achieve the desired signal-to-noise ratio.

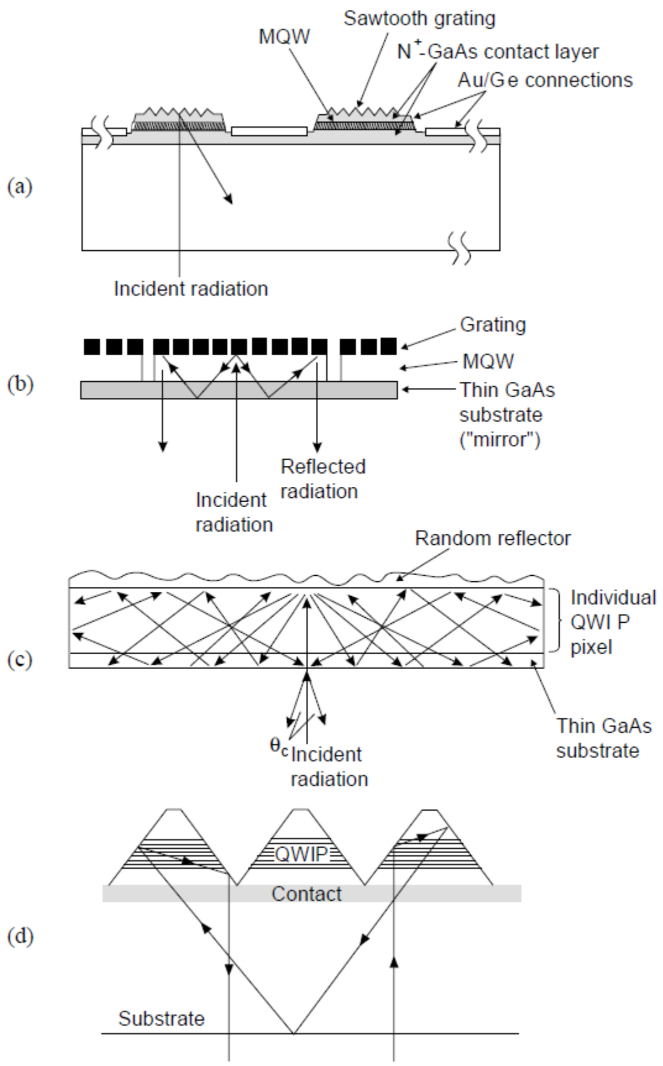

Figure. 3.5. Grating light-coupling mechanisms used in QWIPs: (a) linear or two-dimensional gratings on each detector, (b) gratings with optical cavity, (c) random scatter reflector, and (d) corrugated quantum wells [11].

High-uniformity epitaxial growth over large areas, has led to the development of QWIP two-dimensional (2D) focal plane arrays (FPA) for thermal imaging, operating in the MWIR (generally based on InGaAs/AlGaAs) and LWIR (GaAs/AlGaAs) ranges. The main applications are space science, military applications and some civilian uses [12]. For example, they can be applied for astronomical observations; to discriminate between healthy and damaged tissues, e. g. getting the visible image of a brain tumor; to map geothermal features for applications in volcanology, such as showing a hot lava tube running underground, etc… At liquid nitrogen temperature, the responsivity of QWIP FPAs is around 0.5-1 A/W, with detectivities of ~ 1 x $10^{11}$ cmHz$^{1/2}$/W. NETDs are between 30 and 50 mK [13, 14, 15, 16, 17]. Several important public laboratories and companies are developing QWIP FPAs, e.g. Jet Propulsion Laboratory (NASA) in the United States [18], Lynred (ex Sofradir) [19], AIM Infrarot-module GmbH in Germany [20], and IR-nova in Sweden [21]. In 2005, FPAs containing 1024 x 1024 pixels were demonstrated [22]. In 2018, K. K. Choi et al demonstrated small pixel, 12 µm pitch resonator-QWIP FPAs in 1280x 1024 format [23].

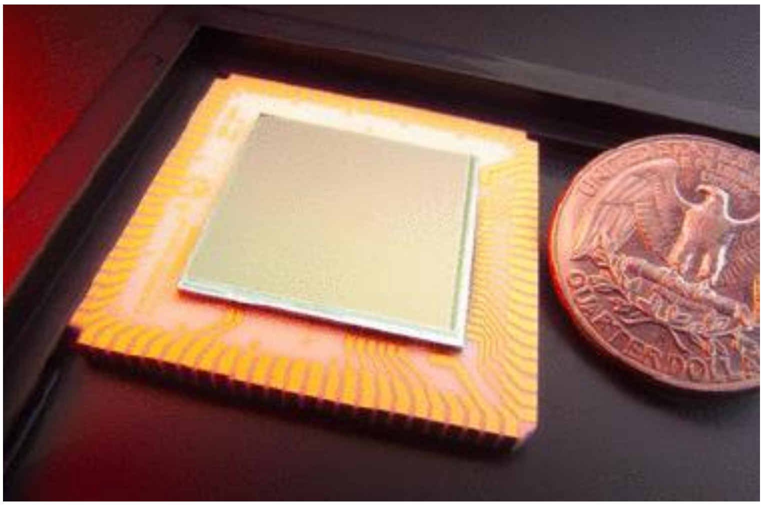

Figure. 3.6. Picture of a 1024x1024 pixel QWIP FPA fabricated made by JPL [22].

More recently, thanks to the broad wavelength tunability offered by the GaAs/AlGaAs materials system, the application range of QWIP detectors has been extended to THz range. In 2005, the first THz QWIP was demonstrated by Liu et al [24].

QWIPs based on patch antennas resonators (PARs) were first proposed in 2001 [25], as an alternative to grating coupling, or coupling through an angle-polished facet. PARs are ideally suited for QWIPs as they allow illumination at normal incidence (see Fig. 3.7), which is clearly advantageous compared to facet illumination [25, 26, 27]. Moreover, the use of antennas allows a reduction of the detector active volume without sacrificing its quantum efficiency thanks to an increased radiation collection area Compared to QWIPs based on standard mesa geometry and of comparable collection area, this brings to a significant reduction of the thermally-activated dark current. A detailed description of the operation of QWIPs based on PARs will be given in Section 3.4.5.

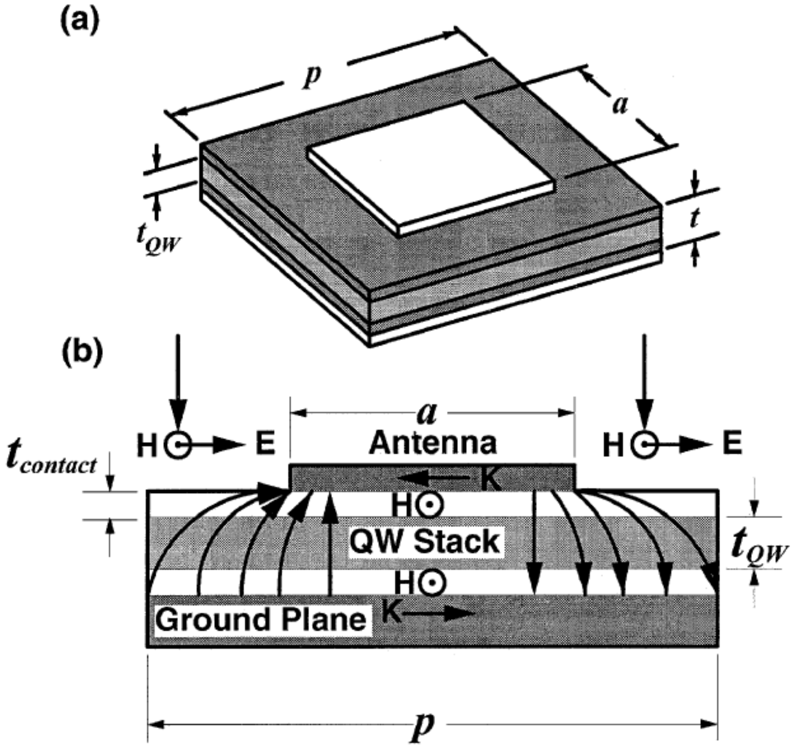

Figure. 3.7. Patch antenna resonators QWIP unit cell. (a) Layout of square antenna and (b) cross-section showing the electric field E, magnetic field H and surface current K. PARs automatically rotate polarization of light at normal incidence [25].

QWIPs based on 2D arrays of PARs were recently demonstrated [28] [29]. At 300K, a 14 times higher detectivity was reported compared to a QWIP reference based on a standard mesa geometry [29].

## 3.3 Intersubband transitions in quantum wells

QWIPs are based on ISB transitions, which refer to the transitions between the confined states in QWs. A comprehensive description of the physics related to the ISB transitions in QWs is treated by Helm [30]. Here we discuss only ISB transitions in the conduction band (CB).

### 3.3.1 The envelope function Hamiltonian

We suppose that the growth direction is along the z axis. Referring to Fig. 3.8, showing the conduction band-edge profile of a semiconductor heterostructure, the regions $z > L_w/2 \; or \; z < -L_w/2$ define the potential *barrier*, whereas the region $-L_w/2 < z < L_w/2$ defines the QW. The reference point-zero-energy is chosen at the bottom of the QW.

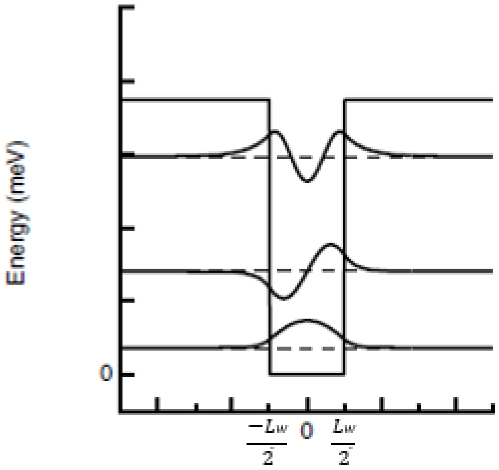

Figure. 3.8. Band-edge profile of the CB in a one-dimensional QW with three bound states.

For simplicity we label the barrier and well regions respectively as A and B. Then, the electronic wavefunction in each layer can be expanded on the periodic parts of the Bloch functions at the center of the Brillouin zone $\mathbf{k}_0 = 0$ [31]:

$$\boldsymbol{\psi}(\boldsymbol{r}) = \sum_l f_l^{A,B} u_{l,\mathbf{k}_0}^{A,B}(\boldsymbol{r}) \quad (3.2).$$

In Eq. (3.2), *l* is an index that runs over all the bands of the semiconductor materials (A or B); $u_{l,\mathbf{k}_0}^{A,B}(\boldsymbol{r})$ are the periodic parts of the Bloch functions, and the *envelope functions* $f_l^{A,B}(\boldsymbol{r})$ are supposed to be slowly varying over the crystal unit cell. Furthermore, it is assumed that the Bloch functions are identical in both materials, i.e. $u_{l,0}^{A}(\boldsymbol{r}) = u_{l,0}^{B}(\boldsymbol{r})$, hence Eq. (3.2) can be written as:

$$\boldsymbol{\psi}(\boldsymbol{r}) = \sum_l f_l^{A,B} u_{l,\mathbf{k}_0}(\boldsymbol{r}) \quad (3.3).$$

Because of the in-plane translational invariance, the envelope functions in each layer can be expressed as $f_l^{A,B}(\boldsymbol{r}) = \frac{e^{i\mathrm{k}_{||}\cdot\mathrm{r}_{||}}}{\sqrt{A}}\chi_l^{A,B}(z)$, where $\mathrm{k}_{||} = (k_x, k_y)$ is the 2D in-plane wavevector, $\mathrm{r}_{||}$ is the position in the plane of layer, and A is the in-plane sample area. Therefore, from Eq. (3.3) we have:

$$\boldsymbol{\psi}(\boldsymbol{r}) = \sum_l \frac{e^{i\mathrm{k}_{||}\cdot\mathrm{r}_{||}}}{\sqrt{A}}\chi_l^{A,B}(z) u_{l,\mathbf{k}_0}(\boldsymbol{r}) \quad (3.4).$$

The Hamiltonian of the heterostructure can be written as

$$H = \frac{p^2}{2m_0} + V_A(r)Y_A(z) + V_B(r)Y_B(z) \quad (3.5),$$

where $p$ is the momentum operator, $m_0$ is the mass of electron, $V_{A,B}(r)$ is the potential in the respective layers, and the function $Y_A(z)$ ($Y_B(z)$) is a step function equals to 1 in the A(B) layer and 0 in the B(A) layer. Since the envelop function is slowly varying over the unit cell, we may write:

$$\int_{cell} d^3r\, f_l^* f_m u_l^* u_m = f_l^* f_m \int_{cell} d^3r u_l^* u_m = f_l^* f_m \delta_{lm} \quad (3.6),$$

where $\delta$ is Dirac delta function. We have also that the periodic parts of the Bloch functions are eigenfunctions of the Hamiltonian in each layer:

$$\left(\frac{p^2}{2m_0} + V_{A,B}(r)\right) u_{m,\mathbf{k}_0}(\boldsymbol{r}) = E_{m,\mathbf{k}_0}^{A,B} u_{m,\mathbf{k}_0}(\boldsymbol{r}) \quad (3.7),$$

where $E_{m,\mathbf{k}_0}^{A,B}$ is the energy for the m<sup>th</sup> band at the center of the Brillouin zone in each layer. By using Eqs. (3.5) to (3.7), one finally obtains the following set of eigenvalue equations in matrix from:

$$D\left(z, -i\hbar\frac{\partial}{\partial z}\right)\chi = E\chi \quad (3.8),$$

where the matrix elements D are given by :

$$D_{lm} = \left(E_l^A Y_A + E_l^B Y_B + \frac{\hbar^2 k_{||}^2}{2m_0} - \frac{\hbar^2}{2m_0}\frac{\partial^2}{\partial z^2}\right)\delta_{l,m} + \frac{\hbar k_{||}}{2m_0}\langle l|p_{||}|m\rangle - \frac{i\hbar}{2m_0}\langle l|\mathrm{p_z}|m\rangle\frac{\partial}{\partial z} \quad (3.9).$$

As shown by Eq. (3.9), different bands are coupled by the matrix elements $\langle l|p_{||}|m\rangle$ and $\langle l|\mathrm{p_z}|m\rangle$. The Ben-Daniel-Duke model, which works well for the lowest conduction states of GaAs-AlGaAs heterostructures, assumes that the envelope function is built from quantum states belonging to a single parabolic band, i.e. the conduction band. In this case, for $\mathrm{k}_{||} = 0$, it can be shown that Eq. (3.8) takes the simple form:

$$-\frac{\hbar^2}{2m^*(z)}\frac{d^2}{dz^2}\chi(z) + V(z)\chi(z) = E\chi(z) \quad (3.10),$$

where V(z) is the conduction band profile. $m^*(z)$ is the effective mass in each layer, given by:

$$(m^*)^{-1} = (m_0)^{-1}(1 + \frac{E_P}{E_g}) \quad (3.11),$$

where $E_g$ is the energy gap, and $E_P$ , the so-called Kane energy, is given by:

$$E_P = \frac{2}{m_0}|\langle u_{c,0}|p|u_{v,0}\rangle|^2 \quad (3.12).$$

Eq. (3.10) is the Schrödinger equation for the envelope function $\chi(z)$, which allows to find the eigenfunctions by applying the continuity of $\chi(z)$ and of $\frac{1}{m^*}\frac{\partial\chi}{\partial z}$ at the interfaces between materials A and B [31].

### 3.3.2 The symmetric quantum well

***Wavefunctions***

We will now use Eq. (3.10) to compute the eigen-functions and eigen-energies of a symmetric QW with a finite barrier height. Then, by applying Fermi's golden rule, this will allow to quantify the absorption of different ISB transitions, i.e. both bound-to-bound and bound-to-continuum transitions, with the inclusion of a Lorentzian broadening to take into account the finite final state lifetime [32].

We assume that there are only two bound states in the QW with energies $E_{1,2} < V_b$. As shown in Fig. 3.9, to avoid problems involving the normalization of the wave functions in the continuum (E > V$_b$), we introduce a fictitious square well of width *L* within which the electrons in the continuum are trapped.

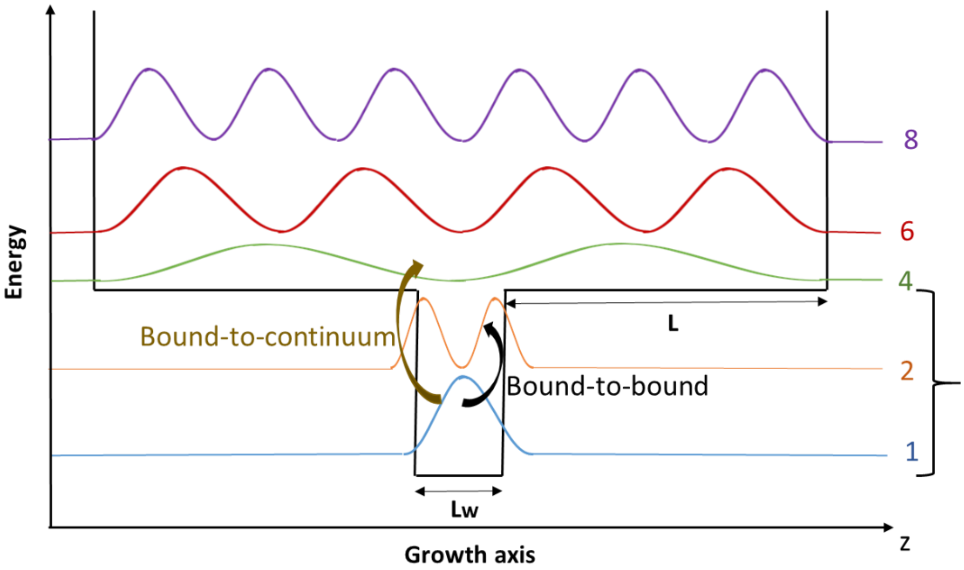

Figure. 3.9. Schematic energy levels and module squared wave-functions in a potential well with finite barrier height V$_b$ and a fictitious potential box of width L.

Form Eq. (3.10), by applying the appropriate boundary conditions for the envelope function, we obtain the following ground state wave function:

$$\psi_1(z) = C_1 \begin{cases} e^{\kappa_1(z+\frac{L_w}{2})} cos k_1 \cdot \frac{L_w}{2} & if\ z < -\frac{L_w}{2} \\ cos k_1 z & if\ -\frac{L_w}{2} \leq z \leq \frac{L_w}{2} \\ e^{-\kappa_1(z-\frac{L_w}{2})} cos k_1 \cdot \frac{L_w}{2} & if\ z > \frac{L_w}{2} \end{cases} \quad (3.13);$$

$$C_1 = \frac{1}{\sqrt{\frac{L_w}{2}+\frac{V_b}{\kappa_1 E_1} cos^2(k_1 \frac{L_w}{2})}} \quad \text{with} \quad \tan(k_1 \frac{L_w}{2}) = \frac{m_a^* k_1}{m_b^* \kappa_1} \quad (3.14).$$

The first excited state wave function is:

$$\psi_2(z) = C_2 \begin{cases} -e^{\kappa_2(z+\frac{L_w}{2})} sin\,(k_2 \cdot \frac{L_w}{2}) & if\ z < -\frac{L_w}{2} \\ sin k_2 z & if\ -\frac{L_w}{2} \leq z \leq \frac{L_w}{2} \\ e^{-\kappa_2(z-\frac{L_w}{2})}\ sin\left(k_2 \cdot \frac{L_w}{2}\right) & if\ z > \frac{L_w}{2} \end{cases} \quad (3.15);$$

$$C_2 = \frac{1}{\sqrt{\frac{L_w}{2}+\frac{V_b}{\kappa_2 E_2} sin^2(k_2 \frac{L_w}{2})}} \quad \text{with} \quad \tan\left(k_2 \frac{L_w}{2}\right) = -\frac{m_b^* k_2}{m_a^* \kappa_2} \quad (3.16),$$

where $k_{1,2} = \frac{\sqrt{2m_a^* E_{1,2}}}{\hbar}$, $\kappa_{1,2} = \frac{\sqrt{2m_b^*(V_b - E_{1,2})}}{\hbar}$, $m_a^*(m_b^*)$ is the effective mass of well (barrier). In fact, all even parity bound states satisfy Eqs. (3.13) (3.14); all odd parity bound states satisfy Eqs. (3.15) (3.16).

For the delocalized continuum eigenstates above the barriers, we chose only those with odd parity. Indeed, as we shall see below, for ISB transitions from the ground state (even parity), only odd party continuum states are allowed as final states. Using a fictitious-box normalization scheme (see Fig 3.9), the odd parity wave function for the continuum states is obtained from Eq. (3.10):

$$\psi_{odd} = \frac{1}{\sqrt{L}} \begin{cases} sin\,[k'\left(z + \frac{L_w}{2}\right) - \beta] & if\ z < -\frac{L_w}{2} \\ sin\,(kz)\ \cdot (sin^2(k\frac{L_w}{2}) + \frac{m_b^* k}{m_a^* k'} cos^2(k\frac{L_w}{2}))^{-1/2} & if\ -\frac{L_w}{2} \le z \le \frac{L_w}{2} \\ sin\left[k'\left(z - \frac{L_w}{2}\right) + \beta\right] & if\ z > \frac{L_w}{2} \end{cases} \quad (3.17),$$

where $k = \frac{\sqrt{2m_a^* E_{odd}}}{\hbar}$, $k' = \frac{\sqrt{2m_b^*(E_{odd} - V_b)}}{\hbar}$, $E_{odd}$ is the energy associated at the odd-nth eigenstate. $\beta$ is given by the relation $\tan(\beta) = \frac{m_a^* k'}{m_b^* k} tan\,(k\frac{L_w}{2})$, and L is a normalization length on either side of the well.

***Oscillator strength and absorption coefficient***

We consider a linearly polarized electromagnetic plane wave with an electric field:

$$\mathcal{E} = \boldsymbol{\varepsilon} \cdot \mathcal{E}_0 e^{i\mathbf{q}\cdot\mathbf{r}} e^{i\omega t} \quad (3.18),$$

where $\mathcal{E}_0$ is the amplitude of the electric field, $\boldsymbol{\varepsilon}$ is the polarization vector, $\omega$ is the photon angular frequency, and **q** is the propagation wavevector. Since the radiation wavelength is much bigger than the width of the QW, the dipole interaction Hamiltonian is given by:

$$\widehat{H}_{int} = \frac{e}{2m^*}(\boldsymbol{\mathcal{A}} \cdot \mathbf{p} + \mathbf{p} \cdot \boldsymbol{\mathcal{A}}) = \frac{ie\mathcal{E}_0}{2m^*\omega}\boldsymbol{\varepsilon} \cdot \mathbf{p} \quad (3.19).$$

where the corresponding vector potential $\boldsymbol{\mathcal{A}}$, which is given by the relation $\mathcal{E} = -\frac{\partial \boldsymbol{\mathcal{A}}}{\partial \boldsymbol{t}}$.

From the Fermi Golden rule, the transition rate from state $|\psi_{i,k}>$ to state $|\psi_{f,k'}>$, under the perturbation $\widehat{H}_{int}$, is then:

$$\begin{aligned} W_{if}(\omega) &= \frac{2\pi}{\hbar}|M|^2\delta\big(E_f - E_i - \hbar\omega\big) \\ &= \frac{2\pi}{\hbar}\left|\langle \psi_{f,k'}\middle|\widehat{H}_{int}\middle|\psi_{i,k}\rangle\right|^2 \delta\big(E_f - E_i - \hbar\omega\big) \\ &= \frac{2\pi}{\hbar}\frac{e^2\mathcal{E}_0{}^2}{4m^{*2}\omega^2}\left|\langle \psi_{f,k'}|\boldsymbol{\varepsilon} \cdot \mathbf{p}|\psi_{i,k}\rangle\right|^2 \delta(E_f - E_i - \hbar\omega) \quad (3.20), \end{aligned}$$

where M is the matrix element of interest between the two states, $\langle \psi_{f,k'}|\boldsymbol{\varepsilon} \cdot \mathbf{p}|\psi_{i,k}\rangle = sin\,(\theta)\delta_{k,k'}\langle \psi_f(z)|p_z|\psi_i(z)\rangle$, and $sin(\theta) = (\boldsymbol{\varepsilon} \cdot \hat{z})$, with $\hat{z}$ the unit vector in the z-direction, i.e. the growth direction. As implied from the term $\langle \psi_f(z)|p_z|\psi_i(z)\rangle$, *the external electric field must have a component along the growth direction in order to induce the ISB transition*. This is known as the **polarization selection rule**. In other words, as shown by the term $\delta_{k,k'}$ , in ISB transitions the in-plane momentum is conserved ($k_{xy} = k'_{xy}$).

Let us now consider a beam propagating at an angle $\theta$ with respect to the growth direction of the QW. The matrix element in Eq. (3.20) is given by:

$$M = \frac{e}{m^*}\sqrt{\frac{\Phi\hbar}{2\epsilon_0 n_r \omega c}}\; sin\,(\theta)\delta_{k_{xy},k'_{xy}}\langle \psi_f(z)|p_z|\psi_i(z)\rangle \quad (3.21),$$

where $\Phi$ is the incident photon flux, $n_r$ is the refractive index of the semiconductor, and $\epsilon_0$ is the permittivity of the free space. The transition rate $W_{if}(\omega)$ is then evaluated defining the absorption quantum efficiency η:

$$\eta = W_{if}(\omega)/(\Phi A cos\theta) = \frac{e^2 h}{4m^*\epsilon_0 n_r c}\frac{sin^2\theta}{cos\theta} n_{2D} f_{if}\delta(E_f - E_i - \hbar\omega) \quad (3.22),$$

where $n_{2D}$ is the 2D density of electrons in the ground state subband ($n_{2D} = \frac{m^* E_f}{\pi\hbar^2}$). The oscillator strength $f_{if}$ is defined by:

$$f_{if} = \frac{2}{m^*(E_f - E_i)} \langle \psi_f(z) | p_z | \psi_i(z) \rangle^2 = \frac{2m^*(E_f - E_i)}{\hbar^2} \langle \psi_f(z) | z | \psi_i(z) \rangle^2 \quad (3.23).$$

The oscillator strength is a dimensionless quantity used to compare transition strengths in different physical systems. It can be shown that it obeys to the following sum rule:

$$\sum_f f_{if} = 1 \quad (3.24),$$

where $f_{if}$ is the oscillator strength from an initial state *i* to all possible final states f. We note that $f_{if}$ is not zero only for transitions of opposite-parity, which explains why we considered only odd-parity states in the continuum in Eq. (3.17). For a QW with infinite barriers the oscillator strength is given by:

$$f_{if}^{\infty} = \frac{64}{\pi^2} \frac{f^2 i^2}{(f^2 - i^2)} \quad (3.25).$$

In the case of finite barriers, the oscillator strengths for the bound-to-bound ($f_{B-B}$) and the bound-to-continuum transition ($f_{B-C}$) can be computed analytically using the wavefunctions derived in Eqs.(3.13)-(3.17) [32].

The bi-dimensional absorption coefficient of a superlattice with $N_{QW}$ QWs, is obtained by summing over all the allowed transition. From Eq. (3.22), it is expressed as:

$$\eta(\omega) = N_{QW} \frac{e^2 h}{4m^* \epsilon_0 n_r c} \frac{sin^2\theta}{cos\theta} n_{2D} \sum_f f_{if}\, \delta(E_f - E_i - \hbar\omega) \quad (3.26).$$

By replacing the Dirac-delta-function with a Lorentzian function to take into account the finite lifetime of the final state we obtain:

$$\eta(\omega) = N_{QW} \frac{e^2 h}{4m^* \epsilon_0 n_r c} \frac{sin^2\theta}{cos\theta} n_{2D} \sum_f f_{if} \frac{1}{\pi} \frac{\Delta E}{(E_f - E_i - \hbar\omega)^2 + \Delta E^2} \quad (3.27),$$

where $\Delta E$ is the half width at half maximum of the Lorentzian peak. Ideally, neglecting elastic broadening mechanisms (e.g, interface roughness or well width fluctuations), $\Delta E$ is related to the life time of the excited carriers by the relation $\tau_c = \frac{\hbar}{2\Delta E}$.

For a bound-to-bound transition the absorption quantum efficiency is trivially evaluated. For bound-to-continuum transitions the sum must be replaced by an integral over the energy continuum: $\sum \rightarrow \int_0^\infty Ldk'/\pi$. We then have:

$$\eta(\omega) = \eta_{B-B}(\omega) + \eta_{B-C}(\omega) \quad \text{(3.28).}$$

With

$$\eta_{B-B}(\omega) = N_{QW} \frac{e^2 h}{4m^* \epsilon_0 n_r c} \frac{sin^2\theta}{cos\theta} n_{2D} \frac{1}{\pi\Delta E} \frac{1}{[(E_2 - E_1 - \hbar\omega)/\Delta E]^2 + 1} f_{B-B} \quad \text{(3.29);}$$

$$\eta_{B-C}(\omega) = N_{QW} \frac{e^2 L\sqrt{2}}{4\sqrt{m^*} \epsilon_0 n_r c} \frac{sin^2\theta}{cos\theta} n_{2D} \frac{1}{\pi\Delta E} \int_{V_b}^{\infty} \frac{dE}{\sqrt{E - V_b}} \frac{1}{[(E - E_1 - \hbar\omega)/\Delta E]^2 + 1} f_{B-C}(E) \quad \text{(3.30).}$$

From these last equations one can compute the absorption quantum efficiency for different well widths, as reported in Fig. 3.10. The transition moves from pure bound-to-bound to bound-to-continuum as the width of well increases. The bound-to-bound transition yields a narrower linewidth and a higher absorption compared to the bound-to-continuum transition. The latter shows an evident asymmetry due to the broadening at high energy.

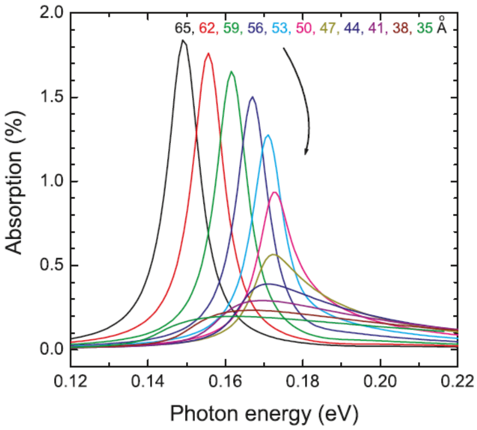

Figure. 3.10. Calculated absorption quantum efficiency vs. photon energy for one well for different widths of well from 35 to 65 Å [4] .

## 3.4 Photoconductive QWIP

### 3.4.1 Photocurrent and responsivity in QWIPs

To derive the responsivity of a QWIP photodetector, a phenomenological model has been developed by H. C. Liu and H. Schneider that takes into account the electron's photoemission and capture processes from/into the QWs [4]. This model is however based on a heuristic approach which is not completely satisfactory. In this thesis, we prefer to go back to basics and adopt Eq. (2.10) and Eq. (2.11), derived for an homogeneous interband photoconductor, and adapt them to the case of a QWIP detector, by replacing the carrier's interband recombination time, τ, with the carrier's capture time in the QWs. As a result, the responsivity of a QWIP detector is given by:

$$\mathcal{R} = \eta g \frac{1}{h\nu/e} \qquad (3.31),$$

where the photoconductive gain can be written as:

$$g = \frac{\tau_c}{\tau_{tr}} = \frac{\tau_c v_d(F)}{N_{QW} L_p} \qquad (3.32).$$

In this equation, *F* is the electric field, $v_d(F)$ is the drift velocity, $L_p$ is the length of one period, and $\tau_{tr} = N_{QW}L_p/v_d(F)$ (3.33) is the total transit time across the QWIP. Since $\eta$ is directly proportional to the number of wells (see Eqs. (3.29), (3.30)), from Eq. (3.31) we find that the responsivity of a QWIP detector is independent from the number of QWs. We note that the expression of the photoconductive gain derived from the model of H. C. Liu and H. Schneider is coincident with Eq.(3.32) if $\tau_c \gg \tau_{tr}/N_{QW}$ [4].

### 3.4.2 Dark current in QWIPs

Dark current is a crucial parameter because it contributes to the detector noise and dictates the operating temperature. The dark current of QWIPs mainly originates from thermionic emission from the QWs. It exponentially increases with the temperature of detector. A good understanding of the dark current is necessary for the optimization of the quantum mechanical design of QWIPs to achieve a better signal-to-noise ratio and higher operating temperature.

To evaluate the dark current, we make the following assumptions and approximations:

a) We neglect the contribution to the dark current of interwell tunneling (the QWIP barrier is sufficiently thick).
b) The electron density in each well remains constant.
c) The heavily doped emitter serves as a perfectly injecting contact

d) Only one bound state is confined in the QW (includes bound-to-continuum transition and bound-to-quasi bound transition).

Having defined the physical regime, in QWIPs the dark current is controlled by the flow of electrons above the barriers and by the emission/capture of electrons in the wells.

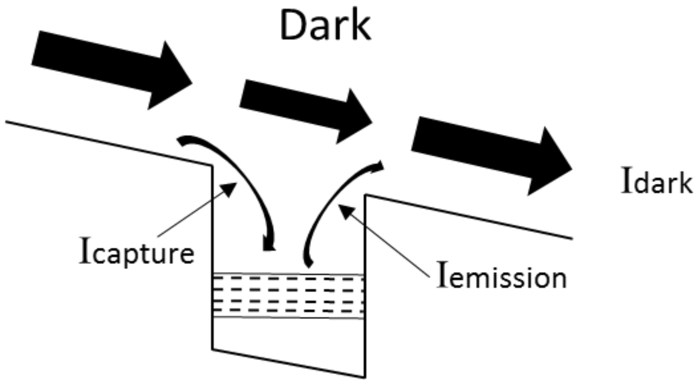

Figure. 3.11. Schematic representation of the capture and emission of electrons in dark condition [4].

At a finite temperature, electrons are not only trapped in the well, but also distributed on the top of the barrier (as shown in Fig. 3.11). On the top of the barriers, we have essentially a 3D density of states, and the dark current is labelled as $J_{dark}$. We label as $j_e$ the component of the current due to the emission of electrons from the well. At steady state this component will be balanced by the trapping or capture of the electrons into the well, i.e. $j_e = j_c$. If we define a trapping or capture probability $p_c$, we have $j_c = p_c j_{3D}$. From the continuity of the electrical current (see Fig.3.11), the following relation must hold:

$$j_{dark} = j_e + (1 - p_c) j_{dark} \quad (3.34).$$

The dark current is thus given by:

$$J_{dark} = j_e / p_c \quad (3.35).$$

An Emission-Capture Model is demonstrated in Ref [4] to express the dark current density as:

$$J_{dark} = \frac{j_e}{p_c} = \frac{eN_{2D} v_d(F)}{L_p} \frac{\tau_c}{\tau_{scatt}} \quad (3.36),$$

where $N_{2D}$ a 2D electron density which only includes electrons on the upper part of the ground state subband (i.e. above the barriers), $\tau_{scatt}$ is the scattering time to transfer these electrons from the 2D subband to the nonconfined continuum states, and $v_d(F)$ takes the usual form:

$$v_d(F) = \frac{\mu F}{[1+(\mu F/v_{sat})^2]^{1/2}} \quad (3.37),$$

where $\mu$ is the low field mobility and $v_{sat}$ is the saturated drift velocity [4]. The typical value of the saturated drift velocity for GaAs QWIPs is $10^7 \mathrm{cms}^{-1}$.

The 2D electron density can be obtained by considering the thermionic emission from the QW [4]:

$$N_{2D} = m_a^* k_B T/\pi\hbar^2 \exp\left(-\frac{E_{act}}{k_B T}\right) \quad (3.38),$$

where $E_{act}$ is the thermal activation energy which equals the energy difference between the top of the barrier and the Fermi level in the well. Assuming a complete ionization, $E_f$ can be obtained from the 2D doping density $n_d$ which equals the electron density in the QW [4]:

$$n_d = (m^*/\pi\hbar^2)E_f \quad (3.39).$$

### 3.4.3 Detector noise

In general, a photoconductor has several sources of noise: (i) 1/f noise, (ii) Johnson noise (thermal noise), (iii) dark current noise and, (iv) photon noise (associated with the current induced by the incident photons). For GaAs QWIPs, 1/f noise seldom limits the detector performance, therefore we neglect its contribution.

As mentioned in Section 2.1.2, thermal noise (Eq. (2.13)) is inherent to all resistive devices, and its contribution is usually small in a photoconductive QWIP [34]. Contributions from the dark current noise and the photon noise usually limit the detector ultimate performance. These noise sources are of the same nature, and are related to the generation-recombination (g-r) noise. From Eq. (2.12), the total noise mean square current related to g-r noise in a QWIP is given by:

$$i_{g-r}^2 = 4eg_{noise}I_{tot}\mathit{\Delta} f \quad (3.40),$$

where $g_{noise}$ is the noise gain, and $I_{tot}$ is the total current through the structure. For bound to quasi-bound and bound-to-continuum structures, such as those studied in this work, with good approximation we have that, $g_{noise} = g_{photo} = \frac{\tau_c}{\tau_{tr}}$ [35].

Here, we discuss the case of a conventional optimized QWIP device where the dominant noise is the g-r noise. We assume that the photodetector is illuminated by a signal wave of power $P_s$. Taking into account also the background radiation $P_B$, the total current $I_{tot}$ is given by:

$$I_{tot} = \mathcal{R}P_s + \mathcal{R}P_B + I_{dark} \quad (3.41).$$

From Eq. (3.41) we can distinguish the detector operation regime from the nature of the dominating noise contribution: signal limited ($\mathcal{R}P_s$ dominates), background limited ($\mathcal{R}P_B$ dominates) and detector limited ($I_{dark}$ dominates).

### 3.4.4 Noise equivalent power and detectivity in QWIPs

Since the object is often surrounded by 300K background, we can neglect the noise contribution from the signal current $\mathcal{R}P_s$. In the following, we will derive the expressions for the detectivity under different operating regimes: detector limited regime and background limited region.

✧ **Detector limited**: when the dark current noise dominates. The $I_{dark}$ can be estimated from Eqs. (3.36) (3.38) as:

$$I_{dark} = A_{det}J_{dark} = \frac{eN_{2D}v_d(F)}{L_p}\frac{\tau_c}{\tau_{scatt}}A_{det} = J_0\, A_{det}T\exp\left(-\frac{E_{act}}{k_BT}\right) \quad (3.42),$$

where $J_0$ is $\frac{\tau_c}{\tau_{scatt}}\frac{ev_d(F)m_a^* k_B}{\pi\hbar^2 L_p}$, a constant that depends solely on the properties of the absorbing region. Therefore, the detectivity is given by (see Eqs. (2.16) (2.17) (3.31) (3.32) and (3.42)):

$$D_{DL}^{*} = \frac{\sqrt{A_{det}}}{NEP} = \frac{\mathcal{R}\sqrt{A_{det}}}{\sqrt{4egI_{dark}}} = \frac{\eta\sqrt{\tau_{scatt}}}{2h\nu\sqrt{N_{QW}N_{2D}}} \quad (3.43)$$

In an ideal QWIP, the absorption from each QW is identical and $\eta = N_{QW}\eta^{(1)}$ (see Eq. (3.27)). We then have that $D_{DL}^{*} \propto \eta^{(1)}\sqrt{N_{QW}}$, i.e. in the detector limited regime the detectivity increases with the number of QWs. By relating the 2D doping density in the well, $n_d$, to $D_{DL}^{*}$, we can get the doping that maximizes the detectivity. From Eq. (3.39), we know $n_d$ is directly proportional to the Fermi energy. We have $\eta^{(1)} \propto n_d \propto E_f$ , and $N_{2D} \propto \exp\left(\frac{E_f}{k_B T_{det}}\right)$ (Eq.(3.38)), which gives $D_{DL}^{*} \propto E_f \exp\left(-\frac{E_f}{2k_B T_{det}}\right)$. The optimum QW doping level for the maximum $D_{DL}^{*}$ is found from:

$$\frac{d}{dE_f} E_f \exp\left(-\frac{E_f}{2k_B T_{det}}\right) = 0 \quad (3.44),$$

which is satisfied for $E_f = 2k_B T_{det}$ , i.e. $n_d = (m^{*}/\pi\hbar^2)2k_B T_{det}$ : for a given detector temperature, there is an optimum doping $n_d$ that maximizes the detectivity under detector limited.

✧ **Background limited**: when the background noise dominates. The detectivity is given by:

$$D_{BL}^{*} = \frac{\sqrt{A_{det}}}{NEP} = \frac{\sqrt{\mathcal{R}A_{det}}}{\sqrt{4egP_B}} = \frac{1}{2}\frac{\sqrt{\eta A_{det}}}{\sqrt{h\nu P_B}} \quad (3.45).$$

As discussed in Chapter 2.1.3, at $T_{BLIP}$, we have:

$$\mathcal{R}P_B = I_{dark} \quad (3.46),$$

and the detector operates in the BLIP regime when $T_{det} < T_{BLIP}$. From Eqs. (3.31) (3.32) (3.42), Eq. (3.46) can be rewritten as:

$$\eta \frac{1}{h\nu}\frac{\tau_c}{N_{QW}L_p} P_B = A_{det} J_0 T_{BLIP} \exp\left(-\frac{E_1 - E_2 - E_f}{k_B T_{BLIP}}\right) \quad (3.47).$$

We can now use Eq. (3.47) to obtain the value of $E_f$ (hence of $n_d$ - see Eq. (3.39)) that maximizes $T_{BLIP}$ . $T_{BLIP}$ is dependent on the Fermi energy. On the other hand we know that $\eta \propto n_d \propto E_f$, therefore, Eq. (3.47) can be rewritten as:

$$\frac{E_f}{k_B T_{BLIP}} \exp\left(-\frac{E_f}{k_B T_{BLIP}}\right) = constant \times \exp\left(-\frac{E_1 - E_2}{k_B T_{BLIP}}\right) \quad (3.48).$$

For a given $E_f$ , we can therefore calculate the corresponding $T_{BLIP}$ . From a simple differentiation we find that the left-hand side of Eq. (3.48) is maximized when $E_f = k_B T_{BLIP}$ [4], which, from inspection of the right hand side, corresponds to a maximum $T_{BLIP} = T_{BLIP}^{max}$. Using Eq. (3.39) we then can calculate the optimum doping density. In Fig. 3.12 we report the experimental (black squares), computed (solid line) detectivity and $T_{BLIP}$ as a function of $n_d$ for a QWIP detector operating at ~9µm [36]. As we can see the agreement is very good, showing that Eqs. (3.43) and (3.48) can indeed be used to optimize the QWIP doping density.

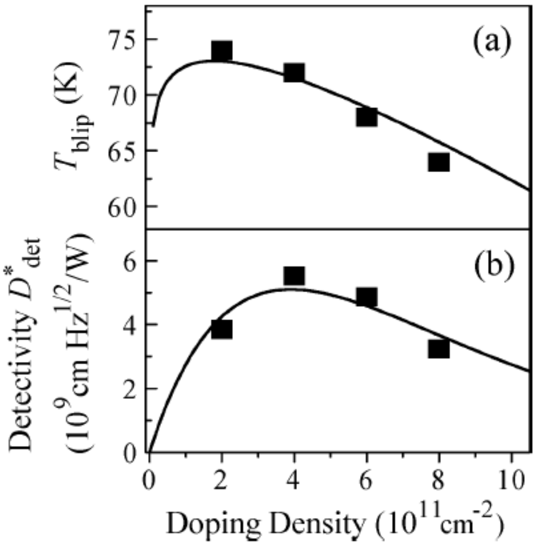

Figure. 3.12. Dependence of (a) BLIP temperature and (b) detector-noise-limited detectivity measured at 80 K under 500-K blackbody radiation on Si doping density in the QWs. The solid lines present the computed values from Eq. (3.43) and Eq. (3.48). The black squares are the experimental results [36].

One of the disadvantages of QWIPs is their relatively low $T_{BLIP}$ compared other IR detectors. In fact, Eq. (3.47) shows that the $T_{BLIP}$ of QWIPs is fundamentally limited by the low carrier life time $\tau_c$, ruled by optical-phonon emission, which is of the order of the *ps*, compared to *ns* in MCT or InSb detectors. On the other hand, such a short carrier life time meets the requirement to realize an ultra-fast MIR detector. A state of the art, “standard” QWIP with $n_d = 2.4 \times 10^{11}\ cm^{-2}$ at 9 µm has a $T_{BLIP} = 72\ K$ [15].

As we shall see in next section, an effective strategy to increase $T_{BLIP}$ consists in coupling the QWIP with a PAR structure, which, essentially, allows reducing the physical detector area (hence the dark current) without reducing the quantum efficiency [29].

### 3.4.5 Patch antenna QWIPs

#### 3.4.5.1 Introduction

Plasmonic nanostructures play an important role in the domain of photonics and nano-electronics [37] [38]. Nano-antennas were first applied to MIR bolometers as a way to increase both their sensitivity and speed [39] [40] [41], and have been actively investigated as tools to compress light in a sub-wavelength region of space [42] [43] [44]. As we shall see, in the context of high-speed QWIPs, the possibility of coupling a QWIP element to PARs opens up interesting perspectives, in particular the possibility (i) to achieve surface illumination and (ii) to reduce the device RC time constant without sacrificing its collection area [29].

In the rest of this thesis, a PAR is defined as a double metal cavity obtained by sandwiching a semiconductor layer between a bottom metallic ground and a square shaped top metal layer, as shown in Fig. 3.13. In general, to obtain a sufficiently large detector collection area, at least equal to the diffraction-limited spot size of the incident beam, we will exploit a PAR 2D array instead of a single PAR element.

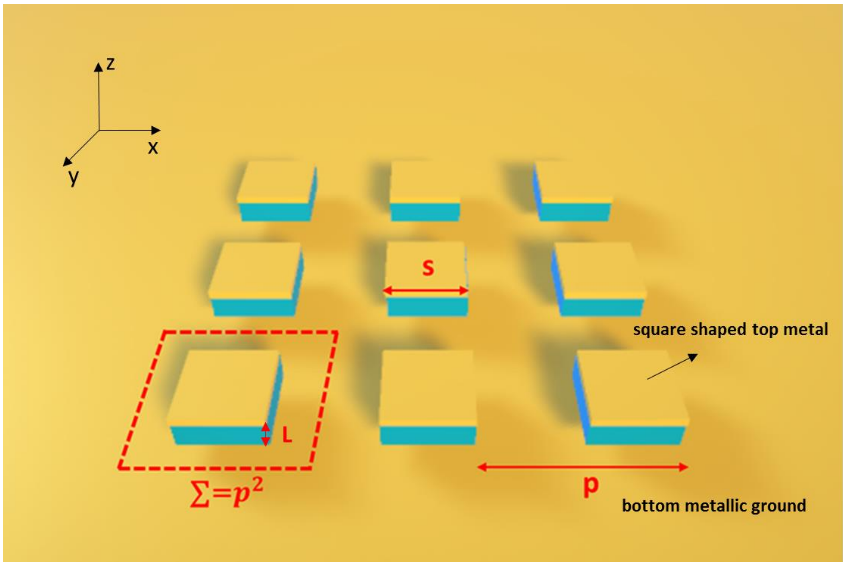

Figure. 3.13. Schematic illustration of 3x3 PAR array. The square patch lateral size is s. The array has periodicity p and Σ is the unit-cell area. L is the thickness of the semiconductor layer.

The method to analyze the electromagnetic behavior of a single PAR structure is based on two approaches: classical antenna theory using a transmission-line model [45], or a wave propagation-confinement model [27] [46]. Here we use the second approach and assume the resonator to be a square box with top and bottom walls made of perfect electric conductors (PECs) (electric field perpendicular to surface), and with the side walls made of perfect magnetic conductors (magnetic field perpendicular to surface). These approximations are equivalent to assuming that the power emitted by the PAR is negligible, which is a good approximation when $L/\lambda$ <<1. Indeed, in this case, an electromagnetic wave generated inside the semiconductor is strongly reflected at the edge of the patch (see below). We will see later how to treat the PAR in the general case. The approximation of perfect electric/magnetic walls is anyway very useful because it allows determining the electromagnetic field inside the PAR in a simple way. The vector potential $A_z$ must satisfy the homogeneous wave equation:

$$\nabla^2 A_z + k^2 A_z = 0 \quad (3.49)$$

whose solution is written in general, using the separation of variables, as

$$A_z = [A_1 \cos(k_x x) + B_1 \sin(k_x x)][A_2 \cos(k_y y) + B_2 \sin(k_y y)][A_3 \cos(k_z z) + B_3 \sin(k_z z)] \quad (3.50),$$

where $k_x$, $k_y$, $k_z$ are the wavenumbers along x, y, z directions, respectively.

The electric and magnetic fields within the cavity can be obtained from the vector potential from [45]:

$$\begin{aligned}
E_x &= -j\frac{c}{\omega n_s}\frac{\partial^2 A_z}{\partial z \partial x} \quad H_x = -\frac{1}{\mu}\frac{\partial A_z}{\partial y}, \\
E_y &= -j\frac{c}{\omega n_s}\frac{\partial^2 A_z}{\partial z \partial y} \quad H_y = \frac{1}{\mu}\frac{\partial A_z}{\partial x}, \qquad (3.51) \\
E_z &= -j\frac{c}{\omega n_s}\left(\frac{\partial^2}{\partial z^2} + k^2\right)A_z \quad H_z = 0,
\end{aligned}$$

where $n_s = \sqrt{\epsilon_s}$ is the semiconductor refractive index (for simplicity we assume a homogeneous medium of real dielectric constant). By applying the boundary conditions we obtain that [45]:

$B_1 = 0$ and $k_x = \frac{m\pi}{s}$ with m=0,1,2…..

$B_2 = 0$ and $k_y = \frac{n\pi}{s}$ with n=0,1,2…..

$B_3 = 0$ and $k_z = \frac{p\pi}{L}$ with p=0,1,2…..

Therefore the final form for the vector potential $A_z$ within the cavity is:

$$A_z = A_{mnp} \cos(k_x x) \cos\left(k_y y\right) \cos(k_z z) \quad (3.52).$$

Since the wavenumbers are subject to the constituent equation:

$$k_r^2 = k_x^2 + k_y^2 + k_z^2 = (\frac{m\pi}{s})^2 + (\frac{n\pi}{s})^2 + (\frac{p\pi}{L})^2 = \omega_r^2 \epsilon_s \quad (3.53),$$

where $\epsilon_s$ is the dielectric constant of dielectric material, the resonant frequencies of the cavity are given by:

$$(\nu_r)_{mnp} = \frac{1}{2\pi n_s} \sqrt{(\frac{m\pi}{s})^2 + (\frac{n\pi}{s})^2 + (\frac{p\pi}{L})^2} \quad (3.54).$$

From Eq. (3.51) the solution for the transverse magnetic mode (TM100) is given by $E_x = 0, E_y = 0, E_z = \cos\, \pi\frac{x}{s}$ and $H_x = 0, H_y = \sin\, \pi\frac{x}{s}, H_z = 0$ for $x, y \in (0, s)$, assuming the origin on the corner of the patch and the ground plane at z=0.

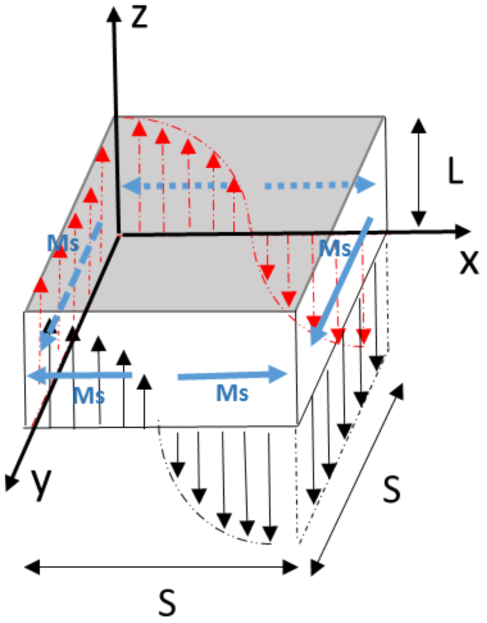

Figure. 3.14. Field configuration of the $TM_{100}$ mode for a square microstrip patch. The black and red arrows are the electric field vector (red arrows are located on the blinded side). The blue arrows are the magnetic current densities $\mathbf{M_s}$ (see Eq. (3.62)).

As pointed out above, a real PAR radiates, i.e. the reflection coefficient at the PAR edge is finite, and not infinite as we assumed to derive Eqs. (3.52)-(3.54). To properly take into account this fact one should solve Maxwell's equations numerically. Here instead, we summarize the semi-analytical approach given in Ref. [42], which only assumes top and bottom PEC walls. Following this approach, the reflection coefficient at the PAR/air boundary is given by:

$$\rho = \frac{n_s - \tilde{n}_g}{n_s + \tilde{n}_g}, \qquad \tilde{n}_g = n_g \frac{2\pi}{\varphi} \frac{1}{\int_{-\infty}^{\infty} \frac{sinc^2(t\varphi/2)}{\sqrt{1-t^2}} dt} \qquad (3.55),$$

where $\tilde{n}_g$ is the (complex) mode effective index of a metal-semiconductor-metal waveguide obtained from standard waveguide theory [47], and $\varphi = n_s L \frac{2\pi v}{c}$. A plot of the modulus and argument of $\rho$ vs cavity thickness L obtained from Eq. (3.55), and computed for the $TM_{100}$ guided mode at $\lambda$ = 100µm, is reported in Fig. 3.15 (the semiconductor is bulk GaAs). As we can see the reflectivity begins to increase dramatically as L/$\lambda$ < ~ 10%, and gets larger than 0.9 for L/$\lambda$ < ~ 1%.

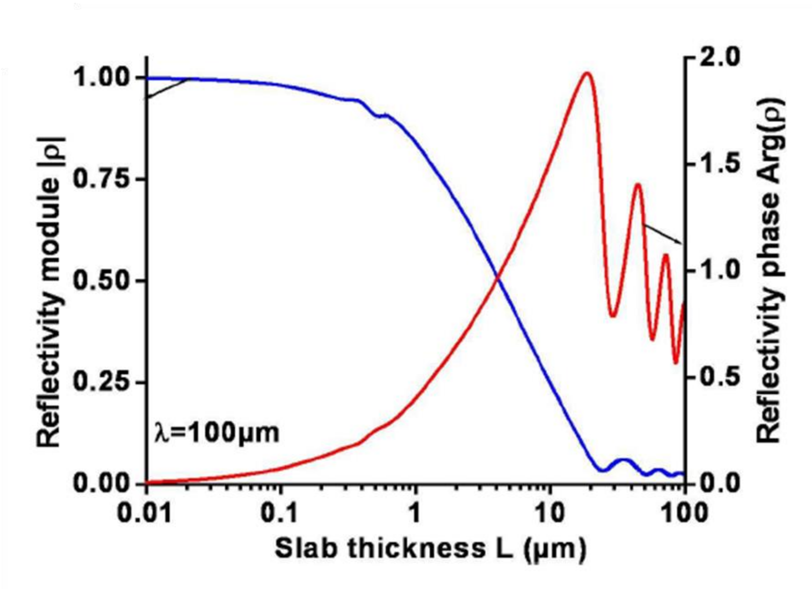

Figure. 3.15. Plot of the module and the argument of the complex reflectivity $\rho$ (Eq. (3.55)), as a function of the thickness L for a wavelength $\lambda$ = 100µm (frequency v = 3 THz), in the single-mode approximation [42].

Since the metal stripe can be considered as a short Fabry-Perot cavity of length $s$, the condition for a resonant mode is given by:

$$1-\rho^2\exp(2i\beta_x s)=0 \quad \text{(3.56)},$$

where $\beta_x = 2\pi v n_g/c$. This equation should be solved numerically to find the resonant frequencies. However, assuming that $n_g$is purealy real, i.e. neglecting losses due to absorption in the metal layers, we obtain the following simplified solution:

$$\tilde{v}_m=\frac{c}{2sn_g}\left(m-\frac{Arg(\rho)}{\pi}\right)+i\frac{c}{2sn_g}\frac{\ln|\rho|}{\pi} \quad \text{(3.57)},$$

where m is an integer. The imaginary part gives the radiation damping and can be used to extract the radiative quality factor:

$$Q_m=\frac{Re(\tilde{v}_m)}{-2Im(\tilde{v}_m)}=\frac{\pi m-Arg(\rho)}{-2\ln|\rho|} \quad \text{(3.58)}.$$

As expected the radiative quality factor increases with increasing reflectivity. The real part of Eq. (3.57) gives the resonant frequency, and can therefore be used to derive the effective index of the mode from the relation:

$$\left(\frac{2\pi}{c}\right) n_{eff} Re(\tilde{\nu}_m) 2s = m2\pi \quad (3.59),$$

which, using Eq (3.57), yields:

$$n_{eff} = \frac{n_g}{1 - \frac{Arg(\rho)}{\pi m}} \quad (3.60).$$

Considering the fundamental $TM_{100}$ mode, the resonant frequency is therefore given by:

$$(\nu_r)_{100} = \frac{c}{2sn_{eff}} \quad (3.61).$$

In Fig 3.16 we report 2D maps showing the electric/magnetic field amplitude in color scale, obtained by Finite-Difference Time-Domain (FDTD) electromagnetic (EM) simulations of a patch cavity under illumination with a plane-wave at normal incidence. The semiconductor material is GaAs and the metal layers (in orange) are PECs. We observe that the $E_z$-polarized standing wave is diffracted at the resonator's openings, i.e. the resonator behaves as a waveguide with open slots.

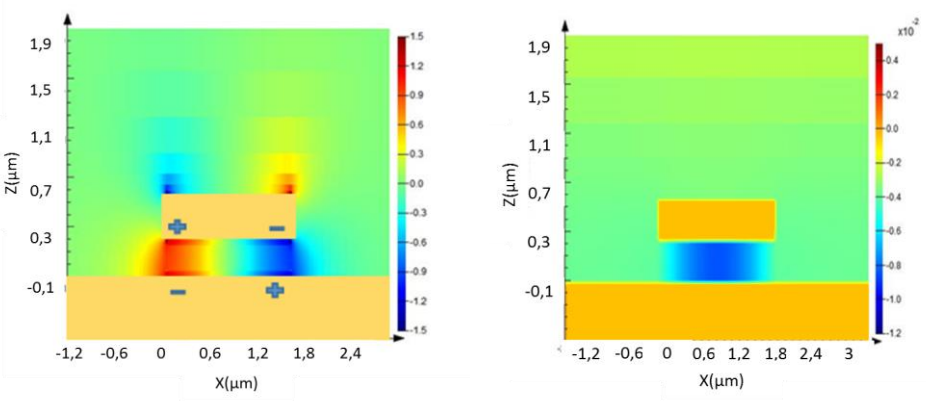

Figure. 3.16. Profile of the electric $E_z$ and magnetic $H_y$ field of $TM_{100}$ mode in a patch cavity made of GaAs sandwiched between two PECs.

Indeed, the radiation pattern of a patch antenna can be computed with good approximation considering that its four sidewalls represent four narrow apertures (slots) through which radiation takes place [45]. Assuming that the dominant mode in the cavity is the $TM_{100}$ (or $TM_{010}$), then it can be shown that among the four slots only two (the radiating slots) account for most of the radiation. These correspond to the slots parallel to the xz-plane in Fig. 3.16, where the z component of the electric field has opposite phases. Emission from the other two slots is negligible. This can be seen using the Field Equivalence Principle (Huygens' Principle). According to this principle each slot radiates the same fields as a magnetic dipole with current density $\boldsymbol{M_s}$ given by:

$$\boldsymbol{M_s} = -2\hat{n} \times \boldsymbol{E} \quad (3.62),$$

where $\boldsymbol{E}$ is the electric field on the slot. Since on the $\boldsymbol{E}$ = (0, 0, $E_z$) has the same magnitude but changes sign from one slot to the other, then the two current densities are in phase and of the same magnitude. Therefore these two radiation sources add up in the direction normal to the patch, forming a broadside pattern. Instead, on the other two slots (parallel to the xz plane), the electric field on each slot undergoes a 180deg phase, generating two current densities of opposite signs and equal magnitude, therefore the fields radiated by these two slots cancel out. The final result is illustrated in Figures 3.17 where the normalized radiation pattern in the xz plane of each radiating slot is sketched individually along with the total pattern of the two. As we can see, in the far field, at the center of the patch the E field is polarized along the x-axis. As a result, from the reciprocity principle, a PAR rotates the polarization of a plane wave at normal incidence from parallel to perpendicular to the surface.

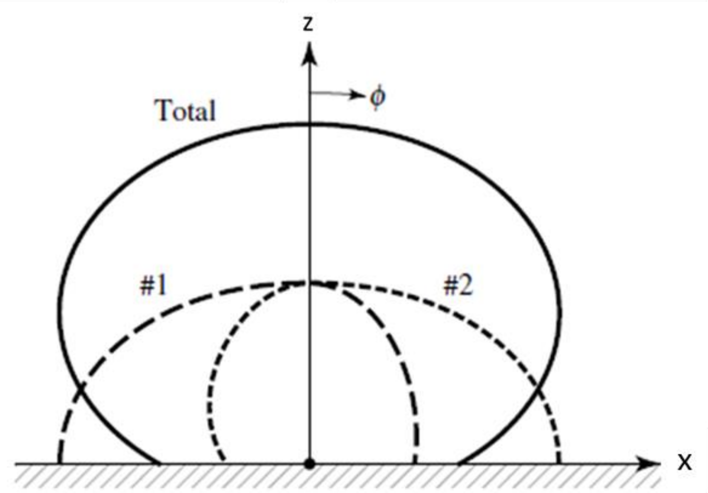

Figure. 3.17. Typical E- plane patterns of each radiating slot, and of the two added together [45].

This is clearly advantageous for a QWIP detector since: thanks to this property, light incident at normal incidence is automatically coupled to the ISB transition in a MQW (see Fig.3.7). This is clearly more convenient than facet illumination.

The reflectivity of a 2D PAR array depends on the array periodicity [48]. Considering the reflectivity spectrum $R(\lambda)$, we can define a coupling efficiency C (so called contrast) as

$$C = 1 - R_{min} \quad (3.63),$$

where $R_{min}$ is the minimum reflectivity. For a given incident photon flux $\Phi$, the fraction of the absorbed photons by a single cell of the 2D array is given by $\Phi C \Sigma$. We can then define the antenna collection area as the surface across which the incident flux is absorbed by the antenna:

$$A_{coll}(\Sigma) = C\Sigma \quad (3.64).$$

The expression of C in the case of normal incidence with x-polarized light (TM polarization) is given by [49]:

$$C = \frac{4\alpha}{(1+\alpha)^2}, \quad \alpha = \frac{A_{eff}Q_{nr}}{\Sigma Q_{rad}} \quad (3.65),$$

where $Q_{rad}$ and $Q_{nr}$ are respectively the radiative Q-factor of the resonator, and the Q-factor accounting for the cavity losses (non-radiative loss, i.e loss in the metal), and $A_{eff}$ is the effective area of an isolated patch antenna, given by $A_{eff} = \lambda^2 \frac{D_0}{4\pi}$, where $D_0$ is the antenna directivity [50]. The quantity $\alpha$ introduced in Eq. (3.65) can be seen as the ratio between the photon in-coupling rate ($1/Q_{rad}$) and the absorption rate ($1/Q_{nr}$) corrected by the geometrical ratio $A_{eff}/\Sigma$. The maximum contrast C = 1 is obtained for $\alpha = 1$, i.e. when all the incident power coupled inside the resonator array is absorbed. This is known in optics as critical coupling condition [49]. From Eq. (3.64) the antenna collection area can be written as:

$$A_{coll}(\Sigma) = C\Sigma = \frac{A_{coll}^{\infty}}{(1+\frac{A_{coll}^{\infty}}{4\Sigma})^2}, \; A_{coll}^{\infty} = 4A_{eff}\frac{Q_{nr}}{Q_{rad}} \quad (3.66),$$

where $A_{coll}^{\infty}$ is the collection area of an isolated patch antenna: $A_{coll}^{\infty} = \lim_{\Sigma\to\infty} A_{coll}(\Sigma)$. From Eq. (3.66) it appears that the collection area of a patch inside an array is always smaller than the collection area of an isolated patch. As shown in Fig. 3.18 (a) $A_{coll}$ increases with $\Sigma$, reaching asymptotically $A_{coll}^{\infty}$ for very diluted arrays. In Fig. 3.18(b) we report the corresponding contrast vs $\Sigma$, obtained from Eq. (3.65): critical coupling (C =1) is reached for $\Sigma = A_{coll}^{\infty}/4$ . In this case the collection area of a single element of the array is only ¼ of the collection area of an isolated patch. Now, using microwave antenna theory we have that for an isolated patch [49]:

$$Q_{rad} = \frac{\pi\epsilon_{GaAs}}{8n_{eff}}\frac{A_{eff}}{sL} \quad (3.67),$$

where, $\epsilon_{GaAs}$ is the GaAs bulk dielectric constant, and $n_{eff}$ is the effective index of the patch antenna fundamental mode, i.e. such that the resonant wavelength is given by: $\lambda_r$= 2s $n_{eff}$. Therefore, from Eq. (3.66) we obtain:

$$A_{coll}^{\infty} = \frac{16\cdot L}{\pi\epsilon_{GaAs}}\lambda_r Q_{nr}^{\infty} = \frac{64\cdot L\cdot n_{eff}^2}{\pi\epsilon_{GaAs}\lambda_r} Q_{nr}^{\infty} s^2 \simeq \frac{64\cdot L}{\pi\lambda_r} Q_{nr}^{\infty} s^2 \quad (3.68),$$

where $Q_{nr}^{\infty}$ is the non-radiative Q factor of an isolated patch antenna,. To derive the last term we have made the approximation $\epsilon_{GaAs} \simeq n_{eff}^2$. Since at critical coupling $A_{coll}(\Sigma) = \Sigma = A_{coll}^{\infty}/4$ , then if we want the condition $A_{coll}(\Sigma) > s^2$ to be satisfied, which corresponds to the physical requirement that the surface of a cell is larger than the physical area of a patch, then we must have that $A_{coll}^{\infty} > 4s^2$ i.e.:

$$Q_{nr}^{\infty} > \frac{\pi\lambda_r}{16L} \quad (3.69).$$

Having a collection area larger than the patch physical area is advantageous since it allows to obtain 100% photon absorption (at critical coupling) with a diluted array, which reduces the dark current compared to the case where the detector collection area is equal or smaller than its physical area.

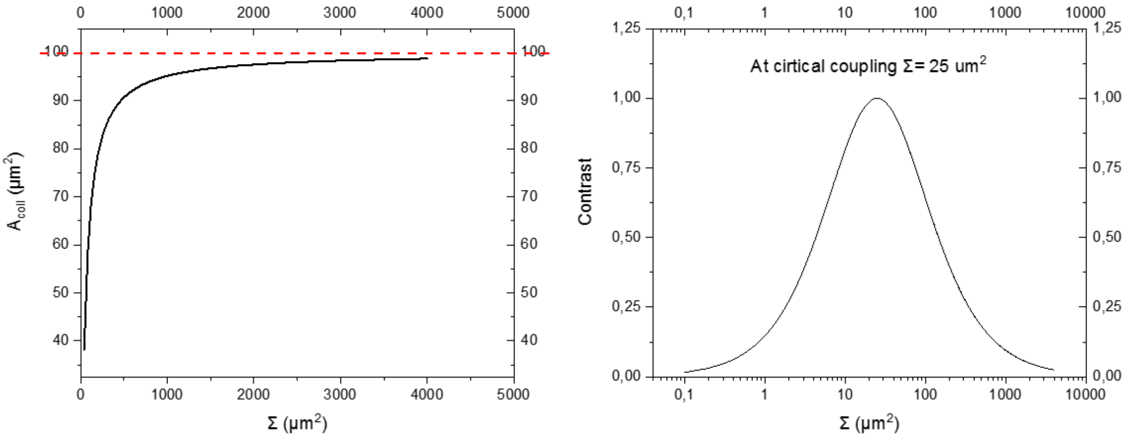

a) b)

Figure. 3.18. a) Plot of $A_{coll}(\Sigma)$ vs $\Sigma$ as derived from Eq. (3.66) setting $A_{coll}^{\infty} = 100$, which yields the collection area at critical coupling found experimentally (~25um$^2$) (Eq. 3.66). b) Corresponding plot of the contrast, C, vs $\Sigma$ (Eq. 3.65).

### 3.4.5.2 Comparison between the figures of merit of PARs and “mesa” QWIPs

*Responsivity and absorption coefficient*

In this section we will derive and compare the figures of merit for a QWIP in mesa and PAR array geometry. First of all, we assume that both detectors have the same geometrical surface and therefore the same thermally activated dark current (Eq. (3.42)). From Eq. (2.9) the photocurrent can be written as:

$$I_{ph} = \mathcal{R}\Phi_0 E_{21} A_{coll} \quad (3.70)$$

with the photon collection area $A_{coll}$, the number of photons incident per unit surface and unit time on the structure $\Phi_0$. $E_{21} = h\nu$ is the ISB transition energy. On the mesa, we have that the photon collection is identical to the physical device area ($A_{coll} = A_{det}$), and the responsivity can be written as (Eq. (2.10)):

$$\mathcal{R}_{mesa} = \eta_{mesa}^{ext} g \frac{1}{E_{21}/e}, \;\; \eta_{mesa}^{ext} = t\xi_{mesa}\eta_{mesa} \quad (3.71).$$

Here $t$ is the substrate transmission coefficient, $\xi_{mesa}$ = 0.5 is the polarization coefficient, since only one polarization couples to the ISB transition, and $\eta_{mesa}^{ext}$ is the mesa external quantum efficiency. From Eq. (3.27) applied to a single ISB transition, the mesa absorption quantum efficiency $\eta_{mesa}$ can be written as:

$$\eta_{mesa} = N_{QW}L_{QW}\frac{E_P^2}{2c\hbar}\frac{sin^2\theta}{cos\theta}\frac{\Delta E}{(E-E_{21})^2+\Delta E^2} \qquad (3.72)$$

$$\text{with } E_p^2 = (\hbar\omega_p)^2 = \hbar^2\frac{f_{12}n_d e^2}{m^*\epsilon_0 n_r L_{QW}} \qquad (3.73).$$

Here, $E_p$ and $\omega_p$ are known as the ISB plasma energy and plasma frequency [51]. θ=45° is the incidence angle, which, corresponds to a mesa coupled through a 45deg polished substrate (Fig.3.19).

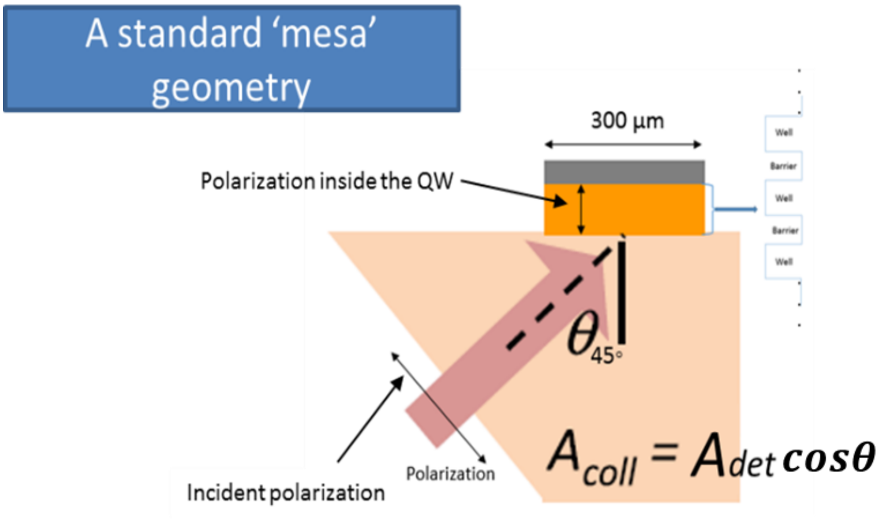

Figure. 3.19. Schematic representation of a standard mesa geometry, where the photon collection area $A_{coll}$ is identical to the physical device area $A_{det}$* $cos\theta$. The light is coupled into the semiconductor from a 45deg polished substrate facet.

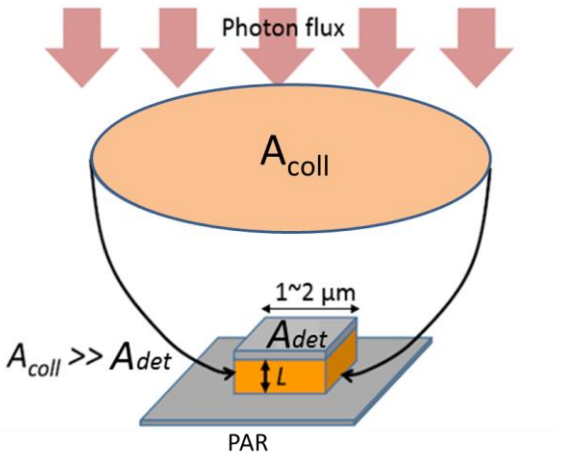

Figure. 3.20. Schematic representation of the collection area of a single PAR. In this case: Acoll >> Adet.

The responsivity of the PAR array is given by [29]:

$$\mathcal{R}_{array} = \eta_{array} g \xi_{array} \frac{1}{\frac{E_{21}}{e}} = \eta_{array}^{ext} g \frac{1}{E_{21}/e} \quad (3.74),$$

$$with\ \eta_{array} = CB_{isb}Q \quad (3.75).$$

Here $\xi_{array}$ ~0.7-0.8 is the polarization coefficient, and $\eta_{array}^{ext} = \eta_{array}\xi_{array}$ is the external quantum efficiency. The former takes into account the fact that patches into an array forming a detector pixel are connected by metallic wires in order to collect the photocurrent from all resonators, which reduces the absorption for one polarization direction (see Section 5.1). $B_{isb}$ is a dimensionless quantity, defined as $B_{isb} = \frac{1}{\omega U}\frac{dU}{dt}|_{isb}$ , where U is the total electromagnetic energy density stored in each resonator, and $\frac{dU}{dt}|_{isb}$ is the ISB absorption rate. It describes the fraction of the electromagnetic field absorbed by the quantum well transition, and averaged per cycle of oscillation. Finally, Q is the total quality factor of the patch array, which has 3 contributions:

$$\frac{1}{Q} = B_{isb} + \frac{1}{Q_{rad}} + \frac{1}{Q_{nr}} = B_{isb} + \frac{1}{Q_{cav}}, \quad Q_{cav} = 1/(\frac{1}{Q_{rad}} + \frac{1}{Q_{nr}}) \quad (3.76).$$

Here $Q_{cav}$ is the patch resonator Q_factor, excluding ISB absorption, and the term $B_{isb}$*Q = $B_{isb}/(B_{isb} + 1/Q_{cav})$ is the so called branching ratio, which corresponds to the array quantum efficiency at critical coupling (Eq. (3.75)). For $B_{isb} \gg \frac{1}{Q_{cav}}$ most of the photons are absorbed by the ISB transition, and the quantum efficiency is maximized.

Analogously to the derivation of Eq. (3.27), $B_{isb}$ is obtained by considering the general theory of electromagnetic absorption and is expressed by a Lorentzian lineshape [52]:

$$B_{isb}(E) = f_w \frac{E_P^2}{2E_{21}} \frac{\Delta E}{(E-E_{21})^2+\Delta E^2} \qquad (3.77),$$

where $f_w$ is a geometrical overlap factor, given by the ratio of the effective thickness of the quantum wells $N_{QW}L_{QW}$ ($N_{QW}$ the total number of QWs) and the width of the semiconductor layer L: $\frac{N_{QW}L_{QW}}{L}$. From Eq. (3.72) $B_{isb}$ can be written in terms of the mesa quantum efficiency:

$$B_{isb} = \eta_{mesa} \frac{cos\theta}{sin^2\theta} \frac{c\hbar}{E_{21}L} \qquad (3.78).$$

Finally, from Eq. (3.71) and Eq. (3.74), the ratio between the responsivities of the array and the mesa is given by:

$$\frac{\mathcal{R}_{array}}{\mathcal{R}_{mesa}} = \frac{\eta_{array}^{ext}}{\eta_{mesa}^{ext}} = C \frac{cos\theta}{sin^2\theta} \frac{\lambda_{21}}{2\pi L} \frac{\xi_{array}}{t\xi_{mesa}} Q \qquad (3.79).$$

We have that $\xi_{mesa} = 0.5$, and for a square patch $\xi_{array} = 0.8 \div 0.9$. For GaAs t ~ 0.7. Therefore, considering C = 1 and $\theta$ = 45deg, from Eq. (3.79) we obtain that for the condition $\frac{\mathcal{R}_{array}}{\mathcal{R}_{mesa}}>1$ to be satisfied, we must have:

$$\frac{\lambda_{21}Q}{L} \gtrsim \frac{\pi}{\sqrt{2}} \approx 2 \qquad (3.80)$$

For the PARs array of Ref. [29], we have Q ~ 3, L~ 0.4µm and $\lambda_{21}$~ 8µm, i.e. $\frac{\lambda_{21}Q}{L}$~ 60 and $\frac{\mathcal{R}_{array}}{\mathcal{R}_{mesa}}$~27.

*BLIP temperature and detectivity*

As we mentioned in Section 2.1.3, the BLIP temperature is defined as the temperature where the background photon noise equals to the dark current noise. From Eqs. (3.42), (3.70), (3.71), (3.74), (3.75), we can derive the BLIP temperature of the PAR array as a function of the BLIP temperature of the reference mesa device $T_{BLIP}^{0}$:

$$T_{BLIP} = \frac{T_{BLIP}^{0}}{1 - \frac{k_B T_{BLIP}^{0}}{E_{21}} \left\{ lnF - linK + \ln\left(\frac{T_{BLIP}^{0}}{T_{BLIP}}\right) \right\}} \quad (3.81)$$

with $F = \frac{A_{coll} \lambda_{21} Q}{V}$ and $K = \frac{2\pi cos\theta}{sin\theta^2} t$ .

Here V=A$_{\text{det}}$ x L is the volume of the single patch, and A$_{\text{det}}$ = s$^2$ is the area of single patch[48]. We note that in this last expression the detectivity is proportional to the responsivity and decreases exponentially with temperature.

From Eq. (2.17), by replacing the detector area by the collection area [48], the specific detectivity of PAR array is written as:

$$D^{*}{}_{array}(T) = \frac{\mathcal{R}_{array} \sqrt{A_{coll}}}{\sqrt{4eg(I_{ph.n} + I_{dark}(T))}} \quad (3.82),$$

where $I_{ph.n}$ is the background photon noise current. Therefore, from Eq. 3.70, we obtain that the detectivity of the PAR array at 0K is equal to:

$$D_{BL,array}^{*}(T = 0K) = \frac{\sqrt{\mathcal{R}_{array}}}{\sqrt{4eg\Phi_0 E_{12}}} \quad (3.83).$$

Instead, in detector limited regime, the $D_{BL,array}^{*}$ is given by Eq. (3.42):

$$D_{DL,array}^{*}(T > T_{BLIP}) = \frac{\mathcal{R}_{array} \sqrt{A_{coll}/A_{det}}}{\sqrt{4egJ_0 T \exp\left(-E_{act}/_{k_B T}\right))}} \quad (3.84).$$

From Eq. (2.17), we have the specific detectivity of the mesa:

$$D^{*}_{mesa} = \frac{\mathcal{R}_{mesa}\sqrt{A_{det}cos\theta}}{\sqrt{4eg(I_{ph.n}+I_{dark}(T))}} = \frac{\mathcal{R}_{mesa}\sqrt{A_{det}cos\theta}}{\sqrt{4eg(\mathcal{R}_{mesa}\Phi_0 E_{12}A_{det}cos\theta+A_{det}J_0T\exp\left({}^{-E_{act}}/_{k_BT}\right))}} \quad (3.85).$$

Here, A$_{\text{det}}$ is the surface of the mesa. Therefore, the specific mesa detectivity at 0 K (background limited regime) is given by:

$$D^{*}_{BL,mesa}(T=0K) = \frac{\mathcal{R}_{mesa}\sqrt{A_{det}cos\theta}}{\sqrt{4eg\mathcal{R}_{mesa}\Phi_0 E_{12}A_{det}cos\theta}} = \frac{\sqrt{\mathcal{R}_{mesa}}}{\sqrt{4eg\Phi_0 E_{12}}} \quad (3.86).$$

The specific detectivity of the mesa at $T > T_{BLIP}$ (detector limited regime) is given by:

$$D^{*}_{DL,mesa}(T > T_{BLIP}) = \frac{\mathcal{R}_{mesa}\sqrt{cos\theta}}{\sqrt{4egJ_0T\exp\left({}^{-E_{act}}/_{k_BT}\right))}} \quad (3.87).$$

From Eqs. (3.83) (3.86) and (3.84) (3.87), we obtain the ratio between the specific detectivities of the PAR array and the mesa at 0K:

$$\frac{D^{*}_{BL,array}(T=0K)}{D^{*}_{BL,mesa}(T=0K)} = \frac{\sqrt{\mathcal{R}_{array}}}{\sqrt{\mathcal{R}_{mesa}}} \quad (3.88),$$

and for T > T_BLIP:

$$\frac{D^{*}_{DL,array}(T>T_{BLIP})}{D^{*}_{DL,mesa}(T>T_{BLIP})} = \frac{\mathcal{R}_{array}}{\mathcal{R}_{mesa}}\sqrt{\frac{A_{coll}}{A_{det}cos\theta}} \quad (3.89).$$

By comparing Eqs (3.88) and (3.89) we note that compared to 0K, at high temperature the PARs array has a larger detectivity than the mesa if the condition $\frac{A_{coll}}{A_{det}} > 1$ is satisfied ((Eq.(3.69), i.e. $A^{\infty}_{coll} > 4s^2$). In addition, if $\frac{\sqrt{\mathcal{R}_{array}}}{\sqrt{\mathcal{R}_{mesa}}} > 1$, then the PARs array presents also a higher detectivity in the background limited regime.

D. Palaferri and co-workers have demonstrated a 8 µm QWIP based on a PAR array in 2018. The device is shown in Fig.3.22, and is based on a 7x7 array of square patches of 1.3µm side. With this device, at 300K, they obtained experimentally a 14-fold higher detectivity compared to a mesa device [29] (Fig.3.21). Theoretically, using the values of [29], one should obtain $\frac{D^*_{BL,array}(T=0K)}{D^*_{BL,mesa}(T=0K)}\sim 5$ and $\frac{D^*_{BL,array}(T>T_{BLIP})}{D^*_{BL,mesa}(T>T_{BLIP})}\sim 70$.

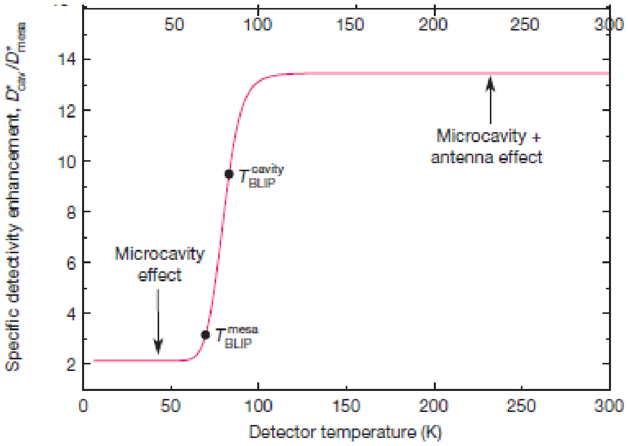

Figure. 3.21. Ratio of the specific detectivities between a PAR array with s = 1.3 µm and p = 3.3µm and the corresponding reference mesa. Dots show the corresponding $T_{BLIP}$: $T_{BLIP}$=70K mesa (mesa) and $T_{BLIP}$ =83K cavity (patch cavity arrays) [29].

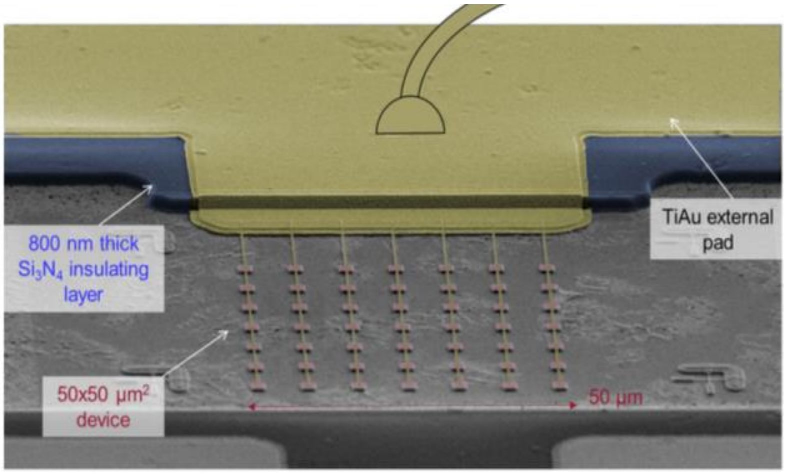

Figure. 3.22. Scanning electron microscope image of the 8um QWIP structure embedded into a 50 × 50 µm$^2$ of PARs array. The top Ti/Au contact is evaporated onto an 800-nm-thick $Si_3N_4$ insulating layer [29].

The PAR array QWIP detector of Fig. 3.22 was characterized at room temperature with a heterodyne experiment based on two QCLs. The results are reported in Fig. 3.23, showing a set of normalized beatnotes up to a maximum frequency of ~4GHz. Indeed this device was not optimized for high-speed operation, and the frequency response is limited by device parasitics as well as wire bondings (see Fig.3.22).

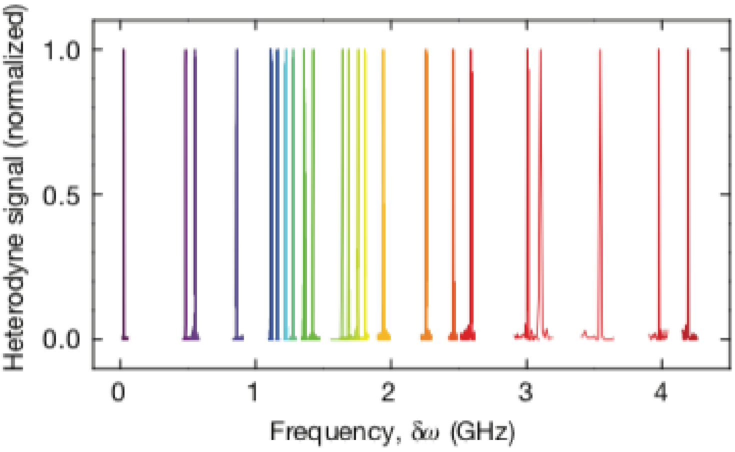

Figure. 3.23. Normalized heterodyne signal measured with the device shown in Fig.3.22 [29].

## 3.5 Ultrafast QWIPs

### 3.5.1 Response time

Thanks to their intrinsically short electron relaxation time, on the ps time scale, due to optical phonon emission, mid-infrared (MIR-3−12 μm) quantum-well infrared photodetectors (QWIP) based on III−V semiconductor materials were identified as ideal candidates for ultrahigh-speed operation at the end of the 80s. Since then, several experiments have been carried out to determine their RF bandwidth using both pulsed mid-infrared excitation or heterodyne detection [53, 54, 55, 56, 57, 58, 59].

S. Steinkogler and co-workers investigated the electron capture time in QWIPs using time-resolved photocurrent measurements in a 100 period InGaAs/GaAs-QWIP [57]. In their experiment, sub-ps infrared pulses were generated by difference frequency mixing of the signal and idler beams of an optical parametric oscillator. To maximize the RF bandwidth the sample (processed in a standard mesa geometry) was connected through a broadband bias-tee to a 45GHz microwave probe. Fig. 3.24 (a) reports the measured photocurrent response after a laser pulse excitation, at 77K and for several bias voltages. The corresponding Fourier transforms of the photocurrent transients are displayed in Fig. 3.24(b). The decay of the photocurrent associated with the captured electrons is exponential, while the decay of the photocurrent due to the arrival of optically excited electrons at the collector contact can be described linearly. Therefore, the decay of the fast photocurrent is proportional to $(1-\frac{t}{\tau_{trans}})e^{-t/\tau_c}$ for $t < \tau_{trans}$. This function was used to fit the data of Fig. 3.24, taking into account also the response of the electrical system to the sub-ps optical excitation, which, however, was not precisely known: from the 45GHz 3dB bandwidth of the probes, the nominally minimum measurable time interval was ~8.5ps. From the fitting procedure, values of $\tau_c$ increasing from 10 ps at 5kV/cm to 20 ps at 20 kV/cm were found.

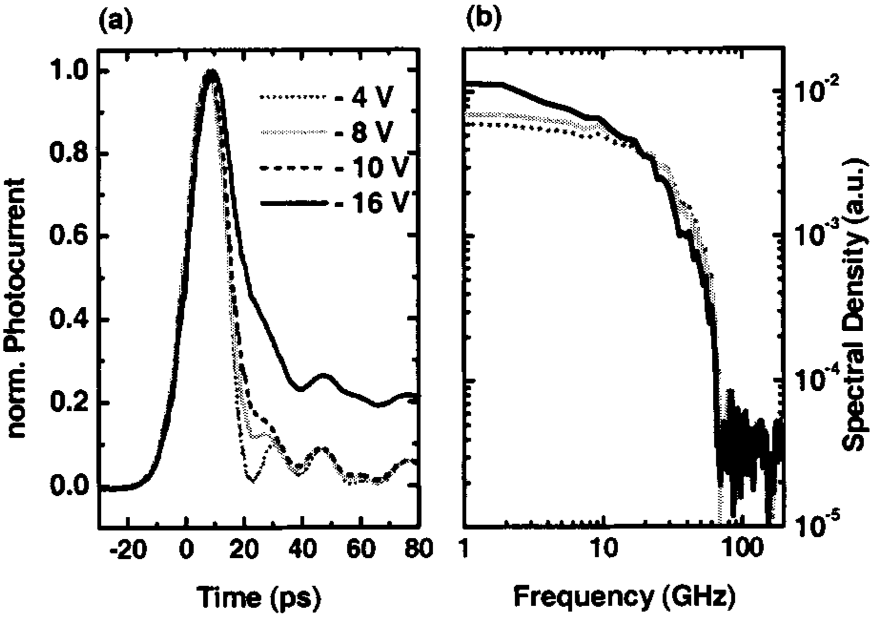

Figure. 3.24. (a) Time dependent photocurrent response after laser pulse excitation at 77 K and several bias voltages. (b) The corresponding Fourier transforms of the transients [57].

### 3.5.2 Heterodyne detection

The exploitation of QWIPs as heterodyne receivers with IF bandwidth of tens of GHz is particularly attractive for a number of applications, including free-space communications, gas sensing and spectroscopy, atmospheric and space science, and so on [60, 61, 62, 63]. Besides enabling the implementation of coherent detection schemes, another advantage brought by heterodyne detection is the possibility to operate QWIPs in the shot-noise regime, overcoming the noise contribution of the thermally activated dark current, which severely impacts the NEP of MIR QWIPs at high temperature [64].

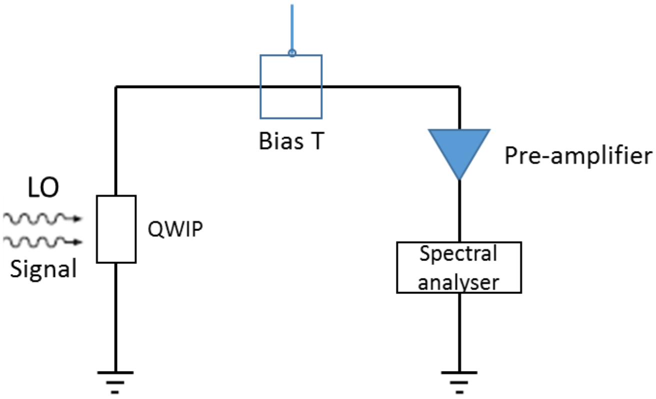

Figure. 3.25. Schematic of an experimental setup for heterodyne detection.

Heterodyne detection involves a local oscillator (LO), commonly a laser that is directly focused on the detector, and a “signal” source. The latter can be another laser emitting at a frequency slightly detuned from that of the LO, or a broadband source, such as a blackbody or, more generally, a hot body. As a result of the quadratic detection process, only the component of the generated photocurrent oscillating at the difference frequency between the two sources, and falling within the detector’s RF bandwidth can be measured. This component is generally referred to as the IF – the intermediate frequency signal. This technique can also be used to characterize the high-frequency behavior of a QWIP by beating two lasers and measuring the IF as a function of frequency [4].

The heterodyne current for signal and LO powers $P_{sig}$ and $P_{LO}$ is given by:

$$i_{het} = 2\mathcal{R}_i\sqrt{P_{LO}P_{sig}} = 2eg\eta\frac{1}{h\nu}\sqrt{P_{LO}P_{sig}} \quad (3.90).$$

For a sufficiently high LO power, the QWIP noise is dominated by the photocurrent noise (signal-limited regime). Hence, from Eqs. (3.31) and (3.40), the g-r noise current spectral density is:

$$S_i = 4egI_{LO} = 4egR_iP_{LO} = (2eg)^2P_{LO}\eta\frac{1}{h\nu} \quad (3.91),$$

yielding a noise current

$$i_{noise} = \sqrt{S_i\Delta f} = 2eg\sqrt{P_{LO}\eta\Delta f\frac{1}{h\nu}} \quad (3.92),$$

where $\Delta f$ is the measurement bandwidth. The minimum detectable signal is when $i_{noise} = i_{het}$, hence, from Eq. (3.90) and Eq. (3.92) we have that

$$\frac{P_{sig}^{min}}{\Delta f} = \frac{h\nu}{\eta} \quad (3.93),$$

and therefore the NEP is given by:

$$NEP = \frac{h\nu}{\eta}\sqrt{\Delta f} \quad (3.94).$$

From Eq.(3.94) we find that for a sufficiently high LO power such that the noise is dominated by the LO photon noise, the heterodyne NEP is proportional to the measurement bandwidth and depends only on the absorption quantum efficiency η and the photon quantum hν. It is independent of the gain g, i.e. it does not depend on temperature.

The measurement of the photo response of a fast QWIP detector is presented in Ref. [59], reporting the largest heterodyne detection bandwidths at room temperature up to date. The device investigated is a single QWIP processed in a 16µm-side square mesa, illuminated from a 45° polished substrate. The small physical surface yields a small capacitance allowing the possibility to achieve an ultra-fast frequency response. To remove the effect of parasitics, such as wire bonds, the QWIP was integrated with 50 Ω coplanar waveguide as shown in Fig. 3.26, allowing to drive the QWIP with a broadband coplanar probe. The high-frequency photocurrent response measured up to 110GHz is reported in Fig. 3.27, showing a 3dB RC cut off frequency of ~25 GHz, followed by a 20dB power loss from 35 GHz to 75 GHz.

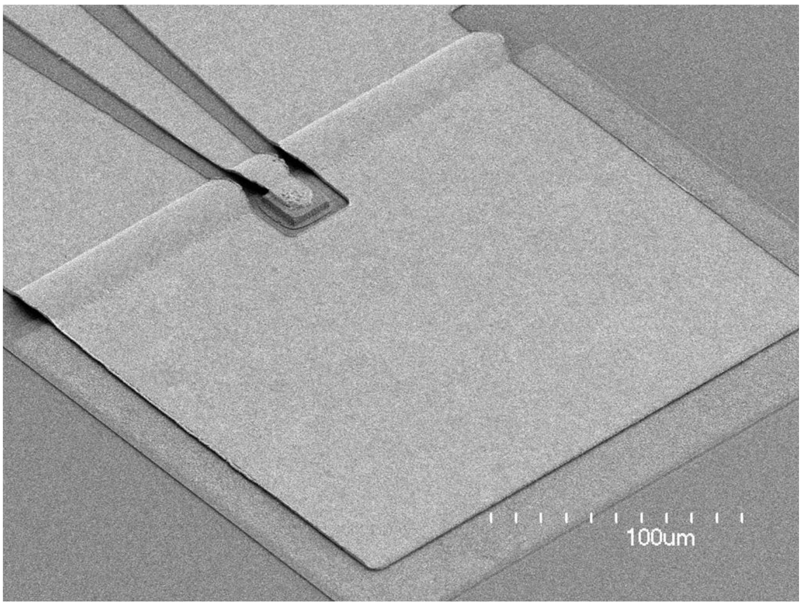

Figure. 3.26. SEM micrograph of the QWIP presented in Ref. [59].

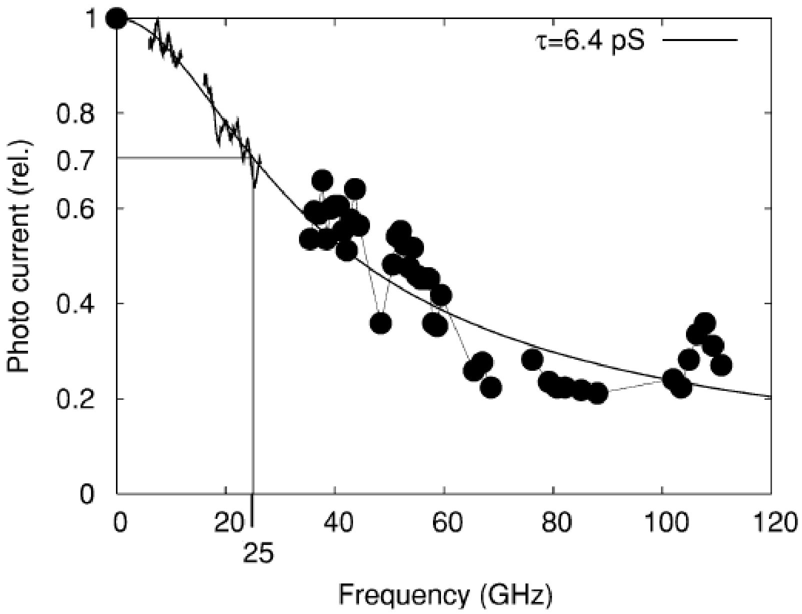

Figure. 3.27. A composite graph (jagged lines were performed by microwave rectification and solid circles are the photocurrent generated by two $CO_2$ lasers incident on the QWIP), showing the overall frequency response for the device presented in Fig. 3.26 at T = 300 K, and under an applied bias of 3.3 kV/cm [59].

### 3.5.3 QWIPs heterodyne detection in a photoconductor: an electrical circuit model

In the following we will present an equivalent circuit model, based on Ref. [65], that can be used to study a photocoductor subject to the illumination of two coherent sources. This model will be applied in Chapter 5 to the QWIP detectors demonstrated in this Thesis.

In an optical heterodyne experiment as described in this work, a *dc* biased photoconductor is illuminated by two laser beams, with $P_1$ and $P_2$ the powers incident on the detector area, and $\omega_b$ their difference frequency. The incident optical power on the photoconductor can be expressed as:

$$\begin{aligned} P(t) &= P_1 + P_2 + 2\sqrt{P_1 P_2}\sin(\omega_b t + \theta) \\ &= (P_1 + P_2)\left[1 + \tfrac{2\sqrt{P_1 P_2}}{P_1 + P_2}\sin(\omega_b t + \theta)\right] \\ &= P_{\text{tot}}[1 + \mathrm{m} \times \sin(\omega_b t + \theta)] \qquad (3.95), \end{aligned}$$

where we have omitted the term oscillating at the sum frequency, and $\mathrm{m}$ is the modulation index. Hence we can re-write the incident light flux impinging on the semiconductor as:

$$\xi_0 = \xi_{\text{tot}}[1 + \mathrm{m}\sin(\omega_b t + \theta)] \qquad (3.96)$$

with $\xi_{\mathrm{tot}} = \frac{P_{\mathrm{tot}}}{lwh\nu}$ (see Fig.2.1).

The resulting carrier concentration produced by this illumination must be of the form:

$$n(z,t) = n_0 + n_1 \sin(\omega_b t + \varphi) \quad (3.97).$$

The carriers continuity equation can be obtained from Eq. (2.3), considering a non-negligible dark carrier concentration $n_d$. Neglecting the diffusion and drift components of the current we have:

$$\frac{dn(z,t)}{dt} = -\frac{n(z,t)-n_d}{\tau} + g \quad (3.98),$$

where $\tau$ is the carrier life time, and the generation rate *g* is obtained from Eq.(2.2) and Eq. (3.96):

$$g = \alpha(1-R)\xi_0 e^{-\alpha z} = \alpha(1-R)\xi_{tot} e^{-\alpha z}[1 + m\sin(\omega_b t + \theta)] \quad (3.99).$$

From Eqs. (3.97)-(3.99) we can then derive $n_0$ and $n_1$ as m [65],:

$$n_0 = \frac{\tau\eta\xi_{tot}}{d} + n_d \quad (3.100)$$

$$n_1 = \frac{m\tau\eta\xi_{tot}}{d[1+(\omega_b\tau)^2]^{1/2}} \quad (3.101),$$

where $\eta = \alpha d(1-R)$ is the quantum efficiency (for simplicity, we have assumed that the thickness, $d$, of the photoconductor is such that d << 1/ $\alpha$ ). By assuming that the photoconductor exhibits a linear I-V characteristic it can be modelled by a  conductance due to the photo-generated carriers is given by:

$$G_{\mathrm{n}} = \frac{I}{V} = \frac{w}{lV}\mu_n qV \int_0^d n(z,t)dx = \frac{w}{l}\mu_n q n(t) d \quad (3.102),$$

where *w x l* is the illuminated area, and d is the thickness of semiconductor (see Fig.2.1). Consequently, from Eqs. (3.97), (3.100), (3.101) and (3.102) the conductance is given by:

$$G(t) = G_0 + G_1 \sin(\omega_b t + \varphi) \quad (3.103).$$

where $G_0$ and $G_1$ are respectively a *dc* and a dynamic conductance term, expressed as :

$$G_0 = q\mu_n \frac{dw}{l} n_0 = \frac{\mu_n}{l^2}[\tau \mathrm{J} + \mathrm{q}l dwn_d] = G_{ph} + G_d \quad (3.104),$$

$$G_1 = \frac{m}{\sqrt{1+(\omega_b \tau)^2}} G_{ph} \quad (3.105)$$

with

$$G_d = \frac{\mu}{l^2} qWldn_d \quad (3.106),$$

and $G_{ph} = \frac{I_{ph}}{V_{dc}} = \frac{\mu_n}{l^2}\tau \mathrm{J}$ (3.107)

( $\mathrm{J} = \eta \xi_{tot} lwq$ is the total number of photons absorbed per unit time). In Eq. (3.106) and (3.107), the term $G_d$ (1/*R*$_d$) is the dark conductance, while $G_{ph}$ (1/*R*$_{ph}$) is the internal photo conductance given by the ratio between the *dc* (i.e. average) conduction photocurrent, $I_{ph}$, generated by the two laser sources, and the *dc* bias voltage, $V_{dc}$ , applied to the photoconductor. In the expression of $G_1$ the denominator reflects the frequency roll-off of the intrinsic recombination or transport mechanism.

An accurate model of the QWIP should include the detector electrical capacitance, $C_{QWIP}$, in parallel with $G(t)$. In this model we also add a series contact resistance $R_s$ in parallel with a capacitance $C_s$. This will be useful in Section 5 to take into account the fact the contacts are not ohmic, but rather of Schottky type.

The resulting electrical circuit model is shown in Fig. 3.28. This circuit also includes the inductor and capacitor ($L_{bias-T}$, $C_{bias-T}$) of the bias-T used to bias the QWIP (see fig. 3.25), allowing the decoupling between *dc* and *ac* currents. Finally, $Z_L$ is the load impedance seen by the QWIP. Voltages and currents in the circuit are time periodic (period *T*=2π/$\omega_b$) and can be expressed in a Fourier series. By neglecting high orders harmonics [65], the voltage across the photoconductor takes the simple form:

$$V(t) = V_{dc} + V_{ac} \cos(\omega_b t + \varphi) \quad (3.108);$$

The current is given by:

$$I(t) = I_{dc} + I_{ac}\cos\left(\omega_b t + \delta\right) \quad (3.109).$$

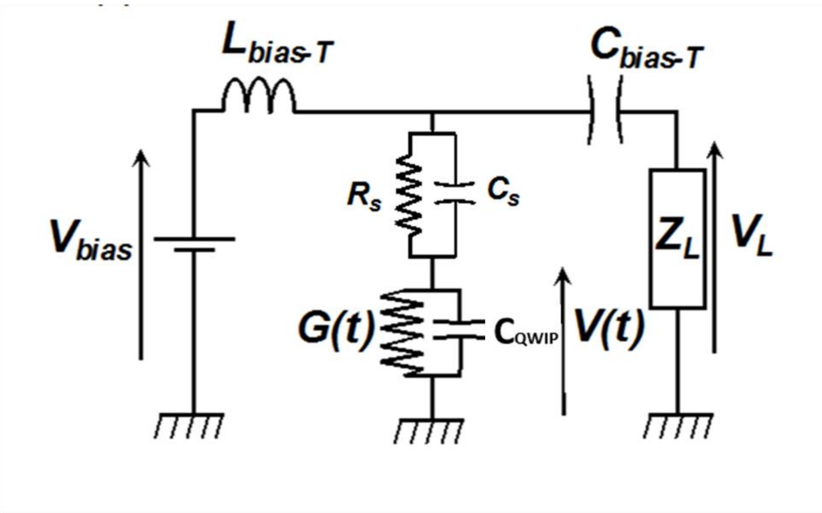

Figure. 3.28. Electrical circuit model of the heterodyne mixing experiment.

The quantities $V_{dc}$, $V_{ac}$, $I_{dc}$, $I_{ac}$, $\varphi$, $\delta$ can be derived from the circuit of Fig. 3.28 by applying Kirchhoff's laws at $\omega = 0$ and $\omega = \omega_b$ (i.e. exploiting the decoupling between *dc* and *ac* currents thanks to the bias-T inductance and capacitance) and by using the constitutive relation:

$$I(t) = G(t)V(t) \quad (3.110),$$

From the equations above, an *ac* small-signal circuit ($\omega = \omega_b$) and a *dc* circuit ($\omega = 0$) can be derived, as shown in Fig. 3.29 (a), (b) [65].

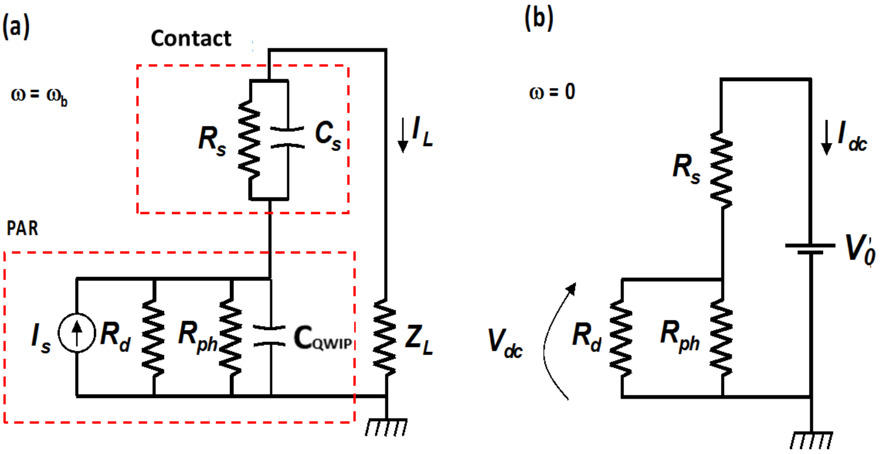

Figure. 3.29. (a) Equivalent small-signal *ac* circuit (ω = ω$_b$). (b) Equivalent *dc* circuit (ω = 0).

In the *dc* circuit the QWIP is modeled by its *dc* photo resistance under illumination,

$$R_0 = \frac{R_d R_{ph}}{R_d + R_{ph}} \quad (3.111),$$

where $R_d$ is the QWIP dark resistance.

In the *ac* circuit (Fig. 3. 29(a)) the QWIP is modeled by an equivalent *ac* current source, $I_s$, with its internal impedance $R_0$ in parallel with the intrinsic capacitance of the QWIP $C_{QWIP}$. The current source can be computed as [65]:

$$I_s = V_{dc} \times G_1 = \frac{m}{\sqrt{1+(\omega_b \tau)^2}} V_{dc} \times \frac{1}{R_{ph}} \quad (3.112),$$

where $I_s$ is in general a phasor (from now on we assume that all currents and voltages are represented by phasors). The *dc* equivalent circuit (Fig. 3.29(b)), can be used to derive $V_{dc}$:

$$V_{dc} = \frac{V_0}{R_0 + R_s} R_0 = I_{dc} R_0 \quad (3.113).$$

From Eqs. (3.111), (3.112) and (3.113) we obtain:

$$I_s = \frac{m}{\sqrt{1+(\omega_b \tau)^2}} I_{dc} \frac{R_0}{R_{ph}} = \frac{m}{\sqrt{1+(\omega_b \tau)^2}} I_{dc} \frac{R_d - R_0}{R_d} \quad (3.114),$$

where $I_{dc}$ is the *dc* current under illumination that can be measured experimentally. It is also useful to express the current source $I_s$ as a function of the *dc* photocurrent of the QWIP, which is obtained by subtracting the dark current from $I_{dc}$. From the *dc* equivalent circuit of Fig. 3. 29(b) the photocurrent is given by:

$$I_{ph} = I_{dc} - I_{dark} = V_0 \left[ \frac{1}{R_0 + R_s} - \frac{1}{R_d + R_s} \right] = I_{dc} \frac{R_d - R_0}{R_d + R_s} \quad (3.115).$$

From this last Equation we find that, as expected, the presence of a contact resistance is detrimental because it reduces the photocurrent for a given applied bias.
By comparing Eq.(3.114) and (3.115) we finally obtain:

$$I_s = \frac{m}{\sqrt{1+(\omega_b \tau)^2}} I_{ph} \frac{R_d + R_s}{R_d} \quad (3.116).$$

From Eq. (3.115) we find that the *dc* photocurrent is equal to the *measured* dc current only if $R_0$ and $R_S$ are negligible compared to $R_d$. As we shall see in Chapter 5, this is often the case at low temperature and for a sufficiently high optical power, but certainly not at 300K. In this case the correction factor $(R_d + R_s)/R_d$ cannot be neglected.

At sufficiently high frequencies $R_S$ is shorted by $C_S$ $(f_b \geq (2\pi R_s C_s)^{-1})$, thus eliminating the power loss in the contact resistance. In this case, from the small-signal circuit model, we have that:

$$I_L = I_s \frac{1}{1+R_L/R_0+i\omega_b R_L C_{QWIP}} \quad (3.117),$$

where $R_L$ is the real part of the impedance load. The dissipated power in the load, $P_L$ , can then be expressed as:

$$P_L = \frac{1}{2} R_L |I_L|^2 = \frac{1}{2} m^2 I_{ph}^2 \frac{(R_d+R_s)^2}{R_d^2} \frac{R_L}{[(1+\frac{R_L}{R_0})^2+(\omega_b R_L C_{QWIP})^2](1+\omega_b^2 \tau^2)} \quad (3.118).$$

If the load is a pure conductance, for $R_s = 0$ and $R_0 \gg R_L$, we obtain the simple case for $P_L$ as:

$$P_L = \frac{1}{2} m^2 I_{ph}^2 \frac{R_L}{[1+(\omega_b C_{QWIP} R_L)^2](1+\omega_b^2 \tau^2)} \quad (3.119).$$

We note that here, the intrinsic time will be either the capture time (photoelectron lifetime) or the transit time, whichever is smaller [4]. For a large number of QWs, the total transit time is normally longer than the capture time, therefore the response time is limited by the carrier lifetime (~ps). For a QWIP with a small number of QWs, photo excited carriers will be swept out before capture, leading to a transit time limited situation (~ps). In either case QWIPs are intrinsically very high-speed devices usually limited in response speed by their parasitic RC-constant or by the external circuitry. As we discussed in Section 3.5.2, an ultra-fast QWIP has been demonstrated up to 110 GHz [58] [59], which integrates a QWIP mesa with co-planar waveguide, yielding the broadest experimental RF bandwidth reported for a QWIP detector before this work (see Section 3.5.2).

# Bibliography

[1] W. P. Mccray, *“MBE deserves a place in the history books”,* Nat. Nanotechnol. vol. 2, no. 5, 2007, pp. 259-261.

[2] H. Manasevit, *“Single Crystal Gallium Arsenide on Insulating Substrates”,* Appl. Phys. Lett, vol. 12, no. 4, 1968, pp. 156-159.

[3] Z. I. Alferov, *“The double heterostructure: Concepts and its applications in physics, electronics and technology”,* 2000, pp. 500-513.

[4] H. Liu and H. Schneider, *"Quantum well infrared photodetectors",* Springer, 2007.

[5] C. Hasnain, B. Levine, D. Sivco and A. Cho, "Mid-infrared detectors in the 3–5 µm band using bound to continuum state absorption in InGaAs/InAlAs multiquantum well structures," *Appl. Phys. Lett,* vol. 56, pp. 770-772, 1990.

[6] A. Haddadi, X. Suo, S. Adhikary, P. Dianat, R. Chevallier, A. Hoang and M. Razeghi, "High-performance short-wavelength infrared photodetectors based on type-II InAs/InAs1-xSbx/AlAs1−xSbx superlattices," *Appl. Phys. Lett,* vol. 107, 2015.

[7] P. Christol and J. Rodriguez, "Progress on type-II InAs/GaSb superlattice (T2SL) infrared photodetector : from MWIR to VLWIR spectral domains," *Proc. SPIE,* vol. 10563, 2014.

[8] B. Xing, H. Liu, P. H. Wilson, M. Buchanan, Z. R. Wasilewski and J. G. Simmons, "Noise and photoconductive gain in AlGaAs/GaAs quantum well intersubband infrared photodetectors," *Journal of Applied Physics,* 1994.

[9] E. Rosencher and B. Vinter, *"Optoelectronics",* Cambridge University Press, 2002.

[10] B. F. Levine, K. K. Choi, C. G. Bethea, J. Walker and R. J. Malik, *“New 10 micron infrared detector using intersubband absorption in resonant tunneling {GaAlAs} superlattices",* Appl. Phys. Lett. vol. 50, no. 16, 1987, p. 1092–1094.

[11] A. Rogalski, *Infrared detectors: status and trends,* Warsaw, Institute of Applied Physics, Military University of Technology: Progress in Quantum Electronics, 2003, p. 59–210.

[12] S. D. Gunapala and et al, "Quantum well infrared photodetector technology and applications," *IEEE,* vol. 20, no. 06, 2014.

[13] H. Schneider, "High-resolution QWIP FPAs for the 8 - 12 µm and 3 - 5 µm regimes," *SPIE 4820, Infrared Technol. Appl. XXVIII,* pp. 297-305, January 2003.

[14] S. D. Gunapla, S. V. Bandara, A. Singh and J. K. Liu, "640 x 480 long-wavelength two-color GaAs/AlGaAs quantum well infrared photodetectors(QWIP) focal plane array camera," *IEEE Trans. Electron. Devices,* pp. 963-971, 2000.

[15] S. D. Gunapla, S. V. Bandara, A. Singh and J. K. Liu, "Recent developments and applications of quantum well infrared photodetector focal plane array," *Physica E, 7,* pp. 108-111, 2000.

[16] S. D. Gunapla, S. V. Bandara, J. K. Liu and S. B. Rafol, "Large format, broadband and multi-color GaAs/AlGaAs quantumwell infrared photodetector focal plane arrays," *Proc. SPIE,* pp. 30-39, 2001.

[17] S. B. Rafol, S. D. Gunapla, S. V. Bandara and J. K. Liu, "Charaterization of QWIP (10-16um) broadband FPA," *Proc. SPIE,* pp. 273-281, 2003.

[18] JPL-NASA, "When Not Seeing Is Believing," 2002. [Online]. Available: www.jpl.nasa.gov.

[19] Sofradir, "QWIP: a highly stable technology", [Online]. Available: www.sofradir.com/technology/qwip/.

[20] AIM-INFRAROT-MODULE-GmbH, " Modules," [Online]. Available: www.aim-ir.com.

[21] IR-NOVA, "IR Detectors for advanced imaging applications," [Online]. Available: www.ir-nova.se/.

[22] S. Gunapala, S. Bandara, J. Liu, C. Hill and S. Rafol, "1024 x 1024 pixel mid-wavelength and long-wavelength infrared qwip focal plane arrays for imaging applications," *Semiconductor Science and Technology,* vol. 20, p. 473, 2005.

[23] K. K. Choi and et al, "Small pitch resonator-QWIP detectors and arrays," *Infrared Physics & Technology,* vol. 94, pp. 118-125, 2018.

[24] H. Luo, H. Liu, C. Song and Z. Wasilewski, "Background-limited terahertz quantum-well photodetector," *Applied Physics Letters,* 2005.

[25] W. Beck and M. Mirotznik, "Microtrip antenna coupling for quantum well infrared photodetectors," *Infrared physics and Technology,* vol. 42, pp. 189-198, 2001.

[26] L. Perchec and et al, *Applied Physics Letters,* vol. 94, 2009.

[27] Y. Todorov and et al, "Optical properties of metal-dielectric-metal microcavities in the THz frequency range," *OPTICS EXPRESS,* vol. 18, no. 13, 2010.

[28] N. Chen and et al, "Antenna-coupled microcavities for enhanced infrared photo-detection," *Applied Physics Letters,* vol. 104, 2014.

[29] D. Palaferri et al, "Room-temperature nine-µm-wavelength photodetectors and GHz-frequency heterodyne receivers," *Nature,* 2018.

[30] M. Helm, " Semiconductors and Semimetals: Chapter1 - The basic physics of intersubband transitions", *Elsevier*, vol. 62, Academic Press Inc, 1999, pp. 1-99.

[31] G. Bastard, Wave Mechanics Applied in Semiconductor Heterostructures, 1988.

[32] H. Liu, "Dependence of absorption spectrum and responsivity on the upper state position in quantum well intersubband photodetectors," *Journal of applicated physics,* pp. 3062-3067, 1993.

[33] M. Kane, S. Millidge, M. Emeny, D. Lee, D. Guy and C. Whitehouse, Intersubband Transitions in Quantum Wells, B. V. B. L. E. Rosencher, Ed., New York, 1992, pp. 31-42.

[34] B. Xing, H. Liu, P. Wilson, M. Buchanan, Z. Wasilewski and J. Simmons, *Appl. Phys,* vol. 76, no. 1889, 1994.

[35] B. Xing, "Noise and photoconductive gain in AlGaAs/GaAs quantum well intersubband infrared photodetectors," *JOURNAL OF APPLIED PHYSICS,* vol. 76, no. 1889, 1994.

[36] Y. Yang, H. C. Liu, W. Z. Shen, N. Li, W. Lu, Z. R. Wasilewski and M. Buchanan, "Optimal Doping Density for Quantum-Well Infrared Photodetector Performance," *IEEE JOURNAL OF QUANTUM ELECTRONICS,* vol. 45, no. 6, 2009.

[37] L. Novotny and N. V. Hulst, "Antennas for light," *Nature photonics,* vol. 5, no. 2, pp. 83-99, 2011.

[38] J. A. Schuller, E. S. Barnard, W. Cai, Y. . C. Jun, J. White and M. Brongersma, "Plasmonics for extreme light concentration and manipulation," *Nature materials,* vol. 9, no. 3, p. 193–204, 2010.

[39] E. N. Grossman, . J. E. Sauvageau and D. G. McDonal, "Lithographic spiral antennas at short wavelengths," *Appl. Phys. Lett.,* vol. 59, no. 3225, 1991.

[40] N. Chong and H. Ahmed, "Antenna-coupled polycrystalline silicon air- bridge thermal detector for mid-infrared radiation," *Appl. Phys. Lett,* vol. 71, no. 1607, 1997.

[41] F. J. González, B. Ilic, . J. Alda and G. D. Borema, "Antenna-Coupled Infrared Detectors for Imaging Applications," *IEEE J. Sel. Top. Qauntum,* vol. 11, no. 117, 2005.

[42] Y. Todorov, L. Tosetto, J. Teissier, A. M. Andrews, P. Klang, R. Colombelli, I. Sagnes, G. Strasser and S. C, "Optical properties of metal-dielectric-metal microcavities in the THz frequency range," *OPTICS EXPRESS,* vol. 18, no. 13, pp. 13886-13970, 2010.

[43] C. . F. Palma, Y. Todorov, A. Vasan and C. Sirtori, "Strong near field enhancement in THz nano-antenna arrays," *Scientific reports,* vol. 3, p. 1361, 2013.

[44] B. Lee, I.-M. Lee, S. Kim, D.-H. Oh and L. Hesselink, "Review on subwavelength confinement of light with plasmonics," *Journal of Modern Optics,* vol. 57, no. 16, p. 1479–1497, 2010.

[45] C. A. Balanis, Antenna theory analysis and design, 2005.

[46] M. Duperron, "Conception et caractérisation de nanoantennes plasmoniques pour la photodétection infrarouge refroidie," 2013.

[47] R . E. Collin, "Field Theory of Guided Waves", New York: Wiley IEEE Press , 1990.

[48] D. Palaferri, Y. Todorov, A. Mottaghizadeh, G. Frucci, G. Biasiol and C. Sirtori, "Ultra-subwavelength resonators for high temperature high performance quantum detectors," *New J. Phys,* 2016.

[49] C. Feuillet-Palma, Y. Todorov, . A. Vasanelli and C. Sirtori, *Sci. Rep,* vol. 3, no. 1361, 2013.

[50] J. S. Orfanidis, Electromagnetic Waves and Antennas, Piscataway: NJ: Rutgers University, http://www.ece.rutgers.edu/,orfanidi/ewa/, last access: 02/10/2013.

[51] T. Ando, . A. Fowler and F. Stern, "Electronic properties of two-dimensional systems," *Rev. Mod. Phys,* vol. 54, no. 432, 1982.

[52] J. D. Jackson and R. F. Fox, "Classical electrodynamics," *American Journal of Physics,* vol. 67, no. 9, pp. 841-842, 1999.

[53] C. G. Bethea, F. Levine, . G. Hasnain, J. Walker and R. J. Malik, "High-speed measurement of the response time of a GaAs/AlxGa1-xAs multiquantum-well long-wavelength infrared detector," *J. Appl. Phys,* vol. 66, no. 963, 1989.

[54] H. C. Liu, J. Li, E. R. Brown, . K. A. McIntosh and M. J. Manfra, "Quantum Well Intersubband Heterodyne Infrared Detection Up to 82 GHz," *Appl. Phys. Lett,* vol. 67, no. 1594, 1995.

[55] S. Ehret, H. Schneider, J. Fleissner and P. Koi, "Ultrafast intersubband photocurrent response in quantum-well infrared photodetectors," *Appl. Phys. Lett,* vol. 71, no. 5, pp. 641-643, 1997.

[56] S. Steinkogler, H. Schneider, . R. Rehm, M. Walther, P. Koidl, P. Grant, R. Dudek and H. Liu, "Time-resolved electron transport studies on InGaAs/GaAs-QWIPs," *Infr. Phys. Technol,* vol. 44, no. 355, 2003.

[57] S. Steinkogler, H. Schneider, M. Walther and P. Koidl, "Determination of the electron capture time in quantum-well infrared photodetectors using time-resolved photocurrent measurement," *Appl. Phys. Lett.,* vol. 82, no. 3925, 2003.

[58] P. Grant, R. Dudek, M. Buchanan, L. Wolfson and H. C. Liu, "An ultra fast quantum well infrared photodetector," *Infrared Physics & Technology,* pp. 144-152, 2005.

[59] P. D. Grant, R. Dudek, M. Buchanan and H. C. Liu, "Room-temperature heterodyne detection up to 110GHz with a quantum well infrared photodetector," *IEEE Photon. Technol. Lett,* vol. 18, no. 2218, 2006.

[60] X. Pang, O. Ozolins, R. Schatz, J. Storck and A. Udal, "Gigabit free-space multi-level signal transmission with a mid-infrared quantum cascade laser operating at," *Opt. Let,* vol. 42, no. 3646, 2017.

[61] J. J. Liu, B. L. Stann, K. K. Klett, P. S. Cho and P. M. Pellegrino, "Mid and Long-Wave Infrared Free-Space Optical Communication," *Proc. SPIE,* vol. 11133, 2020.

[62] N. A. Macleod, F. Molero and D. Weidmann, "Broadband standoff detection of large molecules by mid-infrared active coherent laser spectrometry," *Opt. Expr.,* vol. 23, no. 912, 2015.

[63] D. Weidmann, W. J. Reburn and K. M. Smith, "Ground-based prototype quantum cascade laser heterodyne radiometer for atmospheric studies," *Rev. Sci. Instr. Expr.,* vol. 78, no. 073017, 2007.

[64] E. R. Brown, K. A. McIntosh, K. B. Nichols, F. W. Smith and M. J. Manfra, CO2-Laser Heterodyne Detection with GaAs/AlGaAs MQW Structures, in Quantum Well Intersubband Transition Physics and Devices, Springer, 1994.

[65] P. D. Coleman, R. C. Eden and . J. N. Weaver, "Mixing and Detection of Coherent Light," *IEEE Trans. Electron Devices,* vol. 11, no. 488, 1964.

[66] Vyacheslav, B. Podobedov, George and P. Eppeldauer, "Calibration of spectral responsivity of IR detectors in the range from 0.6 µm to 24 µm," *Proc. SPIE 9819, Infrared Technology and Applications XLII,* May 2016.

[67] M. Planck, *"Ueber das Gesetz der Energieverteilung im Normalspectrum",* Annalen der Physik, 1900, p. 553–563.

[68] R. D. Hudson, *Infared System Engineering,* J. W. a. Sons, Ed., New Yok, 1963.

# 4. Ultrafast QWIPs based on patch antennas: design and fabrication

## 4.1 Introduction

This Chapter is dedicated to the description of the design and fabrication of the PAR-array QWIP structures developed in this Thesis, with the objective of demonstrating at the same time a high responsivity and high-speed operation, with a 3dB bandwidth beyond 150GHz.

For this Thesis, we designed two QWIP structures, targeting a peak detection wavelength close to 10µm. The reason is that the 9-12µm spectral range corresponds to a high transmission atmospheric window (see Fig.1.3), hence ultrafast QWIPs in this spectral range are potentially useful for free-space communications. Moreover, two DFB QCLs operating at ~10µm were already at our disposal in the Laboratory, allowing the characterization of the QWIPs frequency response by heterodyne mixing (see Section 5.2).

## 4.2 Design and simulation

### 4.2.1 Active region design

The active regions of the detectors realized in this thesis are based on $Al_{0.2}Ga_{0.8}As/GaAs$ heterostructures. The wells widths are chosen to obtain a transition energy of ~120meV. Structure labelled “QWIP-1” relies on 6.5nm GaAs quantum wells (QWs), separated by 40nm barriers, giving rise to a bound-to-bound transition. In structure “QWIP-2” the QW is instead 6.0nm thick, therefore the upper state is closer to the top of the barrier, giving rise to a bound-to-continuum transition. The corresponding band diagrams under different electric fields F are shown in Fig.4.1. At F = 20 kV/cm we find a transition energy of $E_{21}$ = 115meV for QWIP-1. For QWIP-2 the transition is blue shift by ~6meV ($E_{21}$ = 121meV).

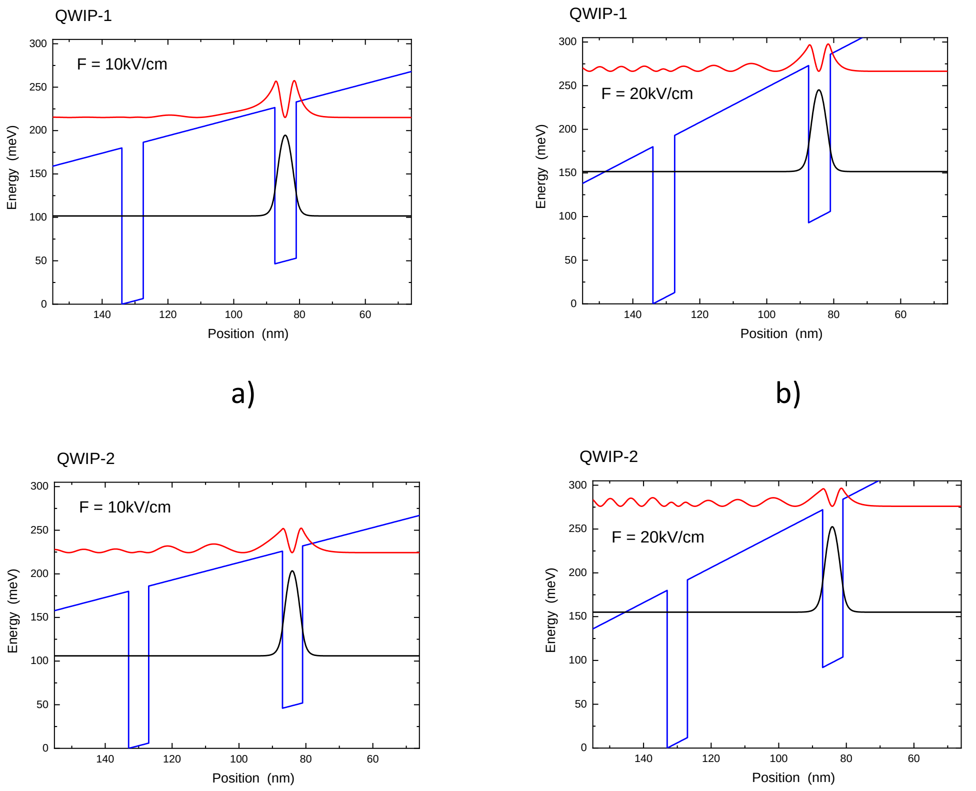

a)

b)

c)

d)

Figure. 4.1. Band diagrams of QWIP-1 at (a) F = 10 kV/cm and (b) F = 20 kV/cm respectively. Band diagrams of QWIP-2 at (c) F = 10 kV/cm and (d) F = 20 kV/cm respectively.

Determining the optimum number of QWs, i.e. ultimately the optimum thickness of the structure is a complex task that goes outside the scope of this Thesis. As a rule of thumb, one should aim at reducing as much as possible the total thickness of the PAR array, L, without overly increasing radiation absorption in the contact and metal layers. Indeed, a thin structure is less demanding in terms of growth, and also minimizes the carrier's transit time. From Ref. [1] a number of QWs in the range 5-10 leads to a non-radiative Q_factor ~ 5 -10, i.e. of the same order of magnitude as $1/B_{isb}$, which represents a good compromise. For both QWIP-1 and QWIP-2 we chose therefore an active region consisting of 7 QWs. The complete layer sequences are shown in Fig. 4.2.

For QWIP-1 (QWIP-2), the 5nm-thick (5.3nm-thick) central region of each QW is n-doped at a level of $6.7x10^{17}$ cm$^{-3}$. In order to avoid polaritonic effects, the QWs doping level was chosen approximately a factor of 2 below the one used in Ref. [2]. The active regions are grown on top of a 100nm-thick, lattice-matched $Ga_{0.51}In_{0.49}P$ etch-stop layer, and are sandwiched between 50nm and 100nm-thick top and bottom n-doped contact layers, n-doped at levels of $3x10^{18}$ cm$^{-3}$ and $4x10^{18}$ cm$^{-3}$ respectively. Considering the barrier thickness of 40 nm, and a linewidth equal to 10% of the transition energy, from Eq. 3.77 we compute, for both structures, $B_{isb}$ ~ 0.06.

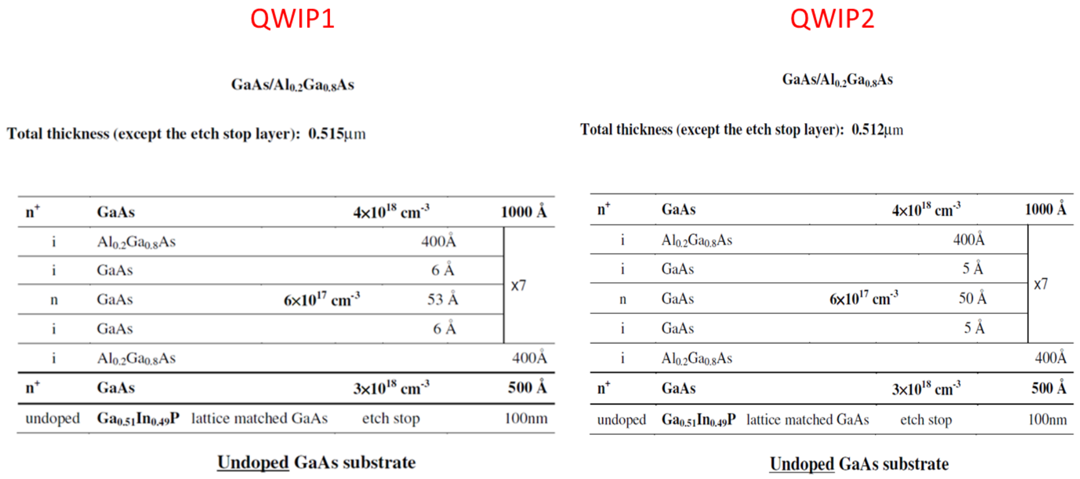

QWIP1

GaAs/$Al_{0.2}Ga_{0.8}As$

Total thickness (except the etch stop layer): 0.515μm

| | | | | |
|---|---|---|---|---|
| $n^+$ | **GaAs** | **$4\times10^{18}$ cm$^{-3}$** | **1000 Å** | |
| i | $Al_{0.2}Ga_{0.8}As$ | | 400Å | x7 |
| i | GaAs | | 6 Å | |
| n | GaAs | $6\times10^{17}$ cm$^{-3}$ | 53 Å | |
| i | GaAs | | 6 Å | |
| i | $Al_{0.2}Ga_{0.8}As$ | | 400Å | |
| $n^+$ | **GaAs** | **$3\times10^{18}$ cm$^{-3}$** | **500 Å** | |
| undoped | **$Ga_{0.51}In_{0.49}P$** lattice matched GaAs | etch stop | 100nm | |

**Undoped GaAs substrate**

QWIP2

GaAs/$Al_{0.2}Ga_{0.8}As$

Total thickness (except the etch stop layer): 0.512μm

| | | | | |
|---|---|---|---|---|
| $n^+$ | **GaAs** | **$4\times10^{18}$ cm$^{-3}$** | **1000 Å** | |
| i | $Al_{0.2}Ga_{0.8}As$ | | 400Å | x7 |
| i | GaAs | | 5 Å | |
| n | GaAs | $6\times10^{17}$ cm$^{-3}$ | 50 Å | |
| i | GaAs | | 5 Å | |
| i | $Al_{0.2}Ga_{0.8}As$ | | 400Å | |
| $n^+$ | **GaAs** | **$3\times10^{18}$ cm$^{-3}$** | **500 Å** | |
| undoped | **$Ga_{0.51}In_{0.49}P$** lattice matched GaAs | etch stop | 100nm | |

**Undoped GaAs substrate**

Figure. 4.2. Layer sequences of (a) QWIP-1 and (b) QWIP-2.

The QWIPs were grown by MBE on a semi-insulating GaAs substrate by the Key Laboratory of Terahertz Solid State Technology in Shanghai. Fig. 4.3(a) shows the dark IV characteristics of the QWIP-1 structure processed in a mesa geometry. We observe an asymmetry between positive and negative bias which may be due to the two different contact layers.

In Fig. 4.4 we report the measured photocurrent spectra at 78K for both positive and negative biases applied to the top contact, obtained by FTIR spectroscopy with QWIP-1 processed in a mesa geometry, therefore showing the effect of the bare ISB transition. For both polarities we observe a progressive reduction of the high energy tail with increasing bias, a signature of a reduced absorption in the continuum of states above the barriers. For all spectra the transition peak is found at 107meV, in good agreement with the expected bound-to-bound transition energy. In Fig. 4.3(b) we report the photocurrent at 77K, obtained by integrating the spectra of Fig. 4.4. As for the dark characteristics, the photocurrent is asymmetric.

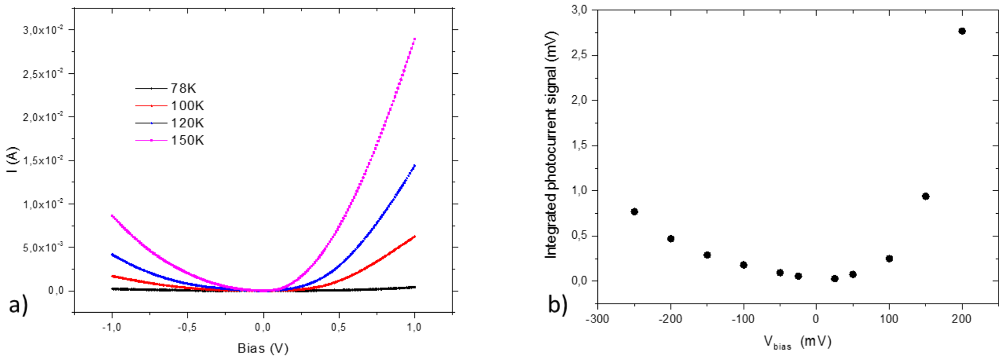

Figure. 4.3. QWIP-1 processed in mesa geometry. (a) Dark IV characteristics at different temperatures. (b) Photocurrent at T = 77K, obtained by integrating the spectra of Fig. 4.4.

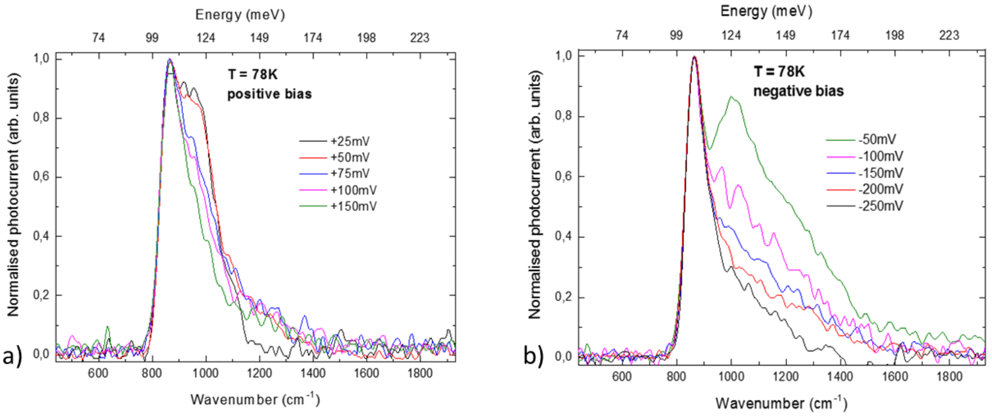

Figure. 4.4. Photocurrent spectra measured at 77K with the QWIP-1 structure processed in a mesa geometry. The resonant energy is around 107meV. The spectra were measured by Raffaele Colombelli and Stefano Pirotta at C2N Laboratory (Palaiseau, France).

### 4.2.2 Patch array design and simulations

The first parameter that must be determined for the design of the PARs is the patch lateral side *s* in order to obtain the desired value of the $TM_{100}$ mode frequency. To this end we implemented FDTD simulations using the commercial code Lumerical®. The simulation box comprises a single unit cell (*p* x *p*) and extends vertically over 20µm. The top and bottom boundary conditions are set to perfectly matching layers (PML). On the sides we have periodic boundary conditions. The source plane is positioned above the patch top metallization, and the source consists of a plane wave, linearly polarized in the x-y plane (Fig. 3.13) with a k-vector normal to the patch. Temporally and spectrally, it consists of a Gaussian pulse covering the 10-50 THz range, and centered approximately at the desired frequency (~30THz) of the PAR $TM_{100}$

mode. The simulated temporal profile of the E-field is obtained using a “time-monitor”, spatially positioned in the middle of the patch height and close to the patch corner. The discrete Fourier transform of the temporal profile provides the spectrum in the frequency domain. Additionally, the E-field amplitude can be also computed in xy-plane and xz-plane, which allows to directly visualize the profile of the EM modes.

An example of simulation results is shown in Fig. 4.5(a), (b), where we report the spectrum of the $TM_{100}$ mode and, in color scale, the amplitude of the electric field excited by a plane wave at normal incidence. Here the patch side is $s$ = 1.9 µm, and the period is $p$ = 3.9 µm.

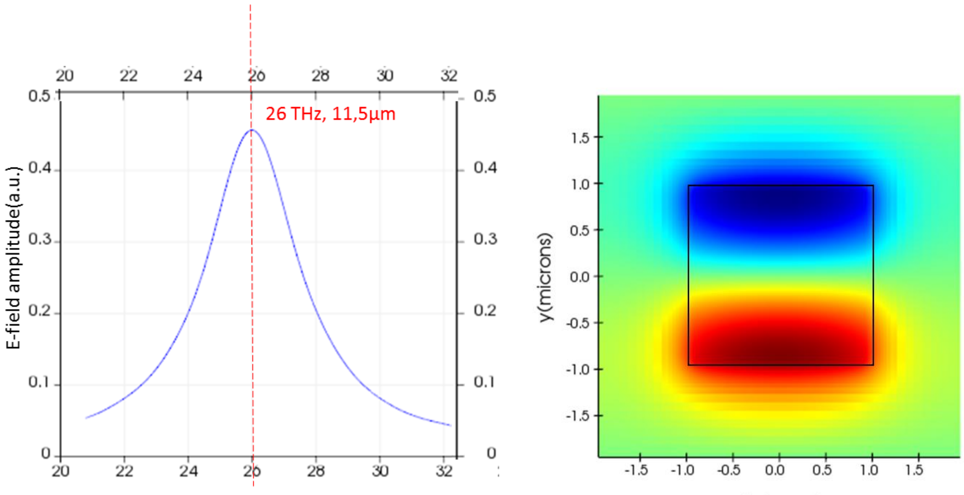

a) b)

Figure. 4.5. a) Computed spectrum centered at 26 THz (~11.5µm) for s=1.9µm and p=3.9µm. b) Spatial profile of the electric field intensity in the x-y plane at 26 THz.

The resonant wavelength vs patch size is shown in Fig. 4.7 (black line). As predicted by Eq. (3.61), on a small wavelength range, the resonant frequency of the PAR depends linearly on the patch size, with a slope given by $2n_{eff}$ [3]:

$$\lambda_{res} = 2sn_{eff} \quad (4.1).$$

From Fig. 4.7 (red and black lines) we find $n_{eff} \approx 3$, and a patch size s=1.87um yields a resonance energy E=107meV, which is coincident with the peak of the ISB transition in Fig. 4.4.

In a real PARs array, individual patches must be electrically connected (see for example Fig. 3.22). Contrary to Ref. [4], where the PARs are connected by metallic bridges deposited on top of the semiconductor material, here, instead, we chose to exploit fully suspended metallic bridges. This allows minimizing the capacitance of the connecting bridges, which helps reducing the device RC time constant. The effect of the connecting bridges on the PARs resonant mode can be quantified using FDTD simulations. As an example, in Fig.4.6 we report the amplitude of the electric field of the fundamental TM modes excited by a plane wave at normal incidence. Here the patch side is $s$ = 1.9 µm, the period is $p$ = 9 µm, and the connecting suspended bridges have a width of 150nm. We can observe that when the plane wave polarization is perpendicular to the bridges, the excited $\lambda/2$ fundamental mode is virtually unaffected and the field is mainly concentrated inside the PAR (compare with Fig.4.5 (b)). This is thanks to the fact that the resonant mode presents a minimum in the center of the cavity. As a result, for a sufficiently thin bridge the effect on the resonant frequency is negligible (Fig.4.7, red line). Instead, when the plane wave is polarized parallel to the bridges the mode is strongly perturbed, and the electric field is delocalized underneath the bridges. This shifts the resonant frequency, as shown in In Fig. 4.7, blue line. Finally, in Fig.4.8 we report the $TM_{100}$ mode resonant wavelength vs bridge width for the E-field polarized perpendicularly to the bridges, for s = 1.85µm. We find that the width of the bridge has virtually no effect on the resonant frequency for wire widths $\lesssim$ 0.5µm.

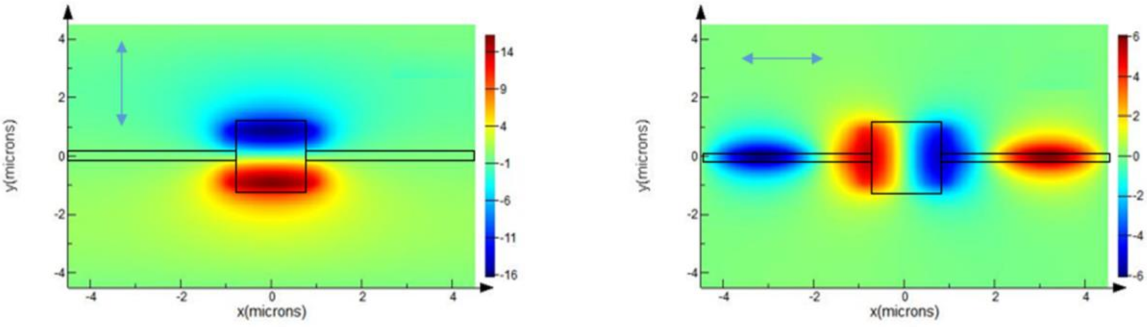

a) b)

Figure. 4.6. 2D mapping of the electric field intensity in color scale for the fundamental modes excited by a plane wave at normal incidence. The patch side is 1.9 µm, the period is 9 µm and the width of bridge is 150 nm. (a) The incident light is polarized perpendicularly to the bridges. (b) The incident light is polarized parallel to the bridges

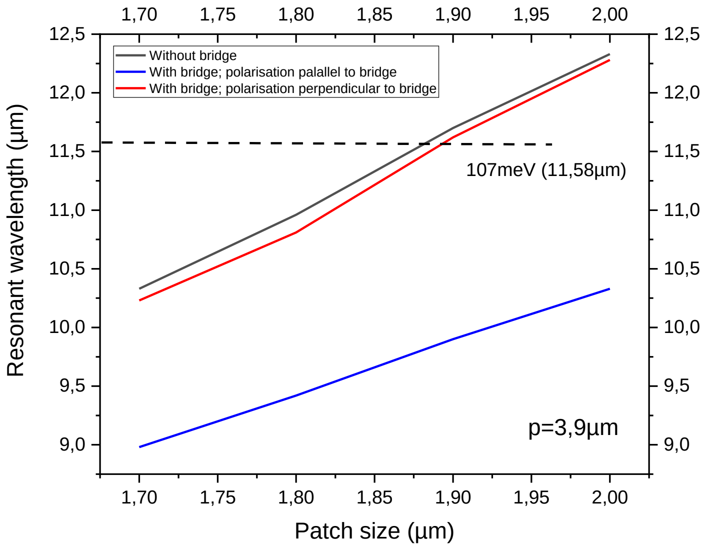

Figure. 4.7. Results of FDTD simulations. Fundamental TM mode resonant wavelength as a function of the patch size for different polarizations of the incident radiation. The cell period is p=3.9 µm and the bridge width is 300nm. The horizontal dashed line corresponds to peak of the ISB transition of QWIP-1 (107meV, see Fig. 4.4)

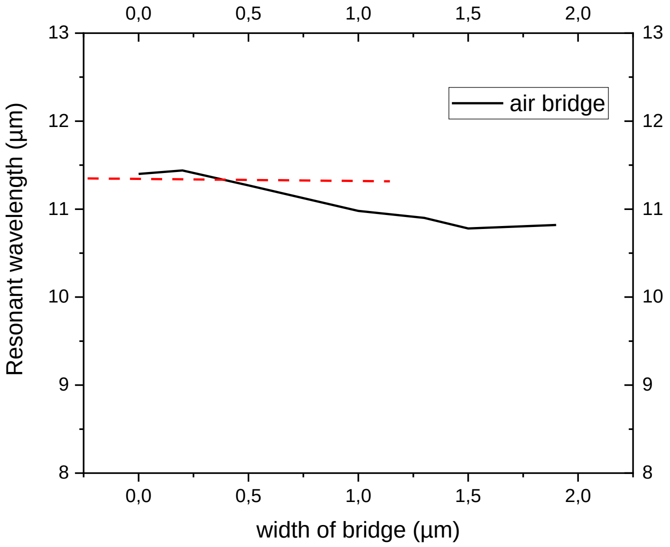

Figure. 4.8. Results of FDTD simulations. $TM_{100}$ mode resonant wavelength vs bridge width for the electric field polarized perpendicularly to the air bridges. The patch size is s = 1.85µm and the period is p = 3.9 µm. The red dotted line shows the resonant wavelength without the bridge.

Finally, in Fig.4.9, we report the resonant wavelength as a function of the period of the array, for a fixed patch size s = 1.85µm.

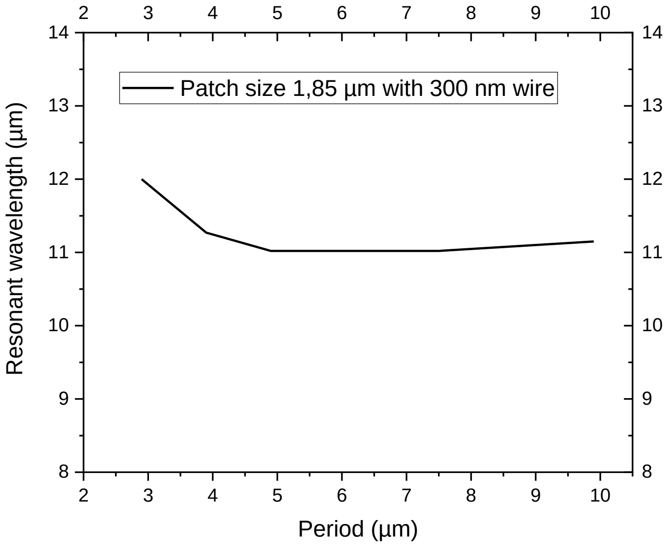

Figure. 4.9. Results of FDTD simulations. Resonant wavelength as a function of period with fixed 1.85µm patch size.

Following the results of the simulations, in order to match the ISB transition energy, and verify the condition of critical coupling, we designed five sets of 300µm x 300µm PARs array with varying patch periods p = 2.9µm, 3.9µm, 4.9µm, 7.4µm, 9.9 µm, and keeping the same patch size s = 1.85 µm. The latter, according to Fig. 4.7 gives the desired resonant wavelength. The optical characterization of these arrays will be presented in Section 5.1. From these measurements we found that the dimensions yielding the largest reflectivity contrast (C ~ 0.8÷0.9) are s = 1.85µm and p = 3.9÷4.9µm.

According to these results we then fabricated a first generation of QWIP detectors, with a specific geometry aimed at maximizing the detection speed. To this end, particular care was taken in the detector microwave design, in order to minimize the effect of parasitic capacitances brought by electrical connections and contact pads, which limited RF operation up to a few GHz in Ref. [4]. This was achieved by integrating a 50Ω, tapered coplanar waveguide (CPW), connected to the PARs array through a micro-fabricated air bridge. Besides minimizing the parasitic capacitance, this solution is ideal for on-wafer testing by means of a 67GHz microwave coplanar probe.

The characteristic impedance of the CPW depends on the material substrate, the dimension of central electrode, the distance between two ground planes, etc. The expression of the impedance is given by [5]:

$$Z_0 = \frac{30\pi}{\sqrt{\varepsilon_{re}}} f(k) \quad (4.2)$$

with $f(k) = \frac{\ln[2(1+(1-k^2)^{\frac{1}{4}})/(1-(1-k^2)^{\frac{1}{4}})]}{\pi}$ (4.3), where $k = \frac{S}{S+2W}$, $\varepsilon_{re}$ is the effective dielectric constant of the CPW. As shown in Fig. 4.10, S is the width of the center electrode, and W is the width of slots. The CPW is tapered to achieve a smooth transition between the device and the pad access, compatible with the pitch of the coplanar probe, of 125um. Following Eqs. (4.2), (4.3), and from the value of the dielectric constant of the Silicon substrate of 11.7, by setting S=5um and W=3um at the beginning of CPW, increasing to S=60 µm and W=36 µm at the end, we obtain a constant CPW impedance of 50 Ohm. The width of the whole CPW is 352µm and the length is 300µm (Fig.4.10).

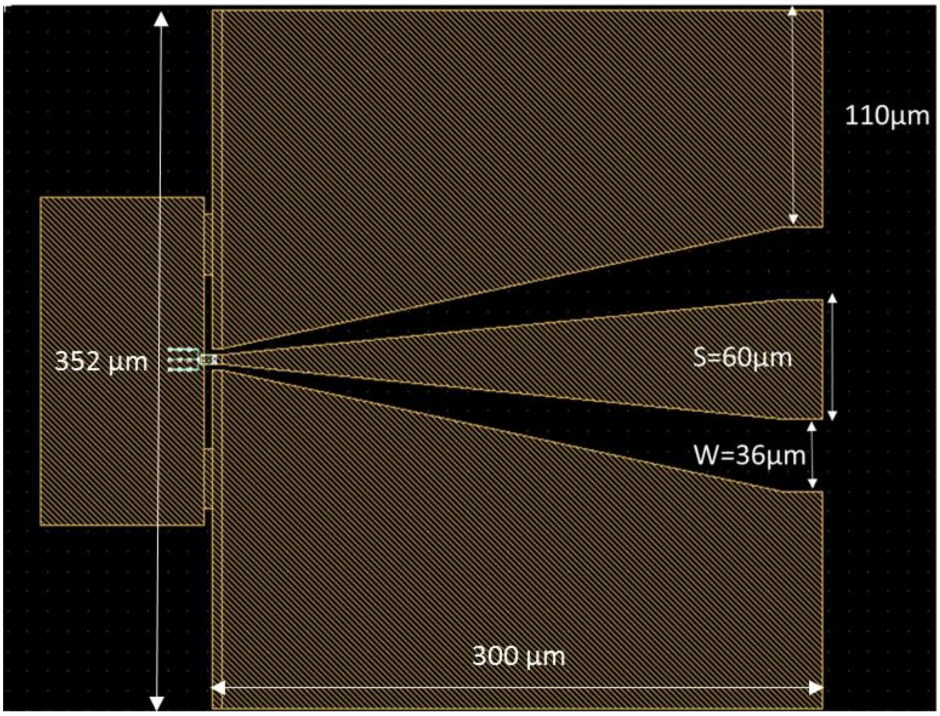

Figure. 4.10. Schematic representations of Layout mask showing the dimensions of the CPW. The end of the central electrode has a width S = 60µm; the width of the slots is W = 36µm. The total length and width of the CPW, are 300µm and 352µm, respectively.

To minimize the array capacitance, we kept the number of patches to the minimum needed to allow collecting 100% of the incident radiation. Since the waist of our laser beam has a diameter of approximately 20µm (see next Section), to optimize the overall collection of the detector array while reducing the capacitance, we designed 5x5 PARs arrays with a patch period p = 3.9 µm (Fig. 4.11). For comparison purposes, we have also designed a 3x3 PARs array with period p = 3.9µm.

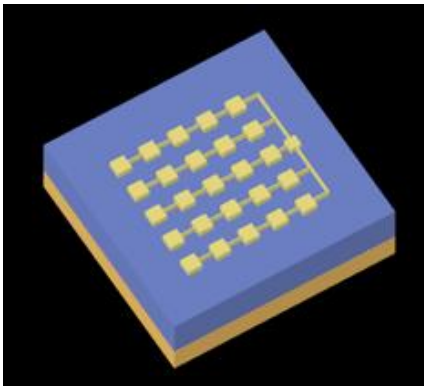

Figure. 4.11. Schematic representations of a 20µm x 20µm PARs array with a period of 3.9 µm.

Finally, individual resonators are electrically connected by suspended gold bridges. As pointed out above, compared to keeping the semiconductor beneath, as in Ref. [4], this solution allows minimizing the bridges capacitance, while simultaneously eliminating the current flow outside the resonators, therefore reducing the dark current.

The designs and simulations described above are all based on QWIP-1 active region. Concerning the QWIP-2 active region we did not measure the ISB transition energy, however from the computed band diagrams (Fig. 4.1 (c) (d)), the ISB transition of QWIP-2 is expected to be around 121meV (115 for QWIP-1). Hence for this active region we used s = 1.8µm and p=5µm. With these values we fabricated sets of 3x3 and 5x5 PARs arrays.

## 4.3 Fabrication Process

This part is devoted to the fabrication process I had to develop during my thesis to obtain PARs-based QWIP detectors monolithically integrated to coplanar waveguides (CPW). As shown on the schematic of Figure. 4.12, the PARs-based QWIP detector consists of an array of individual PARs connected to each other by metallic air-bridges (named air-bridge1 in Fig. 4.12). A “second” air-bridge (air-bridge 2) connects the whole array to a 50-Ohm-CPW. The GaAs/$Ga_{0.2}Al_{0.8}As$ epitaxial layer structures (called QWIP-1/QWIP-2) forming the QWIP detectors have been already described in Section 4.2. It is worth noting that a 100-nm-thick-$Ga_{0.5}In_{0.5}P$ etch stop layer has been grown on the GaAs substrate before the growth of the QWIP layers.

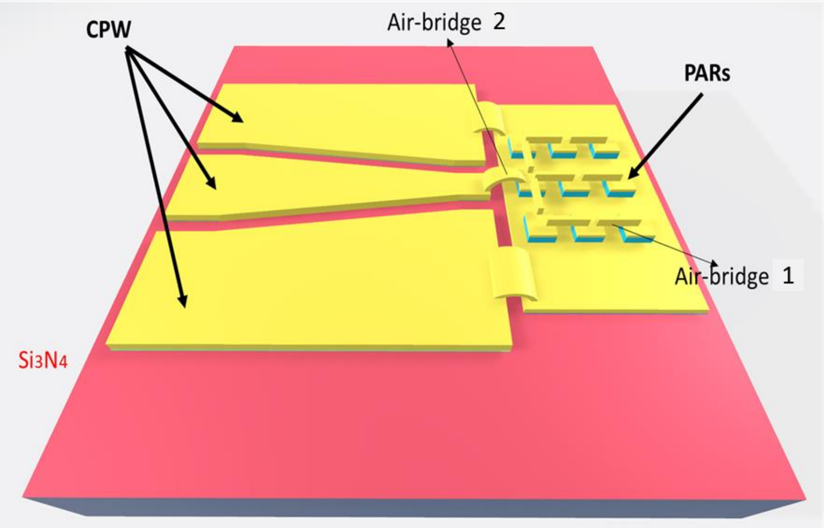

Figure. 4.12. 3D schematic of a PARs-based QWIP detector.

The fabrication process is shown in Figure.4.13 and can be divided in 4 main steps:

I. Transfer of the QWIP layers on a high resistivity silicon substrate (Fig 4.13-1 & Fig. 4.13-2).
II. Fabrication of the Patch antenna resonators (Fig 4.13-3 & Fig. 4.13-4).
III. Patterning of the CPW (Fig 4.13-5).
IV. Air bridges fabrication (Fig 4.13-6).

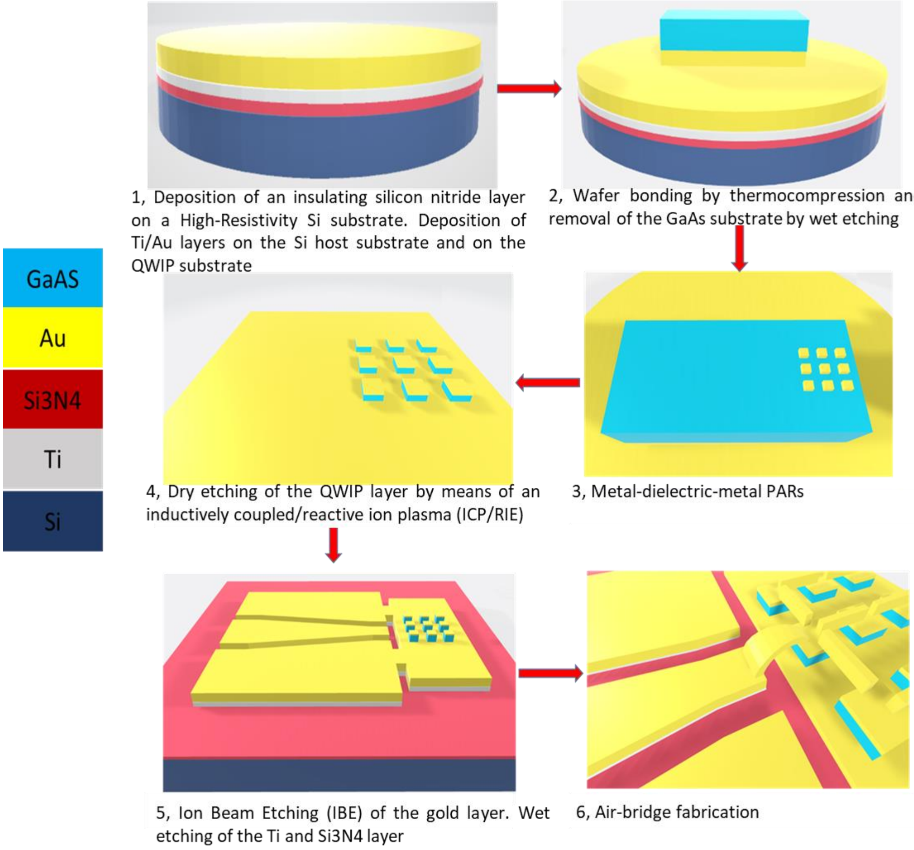

1, Deposition of an insulating silicon nitride layer on a High-Resistivity Si substrate. Deposition of Ti/Au layers on the Si host substrate and on the QWIP substrate

2, Wafer bonding by thermocompression and removal of the GaAs substrate by wet etching

3, Metal-dielectric-metal PARs

4, Dry etching of the QWIP layer by means of an inductively coupled/reactive ion plasma (ICP/RIE)

5, Ion Beam Etching (IBE) of the gold layer. Wet etching of the Ti and Si3N4 layer

6, Air-bridge fabrication

Figure. 4.13. 3D schematic of the fabrication steps.

### 4.3.1 Epitaxial layer transfer

The buried gold metal layer serving as MIR back reflector and bottom Schottky contact is obtained by transferring the QWIP epitaxial layers on a host-substrate with suitable properties (thermal, mechanical, electromagnetic) thanks to an Au-Au thermocompression wafer bonding technique. This technique widely used last years in the THz and IR scientific community has been developed in the THz Photonics groups to fabricate optical microcavity THz photomixers [6].

### 4.3.2 Silicon Nitride coating

Here, we use high resistivity silicon (>5 kΩ.cm) as host substrate because of its low cost, its resistance to etching solution used for III-V semiconductors, and its very low loss tangent. In order to avoid any leakage currents between the electrodes of the coplanar waveguide coming from the silicon, a 100-nm-thick $Si_3N_4$ coating layer is deposited on the latter by using a radio-frequency (RF) plasma-enhanced chemical vapor deposition technique (PECVD) (shown in Appendix) at 200°C.

### 4.3.3 Wafer bonding by Au-Au thermocompression technique

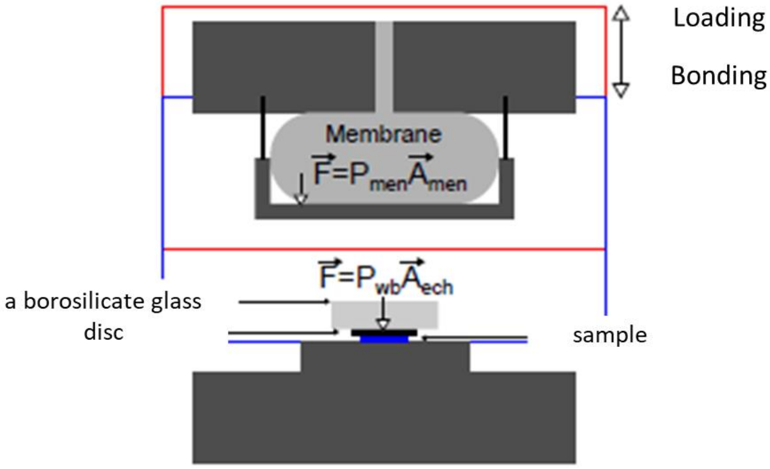

Figure. 4.14. Schematic presentation of the Suss-Microtech bonder [7].

Thermocompression bonding is a form of solid-state welding, in which pressure and heat are simultaneously applied to form a bond between two separate surfaces. At room temperature, very high pressure is needed to obtain interatomic attraction despite surface asperities. The applied pressure on the substrates during the bonding is expressed as: $P_{wb} = P_{men}\frac{A_{men}}{A_{ech}}$, where $P_{men}$ is the pressure given by the membrane with the surface $A_{men} =$

222.23 $cm^2$; $A_{ech}$ is the surface of sample.

As a noble metal, gold is an ideal bonding material since it doesn't require additional steps aimed at removing the surface oxide layer. It has been shown that high bond strength of ~4 MPa could be obtained by using a pressure of 4 Mpa and a bonding temperature of 300 °C [8]. Fig. 4.14 is shown a schematic of the commercial bonder available in the MNFF. It allows bonding in rough vacuum (~1e-3 mbar) at temperature up to 500 °C and pressure up to 2 bars on 6 inches diameter wafers. Here, we use a bonding temperature is 200°C to mitigate the mechanical stress induced by the different thermal expansion coefficients of GaAs and Silicon [9]($\alpha_{GaAs}$ = 5.7 ppm/K, $\alpha_{Si}$ = 2.6 ppm/K). Before the bonding, 8nm of Ti/200nm of Au and 100 nm of Ti/200nm of Au are deposited by e-beam evaporation. The titanium layer acts as an adhesion layer and also as etch stop layer during the physical etching of the gold layer as it will be shown in the following. After the metal deposition, the two substrates are aligned face to face and bonded in the bonder at 200 °C for 90 min under a membrane pressure of 700 mBar corresponding to a bonding pressure of ~4 Mpa (see explanation in the caption of Fig. 4.14).

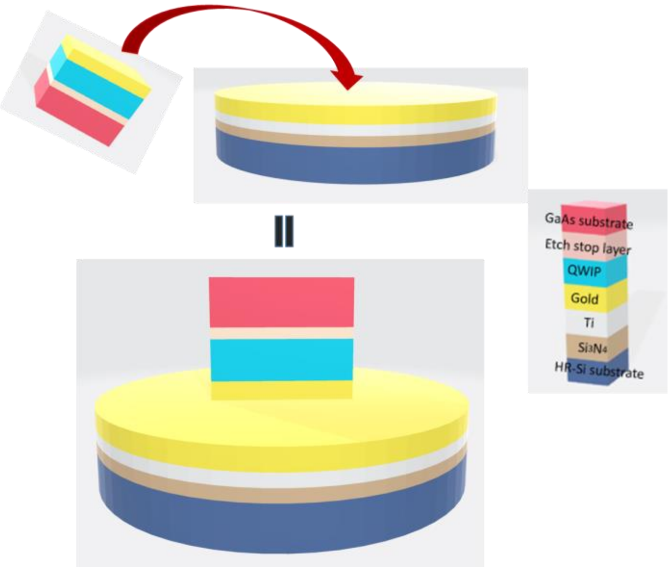

Figure. 4.15. Wafer-level bonding process by Au-Au thermocompression.

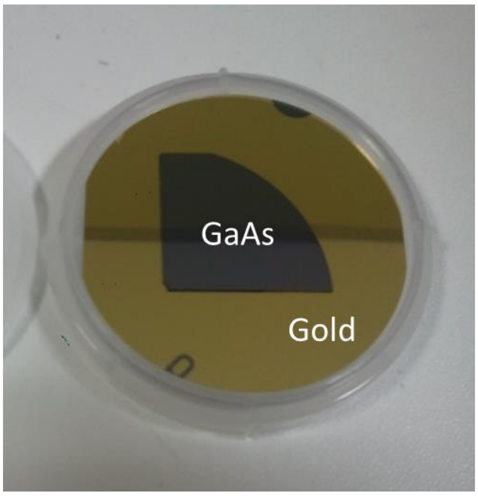

Figure. 4.16. Optical view of the QWIP epitaxial layer bonded on a 2-inche-diameter silicon substrate.

Fig 4.17 shows a close-up of the bonding interface. The bonding joint is not perfect since we can notice some voids here, but has been proven to be sufficient to fabricate reliable devices as it will be shown in the next section.

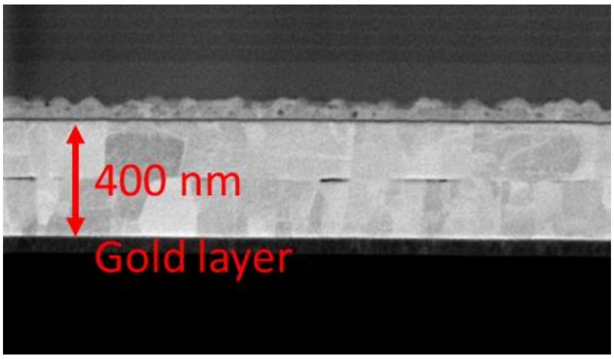

Figure. 4.17. SEM image of the Au–Au thermocompression bond. The transverse cut has been carried out by using a focus ion beam (FIB) tool.

Despite the low bonding temperature, the stress-induced curvature of the bonded substrates prevents mechanical lapping. The GaAs substrate is therefore removed by means of chemical wet etching in a solution of hydrosulfuric acid and hydrogen peroxide ($H_2SO_4$: $H_2O_2$: $H_2O$/1: 8: 1, etch velocity~1µm/min). The high etching selectivity (~1000) between GaAs and GaInP allows us to etch the whole 600µm-thick substrate. The GaInP etch stop layer is then removed in a hydrochloric acid (HCl, 30s for 100nm). Once the buried metal layer is carried out thanks to the epitaxial layer transfer, the top metal layer forming the patch antennas and the top Schottky contacts of the QWIP will be patterned by using e-beam lithography, metal deposition by e-beam evaporation and lift-off technique as described in Fig 4.18.

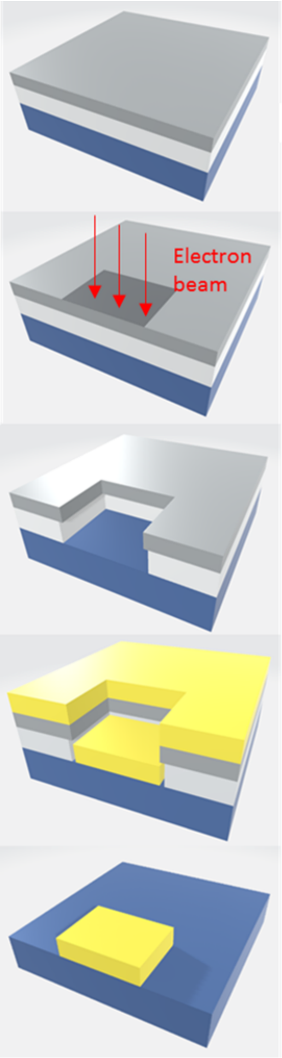

**PMMA**
**+**
**P(MAA/MMA)**

**E-beam exposure**

**PMMA and P(MAA/MMA) development leading to an undercut profile because of their different electron sensitivity**

**Metal deposition by evaporation**

**Resist removal in a suitable solvent. The metal on the resist is also lift-off.**

Figure. 4.18. Metal deposition by lift-off technique using a bilayer of resists of different electron sensitivity resulting in an undercut profile.

In our case, we utilize a bilayer with different electron sensitivities consisting of a poly (methyl methacrylate-*co*-(8.5%) methacrylic acid) copolymer (thickness: 670nm), P[MMA(8.5)MAA)], and a polymethyl methacrylate (PMMA) resist (thickness: 70nm). PMMA, dissolved in anisole, is indeed widely used as an electron beam resist presenting resolution reaching 10 nm when used with a 100-kV electron-beam. After e-beam lithography, development in a mixture of isopropanol and Methylisobutylketone (IPA/MIBK), evaporation of a bilayer of Ti/Au (8nm/300nm), 1.9-µm-square metallic patches (Fig. 4.19) are finally obtained after the dissolution of the resist in a suitable solvent (Acetone or a specific resist remover).

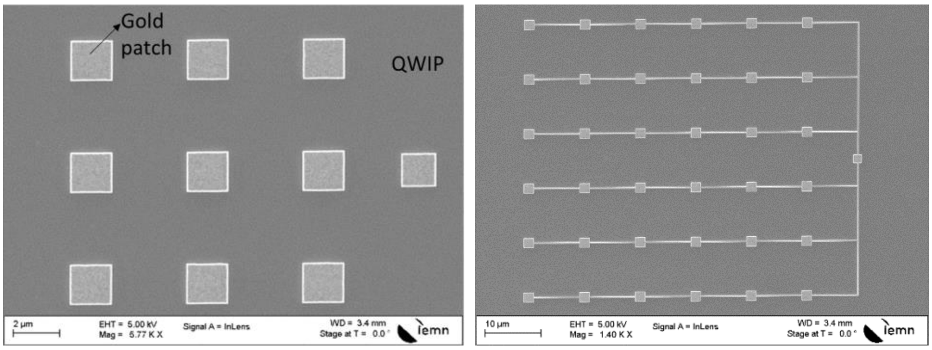

Figure. 4.19. SEM images of the gold patch arrays.

The next step consists in etching the semiconductor layers by using the top metal electrode (1.9 µm square) as self-aligned etch mask (Fig. 4.19). It is achieved by using an inductively coupled/reactive ion plasma (ICP/RIE) of boron trichloride ($BCl_3$) (Principle shown in Fig. A.3). It is worth noticing that the anisotropic feature of the GaAs/AlGaAs etching (as seen in Fig.4.20), required to achieve well-defined structures and subsequent fine control of the patch resonance frequency, is obtained by decreasing the chamber pressure (P=2 mTorr).

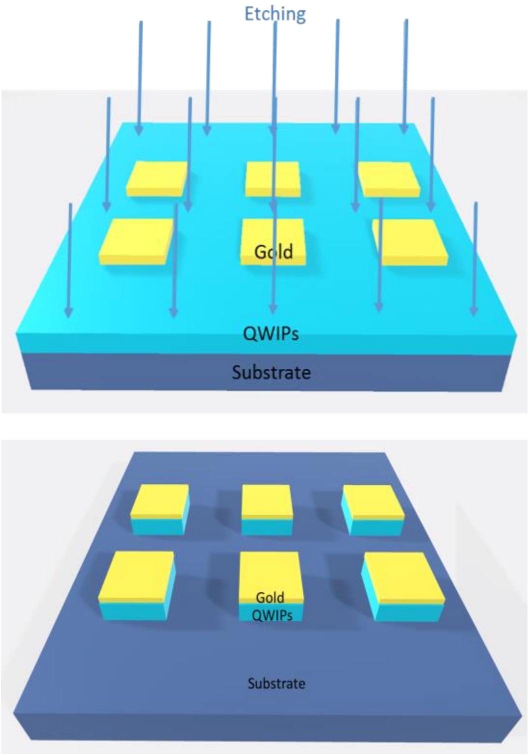

Figure. 4.20. ICP-RIE etching of the QWs. The image above presents the illustration before etching and the below presents the illustration after etching.

The gold mask is also etched during the ICP-RIE process. After the etching, the gold layer thickness has decreased down to 200 nm. SEM images of PARs QWIP devices are shown in

Fig.4.21. We observe the perfect profiles of PARs with 500nm-QWIP+200nm-Au.

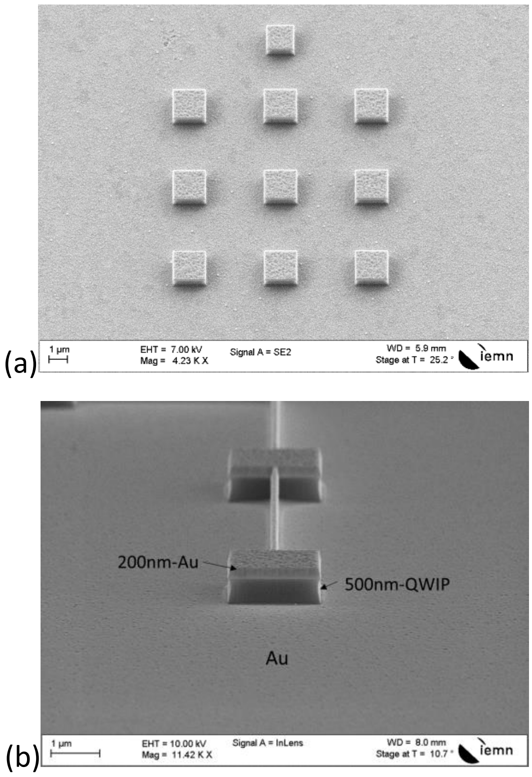

Figure. 4.21. SEM pictures of PARs QWIP devices after ICP-RIE etching. a) Top view of patches without connecting bridges; b) side view of patches with connecting bridges.

### 4.3.4 Coplanar waveguide

My thesis work is aimed at fabricating and characterizing MIR detector with response time being in the picosecond range corresponding to electrical frequency bandwidth much larger than 10 GHz. In this frequency band, a careful design of the electrical access must be done to minimize electrical parasitics (bonding wire inductance, contact electrodes capacitance, etc) and to reach the intrinsic frequency bandwidth of the device. In our case, it is achieved by integrating the PAR's-based QWIP detectors to 50-Ohm-coplanar access through a metallic air-bridge. It allows for on-wafer characterization by using coplanar-probes or microwave-compatible packaging. The layout of the metallic strips forming the CPW (in black) is shown in Fig. 4.22. It can be noticed that the CPW is tapered to achieve a smooth transition between the device and the pad access compatible with coplanar probes (GSS with 125um-signal-ground spacing) used in the low-temperature characterization set-up. The characteristic impedance of the CPW depends on the distance between the ground plane and the center electrode (*W*) and the width of the center electrode (*S*), as presented in Eq. (4.2) (4.3) in Section 4.2.

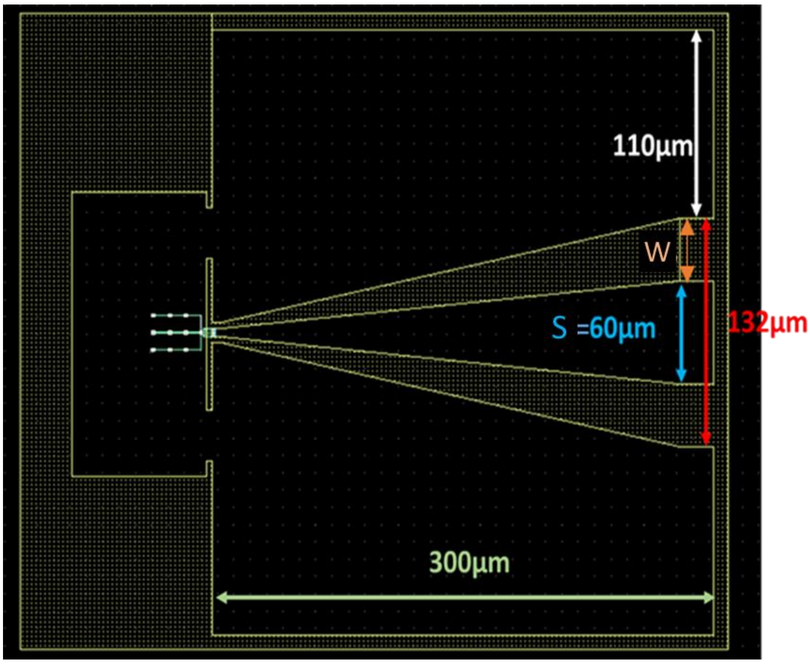

Figure. 4.22. Layout of PARs-based QWIP devices integrated with a tapered CPW. The yellow part corresponds to the part "insolated" by the electron-beam during the lithography step.

The CPW is fabricated by etching directly the buried gold layer resulting from the wafer-bonding step. The gold etching process is based on the argon ion-beam etching (IBE) process described in A.4 and electron-beam resist masks. Due to its superior properties as an etching mask in comparison with PMMA-based resist, we use a positive resist CSAR (main components are poly (α-methylstyrene-co-methyl chloroacrylate), an acid generator, and the solvent anisole) as etching mask during the IBE etching (layout is shown in Fig. 4.22). Figure. 4.23 is presented SEM pictures of the resist mask after e-beam lithography and development.

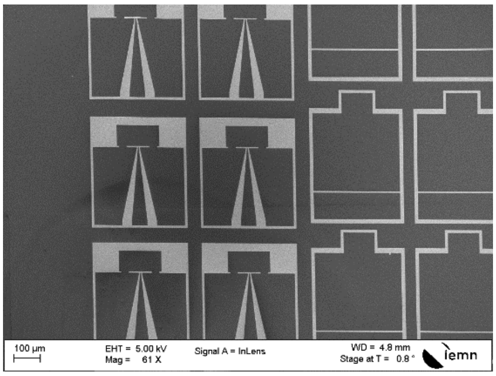

Figure. 4.23. SEM images of the sample after development. The white part will be etched away during the IBE process.

*Ion Beam Etch (IBE)*

A first test campaign has shown that an ion beam with the kinetic energy of 300eV gives an etch velocity of ~20 nm/min (18 min for 400nm) at normal incidence according to the spectrometer data. Furthermore, the much lower etch velocity of the titanium layer underneath allows us to use it as etch stop layer to avoid any damage or ion implantation in the silicon surface. The titanium layer can indeed be removed by a wet etching in a solution of buffered hydrofluoric acid (BOE). However, as shown in Fig. 4.24, it can be noticed that the surface of the silicon wafer is covered by gold flakes after the wet etching of titanium and the resist stripping. It turned out that I had to increase the etching time up to 28 min to get a perfectly clean surface, as presented in Fig.4.25. I measured that in 10 minutes around 22 nm of titanium has been etched. I assume that an intermixing layer of gold and titanium is created during the bonding process which is not etched by BOE. An over-etch is then needed to go beyond this layer.

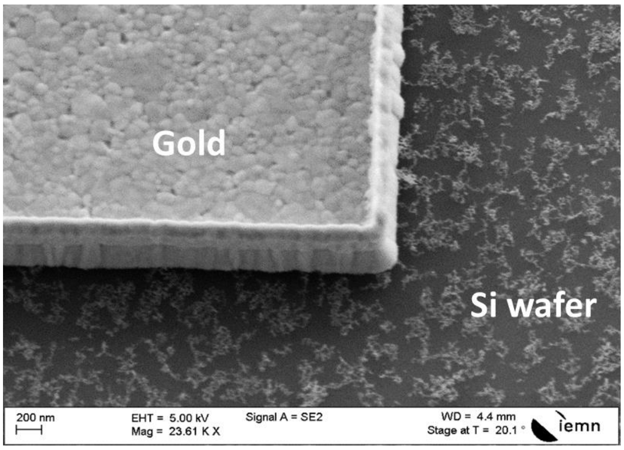

Figure. 4.24. SEM image of the sample surface after 18 min of RIBE at normal incidence /80s in BOE for titanium etching/resist mask stripping.

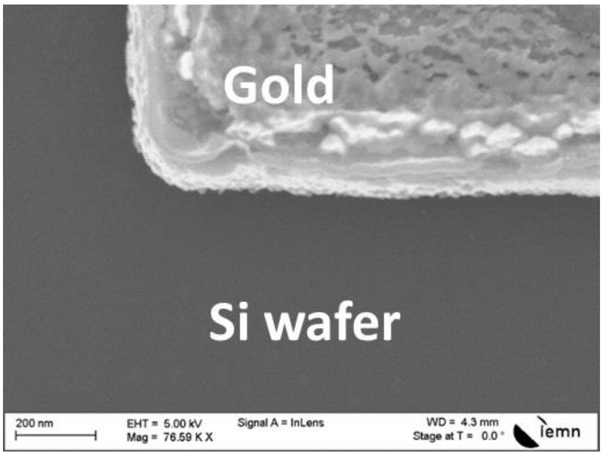

Figure. 4.25. SEM image of the sample surface after 28 min of RIBE at normal incidence /80s in BOE for titanium etching/resist mask stripping

However, we can observe in Fig. 4.26, which shows a side view of the 400-nm-thick gold layer after 28 min of IBE etching with a 1.2-µm-thick mask resist, that there is a thin metallic wall of thickness ~700 nm standing on the edges of the remaining gold layer. This comes from the re-deposition on the resist walls of gold atoms sputtered by the ion beam (see Fig. 4.27).

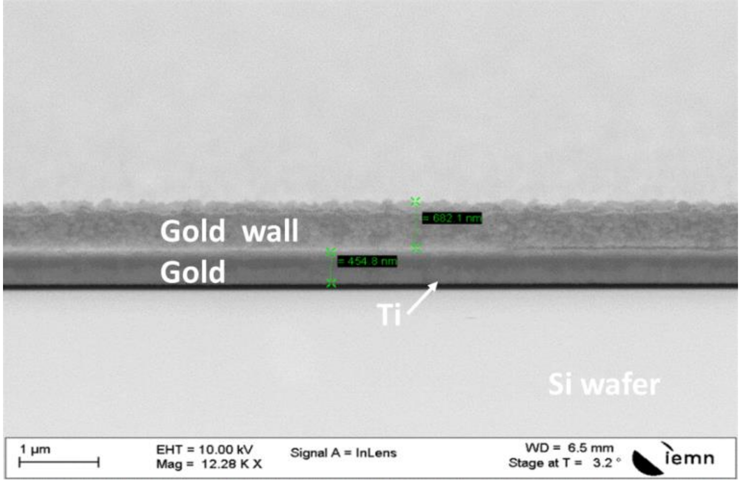

Figure. 4.26. SEM side view of the 400-nm-thick gold layer etched by IBE with 1200-nm-thick resist mask.

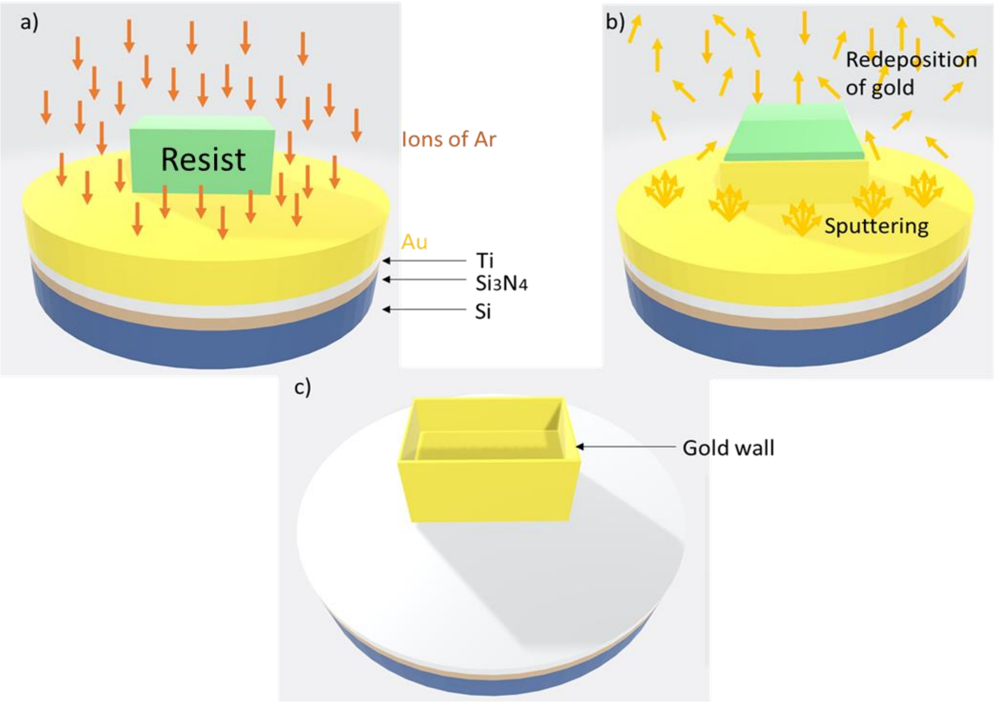

Figure. 4.27. Illustration of the re-deposition of the sputtered gold atoms under normal incidence IBE etching.

We noticed that the height of this wall is proportional to the resist thickness. In order to remove it, the sample is etched in a second time by using a grazing-incidence ion beam (incidence angle~ 70°). As illustrated in Fig. 4.28, at this incidence angle, the target metal layer and the re-deposition layer sticking on the resist are etched at similar etch velocity. In addition, the rotation of the holder during the etching reduces the shadowing effect.

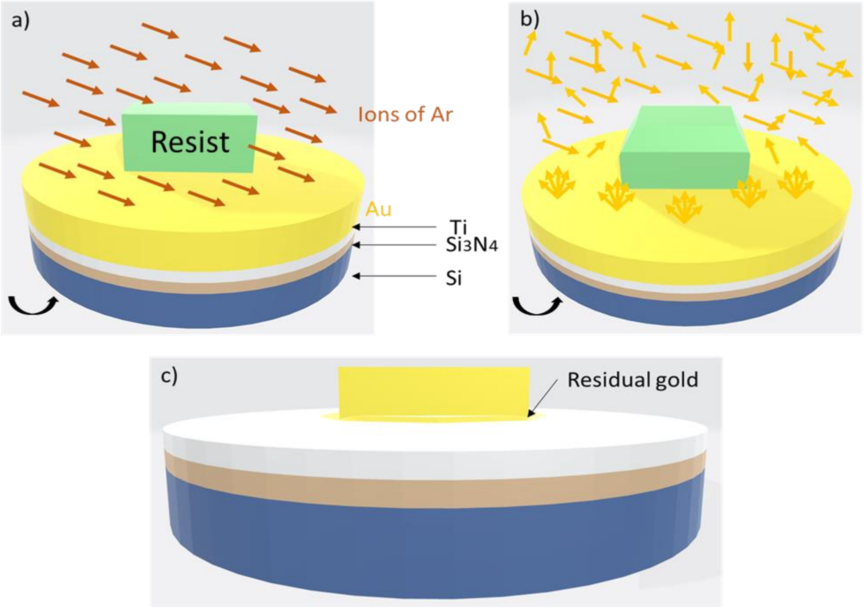

Figure. 4.28. IBE etching under grazing incidence (~70°). The sample holder rotates at a constant speed during the etching.

SEM profiles of samples after four etching times (6, 15, 21 and 30min) under grazing incidence ion beam are shown in Fig. 4. 29. We can see clearly that the metal wall becomes thinner with the increase of the etching time under 70 degree.

It can be seen in Fig. 4.30 that the metallic wall has almost disappeared after 39 min of 70 degree etch. However, we can also note that there are still some traces of gold on the substrate (caused by the re-deposition from the etching on the metallic wall). Finally, it is only after 54 min that clean surfaces are obtained both for the metal wall and the surface of the sample (Figure.4.31).

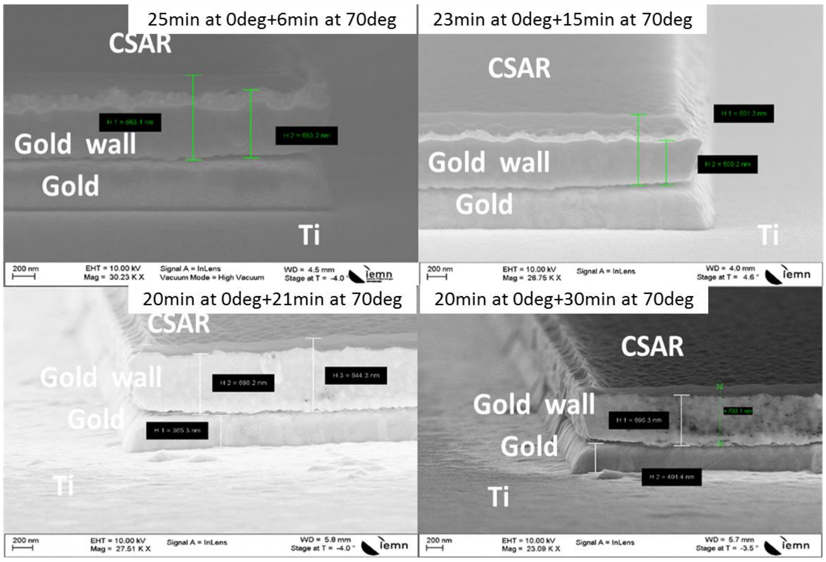

Figure. 4.29. SEM profiles of samples using 1200-nm-thick resist mask after 6, 15, 21 and 30 min etching times at 70°.

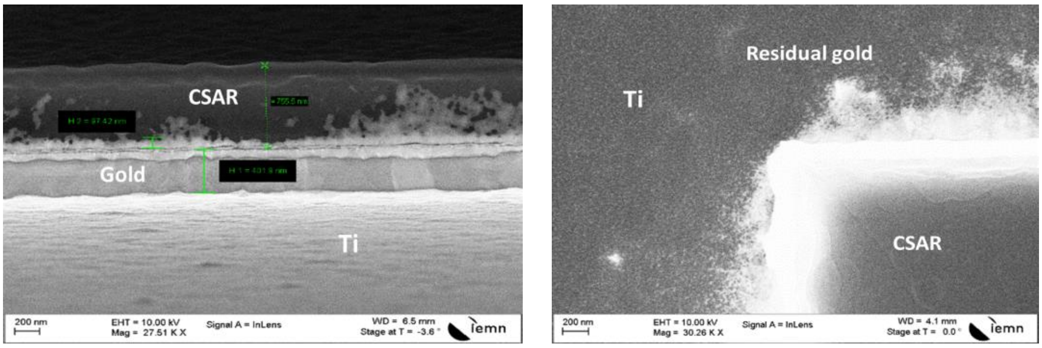

Figure. 4.30. SEM images of the test sample after 20 min at 0° + 39min at 70° of RIBE with the side view on the left and the top view on the right.

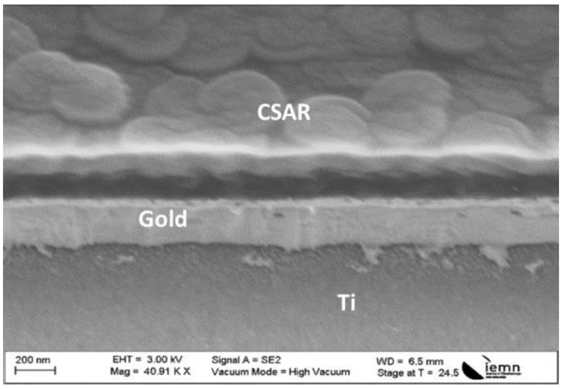

Figure. 4.31. SEM images of the test sample after 20 min at 0° + 54min at 70° of RIBE.

### 4.3.5 Air bridges

The last step consists in building the air bridges between the patches, and between the PARs and the CPW. For this purpose, we developed a fabrication process involving two e-beam lithography steps with two different resists.

In order to make the air bridges, we need a first resist which acts as mechanical support for the suspended part of the bridge. Here, we used a layer of polydimethylglutarimide (PMGI SF11), a deep-UV resist, which can also be patterned by e-beam lithography with sub-micrometer resolution. This resist is based on a polymer of polydimethylglutarimide dissolved in an aqueous solution primarily composed of cyclopentanone. It doesn't react with the organic solvent (MIBK) used for the development of the standard e-beam resists based on PMMA. The whole process for this two steps E-beam lithography is presented in Fig. 4.32.

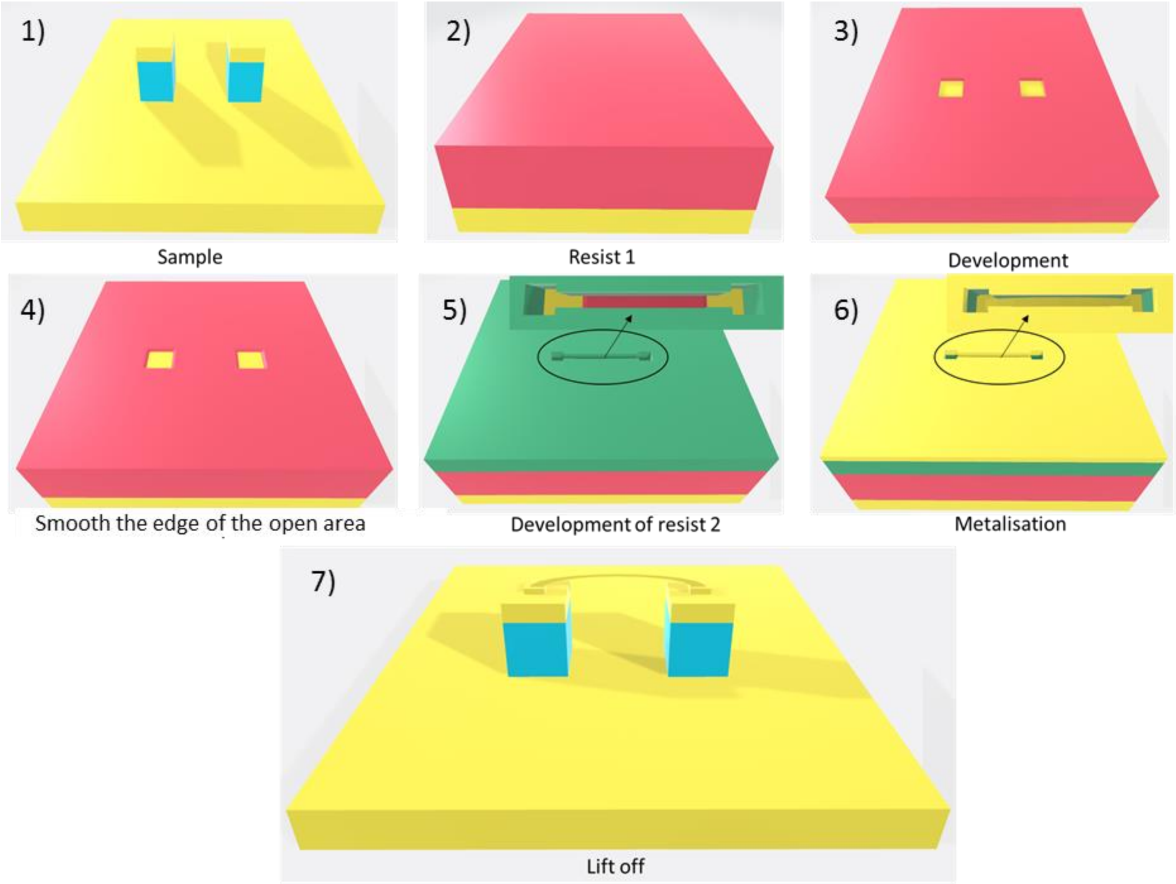

Figure.4. 32 Fabrication process of the metallic air-bridges.

The pattern of the CPW is shown in figure 4.22. The two types of air bridge previously shown in Fig 4.12 will be fabricated at the same time. The purpose of first e-beam lithography step is to define openings in the PMGI layer in order to reach the gold surfaces which will be connected by the air-bridges. In order to fabricate the air-bridge 1 we need to open the PMGI above the PARs as shown in Fig 4.33 by the red circle n°1. As for the air-bridge 2, the PMGI should be open above the PAR's and the center strip of the CPW as shown in Fig. 4.33 by the red circle n°2 and the green circle n°1.

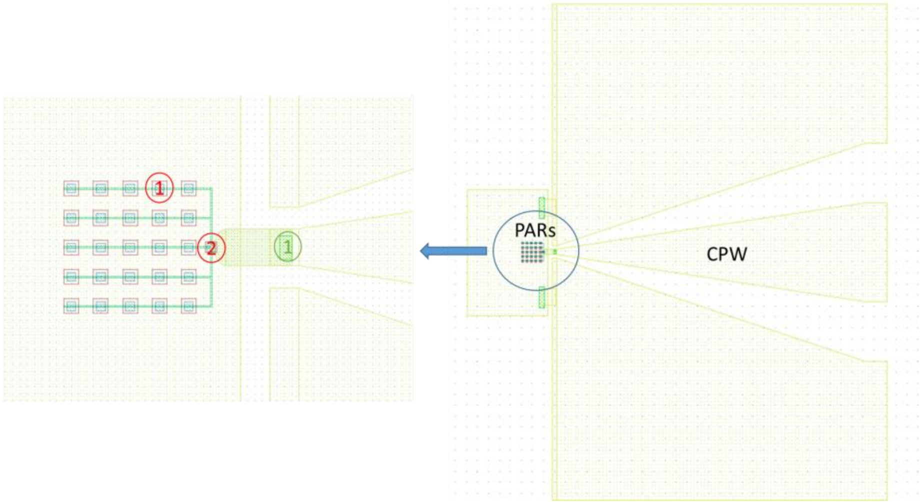

Figure. 4.33 Schematic of the openings in the PMGI layer by E-beam lithography.

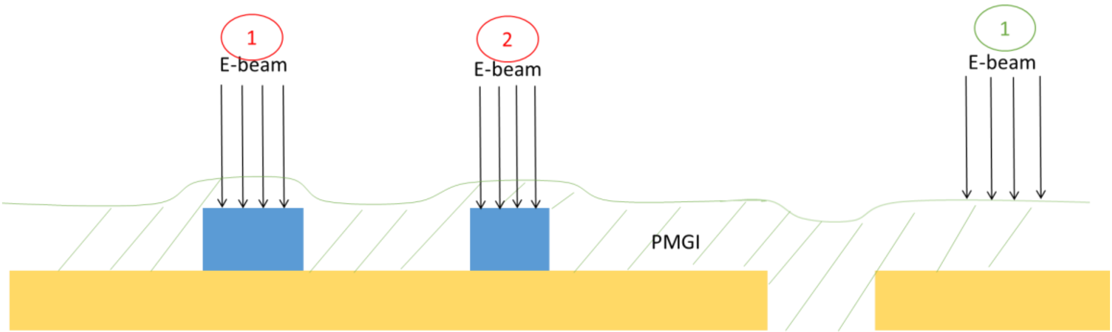

Figure. 4.34 Schematic of the profile of the PMGI layer. Its thickness is not constant across the sample. The circles correspond to the circles marked in Fig. 4.33.

The challenge here stems from the difference in thickness of the PMGI layer above the PARs and above the gold ground plane. We have resolved this problem by using two different electron doses to obtain a sub-micrometer dimension accuracy in both cases. In addition a post bake step is needed after the development to reflow the resist in order to smooth its edges, as shown in Fig. 4.35.

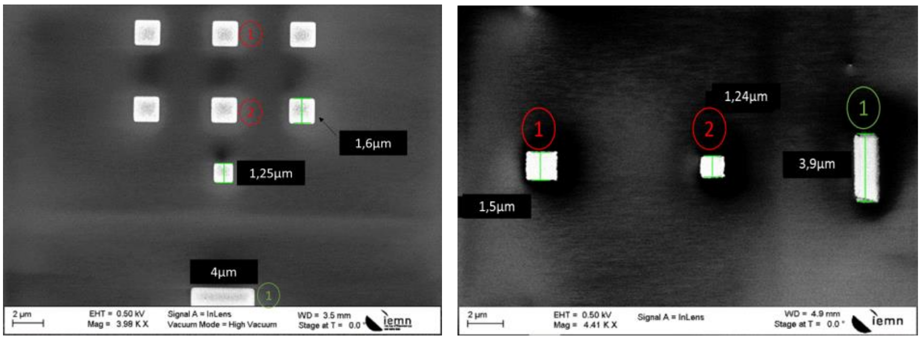

Figure. 4.35 SEM images after e-beam lithography of the PMGI before (left) and after (right) a 30s post-bake at 220◦C.

The air-bridge is then defined by a standard lift-off process based on a P(MMA MAA)/PMMA bi-layer as already described in this chapter. However, difficulties appeared because of the very small bridge dimension (150 nm). As shown in Fig 4.36, we observed that with a standard lift-off process, no sweet spot has been found by performing a dose variation. We can notice in Fig 4.36 the incomplete development of the resist even at very high dose. We had to change both the doses and developing time to obtain perfect results as shown in Fig. 4.37.

After the evaporation of a bilayer of Ti/Au (20nm/600nm) and the lift-off, the complete devices are shown in Figs. (4.38) - (4.40).

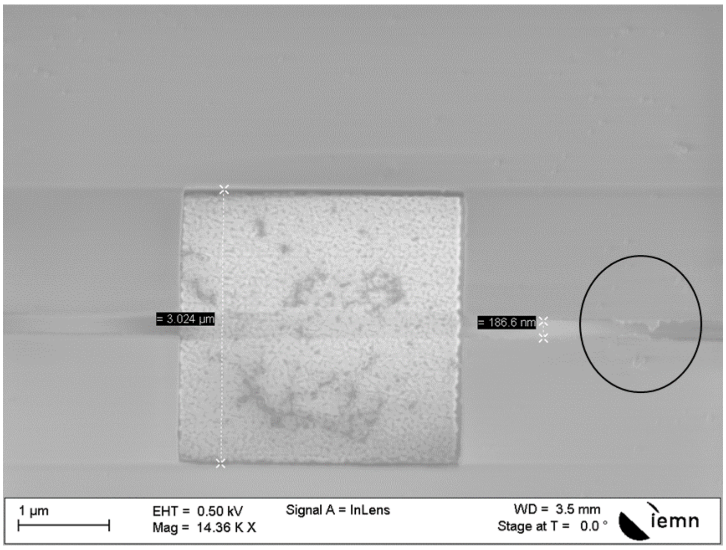

Figure. 4.36 Incomplete development of the PMMA layer despite the use of a high electron dose (640 uC/cm$^2$) and standard development time (60s).

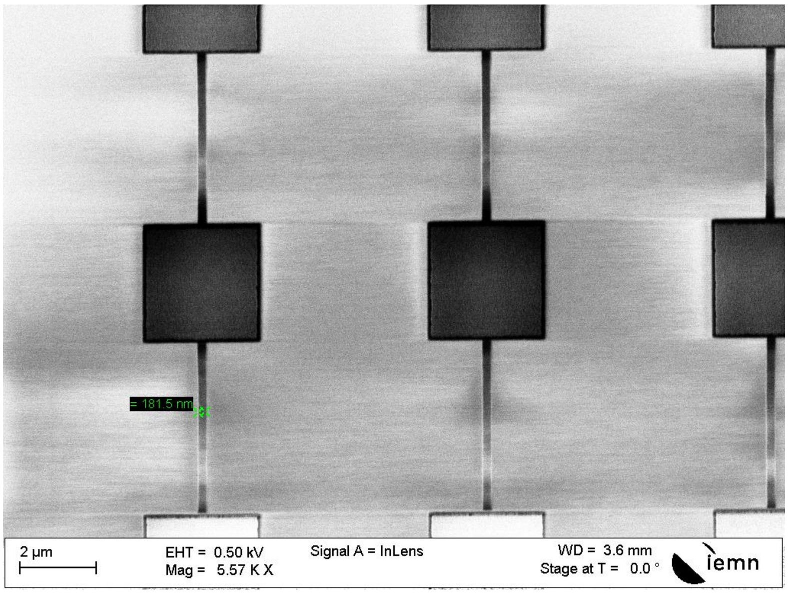

Figure. 4.37 Complete development of the PMMA layer.

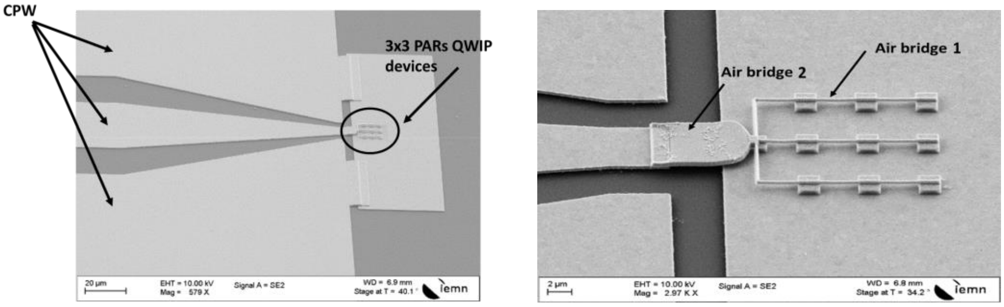

Figure. 4.38 SEM images of complete 3x3 PARs array QWIP-1 devices with s= 1.9µm, p=3.9µm. The air-bridges between two patches have a width of 150 nm.

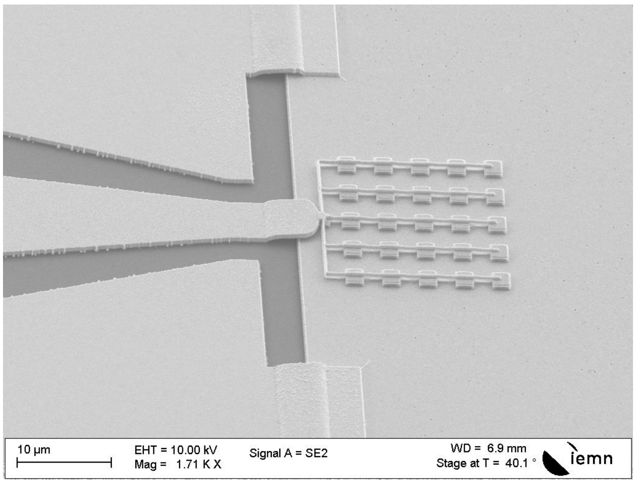

Figure. 4.39 SEM image of complete 5x5 PARs array QWIP-1 devices with s=1.9µm and p=3.9µm.

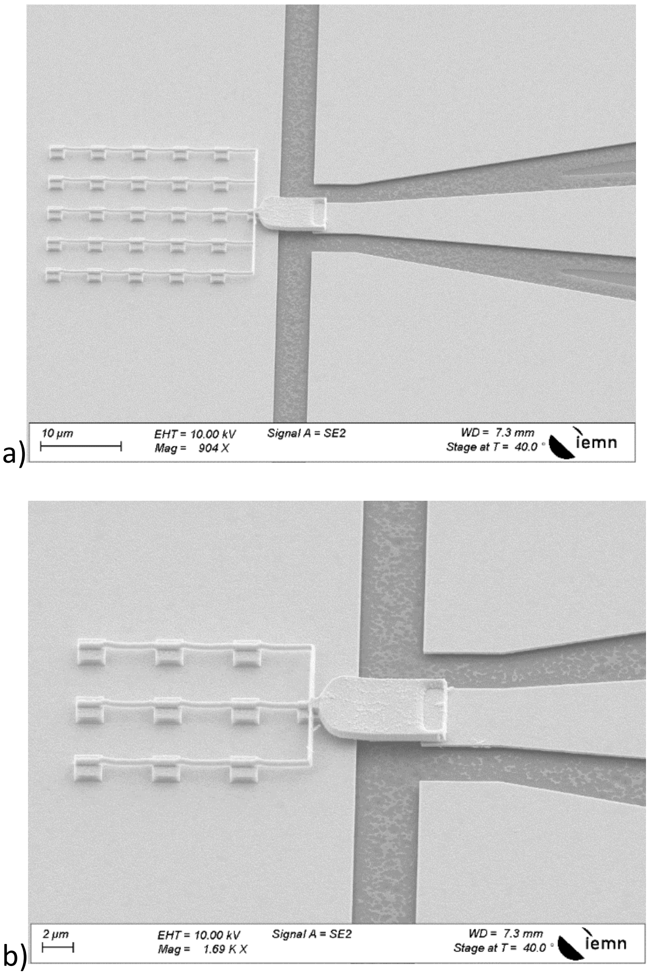

Figure. 4.40 SEM images of the PARs array QWIP-2 devices: a) 5x5; b) 3x3 with s=1.8µm, p=5µm.

In the next chapter, we will present the electro-optics properties of the device: its spectral and dc characterization and its heterodyne frequency response up to 67 GHz.

# Appendix

## A.1 PECVD (Plasma Enhanced Chemical Vapor Deposition)

PECVD includes a top electrode RF driven and a substrate sitting directly on heated electrode [10]. The plasma of reacting gases is generally created by radio frequency (RF) (alternating current (AC)) frequency or direct current (DC) discharge between two electrodes. The vapor of the target material is generated from the chemical reactions occurring in the chamber, and condenses on the substrate from a gas state to a solid state growing thin films on the sample.

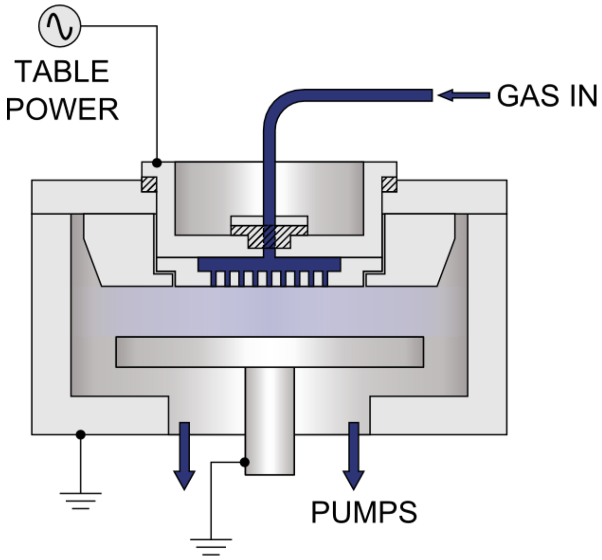

Figure. A.1. The illustration of PECVD machine presented by Oxford [10].

## A.2 Metal deposition

At the laboratory IEMN, we have two methods for metal deposition: sputtering deposition and evaporation.

The sputtering deposition is a physical vapor deposition. The plasma of argon is generated by RF voltage. As shown in Fig. A.2, the target metal is positioned on the cathode of this system, so-called sputtering target. The difference of potential induces the displacement of charged particles of plasma: the positive particles collide to the target, the kinetic energy/momentum of the charged particles is then transferred into the elements of the target causing the sputtering of metal atoms, which grows metallic films on the substrate.

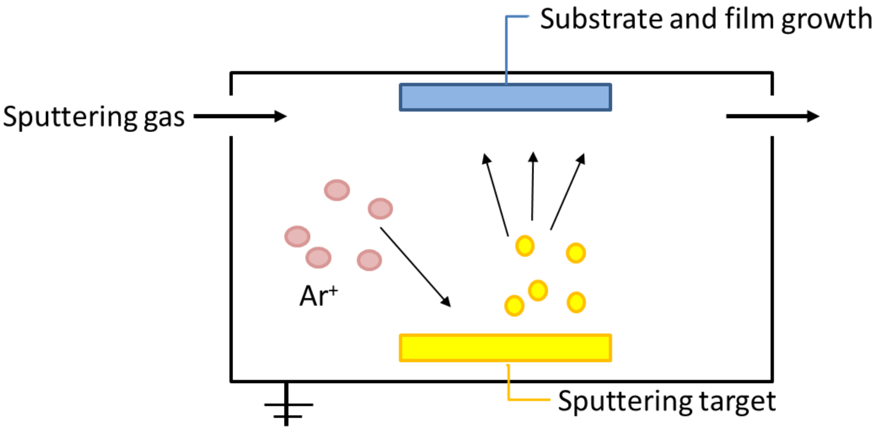

Figure. A.2. The schematic presentation of the sputter deposition.

For the evaporation, the material source is evaporated in a high vacuum (~$10^8$ bar). The target metal achieves its boiling point by the Joule effect, and then is evaporated and condenses on the substrate. In general, there are two methods to heat the metal: by using a resistance passing an intense current or by bombarding the metal with an electron gun.

The sputter deposition allows the metals with a high boiling point to be easily sputtered, while the evaporation of such materials is problematic or impossible. In addition, sputtering deposited films have a composition close to that of the metal source and the adhesion with the substrate is better than the evaporated films. However, the sputtering deposition is more difficult to combine with the lift-off process than the evaporation, because the pressure for sputtering must be high in order to maintain a plasma, which means the free path or the distance between substrate and materials source is much shorter than the evaporation. As a result, the metal atoms would have many collisions with the gases in the chamber before reaching the substrate. The random angle under which they arrive causes more sidewall deposition making the lift-off to be difficult.

## A.3 ICP-RIE (Inductively Coupled Plasma-Reactive Ion Etching)

ICP-RIE is an etching technology involving both chemical reactions and ion-induced etching. ICP source creates a high density plasma by the inductive coupling between the RF antenna and plasma. The antenna, located in the plasma generation region, induces electrons that participate in the ionization of gas molecules and atoms at low pressure by creating an alternating RF magnetic field and RF electric fields. ICP RIE has the separate ICP RF power source connected to the cathode that generates DC bias and attracts ions to the wafer. Materials are etched by chemically reactive plasma under low pressure conditions, potentially combined with ion-induced etching [11].

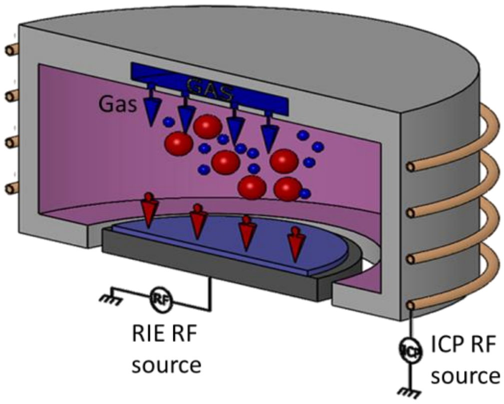

Figure. A.3. The schematic representation of ICP-RIE machine [11].

## A.4 IBE (Ion Beam etching)

Gold is a very stable material that is difficult to etch by chemical methods, however, in our case, we need to etch the gold layer as the desired pattern. Our solution was to etch the gold actively with IBE using Ar+ ions, which act as physical etching mechanisms. In addition, IBE is highly anisotropic and does not etch the part under the mask (resist). The IBE tool we used provided by MeyerBurger consists of an ion source based on a microwave plasma using an electron cyclotron resonance (ECR) architecture [12]. Argon ions are extracted from the plasma and then accelerated toward the target through successive biased grids. To avoid the deleterious effects induced by the accumulation of electric charge on the sample surface, electrons are injected to neutralize the ions beam. The sample is held by rotating support, allowing for tuning the incidence angle of the ion beam to obtain various etch profiles. The etch stop endpoint detection system consists of a secondary-ion mass spectrometer allowing to analysis in-situ and in real-time the composition of the etched material [7] [13].

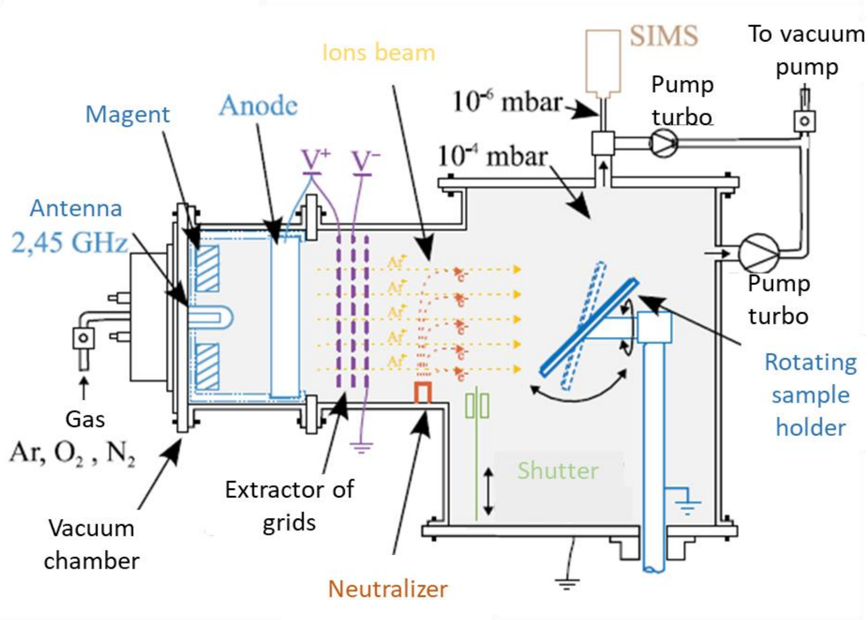

Figure. A.4. Meyer Burger IonSys 500 (RIBE) schematic [7] [13].

# Bibliography

[1] H. Schneider et H. Liu, "Quantum Well Infrared Photodetectors", Berlin Heidelberg New York: Springer, 2007.

[2] Y. N. Chen, . Y. Todorov, B. Askenaz, A. Vasanelli, G. Biasiol, R. Colombelli et C. Sirtori, "Antenna-coupled microcavities for enhanced infrared photo-detection", *APPLIED PHYSICS LETTERS,* vol. 104, no. 031113, 2014.

[3] Y. Todorov, L. Tosetto, J. Teissier, A. M. Andrews, P. Klang, R. Colombelli, I. Sagnes, G. Strasser et S. C, "Optical properties of metal-dielectric-metal microcavities in the THz frequency range", *OPTICS EXPRESS,* vol. 18, no. 13, pp. 13886-13970, 2010.

[4] D. Palaferri et al, "Room-temperature nine-µm-wavelength photodetectors and GHz-frequency heterodyne receivers", *Nature,* 2018.

[5] Coplanar Lines : Coplanar Waveguide and Coplaar Strips.

[6] E. Peytavit, J.-F. Lampin, F. Hindle, C. Yang et G. Mouret, "Wide band continuous-wave terahertz source with a vertically integrated photomixer", *Appl. Phys. Lett,* vol. 95, no. 161102, 2009.

[7] Y. Desmet, "Echantillionnage de signaux rader par voie optoélectronique: étude des non-linéarités des photoconducteurs à cavité résonante", Thèse de dotoral-Université de Lille, Lille, 2018.

[8] M. Taklo, P. Storås, H. Hasting, H. Jakobsen et K. Schjølberg-Henriksen, "Strong, high-yield and low-temperature thermocompression silicon wafer-level bonding with gold", *Journal of Micromechanics Microengineering,* vol. 14, no. 884, 2004.

[9] M. Levinshtein, S. Rumyantsev et M. Shur, "Handbook Series on Semiconductor Parameters", Singapore: World Scientific Publishing Co. Pte. Ltd, 1996.

[10] Oxford, "Plasma Technology", PECVD, [En ligne]. Available: https://plasma.oxinst.com/campaigns/technology/pecvd.

[11] Corial, ICP RIE, [En ligne]. Available: https://www.corial.com/en/technologies/icp-rie-inductively-coupled-plasma-reactive-ion-etching/.

[12] W. Kern, "Thin Film Processes II", *Elsevier,* 2012.

[13] H. Garvin, E. Garmire, S. Somekh, H. Stoll et A. Yariv, "Ion Beam Micromachining of Intergrated Optics Components", *Appl.Opt,* vol. 12, no. 3, pp. 455-459, 1973.

# 5. Ultrafast QWIPs based on patch antennas: electro-optical characterization

## 5.1 Spectral and dc characterization

### 5.1.1 Reflectivity measurements

As we discussed in Section 4.2, five sets of 300µm x 300µm PARs array (fixed patch size s = 1.85µm, w = 150nm) with varying patch periods p = 2.9µm, 3.9µm, 4.9µm, 7.4µm, 9.9 µm were designed and fabricated to investigate the critical coupling condition. One of the realized arrays (p=3.9µm) is presented in Fig. 5.1. The reflectivity spectra measured through Fourier-transform infrared spectroscopy (FTIR) micro-reflectivity are shown in Fig 5.2 (a). These were obtained by (i) measuring the reflectivity on the PARs array area, and (ii) by dividing the latter by the reflectivity spectrum of the pure gold surface. For these measurements the incident electric-field was polarized orthogonally to the connecting bridges. As expected (Eq. 3.65), we find that the reflectivity minimum is period-dependent, and that it is minimized for p= 4-5 µm, yielding a contrast C ~ 0.8 ÷ 0.9. The peak of the absorption is at ~115meV, close to the ISB absorption peak (Fig. 4.4), and with a slight blue shift from short to long period, in a good agreement with the FDTD simulation shown in Fig 5.2 (b).

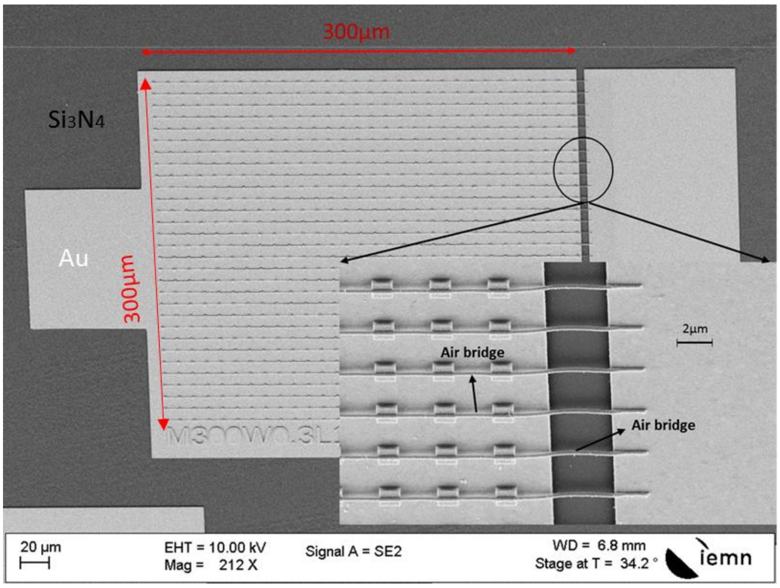

Figure. 5.1. SEM image of a fabricated 300µmx300µm PARs array, used for the reflectivity measurements. Dimension are s = 1.85µm, p = 3.9µm w = 150 nm.

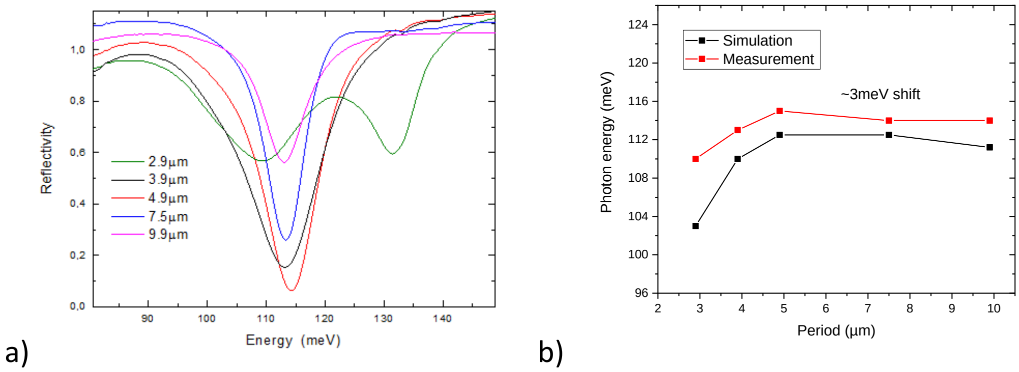

Figure. 5.2. a) Reflectivity spectra for different periods with s = 1.85µm, obtained through FTIR micro-reflectivity. b) Position of the reflectivity minimum *vs* period. Red dots: experimental results (from panel (a)); black dots: simulations (from Fig. 4.9). We observe a systematic 2-3meV shift between measurements and simulations.

### 5.1.2 Spectral response and polarization dependence

Following the results from the reflectivity measurements, we fabricated different sets of 2D PARs arrays with an integrated CPW using the QWIP-1 and QWIP-2 active regions. As discussed in Chapter 4, the sets are the following: a 5x5 and a 3x3 array of square PARs of side *s*=1.85 µm and period *p*=3.9µm. These samples will allow us at the same time to evaluate (i) the minimum array size limit compatible with the spot size of the QCL beam (see below), and (ii) the effect of the array size on the QWIP frequency response (FR).

In the following we will illustrate the full characterization of the sample shown in Fig.5.3, fabricated using the QWIP-1 active region, which consists of a 5x5 periodic array of square PARs of side *s*=1.85 µm and period *p*=3.9µm, sitting on top of a Ti/Au ground plane. In this sample, to minimize the array capacitance, the number of patches is kept to the expected minimum needed to allow collecting 100% of the incident radiation. Indeed, using a knife-edge technique we measured the QCL focused spot size obtained using an AR coated aspheric lens of NA = 0.56 and 5mm focal length, and found a diameter of ~20µm. The patches are electrically connected by suspended metallic bridges of width w = 150nm. As we explained in Section 4.3, for the fabrication of the PARS array we have deliberately chosen Schottky rather than ohmic contacts to avoid the risk of metal diffusion in the QWIP active region due to high temperature annealing, potentially leading to high MIR losses.

We will present the characterizations of this device, including dc and RF characterizations. In this section we focus on the absorption spectra and polarization dependence.

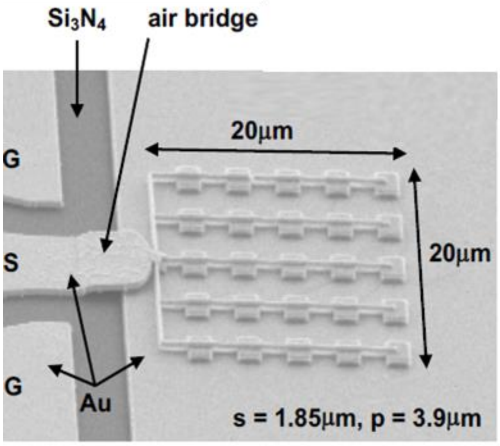

Figure. 5.3. SEM image of the 5x5 PARs array QWIP-1 device with an integrated coplanar waveguide (s=1.85µm; p=3.9µm, w=150nm).

In Fig. 5.4 we report the results of the infrared spectral characterization of the PARs array of Fig. 5.3. Fig. 5.4 (a) shows the absorption $[1\text{-}\mathrm{R}(\omega)]$ spectra at 300K, corresponding to the fraction of the incident power absorbed by the QWIP detector with two orthogonal polarizations of the incident light: orthogonal (black, 90°) and parallel (red, 0°) to the bridges. In good agreement with Fig.5.2 (a) (black line), at the cavity resonance for the orthogonal polarization (116meV – 10.7µm) we find that 90% of the incident photons are absorbed. In this condition, the single PAR collection area at the resonant frequency is given by $0.9\mathrm{x}p^2$ (Eq. (3.64)), yielding a total collection area of ~340µm$^2$ (= (18.5µm)$^2$ ) for the PARs array. As shown in the insets of Fig. 5. 4(a), for the parallel polarization, the spatial distribution of the cavity mode is modified by the presence of the bridges. This yields a blue shift of the cavity resonance, as well as a reduced integrated absorption.

In Fig. 5.4(b), we report the detector photocurrent spectra measured at 77K, represented by the solid lines. These spectra, including those of Fig. 5.4(d), were measured by Raffaele Colombelli and Stefano Pirotta at C2N Laboratory (Palaiseau, France). In Fig.5.4(d), we show the measured photocurrent spectrum at 77K, obtained by FTIR spectroscopy with the QWIP-1 active region (processed in a mesa geometry at +0.25V), which shows the effect of the bare ISB transition (the peak at 107meV). By multiplying this spectrum by the cavity absorptions in Fig. 5. 4(a) we obtain the dashed spectra shown in panel (b), which are in good agreement with the photocurrent spectra. As explained below, this is expected in the approximation where absorption in the resonators is dominated by ohmic losses.

In Fig.5.4(c) we report the polarization dependence obtained by illuminating the QWIP detector with a 10.3µm (120meV) distributed feedback (DFB) quantum cascade laser (QCL) (blue dashed lines in Fig.5.4 (a)(b)(d)): as expected, by changing the polarization from perpendicular (90°) to parallel (0°) to the bridges, the photocurrent goes from a maximum to a minimum.

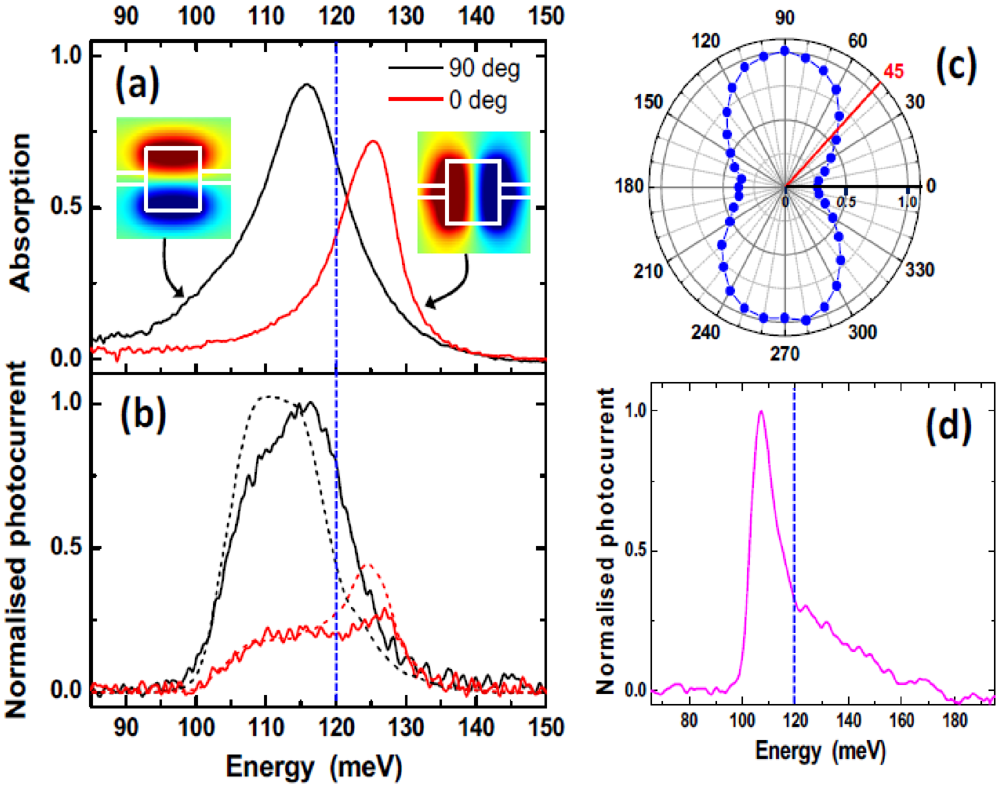

Figure. 5.4. (a) Absorption spectra of the PARs 2D array measured at 300K in two orthogonal polarizations: perpendicular (black) and parallel (red) to the bridges (spectra recorded at 77K, not shown, are virtually identical). The measurements are performed through FTIR micro-reflectivity. Insets. PAR fundamental modes in the two polarizations: computed 2D spatial profiles of the electric field component perpendicular to the surface (blue – positive; red- negative). Plots were obtained using a commercial FDTD solver. (b) Photocurrent spectra measured at 77K in the two orthogonal polarizations (solid lines). Both spectra are normalized to the peak of the photocurrent spectrum at 90°. Dashed lines: spectra obtained by multiplying the spectrum of panel (d) by the absorption spectra of panel (a). (c) Normalized photocurrent vs polarization angle, measured at 300K, with a quantum cascade laser emitting at 10.3µm (120meV – dashed blue lines in panels (a), (b)). The red line indicates the polarization angle (45°) used for the measurements presented in the next Sections. (d) Photocurrent spectrum measured at 77K (Vbias = 0.25V) with the QWIP processed in a mesa geometry. The spectra of panels (b) and (d) were measured by Raffaele Colombelli and Stefano Pirotta at C2N Laboratory (Palaiseau, France).

### 5.1.3 *dc* photocurrent and responsivity under continuous wave laser excitation

For these measurements, the QWIP detector of Fig. 5.3 was placed inside a cryostat which allowed cooling the sample down to 77K. For the *dc* photocurrent measurements the QWIP was biased using a coplanar probe, positioned at the edge of CPW, and a voltage ramp was applied to the device using a Keithley 2400 power supply. To obtain the dc photocurrent vs bias characteristics shown in Fig .5.5 (a) (b), we used a 10.3um (120meV) DFB QCL, driven with a low noise current driver (Koheron, DRV110). The collimated beam from the QCL was focused on the detector using an AR coated aspheric lens (NA = 0.56; 5mm focal length) mounted on a XYZ micrometric stage. For initial alignment the QCL power was modulated using a mechanical chopper and the QWIP detector photocurrent was fed into a transimpedance amplifier followed by a lock-in amplifier. For these measurements, the QCL was polarized at 45° with respect to the bridges (red line in Fig.5.4(c)). As explained in the previous subsection, at 10.3µm we measured a waist diameter of 20µm using a knife-edge technique, i.e. approximately equals to the side of the 5x5 PAR array collection area (0.9x$p^2$: ~ $\sqrt{340\mu m^2}$ , as we explained in Section 5.1.2). Therefore, for the rest of this work, we assume that all the QCL power, measured after the lens, is incident on the QWIP. This corresponds to the power values reported in Fig.5. 5. For each power value in Fig.5.5 (a),(b) we recorded the current, subtracted the dark current, and finally obtained the corresponding photocurrent.

As expected, at 300K the dark current dominates the photocurrent for all power levels. At 77K the situation is reversed, showing that at this temperature the QWIP can be potentially operated in the background photon-noise regime with only a few mW of incident power [1]. At 77K and 3.5-4V (Fig.5.5 (a)) we also observe a pronounced saturation of the photocurrent, that we attribute to negative differential drift velocity, resulting from intervalley scattering [2]. Saturation fields in the 10-20kV/cm range have been found in previous works. Here, at 3.9V (Fig.5. 5(a)) the average electric field is ~100kV/cm, indicating that a large fraction of the applied bias drops on the Schottky contacts.

The photocurrent and responsivity as a function of incident power at 77K and 300K are reported in Fig. 5.5(c), respectively at 3.4V and 2.5V. Responsivities are corrected by the polarization factor (Fig. 5.4(c)), and their value corresponds to the situation where the incident field is polarized orthogonally to the bridges, which is the ideal condition to operate the QWIP. At low power we obtain responsivities R = 1.5A/W and 0.15A/W at 77K and 300K. The decrease of responsivity at 300K is attributed to a decrease of the drift velocity and capture time (see Table 2). Finally, by increasing the power we observe a clear decrease of responsivity at 77K. This is attributed to the presence of the series resistance provided by the Schottky contacts. Indeed, as we shall see in Section 5.2, despite the presence of the Schottky contacts, the equivalent circuits of Figs. 3.29 can still be used to describe the electrical behavior of the QWIP. In this case $R_S$ represents the Schottky junction differential resistance under illumination at the operating point (see Section 5.2). As a consequence, for a given applied bias, the decrease of the detector photo-resistance ($R_0 = \frac{R_d R_{ph}}{R_d + R_{ph}}$ in the circuit of Fig. 3.29) with increasing incident power produces a progressive lowering of the electric field across the QWIP active region [3]. At room temperature Rs is instead negligible (see Section 5.2.4, Table 2), leading to a much less pronounced the saturation effect.

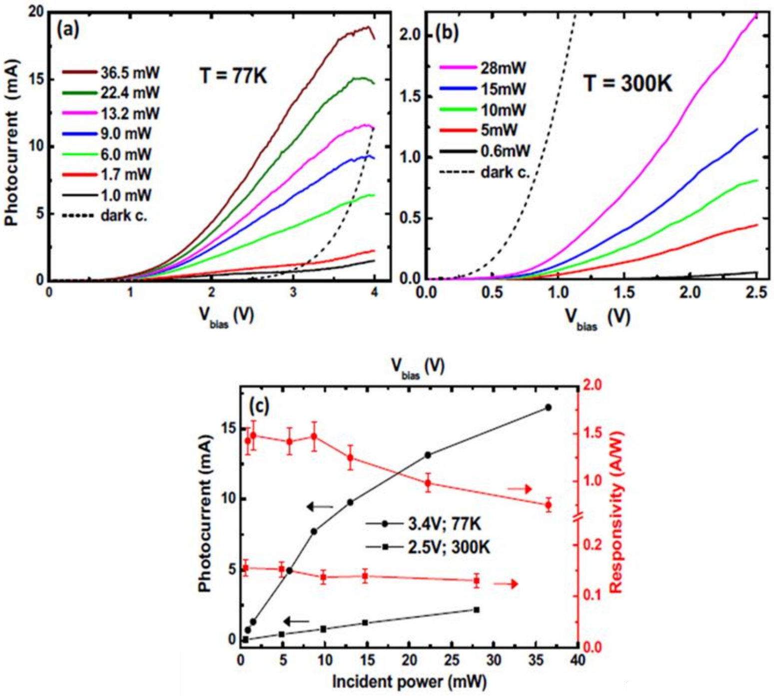

Figure. 5.5. Photocurrent vs applied bias at (a) 77K and (b) 300K for different incident QCL powers. The dark current I/V characteristics are shown in dashed. (c) Photocurrents (black dots) and responsivities (red dots) vs power, measured at 2.5V, 300K (squares) and 3.4V, 77K (circles).

From Eqs. (3.74)(3.76)(3.77), we can derive the responsivity of the PAR array for an incident electromagnetic wave of frequency ω, polarized perpendicularly to the wire bridges:

$$R_{array}\,(\omega) = [1 - \mathrm{R}(\omega)]\left[\frac{B_{isb}(\omega)}{B_{isb}(\omega)+Q_{array}^{-1}}\right]\left[\frac{eg}{\hbar\omega}\right] \quad (5.1),$$

where [1-R$(\omega)$] is the PAR array absorption spectrum shown in Fig. 5.4(a), and $B_{isb}(\omega)$ is the intersubband absorption coefficient of the PAR given by the expression Eq. (3.77). For this device, we compute $B_{isb}(\omega_{12}) = 0.0588$, with $f_w = 0.088$; $\mathrm{E}_p$ =27.5meV; $\mathrm{E}_{21} \approx 107$ meV (extracted from the photocurrent spectrum of Fig.5.4 (d)); $\Delta E \approx 10.7$meV is the FWHM of the ISB transition, which we assume to be approximately equal to 10% of $E_{21}$. $\mathrm{Q}_{array} \approx 8$ is the quality factor of the PAR array (i.e. excluding ISB absorption), that we obtain from the FWHM of [1-R$(\omega)$] (Fig.5.4(a)). This is a good approximation since, due to the spectral shift between $B_{isb}\,(\omega)$ and [1-R$(\omega)$], absorption in the resonators should be dominated by ohmic losses ($B_{isb}(\omega) < Q_{array}^{-1}$). Indeed, results from FDTD simulations performed on a single resonator yield an upper limit of ~15 for the PAR array Q-factor (without ISB absorption). This is smaller than $1/B_{isb}(\omega_{12}) \approx 20$ showing that even without spectral shift, cavity absorption would be dominated by ohmic losses.

Eq. (5.1) can be now used to derive the value of the photoconductive gain g by comparing the responsivity value at 120meV (10.3um) with the experimental value obtained from Fig. 5.5(c) at low power. The responsivity $R_{array}$ (ω), computed from Eq. (5.1) with $g = \tau_c/\tau_{tr}$ =2.5, is shown in Fig.5.6: for $\hbar\omega \approx$120meV, corresponding to the QCL photon energy (λ=10.3µm), we obtain $R_{array}$ =1.5A/W, in agreement with the measured experimental responsivity at 3.4V, 77K and low incident power (Fig.5.5(c)).

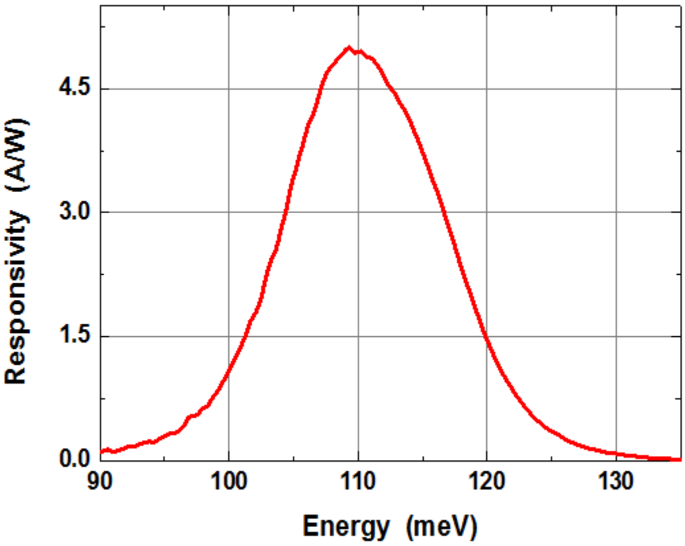

Figure. 5.6. Computed responsivity spectrum from Eq. (5.1).

## 5.2 Frequency response

### 5.2.1 Heterodyne measurement set-up

As illustrated in Section 3.5.2, contrary to dc photocurrent measurements which exploits one single QCL, heterodyne measurement requires two DFB QCLs. The schematic of the heterodyne setup is shown in Fig.5.7. Both QCLs are driven with low noise current drivers (see previous Section), which allows minimizing the linewidth of the heterodyne beat-note to ~ 100kHz. A beam splitter is used to obtain a reference beam allowing the measurement of the QCL power incident on the device, and we exploit an optical isolator to minimize feedback on the QCLs. As for the *dc* photocurrent measurements, a 67GHz RF probe is positioned at the edge of CPW, and lockin-detection is used in order to obtain a perfect overlap of the focused QCL spots on the device. Finally, a dc bias is applied to the PARs QWIP detector through the dc port of a 67GHz bias-T connected to the Keithley power supply. The bias-T ac port is connected to the spectrum analyzer (SA) for the measurement of the heterodyne beat. The frequency of the latter is swept continuously by changing the temperature or the current of the QCLs.

In Fig.5.9 we report two examples of heterodyne beatnote spectra at low incident power recorded in single shot at 77K, under an applied bias of 3V and without any amplification (Fig.5.9(a)), and at 300K, with an applied bias of 1.1V and with a narrow band amplifier of 50dB gain (Fig.5.9(b)). In the first case the noise floor is limited by the SA, while in the second spectrum the noise floor is determined by the amplifiers noise. We find instantaneous linewidths of ~100kHz, limited by the QCL thermal and current fluctuations. At 77K the resolution bandwidth (RBW) is set to 100kHz, yielding a signal-to-noise ratio (SNR) of ~77dB, while at 300K we find a SNR of 72dB with a RBW of 50kHz. Reducing further the RBW produces a decrease of the beatnote intensity because the RBW goes below the instantaneous heterodyne beatnote linewidth.

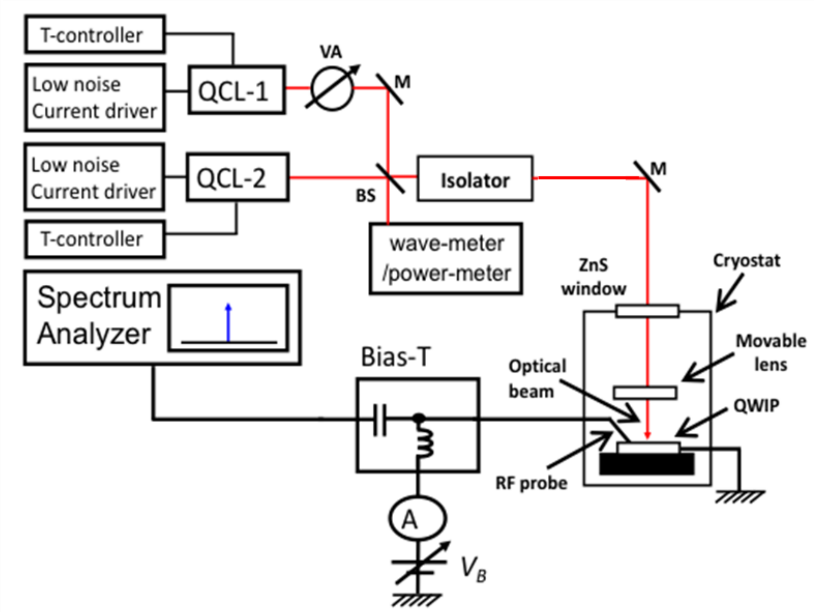

Figure. 5.7. Schematic of the experimental setup used for the measurement of the QWIP FR. VA – variable attenuator; M – mirror; BS - beam splitter.

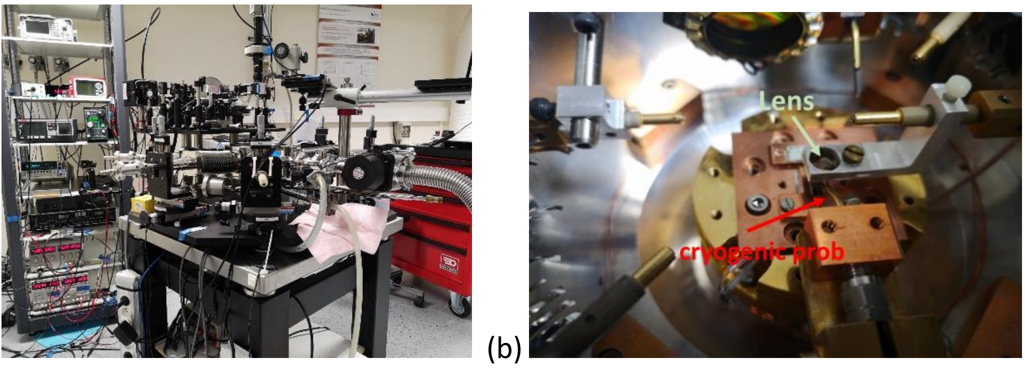

(a) (b)

Figure. 5.8. (a) Photograph of the heterodyne set-up. (b) Inside view of the sample chamber showing the movable focusing lens and RF probe.

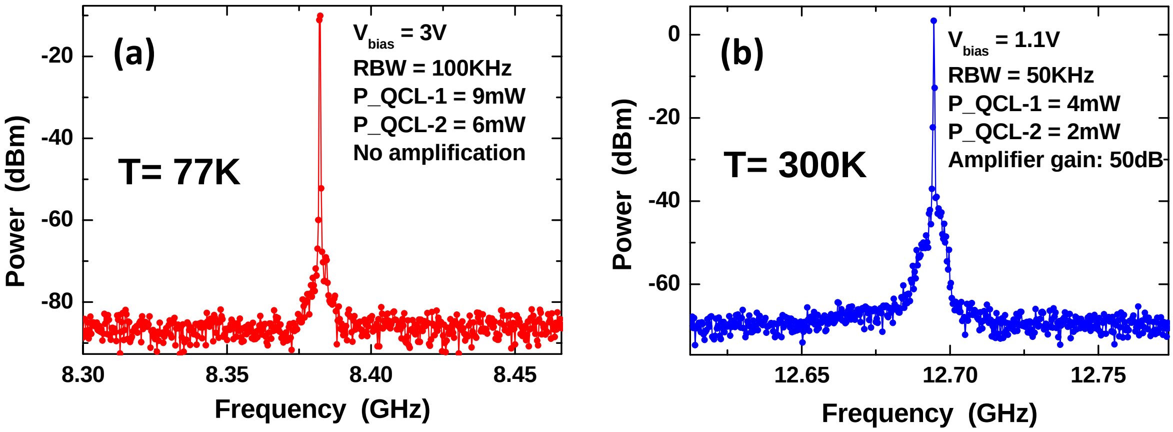

Figure. 5.9. Examples of single shot heterodyne beatnote spectra recorded (a) at 77K without amplification, and (b) at 300K with a low noise, narrow-band amplifier of 50dB gain.

### 5.2.2 Electrical circuit model of PARs QWIP

Before proceeding with the measurement of the PARs QWIP FR we should develop a circuit model of the detector that includes the Schottky contacts. This will allow us to properly model and analyze the detector's FR.

When the detector is under bias, one Schottky contact is polarized in reverse and the other is in forward. In the following we consider the forward biased contact as a short-circuit. The full electrical circuit is shown in Fig. 5.10(a) and is obtained from the circuit of Fig. 3.28 by replacing the series contact resistance $R_s$ in parallel with a capacitance $C_s$ with the reverse biased Schottky contact. From this circuit, by appropriately linearizing the Schottky junction IV curve, a small-signal ac circuit (at $\omega = \omega_b$) and a dc circuit ($\omega = 0$) can be derived (see Fig. 5.11), formally identical to those presented in Fig. 3.29. This linearization is done by defining as $R_S$ the Schottky junction differential resistance under illumination at the operating point $(I_{dc}, V_s)$: $1/R_S = dI/dV|_{I_{dc},V_s}$. Then, as shown in Fig.5.10 (b), the Schottky IV curve (red line) can be approximated by a linear characteristic $I = (V - V_t)/R_S$ (green line) passing through $(I_{dc}, V_s)$ for $V > V_t$, while for $V < V_t$ we consider the Schottky as an open circuit ($I = 0$). The threshold voltage $V_t$ can then be incorporated in the voltage source of the *dc* circuit (Fig.5.11(b)) by writing that $V_0 = (V_{bias} - V_t)$ for $V_{bias} > V_t$, and $V_0 = 0$ for $V_{bias} < V_t$ ($V_{bias}$is the bias effectively applied to the device, see Fig. 5.10 (a)). Clearly, both $V_t$ and $R_s$ will depend on the value of the QWIP point of operation under illumination.

As defined in Section 3.5.3, in the circuits of Fig.5.11, $R_{ph}$ is the internal photo resistance given by the ratio between the *dc* bias voltage, $V_{dc}$, applied to the QWIP and the *dc* (i.e. average) conduction photocurrent, $I_{ph}$, generated by the two laser sources; $R_d$ is the QWIP dark resistance, and $R_0 = R_d //R_{ph}$. The latter corresponds to the QWIP photoresistance under illumination. $C_s$ is the Schottky contact capacitance, and $C_{PAR}$ is the PARs array capacitance. The current source $I_s$ is given by Eq. (3.116).

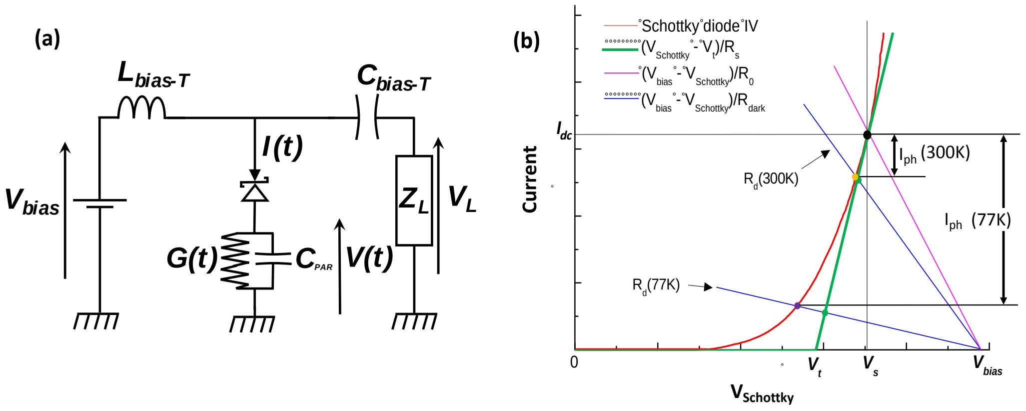

Figure. 5.10. (a) Electrical circuit model of the heterodyne mixing experiment. (b) Schematic Schottky diode IV characteristic in reverse breakdown (red). Linearised Schottky diode IV characteristic (green). Load lines under illumination (pink) and in the dark (blue), obtained from the circuit of Fig.5.11 (b). Operating point under illumination (black circle) and in the dark at 300K (orange circle) and 77K (purple circle). For simplicity, but without loss of generality, we have neglected the temperature dependence of the Schottky IV characteristic.

The purple line in Fig. 5.10 (b), corresponds to the load line of the QWIP under illumination, obtained from the circuit of Fig.5.11, with a slope given by $1/R_0$. The blue lines are instead the load lines of the PARs array in the dark at 300K and 77K, with slopes given by $1/R_d$.

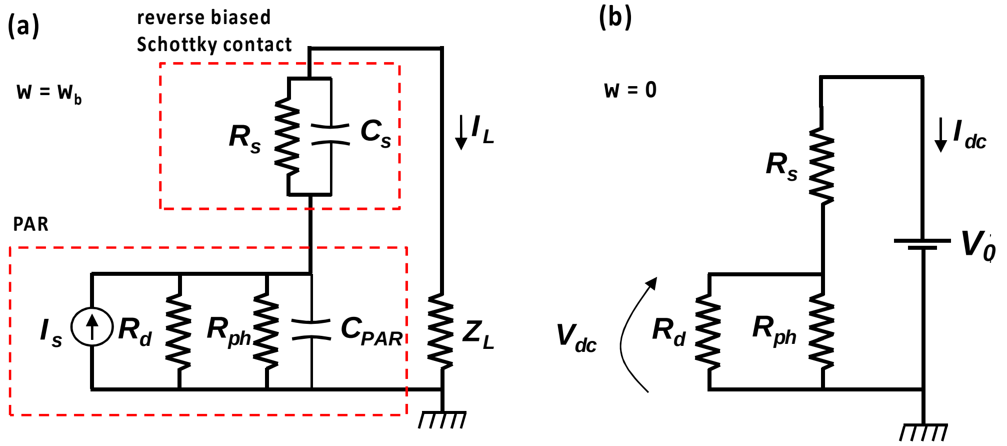

Figure. 5.11. Electrical circuit model of PARs QWIP. (a) Equivalent small-signal *ac* circuit ($\omega = \omega_b$). (b) Equivalent *dc* circuit ($\omega = 0$).

At 300K the QWIP current under illumination is dominated by the dark current component, as can be seen from Fig.5. 5(b) (see also Fig. 5.12(b), (d)). In other words $R_d \sim R_0$, and the change of slope of the load line from illumination to dark (Fig. 5.10(b)) is small, i.e. the linearization of the Schottky IV through $R_s$ is a good approximation. At 77K, the QWIP current under illumination is instead dominated by the photocurrent component (Fig.5.5 (a) and Fig.5.12 (a),(c)), i.e. $R_d$ >> $R_0$ , $R_s$, resulting into a large change of slope of the load line (Fig.5.10(b)). In this case, by linearizing the Schottky using its resistance under illumination, we completely neglect the fact that in the dark the slope of the Schottky IV is much larger. On the other hand, as shown schematically in Fig.5.10(b), the larger is $R_d$ the smaller will be the slope of the load line, thus reducing the difference between the effective dark current and the dark current obtained through the *dc* circuit model (purple and green circles).

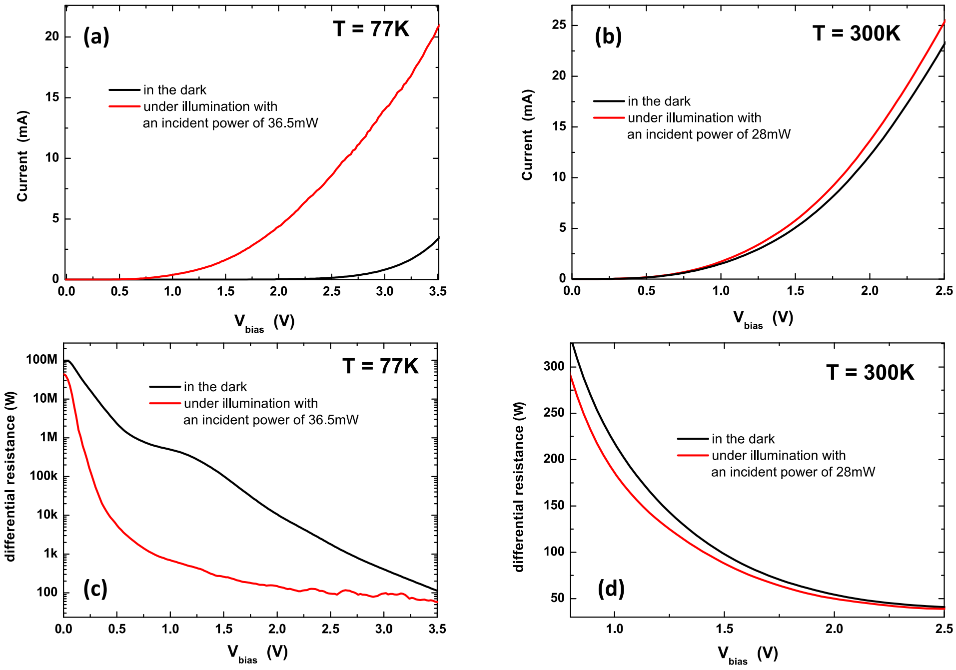

Figure. 5.12. (a),(b) Current under illumination and in the dark at 77K and 300K. (c),(d) Differential resistance under illumination and in the dark at 77K and 300K.

### 5.2.3 Measurement and analysis of PARs QWIP impedance

As we shall see in the next Section, determining the QWIP impedance is essential to interpret the device FR. To this end, we used a VNA analyzer to measure the device $S_{11}$ parameters. At T=77K, the $S_{11}$ parameters were measured under the same operating conditions (bias, temperature and illumination) used to record the FRs, while at 300K they were measured in the dark. This last choice stems from the fact that, as explained in the previous Section, contrary to 77K, at 300K the dark current is much larger than the photocurrent even under illumination at high power (Fig. 5.5(b)) i.e. the QWIP impedance under illumination is very well approximated by the dark impedance ( $R_d \ll R_{ph}$, see Fig.5. 11 (a)).

In Fig.5.13 we report the real and imaginary parts of the QWIP impedances vs frequency (black and red lines) obtained from the $S_{11}$ parameters, after de-embedding the 50Ω integrated coplanar line. We find that, for the chosen PAR array size, at high bias (3.4V; 77K and 2.5V; 300K– Fig.5.13(c),(d))) the QWIP impedance is virtually impedance-matched to 50Ω at any frequency. This is the case also at low bias (1.1V; 77K and 0.9V; 300K – Fig.5.13 (a), (b))) for frequencies ≳20GHz (at 300K) and 30GHz (at 77K).

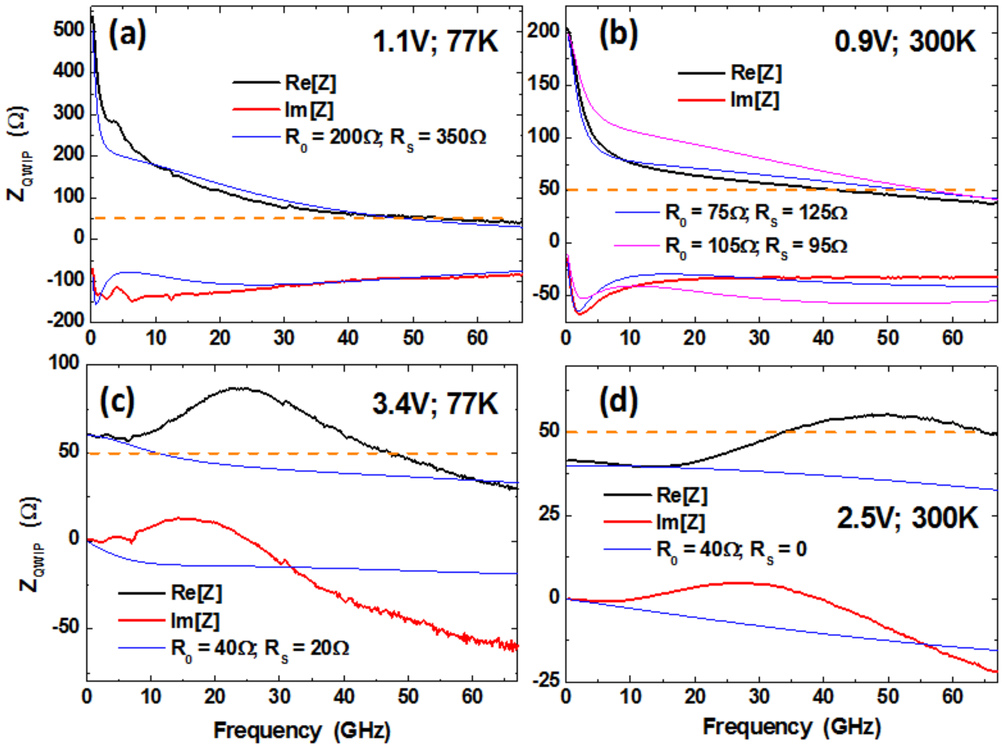

Figure. 5.13. Real (black) and imaginary (red) parts of the QWIP impedance. The measurements at 77K (panels (a), (c)) were recorded under illumination with a power P$_{tot}$= P$_1$+P$_2$=33.5mW. The measurements at 300K (panels (b),(d)) were done in the dark. The blue and purple lines represent the impedance computed from the small-signal equivalent circuit.

The impedances at low biases (Fig.5.13 (a),(b)) are well reproduced by the equivalent circuit of Fig.5.11(a), where the QWIP impedance (blue lines) is given by the sum of the PAR array and Schottky contact impedances:

$$Z_{QWIP}(\omega_b) = \frac{R_0}{1+i\omega_b R_0 C_{PAR}} + \frac{R_S}{1+i\omega_b R_S C_S} \quad (5.2).$$

Here, $Z_{QWIP}(\omega)$ is computed using the values of $R_0$, $R_S$- reported in the first and second column of Table 2 (Section 5.2.4), with $C_{PAR} = 30\text{fF}$ and $C_S$= 0.7pF (see also Section 5.2.5). In particular, when $f \rightarrow 0$, we see clearly the effect of $C_S$, producing a fast increase of the real part of $Z_{QWIP}(\omega_b)$, until, at $f_b = 0$ ( $f_b = \omega_b/2\pi$ ), $Re[Z_{QWIP}(\omega_b = 0)] = R_0 + R_s$ . At higher frequencies ( $f_b \gg$

$(2\pi R_s C_s)^{-1}$), $R_S$ is shunted by $C_s$, and $Z_{QWIP}(\omega_b)$ coincides with the impedance of the PAR array, with a roll-off corresponding to a time constant equal to $R_0 C_{PAR}$(first term in Eq.(5.2)). As shown in Fig.5.13 (c),(d), at high biases the QWIP impedances change completely. Firstly, the fast increase as $f_b \rightarrow 0$, disappears, which we interpret as the evidence that the Schottky junction becomes more transparent, i.e. $R_s$ shunts $C_s$ at all frequencies. At higher frequencies both the real and imaginary parts of $Z_{QWIP}(\omega_b)$ show a maximum, followed by a slow decay. As shown by the blue lines this behavior cannot be fully reproduced by our simple circuit model using the parameters reported in the third and fourth column of Table 2. In particular the imaginary part becomes inductive around 15-30 GHz. This phenomenon is probably linked to the fact that the QWIP is operated close to the onset of intervalley scattering. A more detailed analysis is needed, which is beyond the scope of this work.

Finally, in Fig. 5.14 we report the measured load impedance, $Z_L$, i.e. the impedance seen by the QWIP in the plane of the coplanar probes. As for the QWIP impedance, this was extracted from $S_{11}$parameter measurements. As can be seen, $Z_L$ can be approximated by its real part $Re[Z_L] = R_L \cong 50\Omega$.

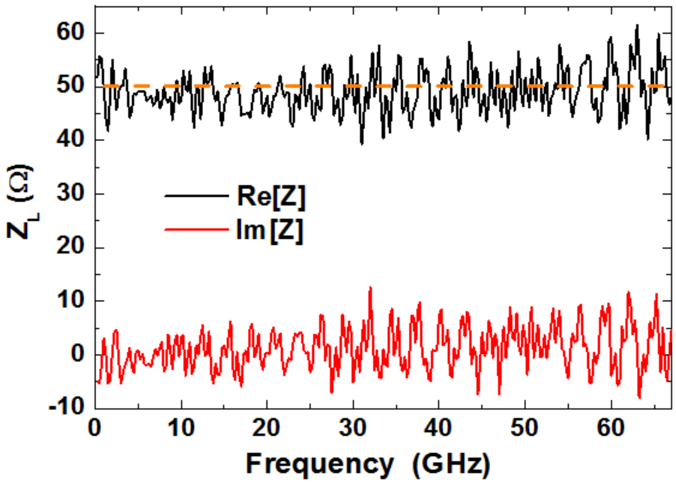

Figure. 5.14. Real and imaginary part of the impedance seen by the QWIP in the plane of the coplanar probes ($Z_L$).

### 5.2.4 Measurement and analysis of PARs QWIP frequency response

To obtain the FR, the current of one QCL was kept constant while the current and temperature of the second one were fine-tuned in order to sweep the heterodyne beat frequency in the range 0-67GHz. The heterodyne beat note is recorded by setting the SA in max hold trace mode. In Fig. 5.15 the powers incident on the QWIP from the two QCLs are $P_1$ = 27.5mW and $P_2$ = 6mW (33.5mW total), and each vertical line corresponds to a heterodyne beat between the two QCLs (NO amplifier was used in these measurements). From the spectrum of Fig.5. 15(a), to extract the QWIP FR we proceed as follows. First, using a VNA analyzer we measure the power attenuation from the QWIP to the SA, due to the insertion loss in the probes, cables and bias-tee (red dots in Fig.5.15 (a)). This curve is then corrected to include the power variation of the QCL due to the frequency tuning. The resulting blue dotted curve in Fig. 5. 15(a) is finally subtracted by the raw heterodyne spectrum, yielding the spectrum shown in Fig.5.15 (b). Here, the black circles, corresponding to the line peaks recorded every 500 MHz give the QWIP FR. We note that the heterodyne spectra were recorded with a RBW of 3.5MHz. This is larger than the actual heterodyne beat linewidth, therefore guaranteeing that the intensity of the heterodyne beats is not reduced by the SA filtering.

In Fig.5.16 we report 3 other heterodyne spectra, used to extract the FRs of QWIP-1 detector (Fig. 5.3) and obtained at representative operating conditions: 300K, 0.9V - 77K, 1,1V - 77K, 3.4V. The dependence of the SNR on the heterodyne beatnote frequency, can be directly extracted from the spectra. At 30GHz and 60GHz, with a RBW of 3.5MHz, we obtain SNRs of 50dB and 35dB, and of 35dB and 25dB, respectively at 77K (3.4V) and 300K (2.5V).

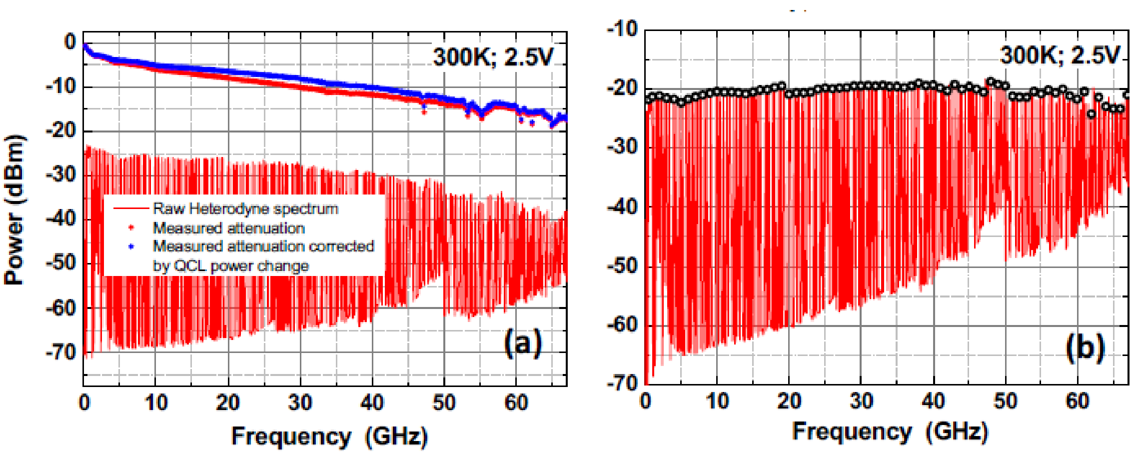

Figure. 5.15. Example of extraction of the FR of the QWIP-1 detector (Fig.5.3) at 300K-2.5V. (a) Raw heterodyne spectrum, collected with the SA set in max-hold trace mode, with a RBW of 3.5MHz (red solid line). Measured attenuation due to the insertion loss in the probes, cables and bias-tee (red dots, in dB). Measured attenuation corrected by the QCL power change (blue dots, in dB). (b) Heterodyne beat spectrum obtained by subtracting the blue dotted trace in panel (a) from the raw heterodyne spectrum. The black circle corresponds to the data of RF after all corrections.

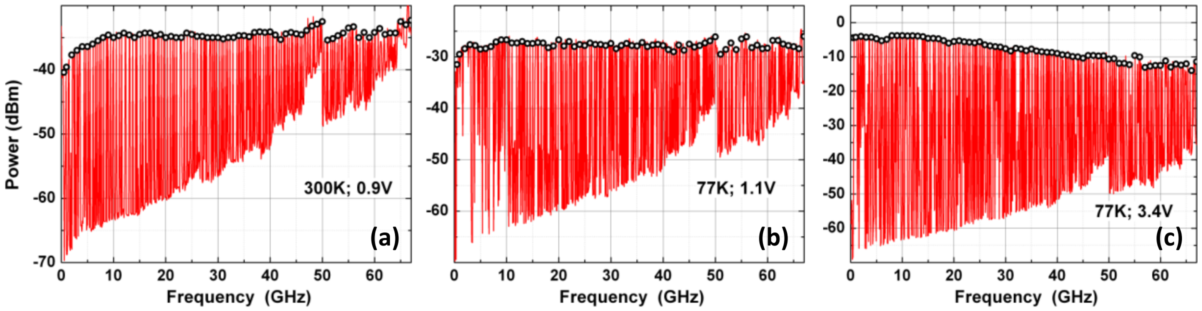

Figure. 5.16. Heterodyne beat spectra of the QWIP-1 detector (Fig.5.3) corrected by the attenuation and QCL power change, following the same procedure used to obtain the spectrum of Fig.5. 15 (b). The black dots are those displayed in Fig.5.17: (a) 300K, 0.9V. (b) 77K, 1,1V. (c) 77K, 3.4V.

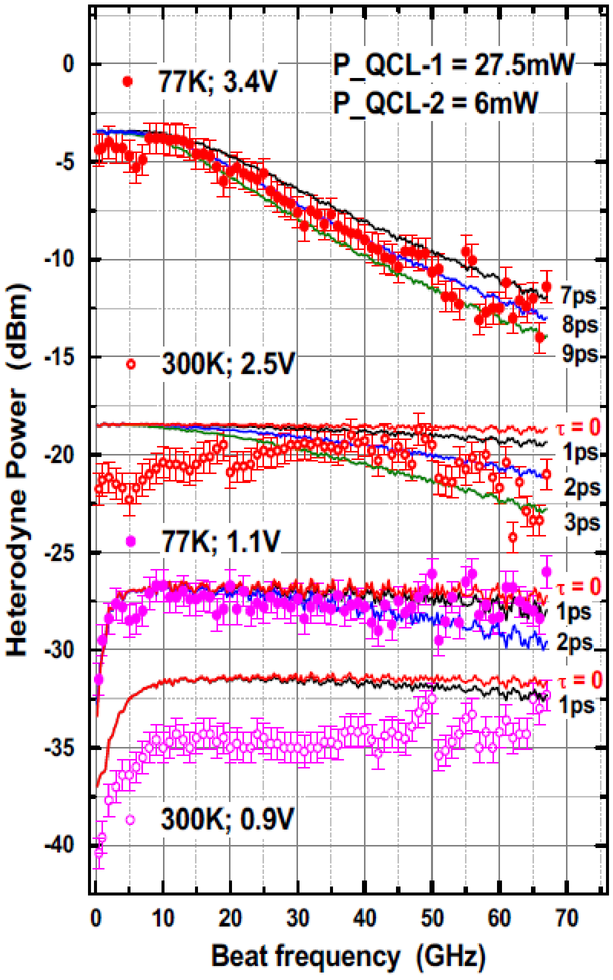

Figure. 5.17. QWIP-1 detector (Fig.5.3) FRs at different temperatures and biases (dotted curves) extracted from the spectra of Fig.5.15 and Fig.5.16. The incident powers from the two QCLs are $P_1$ = 27.5mW and $P_2$ = 6mW (33.5mW total). The spectra are corrected by the attenuation from the QWIP to the SA, measured with a VNA analyzer. The solid lines correspond to fits obtained using the small-signal circuit model for different carrier's lifetimes.

In Fig. 5.17 we report the complete set of FRs of the QWIP detector, which, we recall, was fabricated using the QWIP-1 active region. The FRs correspond to the black dots shown in Fig. 5.15 and Fig. 5.16. The top two traces in Fig.5.17 show the detector FR at high bias, i.e. 3.4V (77K) and 2.5V (300K). From Fig.5.5(c), the corresponding responsivities are ~0.75A/W and ~0.13A/W. At 77K we find a monotonic decrease with frequency, with a 3dB-cutoff frequency of ~30GHz, while at 300K the response is much flatter, with a ~2dB increase from 0 to ~40GHz, followed by a 3dB drop at ~67GHz. At low biases the shape of the FR is rather different. As shown by the two bottom traces, recorded at 1.1V(77K) and 0.9V(300K), the FR is virtually flat up to 67GHz, except at low frequencies where we observe a pronounced drop below ~5GHz(77K) and ~10GHz(300K).

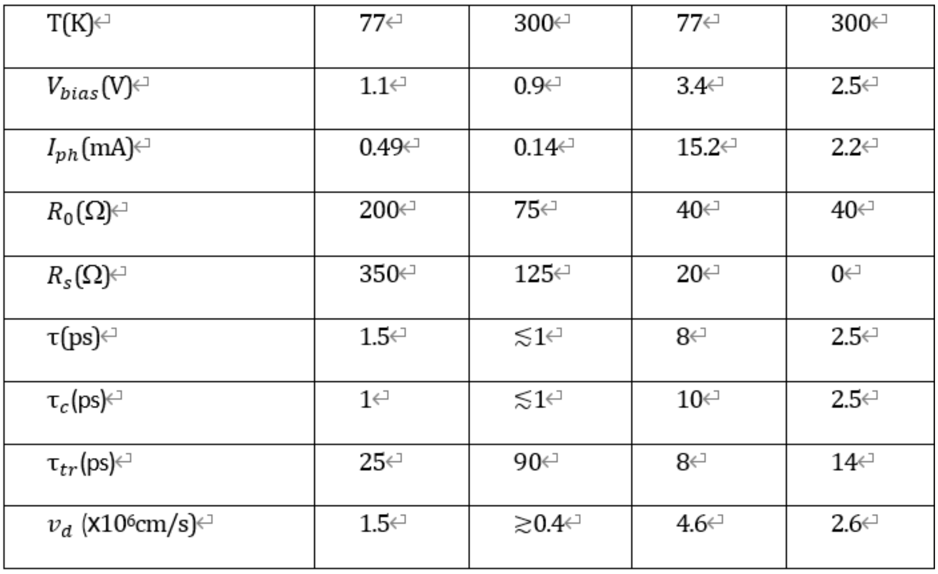

| T(K) | 77 | 300 | 77 | 300 |
|---|---|---|---|---|
| $V_{bias}$(V) | 1.1 | 0.9 | 3.4 | 2.5 |
| $I_{ph}$(mA) | 0.49 | 0.14 | 15.2 | 2.2 |
| $R_0$(Ω) | 200 | 75 | 40 | 40 |
| $R_s$(Ω) | 350 | 125 | 20 | 0 |
| τ(ps) | 1.5 | $\lesssim$1 | 8 | 2.5 |
| $\tau_c$(ps) | 1 | $\lesssim$1 | 10 | 2.5 |
| $\tau_{tr}$(ps) | 25 | 90 | 8 | 14 |
| $v_d$ (X10$^6$cm/s) | 1.5 | $\gtrsim$0.4 | 4.6 | 2.6 |

**Table 2.** Measured photocurrents ($I_{ph}$) and small-signal circuit resistances under illumination ($R_0$, $R_s$), used to compute the solid lines in Fig. 5.17 for different operating conditions (bias and temperature). The value of the roll-off time constant is the one yielding the best fit of the experimental data. The capture time ($\tau_c$) and transit time ($\tau_{tr}$) are obtained from τ and the photoconductive gain. The corresponding drift velocity ($v_d$) is obtained from the ratio between the thickness of the QWIP active region (365nm) and $\tau_{tr}$.

From the small-signal circuit of Fig.5.11, the QWIP FR can be obtained from the expression of the power dissipated into the load resistance $Z_L \approx 50\Omega$ (see Fig. 5.14), which is equal to the input impedance of the SA:

$$P_L = \frac{1}{2}\mathcal{R}e[Z_L] \cdot |I_L|^2 = \frac{1}{2} R_L \cdot |I_L|^2 \quad (5.3).$$

From this last equation, using the values of $R_0$, $R_s$ and $I_{\text{ph}}$ (i.e. the average dc photocurrent generated by the two QCLs) shown in Table 2, we obtain the solid lines shown in Fig.5.17, plotted for different values of the carrier's intrinsic lifetime. As explained in Section 3.5.3 (Eq.3.116), the latter is present in the current source $I_S$ ($I_s = \frac{m}{\sqrt{1+(\omega_b\tau)^2}} I_{ph} \frac{R_d+R_s}{R_d}$) of the QWIP small-signal equivalent circuit (Fig. 5.11 (a)).

The solid curves corresponding to the two bottom FRs in Fig.5.17 (low bias) are obtained using (i) $R_0$ =200Ω, $R_s$=350Ω, for the spectrum at 1.1V (77K) with $I_{\text{ph}}$ =0.49mA and $\tau$ =1- 2ps; and (ii) $R_0$ =75Ω, $R_s$=125Ω, for the spectrum at 0.9V (300K) with $I_{\text{ph}}$ =0.14mA and $\tau$ ~1ps (see Table 2, 1st and 2nd column). Despite the fairly simple electrical model and the measurement uncertainties, the agreement with the experimental FRs is very good, both in terms of absolute power and spectral shape. In particular the observed drop at low frequency reflects the additional conversion losses due to the heterodyne power dissipated in $R_S$ when $f_b \lesssim (2\pi R_s C_s)^{-1}$. At higher frequencies $R_S$ is instead shorted by $C_S$, thus eliminating the power loss in the contact resistance. In this case, from the small-signal circuit model, we have that:

$$I_L = I_S \frac{1}{1+R_L/R_0+i\omega_b R_L C_{PAR}} \qquad (5.4)$$

yielding a parasitic roll-off time constant $R_L C_{PAR}/(1+R_L/R_0) \lesssim$1ps ($R_L = Re[Z_L] \cong 50\Omega$, see Fig.5.14).

At high biases the effect of $C_S$ is much less pronounced and the power drop at low frequencies disappears (Fig.5.17, top two spectra). From the small-signal circuit this can be explained by a reduction of $R_S$ due to the Schottky barrier becoming more transparent, therefore effectively shunting $C_s$ at low frequencies. As a result, the QWIP impedance does not display the strong increase at low frequency found at low biases (see Fig. 5.13(c), (d)).

From the small-signal circuit we find a good agreement with the measured FRs for the spectrum at 3.4V (77K) using $\tau$ ~ 8ps, spectrum at 2.5V (300K) with $\tau$ ~2-3ps and $I_{\text{ph}}$ =2.2mA (see Table 1, 3d and 4th column). We note that our small signal circuit model does not explain the ~2dB increase in the FR from 0 to ~40GHz observed at 2.5V.

As shown above, thanks to the very small device capacitance, by fitting the measured FRs using the small signal circuit model we can extract the intrinsic detector response times, which, as shown by the solid curves in Fig.5.17, dependent on the operating conditions. From the values of $\tau$ and from the photoconductive gain derived from the responsivities, we can then obtain the values of $\tau_c$ and $\tau_{tr}$ shown in Table 2 (see Section 5.2.6 for the derivation): except at 77K under high bias, the QWIP intrinsic response time appears to be dominated by electron capture. We also find the expected decrease/increase of $\tau_{tr}$ with increasing bias/temperature [4]. Interpreting the dependence of $\tau_c$ on bias and temperature is beyond the scope of this work and will require more systematic measurements that are presently under way. At the same time, on this subject there appears to be a lack of experimental data in the literature [5].

### 5.2.5 Determination of small-signal circuit parameters

The various elements, $R_0$, $R_s$, $C_{PAR}$ and $C_s$ in the circuit of Fig. 5.11 depend in principle on the QWIP operating temperature, bias, and illumination conditions. Concerning the capacitance, we fix $C_{PAR}$ = 28fF, i.e. the static capacitance of the PARs array. $C_s$ is instead determined by fitting the decay of the experimental FRs at low frequency (see below), yielding $C_s \approx 0.7pF$. We note that this value is in agreement with the theoretical capacitance expected for a Au/GaAs Schottky junction with a doping density of 4x10$^{18}$ cm$^{-3}$ (~15nm depletion region width) [5].

To determine the values of $R_0$ and $R_s$, we rely on the experimental FR spectra displayed in Fig.5.17 and on the corresponding QWIP impedances shown in Fig. 5.13. The first equation used is given by:

$$R_0 + R_s = Re[Z_{QWIP}(\omega_b = 0)] \quad (5.5).$$

The second equation is given by Eq. (5.3). As pointed out in the previous Section, in Eq.(5.3) the load current $I_L$ depends on the source current $I_s$ (Fig. 5.11(a)), given by Eq. (3.116): $I_s = \frac{m}{\sqrt{1+(\omega_b\tau)^2}} I_{ph} \frac{R_d+R_s}{R_d}$. Here the dark resistance $R_d$ can be de facto eliminated as independent variable, by noting that at 300K $R_d \approx R_0$, while at 77K $R_d \gg R_s$. As a result $P_L$ in Eq. (5.3) depends only on $R_0$ and $R_s$, and by comparing it with the power levels in the FRs of Fig.5.17, gives the second equation, which, together with Eq. (5.2), allows the determination of the QWIP ($R_0$) and Schottky ($R_s$)resistances separately.

The details of the calculations of the circuit elements, respectively at low bias ($V_{bias}$ = 1.1V, 77K, and $V_{bias}$ = 0.9V, 300K) and high bias ($V_{bias}$ = 3.4V, 77K, and $V_{bias}$ = 2.5V, 300K) are given below. The values of the measured *dc* photocurrent of the QWIP, $I_{ph}$, and the values obtained for $R_0$ and $R_s$ at the different operating points are reported in Table 2 below.

**<u>Low bias</u>**

We start by assuming to be at a sufficiently high frequency such that $R_S$ is shunted by the parallel capacitance $C_s$ ($f_b \gg (2\pi R_s C_s)^{-1}$) and can therefore be neglected (see Eq. (5.2)). Therefore, we have that the current on the load presented in Eq. (5.4), where we have approximated $Z_L$with its real part $R_L \cong 50\Omega$. Now, provided that the frequency is not too high, e.g. $f_b \approx 10\text{GHz}$, the last term at the denominator can also be neglected thanks to the extremely low value of $C_{PAR}$ (note: the validity of these last two assumptions can be verified *a posteriori* from the values of $R_0$ and $R_s$). The power dissipated into the load is then given by:

$$P_L = \frac{1}{2} I_S^2 R_L \left[\frac{R_0}{R_0+R_L}\right]^2 \quad (5.6).$$

At T=77K we have that $R_d \gg R_s$, hence, from Eq. (3.116), we have that $I_s \approx m \times I_{ph} = 0.38\text{mA}$ (at $f_b \approx 10\text{GHz}$, $\omega_b \tau$~0). At this point Eq. (5.6) can be used to determine the value of $R_0$ by comparing $P_L$ with the measured value of the FR at 10GHz (1.1V, 77K curve in Fig. 5.17). The value of $R_s$can finally be obtained from Eq. (5.5) with $Re[Z_{QWIP}(\omega_b = 0)] = 550\Omega$ (see Fig. 5.13(a)). We find $R_0 = 200\Omega$ and $R_S = 350\Omega$ (first column of Table.2).

The last step consists in determining the value of $C_s$. This is obtained by fitting the decay of the experimental FR at low frequency (see Fig.5.17), yielding $C_s \approx 0.7pF$. The computed QWIP impedance is represented by the blue curves in Fig.5.13 (a), showing a good agreement with the impedance derived from the $S_{11}$ parameter. Also, the computed FR using Eq. (5.3) reproduces very well the experimental one as shown in Fig.5.17 for τ~1ps.

Concerning the measurement at T=300K and 0.9V, we have that $R_\text{d} \approx R_0$. In this case, from Eq. (3.116) and Eq. (5.6) we obtain:

$$P_L = \frac{1}{2} m^2 I_{ph}^2 \left[\frac{R_0+R_s}{R_0}\right]^2 \left[\frac{R_0}{R_0+R_L}\right]^2 R_\text{L} = \frac{1}{2} m^2 I_{ph}^2 \left[\frac{R_0+R_s}{R_0+R_L}\right]^2 R_\text{L} \quad (5.7),$$

where, again, we used the fact that at $f_b \approx 10\text{GHz}$, $\omega_b \tau$~0. In this last equation the term $R_0 + R_s$is known from Eq. (5.5) and Fig. 5.13 (b) ($R_0 + R_s = Re[Z_{QWIP}(\omega_b = 0)] = 200\Omega$). Then, again, $R_0$ is determined by comparing $P_L$ in Eq. (5.7) with the measured value of the FR at 10GHz (0.9V, 300K curve in Fig.5.17). From this procedure we obtain $R_0 = 105\Omega$ and $R_S = 95\Omega$, which, however, do not allow to reproduce the QWIP impedance in a satisfactory way, as shown by the purple traces in Fig.5.13(b) (here we used $C_s = 0.7\text{pF}$). We find that the values $R_0 = 75\Omega$ and $R_S = 125\Omega$, allow to obtain the closest agreement between the FR and $P_L$, compatibly with a good fit of the QWIP impedance (blue traces in Fig.5.13 (b)). The resulting computed FR, shown in Fig.5.17, is ~2dBm above the measured FR. This spectrum was obtained with $C_s = 0.7\text{pF}$, yielding, as for the 77K, 1.1V FR, a decay at low frequency in good agreement with the measurement.

**High bias**

As already pointed out, at high bias we don't observe anymore the drop in the FR as $f_b \rightarrow 0$. In other words, $C_s$ is shunted by $R_s$, which can be taken as the Schottky contact impedance at virtually all frequencies. As we did at low bias, we also assume that the frequency is sufficiently low that $2\pi f_b R_0 C_{PAR} \ll 1$ (e.g. $f_b$ = 1GHz). Under these assumptions we have that with $I_L = I_s \times R_0/(R_0 + R_S + R_L)$, yielding:

$$P_L = \frac{1}{2} I_s^2 R_L \left[\frac{R_0}{R_0+R_S+R_L}\right]^2 \quad (5.8),$$

where, as usual, $R_0 + R_s = Re[Z_{QWIP}(\omega = 0)]$.

At T=77K, since $R_d \gg R_s$, we have that $I_s \approx m \times I_{ph} = 11.7mA$, and $R_0 + R_s = 60\Omega$ (see Fig.5.13(c)). By using $P_L$ from Eq. (5.8) to fit the value of the measured FR at 1GHz (3.4V, 77K curve in Fig 5.17) we obtain $R_0 = 40\Omega$ and $R_s = 20\Omega$. As shown in Fig.5.17, from Eq. (5.3) we obtain an excellent agreement with the measured FR using τ ~8ps.

At T=300K we still have $R_d \ll R_{ph}$, i.e. $R_\mathrm{d} \approx R_0$. Hence, from Eqs. (3.116) and (5.8) we have:

$$P_L = \frac{1}{2} m^2 I_{ph}^2 \left[\frac{R_0+R_S}{R_0+R_S+R_L}\right]^2 R_\mathrm{L} \quad (5.9)$$

with $R_0 + R_s = Re[Z_{QWIP}(\omega_b = 0)] = 40\Omega$ (see Fig. 5.13(d)). Since Eq. (5.9) also depends on the sum $R_0 + R_s$, in this case the values of $R_0$ and $R_S$ are determined by fitting the measured FR over the full frequency range using Eq. (5.3) (with $m \times I_{ph} = 1.7$mA). The best agreement is obtained with $R_0 = 40\Omega$ and $R_s = 0$ (Fig. 5.17). As shown in Fig. 5.13(c), (d), contrary to what happens at low bias, the computed impedances at high bias provide only an approximated value of the actual QWIP impedance.

### 5.2.6 Evaluation of carriers capture and transit times

**T = 77K, $V_{\mathrm{bias}}$ = 3.4V.**

From the responsivity reported in Fig.5.5 (c) at $P_\mathrm{tot} = P_1 + P_2$ =33.5mW, we obtain $g(77\mathrm{K}, 3.4\mathrm{V}) = \tau_c/\tau_{tr} \simeq 1.25$ (i.e. ~ half the value at low incident power $g \simeq 2.5$). The roll-off time constant $\tau$ can therefore be approximated by the transit time [4]. From the fit of Fig.5.17, we then have that τ $\simeq \tau_{tr} \simeq$ 8ps and $\tau_c = 1.25 \times \tau_{tr} \simeq 10$ps

**T = 77K, $V_{\mathrm{bias}}$ = 1.1V.**

We have that that $I_{ph} \propto g$, therefore (see Table 2):

$g$(77K, 1.1V) =$g$(77K, 3.4V)× $\frac{I_{ph}(77K,1.1V)}{I_{ph}(77K,3.4V)}$ ≃1.25× $\frac{0.49mA}{15.2mA} = 0.04$ (5.10).

The roll-off time constant τ can therefore be approximated by the capture time. From the fit of Fig. 5.17, we then have that τ $\simeq \tau_c \simeq$ 1ps, and $\tau_{tr} = \tau_c/0.04 \simeq 25$ps.

**T = 300K, $V_{bias}$ = 0.9V**.

Following the same procedure described above we obtain obtain $g$(300K, 0.9V) $\simeq 0.011$. From the fit of Fig.5.17, we then have that $\tau \simeq \tau_c \lesssim$ 1ps, and $\tau_{tr} \gtrsim \tau_c/0.011 \simeq$ 90ps.

**T = 300K, $V_{bias}$ = 2.5V**.

Following the same procedure described above we obtain $g$(300K, 2.5V) $\simeq 0.18$. From the fit of Fig.5.17, we then have that $\tau \simeq \tau_c \simeq$ 2.5ps, and $\tau_{tr} \simeq \tau_c/0.18 \simeq$ 14ps.

### 5.2.7 Power dependence

In addition to the FR, we measured the relation between the heterodyne power (at 20 GHz) and incident optical power by illuminating the detector with one QCL kept at a constant power, $P_{QCL-1}$ = 8 mW, while changing the power, $P_{QCL-2}$, of the second one. Fig. 5.18 shows the results of these measurements at 77K and 300K. We find a rather linear dependence. In fair agreement with Fig. 5.5(c) (black curves) we observe a rather linear dependence up to ~10dBm, followed by a weak saturation.

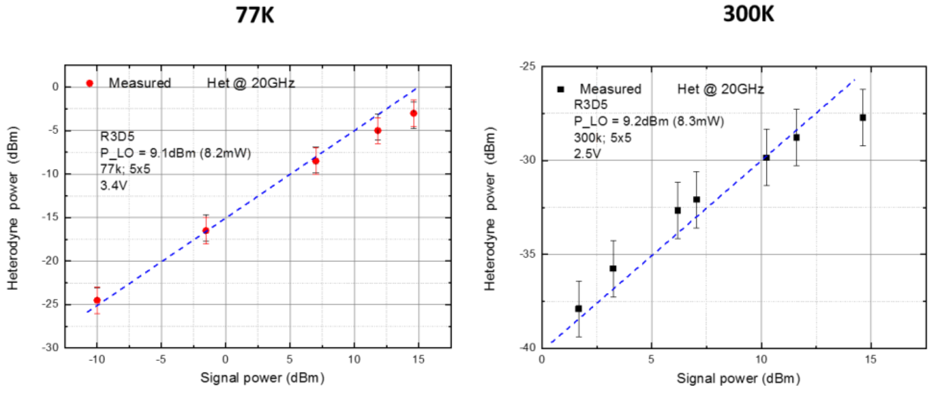

Figure. 5.18. Heterodyne power vs signal power up to 25-30mW total power (a) at 77K-3.4V, (b) at 300K-2.5V.

### 5.2.8 dc characterization and frequency response of QWIP-2 PARs detector

*dc characterization of PARs detector based on QWIP-2 active region*

So far, we described the characterization of the PARs QWIP based on QWIP-1 active region. In this section, we present a short summary of the characterization of the PARs QWIP based on QWIP-2 active region, which, compared to QWIP-1, is based on thinner QWs (Fig.4.1 and Fig.4.2) giving rise to a bound-to-continuum transition. Representative dc characterizations of a 5x5 PARs array (see Fig. 4.40 (b)), obtained as described in Section 5.2, are shown in Fig. 5.19 at T = 77K and 300K.

By comparing with Fig.5.5 (a) (b), we find that both QWIP-2's dark current and photocurrent are significantly lower than QWIP-1's at the same bias, which we attribute to a higher Schottky contact resistance. This interpretation is supported by the fact that at T = 77K we find that the photocurrent saturates for an applied bias of approximately 5V (Fig. 5.19(a)), contrary to 3.8V for QWIP-1 (Fig. 5.5(a)). Indeed, as explained in Section 5.1.3 we attribute the saturation of the photocurrent to the onset of negative differential drift velocity due to intervalley scattering, with expected saturation fields in the 10-20kV/cm range that should be identical for QWIP-1 and QWIP-2 active regions [2]. At 77K and low incident power (up to 12.3mW in Fig.5.19(a)) we find a non-monotonic dependence of the photocurrent on the applied bias for which, at the moment, we do not have a clear explanation.

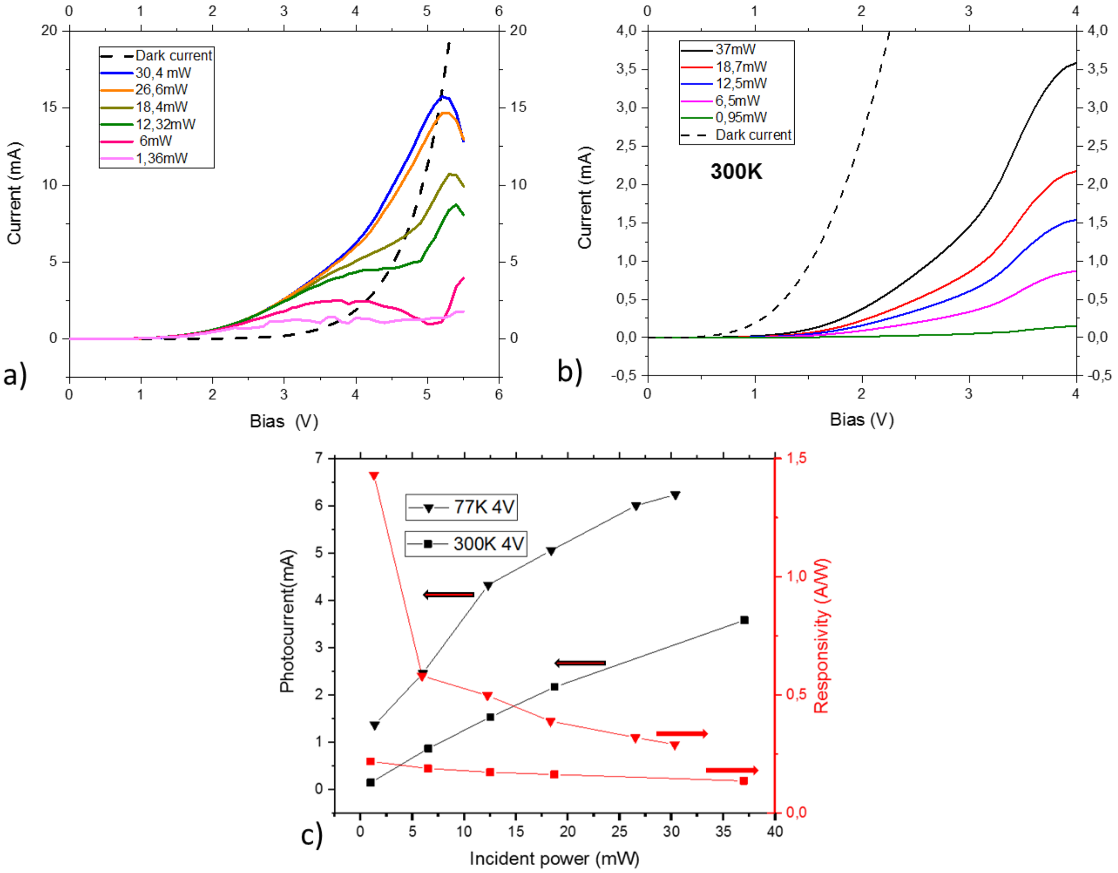

Figure. 5.19. Photocurrent vs applied bias (solid lines) for a 5x5 array PARs QWIP based on QWIP-2 active region, under different incident powers at (a) 77K and (b) 300K. The dark current I/V characteristics are shown in dashed. (c) Photocurrents (black dots) and responsivities (red dots) vs incident power, measured at 4V, 300K (squares) and 4V, 77K (triangles).

Figure 5.19 (c) shows the responsivity vs the incident power for QWIP-2, measured at 300K (squares) and 77K (triangles) under an applied bias of 4V. The maximum responsivity at 300K-4V (~0.25A/W) is higher than the responsivity of QWIP-1 at 300K-2.5V (~ 0.15A/W) at low incident power; the responsivity at 77K-4V of QWIP-2 (~1.5 A/W) is the same as the responsivity of QWIP-1 (~1.5 A/W; 77K- 3.4V) at low incident power, with a more pronounced reduction as the incident power increases. As discussed in Section 5.2, we attribute the saturation of the responsivity with incident power to the series resistance introduced by the Schottky contacts. Again, compared to QWIP-1, the more pronounced saturation observed on the detector based on QWIP-2 active region, points towards a higher Schottky series resistance.

*Frequency response of PARs detector based on QWIP-2 active region*

As discussed in Chapter 4, I realized 2 sets of devices based on QWIP-2 active region: a 3x3 and a 5x5 square of PARs of side *s*=1.8 µm and period *p*=5 µm (see Fig. 4.40). To characterize their FR I have used the setup and the technique described in Section.5.2.1.

The heterodyne spectra (corrected by the insertion loss and QCLs power variations) of the 5x5 array at 300K/77K at 4V are shown in Fig.5.20. At 300K – 4V we obtain a flat FR up 67GHz (black circles in Fig. 5.20 (a)). The measured heterodyne power is very close to the heterodyne power of QWIP-1 at 300K-2.5V (Fig.5.15 and Fig.5.17). Fig.5.20 (b) shows the heterodyne spectrum obtained at 77K, under an applied bias of 4V. Compared to QWIP-1 (Fig.5.15 and Fig.5.17) we find a steeper roll-of at low frequency, with a 3dB-cutoff of ~15GHz. The overall power drop, ~10dBm from 1GHz to 67GHz, is instead comparable. Concerning the heterodyne power, compared to QWIP-1 (77K 3.5V), we find a decrease of ~ 8÷9 dB. This agrees with the fact that the ratio between the photocurrent of QWIP-2 (at 77K-4V) and of QWIP-1 (at 77K-3.5V) is around 1/3, which means a factor ~9 reduction in power (~10dB). However, as for the FR at 300K, a quantitative comparison between the FRs of the two detectors would require a complete modelling of QWIP-2 detector, based on the impedance measurements and on the equivalent circuits of Fig.5.11. In this respect, we note that, at T=77K, under an applied bias of 5V we found a heterodyne power of -18dBm at 1GHz, i.e. ~8dBm below that obtained at 4V (Fig.5.20(b)), which yielded the maximum heterodyne power despite a lower *dc* photocurrent ($I_{ph} \approx$6mA at 4V and $I_{ph} \approx$15mA at 5V – see Fig.5.19).

The FR of a representative 3x3 PARs array, measured at T = 300K, under an applied bias of 4V, is reported in Fig. 5.21: as for the 5x5 array, the spectrum is virtually flat up to 67GHz. The heterodyne power is 8÷9 dB lower compared to the 5x5 array under the same operating conditions (300K-4V). This is in agreement with the observed reduction of the photocurrent by a factor of ~3 (not shown), stemming from the decrease of the overall collection area, from ~202µm$^2$ (= 0.9*9 x p$^2$) for the 3x3 array, to ~562µm$^2$ for the 5x5 array.

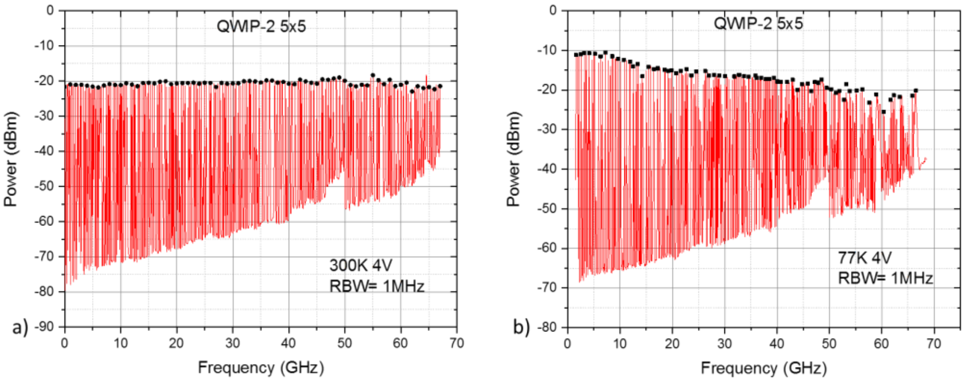

Figure. 5.20. Heterodyne beat spectra of a 5x5 array of PARs based on QWIP-2 active region, corrected by the attenuation and QCL power change, following the same procedure used to obtain the spectrum of Fig.5. 15 (b). (a) 300K, 4V. (b) 77K, 4V.

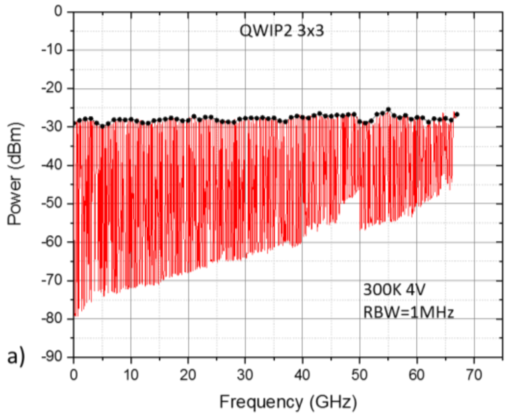

Figure. 5.21. Heterodyne beat spectrum of a 3x3 array of PARs based on QWIP-2 active region, corrected by the attenuation and QCL power change, following the same procedure used to obtain the spectrum of Fig.5. 15 (b). The spectrum is measured at 300K, under an applied bias of 4V.

## 5.3 Conclusions

In this chapter we have characterized the FR of the fabricated PARs QWIP photodetectors and derived, for QWIP-1 active region, the carrier's capture and transit times at different operating temperatures and applied biases. The first main conclusion of this study is that at 300K the intrinsic response time of the QWIP is dictated by the electron's capture time of the order of 1-2ps, with a much longer transit time, of ~90ps at low bias, down to ~10ps at high bias. At 77K, while at low bias we observe a rather similar situation ($\tau_c$ ~1ps and $\tau_{tr}$ ~25ps), at high bias we find instead a dramatic increase of $\tau_c$ to approximately 10ps. As a result, compared to the other operating conditions, where the measured FR is flat up to 70GHz (neglecting the drop at low frequency due to the contact capacitance), at 77K the QWIP FR bandwidth shows a transit time-limited 3dB cutoff of approximately 30GHz ($\tau_{tr}$ ~8ps). From T = 300K to 77K the observed increase in responsivity from ~0.1A/W to 0.75A/W at high bias, is also dominated by the increase of $\tau_c$ from 2.5ps to 10ps.

The second main conclusion is that, as expected, the presence of Schottky contacts is detrimental for QWIP operation, producing (i) an overall reduction of the heterodyne conversion efficiency, (ii) a saturation of the photoresponse at high powers, and (iii) a drop of conversion efficiency at low frequency due to the presence of the contact parasitic capacitance.

Finally, we always find a flat FR up to 70GHz at room temperature and high bias, regardless on the size of the array (3x3 – not shown for QWIP-1 - and 5x5). This is consistent with the fact that according to Table 2, the Schottky resistance at 300K, can be neglected, yielding, from the small-signal circuit of Fig.5.11, a parasitic 3dB cutoff of (1+$R_{\mathrm{L}}/R_0$)/(2*pi* $R_{\mathrm{L}}C_{\mathrm{PAR}}$ ) ~220GHz for the 5x5 patch array, i.e. ~600GHz for the 3x3 array.

# Bibliography

[1] H. C. Liu, . J. Li, E. R. Brown, K. A. McIntosh, K. B. Nichols et M. J. Manfra, "Quantum Well Intersubband Heterodyne Infrared Detection Up to 82 GHz", *Appl. Phys. Lett,* vol. 67, no. 1594, 1995.

[2] H. Schneider, C. Mermelstein, R. Rehm, C. Schönbein, . A. Sa'ar et M. Walther, "Optically induced electric-field domains by bound-to-continuum transitions in n-type multiple quantum wells", *Phys. Rev. B ,* vol. 57, 1998.

[3] M. Ershov, H. C. Liu, M. Buchanan et Z. R. Wasilewsk, "Photoconductivity nonlinearity at high excitation power in quantum well infrared photodetectors", *Appl. Phys. Lett,* vol. 70, no. 414, 1997.

[4] H. Schneider et H. C. Liu, "Quantum Well Infrared Photodetectors: Physics and Applications", Springer, 2007.

[5] S. Steinkogler, H. Schneider, R. Rehm, M. Walther, P. Koidl, P. Grant, . R. Dudek et H. Liu, "Time-resolved electron transport studies on InGaAs/GaAs-QWIPs", *Infr. Phys. Technol,* vol. 44, no. 355, 2003.

[6] C. G. Bethea, F. Levine, G. Hasnain, J. Walker et R. J. Malik, "High-speed measurement of the response time of a GaAs/AlxGa1-xAs multiquantum-well long-wavelength infrared detector", *J. Appl. Phys,* vol. 66, no. 963, 1989.

[7] P. D. Coleman, R. C. Eden et J. N. Weaver, "Mixing and Detection of Coherent Light", *IEEE Trans. Electron Devices,* vol. 11, no. 488, 1964.

[8] P. D. Coleman, . R. C. Eden et . J. N. Weaver, "Mixing and Detection of Coherent Light", *IEEE Trans. Electron Devices,* vol. 11, no. 488, 1964.

# 6. Conclusions and outlook

## 6.1 Summary of the main results

The main result of this Thesis has been the demonstration of a GaAs/$Al_{0.2}Ga_{0.8}As$ heterostructure QWIP detector based on patch-antenna technology, showing a flat frequency response up to, and beyond, 70GHz at room temperature with a responsivity of 0.15A/W. A flat RF bandwidth as also been demonstrated at 77K, although not at the maximum responsivity of 1.5A/W, for which we find instead a 3dB cutoff of ~30GHz.

My most important contribution to this work has been, first of all, the demonstration of a complete and reproducible micro-fabrication process for the realization of a 2D array of ~500nm-thick, GaAs/$Al_{0.2}Ga_{0.8}As$-based PARs, electrically connected by fully suspended metallic bridges, forming the core of the QWIP detector. In addition, I have fabricated a 50Ω coplanar waveguide, monolithically integrated to the 2D array, providing a broadband microwave access to the device. In the second part of the Thesis, I have performed a complete electro-optical characterization of the device, from the measurement of its optical properties (reflectivity, polarization dependence), to the assessment of its *dc* characteristics (dark current, photocurrent, responsivity), and the characterization of its FR. For this last measurement I have contributed to the realization of a dedicated MIR optical bench, based on two DFB QCLs, allowing the measurement, from 77K to 300K, of the QWIP heterodyne response up to 67GHz. In the last part of the Thesis I have done a quantitative modelling of the FR and of the QWIP impedance, based on a small-signal equivalent circuit. Through this modelling I have obtained a parasitic RC time constant $\lesssim$1ps. Thanks to this exceptionally low value, I have been able to extract the intrinsic carrier's capture and transit times under different operating conditions. In particular this analysis has shown that at T = 300K the device FR is limited by the carriers capture time, with an upper limit of ~1ps. This is the case also at T = 77K at low bias, while at high bias the high-frequency roll-off is governed by the electron's transit time of ~8ps. This the first time that the experimental measurement of the electronic FR of a QWIP detector allows to extract information on the carrier's lifetimes, demonstrating that it is indeed possible to realize a QWIP with a ps-long response time. These conclusions have been confirmed through the fabrication of two generations of detectors, based on two slightly different GaAs/$Al_{0.2}Ga_{0.8}As$ MQW heterostructures.

The results summarized above are just a first demonstration and set the basis for future work, on one hand for the improvement of the actual photodetector performance, on the other hand, to explore the possibility to exploit the demonstrated devices, rather than as detectors, as MIR photomixers, for the generation of sub-mm wave and THz radiation.

## 6.2 Improving the performance of the PARs QWIP

From this study it clearly appears that a first issue to address is related to the Schottky contacts. As demonstrated in Chapter 5, the latter introduce an additional resistance in series with the QWIP active region, which has the effect of reducing the voltage drop on the QWIP active region for a given applied external bias, resulting into (i) a drop of responsivity with increasing optical power (Fig.5.5(c)), and (ii) a reduction of the generated heterodyne power. For instance, in the device studied in this thesis, the impact of the Schottky contact resistance on the heterodyne power at T = 77K, can be estimated from Eq.(3.116), yielding the photocurrent as a function of the external bias, and the expressions of the power dissipated in the load, given by Eq.(5.6) (low bias) and Eq.(5.8) (high bias). From these equations, and using the values of $R_0$ and $R_s$ in Table 2 (and remembering that at low temperature $R_d >> R_0, R_s$), we compute a power increase of ~+3dB and ~+8dB respectively at high (3.4V) and low (1.1V) bias, in the case where $R_s$ is negligible compared to $R_0$. Similarly, we compute an increase of ~+8dB at T = 300K and low bias (0.9V). To remove the Schottky contacts, a new processing, to which I have contributed, is presently under way, based on Pd/Ge/Ti/Au metallic contacts leading, after annealing, to ohmic contacts presenting (i) a low contact resistance, (ii) a good surface morphology and (iii) a low diffusion.

In terms of device performance, another parameter that it should be possible to improve significantly is the PARs QWIP responsivity. In the ideal case of unit external quantum efficiency (1 incident photon → 1 photoelectron) the responsivity is given by R [A/W] = $\left(\frac{h\nu}{e}\right)^{-1}$, which, at 10µm wavelength, gives 8.3 A/W, assuming a photoconductive gain g = 1. The maximum responsivity obtained experimentally at 10.3µm with the device studied in this work is instead 1.5A/W (T=77K and 3.4V bias, with an incident power < 10mW – see Fig.5.5(c)). From Eq. (5.1), considering the measured PARs array absorption (Fig.4.4(a), black line) and an ISB transition centered at 107meV (Fig.5.4(d)), I obtain the responsivity spectrum of Fig.5.6, showing that (i) the experimental value of the responsivity is consistent with a photoconductive gain g = 2.5, and that (ii) a peak responsivity of 4.5A/W should be observed at 11.2µm wavelength. Again, from Eq.(5.1), I predict a peak responsivity close to 9A/W, in the case where the peak of the PARs array absorption is coincident with that of the ISB transition. As explained at the end of Section 4.2, compared to QWIP-1, the detector based on QWIP-2 active region should satisfy better this condition, and therefore yield a higher responsivity. At the moment I don't have a clear explanation why we observe the same maximum responsivity at low temperature (and low power) for QWIP-1 and QWIP-2. Clearly, to shed light on this issue, measurements of the photocurrent spectra of QWIP-2 processed in a mesa geometry and in a PARs array geometry must be done. Another very useful measurement would be an experimental assessment of the PARs QWIPs responsivity using a broadly tunable external cavity QCL that allows covering the full detector spectrum.

Despite these initial results and pending measurements, based on the above considerations, I don't see any fundamental reason that should prevent a significant improvement of the responsivity, by adjusting the lateral size of the PARs in order to find an optimum match between the $TM_{100}$ mode frequency and the peak of the ISB transition.

In terms of photodetection, as I have discussed in Section 3.5.2, besides enabling the implementation of coherent detection schemes, the main advantage brought by heterodyne detection is the possibility to operate QWIPs in the shot-noise regime, overcoming the noise contribution of the thermally activated dark current, which severely impacts the NEP of MIR QWIPs at high temperature. As shown in Fig. 5.5, this is not possible at 300K, where the dark current is much larger than the photocurrent. Instead, at 77K, it should be possible to operate the QWIP as a shot-noise limited heterodyne receiver with only a few mW of local oscillator power. Demonstrating experimentally this possibility by combining the QWIP detector developed in this thesis with a suitable low-noise amplifier (probably operating at low temperature) would be a very nice achievement. To this end it would be first necessary characterize the noise of the QWIP using an FFT analyzer.

Concerning the frequency response of the detector at 77K and high bias, although the actual ~30GHz 3dB cutoff is probably sufficient for most applications (including free-space communications), based on the fact that the response appears to be limited by the transit time it should be possible to expand the RF bandwidth by reducing the thickness of the QWIP active region. This could be done by reducing the width of the barrier: we expect that it should be possible to reduce the latter from the actual 40nm, down to ~20nm without increasing significantly the inter-well tunneling, hence the dark current [1]. In this respect, as pointed out above, when the QWIP is operated as heterodyne receiver, a higher dark current can be compensated by increasing the LO power, which could further relax the constraint on the minimum barrier width. Clearly, this is a question that would be worth investigating experimentally. Another possibility, is to reduce the number of periods of the active region, which, according to Eqs.(3.74)-(3.77), should leave the responsivity unaltered, as long as $Q_{cav}$ (Eq. (3.76)) does not change significantly: how far the number of periods can be reduced without reducing the responsivity because of higher absorption in the metal + contact layers, and how this affects the QWIP RF bandwidth is another question that should be addressed experimentally. In terms of RC cutoff, reducing the thickness of the active region is detrimental since it increases the device parasitic capacitance. However, as we have shown in Chapter 5, the actual RC cutoff for a 5x5 array is > 150GHz, which makes a reduction of the active region thickness by a factor of two compatible with a bandwidth of ~70GHz. Moreover, if more bandwidth is needed, the size of the array can be reduced at the expense of a lower responsivity due to a reduced collection.

## 6.3 PARs QWIPs as MIR photomixers for sub-mm and THz generation

To pursue the work initiated in this Thesis, it is clear that it would be worth extending the RF characterization of the PARs QWIPs FR beyond 70GHz, up to, possibly, several hundreds of GHz or more. Firstly, this would allow to confirm experimentally the conclusions drawn in Chapter 5 about the RC and intrinsic time constants, based on the equivalent-circuit model. Secondly it would allow to explore the relevance of exploiting the QWIP devices as photomixers for the generation of sub-mm/THz radiation.

In traditional photomixers based on GaAs or InGaAs, two CW laser diodes emitting at 800nm or 1500nm are used to create electron-hole pairs through interband absorption [2]. These are then accelerated by applying a bias between two metallic electrodes (or by the built-in potential in the case of PN junctions), thus generating a photocurrent that beats at the difference frequency between the two laser sources. Analogously to what shown in Section 5.2, by tuning the two laser frequencies, their difference can be changed at will and can therefore span from virtually *dc* to the THz range. Usually the metallic electrodes are patterned in a broadband antenna, in order to allow free space coupling of the electromagnetic wave generated by the oscillating photocurrent. As for the heterodyne power dissipated by the QWIP detector into the load resistance (Eq.(5.3)), the THz power emitted by a photomixer is proportional to the square of the generated photocurrent, which, in turns, is proportional to the photomixer responsivity. As a result, for the same optical power, a photomixer based on MIR pump photons rather than near-IR photons, allows theoretically a gain of a factor $(\frac{v_{near-IR}}{v_{mid-IR}})^2$, i.e. from 25(7) to 150(45) if pump photons at 800nm(1550nm) are replaced with photons at 4µm or 10µm respectively.

In real-life photomixers, optical responsivities are actually rather far from the ideal $\left(\frac{hv}{e}\right)^{-1}$ = 0.65A/W at $\lambda$=800nm (1.2A/W at $\lambda$=1550nm), with typical values of a few $10^{-1}$ A/W, for planar GaAs-based photomixers operating at 800nm, up to record ~0.1 ÷ 0.2A/W for vertical photomixers operating up to ~300GHz or UTC photodiodes pumped at 1550nm wavelength [3][4]. This makes the responsivities achieved in this Thesis already particularly appealing.

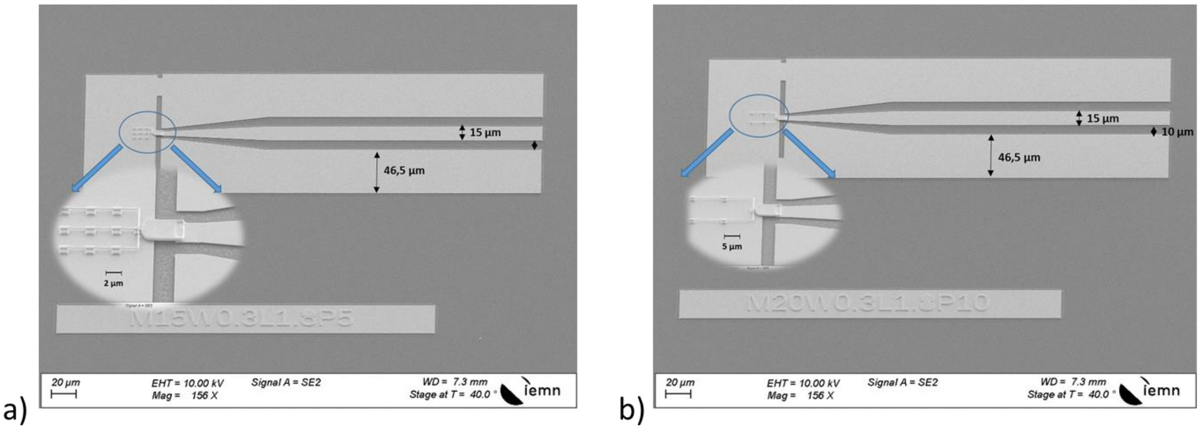

Figure 6.1. SEM photographs of fabricated PARs QWIPs based on QWIP-2 active region, featuring a CPW adapted to the 25-µm-pitch of THz coplanar probes. (a) 3x3 PARs array with s= 1,8µm and p=5µm. (b) 2x2 PARs array with s= 1,8µm and p=10µm.

To allow investigating the PARs QWIP FR beyond 70GHz, and up to 1THz or more I have fabricated two new sets of devices, as shown in Fig.6.1 based on the QWIP-2 active region and Fig.6.2 based on the QWIP-1 active region. The first set of devices (Fig.6.1) exploits a much narrower CPW compared to that of Fig. 4.22, adapted to the 25-µm-pitch of THz coplanar probes. By combining this probe with harmonic mixers available at IEMN, it will be possible to extend the characterization of the FR up to approximately 1THz. As shown in Fig.6.2, in the second set of devices, the PARs array is instead coupled to a log-spiral antenna, allowing the emission of the difference frequency signal, directly in free-space. This device realizes de facto a MIR-pumped QWIP photomixer. Similarly to standard interband photomixers [2], it will be illuminated by two QCLs from the back of the substrate using a Silicon hemispheric lens. The generated signal will then be irradiated in free-space and measured with the help of a Silicon bolometer, operating up to a few THz. The electro-optical characterization of the devices shown in Fig.6.1 and Fig. 6.2 is presently under way.

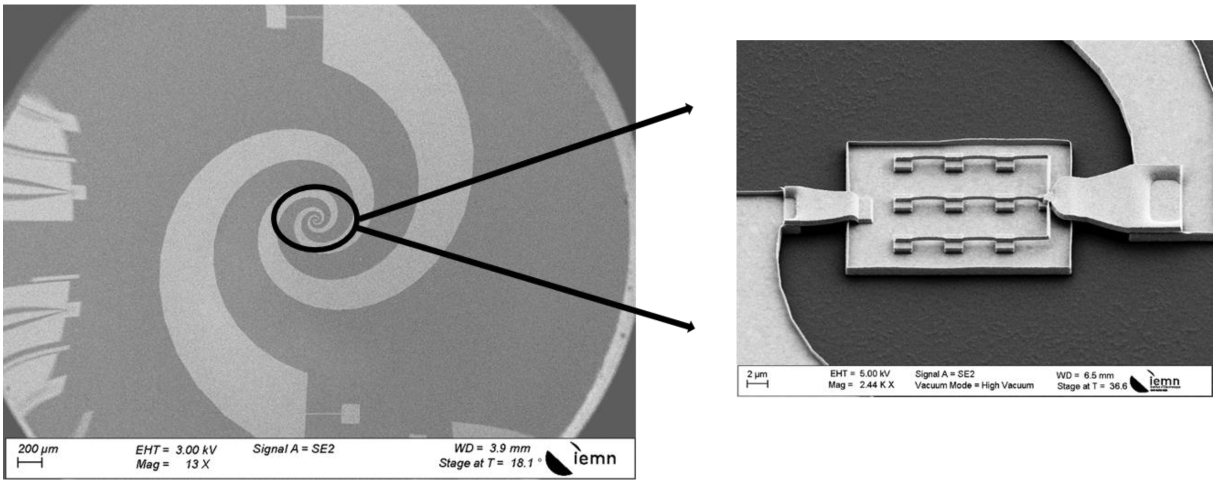

Figure 6.2. SEM photographs of a fabricated PARs QWIP based on QWIP-1 active region, featuring an integrated log-spiral antenna for free-space emission. The device shown is based on a 3x3 array of PARs with s= 1,9µm and p=5µm.

In addition to THz generation by pumping with CW QCLs, the envisaged MIR photomixers are also relevant in the context of MIR QCL frequency combs. These devices have been developed during the last decade, and display a rich phenomenology and physics that is only starting to be fully understood based on the non-linear Schrodinger equation [5] [6]. Thanks to the inherent broad gain of QCLs, that can be artificially tailored through bandgap engineering, MIR QCL combs with spectra spanning up to several THz have been demonstrated, and, equally interestingly, so-called harmonic combs have been experimentally observed [7] [8]. These devices, lasing takes place on Fabry-Perot modes separated by many cavity free spectra range, leading to intermodal spacing from several tens up to several hundreds of GHz. Thanks to the high degree of correlation among the Fabry-Perot modes, using QCL harmonic combs to pump MIR photomixers such as those shown above would allow the generation of sub-mm and, possibly, THz waves with much higher spectral purity compared to pumping with two different DFB QCLs. Such waves could find applications in future wireless terahertz communication links [9].

# Bibliography

[1] K. S. Steven, "Effect of barrier width on the performance of quantum well infrared photodetector", *Infrared Physics & Technology,* vol. 42, pp. 115-121, 2001.

[2] S. Preu , "Tunable, continuous-wave Terahertz photomixer sources and applications", *J. Appl. Phys,* vol. 109, no. 061301, 2011.

[3] E. Peytavit, "Milliwatt-level output power in the sub-terahertz range generated by photomixing in a GaAs photoconductor", *Appl. Phys. Lett,* vol. 99, no. 223508, 2011.

[4] C. Renaud, "Antenna Integrated THz Uni-Traveling Carrier Photodiodes", *IEEE J. Sel. Top. Quantum Electron,* vol. 24, no. 8500111 , 2018.

[5] D. Burghoff, "Unraveling the origin of frequency modulated combs using active cavity mean-field theory", *Optica ,* vol. 7, pp. 1781-1787, 2020.

[6] N. Opačak et B. Schwarz, "Theory of frequency-modulated combs in lasers with spatial hole burning, dispersion, and Kerr nonlinearity", *Phys. Rev. Lett,* vol. 123, no. 243902 , 2019.

[7] T. s. Mansuripur, C. Vernet, P. Chevalier, G. Aoust, B. Schwarz, F. Xie, C. Caneau, K. Lascola, C. E. Zah, D. P. Caffey, T. Day, L. J. Missaggia, M. K. Connors, C. A. Wang, A. Belyanin et F. Capasso, "Single-mode instability in standing-wave lasers: the quantum cascade laser as a self-pumped papametric oscillator", *Phys. Rev,* vol. 94, no. 063807, 2016.

[8] D. Kazakov , M. Piccardo, Y. Wang, P. Chevalier, T. S. Mansuripur, F. Xie, C. Zah, K. Lascola, A. Belyanin et F. Capasso, "Self-starting harmonic frequency comb generation in a quantum cascade laser", *Nat. Photonics ,* vol. 11, p. 789–792, 2017.

[9] T. Nagatsuma, G. Ducournau et C. C. Renaud, "Advances in terahertz communications accelerated by photonics", *Nat. Photon,* vol. 10, p. 371–379 , 2016.

# Publications

[1] M. Hakl*, Q. Lin*, S. Lepillet, J-F. Lampin, S. Pirotta, R. Colombelli, W. J.Wan, J. C. Cao, H. Li, E. Peytavit, and S. Barbieri, "Ultrafast quantum-well photodetectors operating at 10µm with flat frequency response up to 70GHz at room temperature". *ACS photonics*, American Chemical Society, 2021, 8 (2), pp.464-471.

[2] F. Bavedila, C. Tannoury, Q. Lin, S. Lepillet, V. Avramovic, E. Okada, D. Yarecka, M. Faucher, D. Troadec, J–F. Lampin, G. Ducournau, G. Loas, V. Magnin and E. Peytavit, "Development of a Travelling wave THz photomixer for mW power level and multi-THz Frequency range operation". *Journal of Lightwave Technology*, vol. 39, no. 14, pp. 4700-4709, July15, 2021, doi: 10.1109/JLT.2021.3078226.

# Conferences

Poster. Q. Lin, M. Hakl, S. Pirotta, R. Colombelli, H. Li, J. C. Cao, J-F. Lampin, E. Peytavit, and S.Barbieri*. "Development of high-speed patch-antenna mid-infrared photodetectors at 10.3um". French-German THz conference, FGTC 2019, (Gartenschau, Germany).

Oral Presentation. Q. Lin, M. Hakl, S. Pirotta, R. Colombelli, H. Li, J. C. Cao, J-F. Lampin, E. Peytavit, and S. Barbieri*. "Development of high-speed patch-antenna mid-infrared photodetectors at 10.3um". International Conference on Infrared, Millimeter, and Terahertz Waves, IRMMW-THz 2019, Article number 8874176, (Paris, France)

Oral Presentation. Q. Lin, M. Hakl, S. Pirotta, R. Colombelli, H. Li, J. C. Cao, J-F. Lampin, E. Peytavit, and S. Barbieri*. "Development of high-speed patch-antenna mid-infrared photodetectors at 10.3um". Photonics West 2020 (San-Francisco, USA).

Oral Presentation. Q. Lin, M. Hakl, S. Pirotta, R. Colombelli, H. Li, J. C. Cao, J-F. Lampin, E. Peytavit, and S. Barbieri*. "Development of high-speed patch-antenna mid-infrared photodetectors at 10.3um". International Conference on Infrared, Millimeter, and Terahertz Waves, IRMMW-THz 2020, Article number 9370361, (Buffalo, USA).

Poster. Q. Lin, M. Hakl, S. Pirotta, R. Colombelli, H. Li, J. C. Cao, J-F. Lampin, E. Peytavit, and S. Barbieri*. "Development of high-speed patch-antenna mid-infrared photodetectors at 10.3um". International Quantum Cascade Laser School and Workshop, IQCLSW 2020, (Ascona, Switzerland)